Experimental investigation into non-Newtonian fluid flow through gradual contraction geometries

Thesis submitted in accordance with the requirements of the University of Liverpool for the degree of Doctor in Philosophy

by

Fiona Lee Keegan

September 2009

Acknowledgements

I would like to start by thanking my two supervisors, Dr. R.J. Poole and Professor M.P. Escudier. Without their constant guidance, support and encouragement this thesis would not have been possible. I must also thank EPSRC for funding my research.

I am grateful to have shared an office and a lab at various times in the last four years with Dr. A.K. Nickson, Dr. S. Rosa and Mrs. A. Japper-Jaafar. They have been a great source of moral support as well as providing technical help and asking challenging (but useful!) questions.

Without the assistance of our excellent technical support team I would not have been able to perform any of the experiments needed to write this thesis. I'd particularly like to thank John Curran, John McCulloch, Steven Bode and Derek Neary. I would also like to thank Janet Gaywood, Nataly Jones and Elaine Cross for their support to our research group.

I am thankful for an opportunity to visit Unilever in Port Sunlight and use one of their rheometers to perform some measurements. For this I must thank Dr. A Kowalski and Mr. G. Roberts for taking time out from their work to assist me and for making me feel very welcome there.

All of my friends have constantly supported me throughout the last 4 years. Special thanks go to Claire Jones for listening, trying to understand and remembering what I've been doing and Claire Batty for keeping me sane nearly every Wednesday night for the last 2 years.

Finally I'd like to thank my (ever expanding) family for always being there for me and believing in me when things get difficult, especially my mum, Deborah, whose belief that you can achieve anything if you work hard enough is inspirational.

Summary

This thesis presents the results of an investigation into the flow of several non-Newtonian fluids through two curved gradual planar contractions (contraction ratios 8:1 and 4:1). The objectives were to determine whether a newly discovered effect (velocity overshoots were observed in the flow of a 0.05% polyacrylamide solution close to the sidewalls of a gradual contraction followed by a sudden expansion by Poole *et al.*, 2005) could be reproduced in the absence of the expansion, learn more about the phenomenon and to provide a comprehensive set of experimental results for numerical modellers to compare their results to. Previous research on contraction flows, both numerical and experimental, has been summarised.

The fluids investigated were a Newtonian control fluid (a glycerine-water mixture), four concentrations of polyacrylamide (PAA), varying from the 'dilute' range to the 'semi-dilute' range and two concentrations of xanthan gum (XG), both in the 'semi-dilute' range. All fluids were characterised using shear rheology techniques and where possible extensional rheology measurements were also undertaken. This characterisation showed that both PAA and XG are shear-thinning fluids but XG is less elastic than PAA. The fluid properties determined from the characterisation were used to estimate various non-dimensional numbers such as the Reynolds and Deborah numbers, which can then be used to characterise the flow.

The flow under investigation was the flow through a gradual contraction section. Two smooth curved planar gradual contractions were used: the contraction ratios were 8:1 and 4:1. The contractions were made up of a concave 40mm radius followed by a convex 20mm radius. The upstream internal duct dimensions were 80mm by 80mm in both cases and the downstream internal duct dimensions were 80mm by 10mm for the 8:1 contraction and 80mm by 20mm for the 4:1 contraction. Polymer degradation within the test rig was assessed and the maximum time that the solutions could be reliably used was found to be six hours. The fluid velocity was measured at discrete locations within the flow using laser Doppler anemometry (LDA), which is a non-intrusive flow measurement technique. In both contractions

measurements were taken across the XZ-centreplane (side to side) and in some cases across the XY-centreplane (top to bottom).

The flow of the Newtonian control fluid through the 8:1 contraction was as expected with the flow flattening into the 'top hat' shape usually observed in Newtonian flow through a gradual contraction (as utilised in wind tunnel design for example). The flows of 0.01% PAA ('dilute') and 0.07% XG ('semi-dilute') also flattened as the flow progressed through the 8:1 contraction as the Deborah numbers in these flows were very low. Velocity overshoots close to the plane sidewalls were observed in both the 0.03% and 0.05% PAA solutions through the 8:1 and 4:1 contractions. The overshoots through both contractions seemed to be influenced most by the Deborah number (i.e. the extensional properties of the flow and fluid). Velocity overshoots were observed in the 0.3% PAA solution through both contractions but they were different in shape to those seen at the lower concentrations. The overshoots were closer to the centre of the flow growing into one large 'overshoot' at the end of the contraction.

This investigation showed that the velocity overshoots can be reproduced in both the 8:1 and 4:1 gradual contraction in several concentrations of PAA providing the right parameters are met (i.e. fluid properties, flow rate etc.). Good quality sets of data have been produced, which can be used in the future by researchers interested in numerical modelling of non-Newtonian fluid flows through curved gradual contractions.

Contents

List of Tables

List of Figures

Figure 5.25: Non-dimensionalised (a) shear and (b) extensional stresses for 0.03% PAA in the 4:1 contraction at $Re \approx 115$, $De_C \approx 0.06$ (□) and $Re \approx 290$, $De_C \approx 0.13$ (■); (c) shear and (d) extensional stresses for 0.05% PAA in the 4:1 contraction at $Re \approx 30$, $De_C \approx 0.13$ (□) and $Re \approx 65$, $De_C \approx 0.24$ (■); (e) shear and (f) extensional stresses for 0.3% PAA in the 4:1 contraction at $Re \approx 2$, $De_C \approx 8.4$.

Nomenclature

a	power law index
A	cross sectional area (mm^2)
c	concentration
c^*	critical overlap concentration
CR	contraction ratio
d	downstream duct height (mm)
D	upstream duct height (mm)
D_1	fitting parameter (mm)
De	Deborah number
De_C	Deborah number from CaBER
De_{N1}	Deborah number from N_1
D_f	filament diameter (mm)
D_H	hydraulic diameter (mm)
$D_{mid}(t)$	filament diameter (mm)
D_P	platen diameter (mm)
E	modulus of elasticity (Young's modulus) (Pa)
El	Elasticity number
El_1	Elasticity number found using a Deborah number
$El_{1,C}$	Elasticity number 1 from CaBER
$El_{1,N1}$	Elasticity number 1 from N_1
El_2	Elasticity number found using a Weissenberg number
$El_{2,C}$	Elasticity number 2 from CaBER
$El_{2,N1}$	Elasticity number 2 from N_1
f_D	frequency of reflected light (Doppler burst) (Hz)
F_L	focal length of laser lens (mm)
F	force (N)
G_C	complex viscosity (Pa.s)
G'	storage modulus (Pa)
G''	loss modulus (Pa)
h	parallel plate gap height (m)
h_f	final sample height (mm)
h_i	initial sample height (mm)
H	double concentric cylinder height (mm)
k	power law index
k_1	fitting parameter (mm.s)
K	velocity overshoot quantifying factor
l	characteristic length scale (m)
L	contraction length (mm)
$\dot{m}$	mass flow rate ($kg.s^{-1}$)
n	parameter introduced by Yasuda *et al.* (1981)
n, n_1, n_2	refractive indices
n_f	refractive index of fluid
n_w	refractive index of the wall
N_1	first normal stress difference (Pa)
$N_1/2$	recoverable shear (Pa)
N_2	second normal stress difference (Pa)
N_S	sample size
P	wetted perimeter (mm)

r_1	concave radius of contraction (mm)
r_2	convex radius of contraction (mm)
r_a	position of probe (m)
r_f	position within flow (m)
R	radius (m)
R_1	internal radius of stationary cylinder (m)
R_2	internal radius of rotating cylinder (m)
R_3	external radius of rotating cylinder (m)
R_4	external radius of stationary cylinder (m)
R_d	convex radius of contraction (mm)
R_D	concave radius of contraction (mm)
R_O	outer radius of pipe (m)
Re	Reynolds number
t	thickness of the wall (m)
t	time (s)
t_1	fitting parameter (s)
t_2	fitting parameter (s)
T	characteristic time of a deformation process (s)
u	velocity ($m.s^{-1}$)
u_1	upstream flow velocity ($m.s^{-1}$)
u_2	downstream flow velocity ($m.s^{-1}$)
U	particle velocity ($m.s^{-1}$)
U_B	bulk velocity ($m.s^{-1}$)
U_C	centreline velocity ($m.s^{-1}$)
U_d	bulk velocity at the end of the contraction ($m.s^{-1}$)
U_L	velocity at change in velocity gradient ($m.s^{-1}$)
U_O	maximum overshoot velocity ($m.s^{-1}$)
U_{SQ}	bulk velocity in the square duct section ($m.s^{-1}$)
V_2	fitting parameter ($mm.s^{-1}$)
w	contraction width (mm)
Wi	Weissenberg number
Wi_C	Weissenberg number from CaBER
Wi_{N1}	Weissenberg number from N_1
x_{exp}	experimental data point
x_{th}	theoretical data point
x	longitudinal axis/direction
y	transverse axis/direction
z	spanwise axis/direction
Z_C	constant defined by Yanta & Smith (1973)
α	angle of cone (°)
$\dot{\gamma}$	shear rate (s^{-1})
$\dot{\gamma}_r$	relevant shear rate (s^{-1})
$\dot{\gamma}_{CH}$	characteristic shear rate (s^{-1})
$\dot{\gamma}_w$	wall shear rate (s^{-1})
δ	interference fringe spacing (m)
ΔF	reduction in force (N)
ε	strain
ε_H	Hencky strain
$\dot{\varepsilon}$	strain rate (s^{-1})

$\dot{\varepsilon}_c$	centreline strain rate (s^{-1})
η'	dynamic viscosity (Pa.s)
$\eta'(\omega)$	dynamic viscosity (Pa.s)
η	viscosity (Pa.s)
θ	angle between laser beams (°)
θ_1, θ_2	angles of refraction (°)
λ	characteristic time for the material / relaxation time (s)
λ_w	wavelength of laser light (m)
λ_C	relaxation time from CaBER (s)
λ_{CY}	constant representing onset of shear thinning in Carreau-Yasuda model (s)
λ_{N1}	relaxation time from N_1 (s)
Λ_f	final aspect ratio
Λ_i	initial aspect ratio
μ	viscosity (Pa.s)
μ_{CH}	characteristic shear viscosity (Pa.s)
μ_{CY}	shear viscosity calculated using the Carreau-Yasuda model (Pa.s)
μ_{EXP}	experimental shear viscosity (Pa.s)
μ_S	sample average
μ_w	shear viscosity at the wall (Pa.s)
$\mu(\dot{\gamma})$	shear viscosity (Pa.s)
μ_0	zero shear rate viscosity (Pa.s)
μ_∞	infinite shear rate viscosity (Pa.s)
$\lvert\mu^*\rvert$	complex viscosity (Pa.s)
ρ	density ($kg.m^{-3}$)
σ	extensional stress (Pa)
σ_D	standard deviation
τ	shear stress (Pa)
τ_c	centreline shear stress (Pa)
τ_w	wall shear stress (Pa)
ω	angular velocity ($rad.s^{-1}$)

1. Introduction

Much less is known about non-Newtonian fluid flow compared with the comprehensive knowledge we have about Newtonian fluid behaviour. Newtonian laminar flow has previously been particularly well researched. Virtually all man-made fluids, such as those used in manufacturing and other industries (for example polymer melts used to produce various plastic items and drilling mud used to assist oil retrieval) and everyday fluids like shampoo and toothpaste, are non-Newtonian and to this end it is extremely important to further develop the understanding of non-Newtonian fluid behaviour. Contraction flows, such as those we investigate in the current study, are particularly important in polymer processing techniques such as extrusion and injection moulding and also as so called 'benchmark' flows for validating and developing numerical simulation techniques.

1.1. Newtonian fluids

In 1687 Newton postulated in his *Principia* (translated, 1999),

> *The resistance which arises from the friction [*lit. *lack of lubricity or slipperiness] of the parts of a fluid is, other things being equal, proportional to the velocity with which the parts of the fluid are separated from one another.*

The *resistance* is equivalent to the shear stress (τ, Pa), the *friction [lack of slipperiness]* is now known as the viscosity (μ, Pa.s) and the *velocity with which the parts of the fluid are separated* is the velocity or shear rate ($\dot{\gamma}$, s^{-1}). Using these definitions the postulate says that the shear stress is proportional to the shear rate and the viscosity is the constant of proportionality, which gives the following equation,

$$\tau = \mu\dot{\gamma}. \qquad (1.1)$$

This law is linear and assumes that the shear stress is directly proportional to the strain, or rate of strain, regardless of the variation in stress. The most common fluids, water and air, followed Newton's postulate and it was not until the 19th century that scientists started to doubt that the postulate covered all fluids.

In the 19th century Navier and Stokes, independently of one another, developed a three-dimensional theory for Newtonian fluid flow. The Navier-Stokes equations are the governing equations for the flow of a Newtonian fluid.

Some examples of Newtonian fluid behaviour are:

(a) At constant temperature and pressure the shear viscosity for a Newtonian fluid is constant and does not vary with shear rate.
(b) The viscosities due to different types of deformation or flow (see Figure 1.1 for examples of shear and extensional deformation) are always in simple proportion to one another, for example the uniaxial extensional viscosity is always three times the shear viscosity.
(c) The only stress generated in simple shear flow is the shear stress.
(d) The shear viscosity is constant regardless of the length of time of shearing.
(e) In the absence of inertia, the shear stress in the fluid falls immediately to zero when shearing stops.

Any deviation from the above would characterise a fluid as being 'non-Newtonian'.

1.2. Non-Newtonian fluids

There are several types of non-Newtonian fluid, for example shear-thinning (breaking rule (a) above), thixotropic (breaking rule (d)) and viscoelastic (breaking rules (c) and (e) and possibly (a), (b) and (d)!).

Newton's postulate was obeyed by common fluids such as water, air and glycerine so it was believed to be true for all fluids, hence all fluids were assumed to be purely viscous. Similarly Hooke's law, published in 1678, that the extension of a solid is directly proportional to the force exerted on the material had been used to describe solid behaviour and all solids were assumed to be elastic. Hooke's law is given as

$$\sigma = E\varepsilon, \tag{1.2}$$

where σ is extensional stress (Pa), E is Young's modulus or the modulus of elasticity (Pa) and ε is strain. If a stress is placed on an elastic solid obeying Hooke's law the material will strain immediately and once the stress is removed the

material will immediately return to its original state (a viscous fluid would not return to its original state once the same stress was removed). In contrast to this behaviour if a stress is placed on a viscoelastic material the material will strain linearly over time and once the stress is removed the material will return to its original state over time, this phenomenon is known as 'fading' memory (Brinson and Brinson (2008)).

In 1835 Weber experimented on silk threads and discovered that they were neither perfectly elastic nor perfectly viscous (Weber (1835)). He found that on applying a load to a silk thread the thread would immediately extend, then there would be a continuing elongation. On removing the load an immediate contraction was observed followed by a slow contraction to the initial thread length. The immediate extension and contraction both follow Hooke's law, exhibiting elastic behaviour, however the slower elongation and contraction are viscous behaviour. This combination of viscous and elastic behaviour from one material seemed unusual at the time but is now known as viscoelastic behaviour. Viscoelasticity describes behaviour between the two extremes of Newtonian behaviour and the Hookean elastic response. Creep (increase in strain at constant stress) and relaxation (decrease in stress at constant strain) are both viscoelastic effects (Brinson and Brinson (2008)) occurring over a period of time, hence viscoelasticity is often observed as a time effect.

1.2.1. Shear-thinning fluids

Shear-thinning fluids are fluids that exhibit a decrease in shear viscosity with an increasing shear stress. If the applied shear stress is increased, the corresponding shear rate also increases and the shear viscosity is seen to decrease. Many inelastic mathematical models have been suggested to describe this relationship, such as the power law, Sisko and Carreau fits (Barnes *et al.* (1989)). Some of these models will be discussed further in Chapter 2.

The shear viscosity of a shear-thinning fluid decreases with an increase in shear rate because the molecules in the fluid align under the shear stress that is being exerted on the sample (Rosen (1993)). For each shear-thinning fluid there are two plateaus on a log-log plot where the viscosity is constant, one at low shear rates (zero shear

rate viscosity, μ_0, Pa.s), which occurs when the molecules are entangled, and one at high shear rates (infinite shear rate viscosity, μ_∞, Pa.s), which occurs once the molecules are fully aligned and untangled. Some examples of every day shear-thinning fluids are

- Paint - it can be picked up by a brush or roller and transferred to walls or ceilings but will not run down the wall or drip from the ceiling.
- Shampoo - it can be squeezed from the bottle but will sit on your hand without flowing.

1.2.2. Shear-thickening fluids

Shear-thickening fluids are less common than shear-thinning fluids and although shear-thickening fluids have not been investigated here they are considered to be of sufficient interest for a brief inclusion in this Introduction. The shear viscosity of a shear-thickening fluid increases with an increase in shear rate. As with shear-thinning fluids for each shear-thickening fluid there are two plateaus on a log-log plot where the viscosity is constant, one at low shear rates and one at high shear rates. Examples of every day shear-thickening fluids include any sauces in which a thickening agent (for example corn starch) has been used such as gravy and custard – both appear to thicken as they are stirred.

1.3. Reynolds, Deborah, Weissenberg and Elasticity numbers

1.3.1. Reynolds number

The Reynolds number, *Re*, is a dimensionless number used to characterise fluid flows in classical Newtonian fluid mechanics, it is the ratio of inertial forces to viscous forces within a flow (Escudier (1998)). A flow with a 'low' Reynolds number is more likely to be laminar as the viscous forces will dominate the flow. A flow with a 'high' Reynolds number is more likely to be turbulent as the inertial forces will dominate. For an internal flow the Reynolds number is determined using characteristics of the fluid (the density and the viscosity), a length scale from the

geometry of the test rig and a characteristic fluid velocity. The Reynolds number is usually defined as

$$Re = \frac{\rho U_B l}{\mu(\dot{\gamma})} \tag{1.3}$$

where ρ is the density (kg.m^{-3}), U_B is the bulk velocity (m.s^{-1}), l is a characteristic length scale (m) and $\mu(\dot{\gamma})$ is the shear-viscosity (Pa.s). It is not possible to determine a single shear-viscosity for most non-Newtonian fluids. The fluids under investigation here are shear-thinning so the approach we adopt is to estimate a characteristic shear-viscosity at a characteristic shear rate. This problem is discussed in further detail in Chapter 3. Examples of typical flows expected across a range of Reynolds numbers for internal Newtonian flows are given in Table 1.1.

1.3.2. Deborah number

The Deborah number, *De*, is used to characterise the degree of viscoelasticity within a fluid flow or how 'fluid' a material will behave under different types of deformation. A Newtonian fluid flow always has a Deborah number equal to zero, whereas a perfectly elastic solid will have an infinite Deborah number (McKinley (1991), Phan-Thien (2002)). A viscoelastic fluid flow will have a Deborah number somewhere between these two extremes and significant elastic effects are generally not observed until $De \geq 0.5$ (Haas and Durst (1982)). The Deborah number is defined as

$$De = \frac{\lambda}{T} \tag{1.4}$$

where λ is a characteristic time of the material (s) (often called a relaxation time) and T is a characteristic time of the deformation process being observed (s), usually taken as an inverse characteristic shear rate, e.g. U_B/l.

The Deborah number for a given material can vary greatly depending on the deformation process that it is undergoing (Bird *et al.* (1987)). If we take a nominal material with relaxation time 1s and a process such as flow through a section of converging duct taking 5s we obtain a Deborah number of 0.2 giving weakly viscoelastic behaviour. If however, we take the same material and subject it to an impact lasting, say, 10ms we obtain a Deborah number of 100 indicating much more

elastic behaviour. This example is an extreme simplification used to illustrate the importance of the process the material is undergoing when calculating the Deborah number and estimating viscoelastic effects.

1.3.3. Weissenberg number

The Weissenberg number, *Wi*, is defined as the ratio of elastic to viscous forces within a flow. For a pure shear flow, the Weissenberg number can be expressed as the ratio of the elastic recoverable shear ($N_1/2$, Pa) to the applied shear stress

$$Wi = \frac{N_1/2}{\tau}. \tag{1.5}$$

For arguably the simplest viscoelastic model (the upper convected Maxwell model (Samsal (1995), Owens and Phillips (2002))), $N_1 = 2\lambda\tau\dot{\gamma}$ and therefore

$$Wi = \frac{\lambda\tau\dot{\gamma}}{\tau} = \lambda\dot{\gamma} \tag{1.6}$$

where $\dot{\gamma}$ is the shear (or strain, $\dot{\varepsilon}$) rate (s^{-1}). We note that this is essentially the same definition as the Deborah number where *T* is taken as the inverse of the shear rate.

1.3.4. Elasticity number

The Elasticity number, *El*, is another measure of how elastic a fluid flow is: the higher the Elasticity number the more elastic the flow. The Elasticity number is defined as the Deborah number divided by the Reynolds number (McKinley (1991)),

$$El_1 = \frac{De}{Re} = \frac{\lambda\mu}{\rho l^2}, \tag{1.7}$$

and can be seen to be dependent on the fluid properties and the dimensions of the test section only. For fluids of constant viscosity and relaxation time, *El* is the same no matter what the flowrate. However, for shear-thinning fluids where the viscosity and relaxation time are dependent on the shear rate, and hence also dependent on the flow velocity, *El* will vary with the flow rate.

We can also define a second Elasticity number (Astarita and Marucci (1974)) using the Weissenberg number, i.e.

$$El_2 = \frac{Wi}{Re}. \tag{1.8}$$

1.4. Gradual contractions

Gradual contractions are used in pipe or duct flows to slowly decrease the cross-sectional area that the flow passes through; this slowly increases the flow velocity whereas using a sudden contraction changes the area and the velocity immediately and causes recirculating flows/vortices at the corners of the contraction. Gradual contractions can be either tapered or curved and can be used in both planar and axisymmetric duct flow: Figure 1.2 shows schematics of curved and tapered gradual contractions and an abrupt contraction for comparison. The type of gradual contraction under investigation in this study is a planar curved gradual contraction and is discussed in detail in Chapter 3. It is well known that for Newtonian fluid flow at high Reynolds numbers through a curved gradual planar contraction the flow profile flattens producing a 'top hat' flow on exit from the section. This type of contraction is commonly used in wind tunnels to increase the flow velocity while producing a uniform flow within the test section (Pankhurst and Holder (1965), Mehta and Bradshaw (1979)). In contrast, little research has been undertaken on the study of non-Newtonian fluid flow through gradual contractions. However, due to it being a 'benchmark' problem in computational rheology (Hassager (1988), Phillips and Williams (2002)), there are numerous studies investigating abrupt contraction flow.

1.5. Background

As mentioned, much of the experimental work concerned with non-Newtonian fluid flow through contractions has concentrated on abrupt contractions, both axisymmetric and planar, and mostly focuses on two phenomena, the enhanced pressure drop and vortex enhancement. Vortex enhancement is the increase in the size and strength of the corner vortex observed as the relevant dimensionless number (the Deborah number, for example) is increased and the enhanced pressure drop is the difference between the actual observed pressure drop and the equivalent pressure drop that would be observed if only the pressure losses expected in fully developed

flow were considered. There is an abundance of literature in this area so we have concentrated on the most significant works, favouring that which is the most recent. Astarita *et al.* (1968 (a) and 1968 (b)) investigated the excess pressure drop in axisymmetric flow for both Newtonian (1968 (a)) and non-Newtonian (1968 (b)) fluids. They found that the pressure drop had been hugely underestimated for Newtonian flow (the pressure drop had been estimated previously using inaccurate Hagenbach and Couette corrections, however Astarita *et al.* were unable to provide alternative values for these corrections as they appear to be dependent on the contraction geometry). They also found that it is not always true that the observed enhanced pressure drop is larger for elastic fluids than for viscous fluids as previously hypothesised. Cable and Boger experimentally explored axisymmetric flow of viscoelastic fluids (1978 (a), 1978 (b), 1979). They investigated in detail 11 flows of a polyacrylamide, with concentrations from 0.4% to 2% by weight, at different flow rates through a 4:1 abrupt axisymmetric contraction and six flows through a 2:1 abrupt axisymmetric contraction. They identified two distinct flow regimes: the vortex growth regime where the flow patterns appear to be independent of inertia effects and the divergent flow regime where inertia appears to affect the flow. Since this comprehensive study was performed many more investigations have been undertaken on axisymmetric contraction and expansion flows including, more recently, an experimental investigation into the effects of extensional rheology (Rothstein and McKinley (2001)). In this study the flow of a Boger fluid (an elastic fluid with constant viscosity, often used to separate viscous effects from elastic effects in viscoelastic flows (Boger (1977))) through abrupt axisymmetric contraction expansion ratios of 8:1:8, 4:1:4 and 2:1:2 with both a sharp and curved re-entrant corner was investigated and it was found that introducing a curved re-entrant corner delays the vortex development. They observed an enhanced pressure drop larger than that seen in a Newtonian fluid, which was seen to grow with an increase in Deborah number.

Evans and Walters (1986) investigated abrupt planar and square-square contractions. They tested Boger fluids and shear thinning aqueous polyacrylamide (PAA) solutions through several contraction ratios and attempted to change the re-entrant corner conditions by inserting ‘ramps’ and cutting away the re-entrant corners from the geometries. They had previously thought (Walters (1985)) that for Boger fluids

vortex enhancement would always be present in the square-square contraction and it would never be observed in the planar contraction. However, during this study, Evans and Walters observed no vortices in the square-square contraction for the low elasticity Boger fluid at the lowest flow rate while they did observe vortices and asymmetry in the higher elasticity Boger fluid through the planar contraction. In the 1% PAA solution through the 4:1 planar contraction corner vortices are observed, which grow as the flow rate is increased. Through the 16:1 contraction, corner vortices are also observed but they grow more slowly and extend towards the re-entrant corner until, for a range of Deborah numbers, two vortices are seen. This effect showed that contraction ratios above 4:1 might be worth investigating as, until then, they were thought to be of less interest (the selection of the 4:1 contraction ratio as the 'benchmark' (Hassager (1988)) supports this statement). A further study by Evans and Walters (1989) investigated flow of aqueous PAA solutions through abrupt and tapered planar contractions. In an attempt to observe a lip vortex they decreased the concentration of the PAA. While no lip vortex was seen in concentrations of 0.3% and 0.5% PAA, a lip vortex was observed in 0.2% PAA. The contraction angle was found to affect the occurrence and formation of both the corner and lip vortices: at an angle of 150° the lip vortex is not visible and the corner vortex barely so.

A further experimental study by Nigen and Walters (2002) compares Boger fluid flow through both abrupt axisymmetric contractions and abrupt planar contractions of varying ratios. The vortices seen in the axisymmetric case were not observed in the planar contractions and the planar contractions appear to be much less sensitive to elasticity effects. They also note that for axisymmetric contractions the enhanced pressure drop is larger for a Boger fluid than for a Newtonian fluid; however in the planar contraction there is no difference in the pressure drop between the Newtonian and Boger fluids. Nigen and Walters question whether an axisymmetric contraction can be compared to a planar contraction. To this end, it is worth mentioning square-square contractions, which may be considered more similar to an axisymmetric contraction than a planar contraction. Alves *et al.* (2005) investigated experimentally both Boger and Newtonian fluid flow through a 4:1 square-square contraction. For the Newtonian fluid flows, inertia was seen to cause a reduction in the corner vortex, which showed good agreement with their numerical simulations. The less elastic of

the two Boger fluids under investigation showed that as the Deborah number was increased the corner vortex initially increased slightly before shrinking to around a quarter of the maximum vortex size, while as the Deborah number was increased further divergent flow was observed (i.e. as was observed by Cable and Boger (1978 (a))). The more elastic of the two Boger fluids shows a more intense initial increase in vortex size with increase in Deborah number and the divergence seen in the lower elasticity flow is also seen here. For the higher elasticity fluid a lip vortex is observed for a range of Deborah numbers whereas it is not seen in the lower elasticity fluid.

There has also been much numerical research concerned with contraction flow, both axisymmetric and planar, but similar to the experimental works, the main focus has been on abrupt contractions and attempting to improve numerical methods. A growing interest in numerical simulations based on finite-volume methods rather than finite-element methods has been seen in recent years (Wachs and Clermont (2000)). This growth in interest may be due to the ease of use of finite-volume methods (Wachs and Clermont). It has also been found that results obtained using the finite-volume method provide a better approximation to theory in some cases (O'Callaghan *et al.* (2003)). Wachs and Clermont investigated flow of an upper convected Maxwell (UCM) fluid through an abrupt axisymmetric contraction using five meshes of varying refinement throughout the contraction. It was found that, although the coarsest mesh could qualitatively describe the vortex shape, finer resolution was required close to the re-entrant corner in order to predict the flow characteristics accurately and that with an increase in Weissenberg number the corner vortex is seen to grow. Alves *et al.* (2000) also used a finite-volume method to investigate the flow of a UCM fluid through a 4:1 abrupt planar contraction using four meshes of varying resolution and provided benchmark results up to a Deborah number, *De*, of three. Their results (similar to those of Wachs and Clermont (2000)) show that more refinement of the mesh is required close to the re-entrant corner in order to accurately predict the characteristics of the flow. Alves *et al.* also find that as the Deborah number increases the corner vortex decreases while the lip vortex increases until they merge into one vortex ($De \approx 5$) and the pressure drop is seen to decrease with increasing *De* (however this is not greatly affected by mesh refinement). Further investigations by Alves *et al.* (2003) provide benchmark

solutions for Oldroyd-B and Phan-Thien/Tanner (PTT) fluids flowing through a 4:1 abrupt planar contraction. For the Oldroyd-B fluid the corner vortex is seen to shrink with an increase in Deborah number while the lip vortex is seen to grow and the pressure drop is seen to decrease, agreeing with their previous work investigating a UCM fluid. For the linear PTT fluid the corner vortex is seen to grow with an increase in Deborah number and the exponential PTT fluid exhibits an increase in vortex size up to a maximum at $De \approx 6-7$, followed by a decrease in vortex size. For both the linear and exponential PTT fluid they observe an initial decrease in pressure drop with an increase in Deborah number, followed by an increase in the pressure drop after minima observed at $De \approx 20$ (linear PTT) and $De \approx 1$ (exponential PTT).

Over the years there have been several papers that summarise the research on contractions. The interested reader is referred to the recent papers of Rodd *et al.* (2005, 2007) and Alves *et al.* (2005) along with earlier papers such as Cable and Boger (1978 (a)), White *et al.* (1987) and Boger (1987) for a more in-depth discussion. In order to briefly overview some of the most important works in Tables 1.2 and 1.3 we present a summary of some of the previous works, both experimental (1.2) and numerical (1.3), on contraction and expansion flows.

While experimentally investigating the flow of a viscoelastic fluid through a sudden expansion preceded by a curved gradual contraction section Poole *et al.* (2005) discovered an unusual phenomenon within their gradual contraction section. The aim of their study was to investigate the asymmetry seen in planar sudden expansion flows (bifurcation). This effect is known to occur in Newtonian fluid flow above a critical Reynolds number of the order of 10 (the exact critical Reynolds number is dependent on the expansion ratio, inlet velocity profile and several other factors (Drikakis (1997)). The aim of the investigation was to determine whether or not viscoelasticity has any effect on the occurrence of this asymmetry (numerical investigations had shown that viscoelasticity increases the critical Reynolds number, Oliveira (2003)). A gradual contraction was used prior to the sudden expansion because, for Newtonian fluid flow, this produces a virtually uniform velocity profile across the contraction exit as we have already mentioned. The geometry was a planar 8:1 gradual contraction followed by a 1:4 sudden expansion and the fluid used was

0.05% polyacrylamide in water, which is a shear thinning viscoelastic fluid. A transverse velocity profile, shown in Figure 1.3, measured at the exit of the contraction indicated a major deviation from the 'top hat' profile that was anticipated. The figure clearly shows two peaks towards the top and bottom of the section when it would be expected that the flow would be uniform; this prompted further investigations into the flow within the contraction itself. Figure 1.4 shows spanwise velocity profiles measured within the gradual contraction along the XZ-centreplane. Close to the sidewalls of the contraction huge velocity overshoots are clearly visible. These overshoots were dubbed 'cat's ears' by the authors due to their appearance. Poole *et al.* (2007) extended their earlier work by investigating a gradual contraction followed by a sudden expansion with a lower contraction/expansion ratio than that used previously and also by conducting some numerical simulations. The velocity overshoots observed in the previous study were reproduced experimentally in the new geometry and the numerical results agreed qualitatively with the experimental results, although the overshoots were much weaker in the simulations.

Afonso and Pinho (2006) conducted a detailed numerical investigation into the viscoelastic smooth contraction flow problem in an attempt to reproduce the results of Poole *et al*. (2007). These numerical investigations agreed qualitatively with the experimental results and showed that the velocity overshoots were dependent on large Weissenberg numbers, large second-normal stress differences, strain hardening of the extensional viscosity, intense shear-thinning of the fluid and non-negligible inertia. As discussed, previous numerical investigations were predominantly two dimensional in nature, again focussing mainly on abrupt contractions, and hence fundamentally different to the work of Poole *et al*. (2005). An exception is the work of Binding *et al.* (2006), who investigated abrupt contractions/expansions with rounded corners. However, their investigation was concerned primarily with the pressure at various locations within the flow and, in particular, with understanding the enhanced pressure drop that is known to occur for viscoelastic fluid flow through sudden contractions. Alves and Poole (2007) investigated the flow of viscoelastic fluids through smooth gradual planar contractions of varying contraction ratio in an attempt to determine the divergence of the flows (divergence is used to mean the divergence of the streamlines throughout the contraction, the streamlines would normally be expected to be parallel with one another then become closer together as

the flow progresses through a contraction but, actually, they have been seen to separate or 'diverge' inside contractions). They observed divergent flows with the degree of divergence increasing for smaller contraction ratios.

1.6. Objectives of PhD

The main objective of the research discussed in this thesis was to determine whether the effect observed by Poole *et al*. (2005) through a sudden expansion preceded by a gradual contraction can be reproduced when a sudden expansion is not present and to gain physical insight into the phenomenon. To this end the fluids investigated are aqueous polyacrylamide and xanthan gum solutions at various concentrations; they are tested at several Reynolds, Deborah and Weissenberg numbers in an attempt to 'separate out' various effects (e.g. shear thinning vs increased elasticity effects, extensional effects) and determine the conditions required for the velocity overshoots or 'cat's ears' to be observed. A further objective is to provide high quality data that can be utilised as a benchmark set of 3D experimental results, which can be used by researchers who investigate numerical flows of non-Newtonian fluids to test their codes: the gradual contraction alone is much more attractive from a modelling perspective as the, often troublesome (Afonso and Pinho (2006)), sharp corners of the sudden expansion are removed.

The current work investigates the flow of several non-Newtonian fluids through two gradual planar contractions of contraction ratio of 8:1 and 4:1. The fluids have been characterised using a steady-state shear rheometer and a capillary break-up extensional rheometer in order to determine shear viscosities and relaxation times with which to estimate the appropriate Reynolds, Deborah, Weissenberg and Elasticity numbers for each flow. These techniques are discussed in detail in Chapter 2. The shape of the 8:1 contraction section is identical to that used in Poole *et al.* (2005), the 4:1 contraction was designed using the same methodology as the 8:1 contraction but the end height is necessarily different in order to produce a smaller contraction ratio. Both contractions are discussed in Chapter 3 along with a detailed description of the complete test rig. The technique utilised for measuring the flow velocities was laser Doppler anemometry, which can be used to measure the velocity at discrete locations within the flow without affecting the flow in any way.

Information regarding the laser Doppler anemometry set up is also provided in Chapter 3. The corresponding results of the investigations are presented in Chapter 4 and the results are discussed in Chapter 5 where comparisons are drawn between the flows through both contractions. The thesis ends with some conclusions, which place the work in context, and recommendations for further studies.

1.7. Tables

Table 1.1: Flow characteristics for approximate ranges of Reynolds Numbers for internal flows of Newtonian fluids (from White (1999)).

Re	**Flow characteristics**
$0 < 1$	Highly viscous, laminar 'creeping' motion
$1 < 100$	Laminar, strong Reynolds number dependence
$100 < 1000$	Laminar, boundary layer theory useful
$1000 < 10^4$	Transition to turbulence
$10^4 < 10^6$	Turbulent, moderate Reynolds number dependence
$10^6 < \infty$	Turbulent, slight Reynolds number dependence

Table 1.2: Summary of experimental works on contraction and expansion flow.

Author	Year	C/E*	Type	Ratio	Fluid	Comments
Astarita & Greco	1968	C	Abrupt axisymmetric	2.49:1	Newtonian, water and glycerol	Enhanced pressure drop previously hugely underestimated.
Astarita *et al.*	1968	C	Abrupt axisymmetric	2.49:1	Non-Newtonian, ET-597 (drag reducing additive) and carboxypolymethylene	Qualitative agreement with previous works.
Cable & Boger	1978	C	Abrupt axisymmetric	2:1 4:1	Several concentrations of aqueous polyacrylamide (PAA)	Differences in velocity profiles observed along the centreline in the two regimes.
Cable & Boger	1978	C	Abrupt axisymmetric	2:1 4:1	Several concentrations of aqueous PAA	Identified vortex growth and divergent flow regimes. In vortex growth regime the detachment length is a function of *Wi*. In divergent flow regime flow diverges at centreline, vortex size decreases with as flow rate increases.
Cable & Boger	1979	C	Abrupt axisymmetric	2:1 4:1	Several concentrations of aqueous PAA	Increasing flow-rate above a 'limit' leads to disturbances to the stable flow patterns observed in previous work.
Evans & Walters	1986	C	Abrupt square, planar, tapered corners	16:1 (S) 80:1 (P) 16:1 (P) 4:1 (P)	Boger fluid, non-Newtonian fluid, 1% PAA in water	At larger contraction ratios the re entrant corner vortex has important influence on vortex enhancement.
White & Baird	1986	C	Abrupt planar	4:1	Low density polyethylene (LDPE) and polystyrene	Vortices were observed in LDPE but not in polystyrene (PS).
White & Baird	1988	C	Abrupt planar	8:1, 4:1	Polymer melts, polystyrene, LDPE	Proposed that vortex growth and intensity are a function of extensional and shear viscosity.

* C – contraction, E – expansion, C-E – contraction-expansion

Author	Year	C/E*	Type	Ratio	Fluid	Comments
Evans & Walters	1989	C	Abrupt planar and tapered	4:1 4:1 150° 4:1 120°	Aqueous polyacrylamide	Lip vortex mechanism can be responsible for vortex enhancement for planar contractions.
Quinzani *et al.*	1994	C	Abrupt planar	3.97:1	Non-Newtonian, 5% by weight polyisobutylene in tetradecane	Demonstrates onset of elastic effects in flow and shear thinning. No vortex growth or lip vortex observed.
Townsend & Walters	1994	C / E	Abrupt planar	6.8:1 / 1:6.8	Non-Newtonian, 0.15% polyacrylamide in water, suspension of glass fibres in Newtonian matrix and 0.1% xanthan gum in water / glucose mix	Viscoelasticity 'damps' vortex activity and makes flow more chaotic in PAA (planar expansion). Substantial vortex enhancement seen in xanthan gum (axisymmetric contraction). Vortex enhancement observed in both contraction and expansion in glass suspension.
Rothstein & McKinley	1999	C / E	Abrupt axisymmetric	4:1 / 1:4	Boger fluid, polystyrene	Enhanced pressure drop increases with *De*, it is larger than the Newtonian equivalent. Large upstream growth in corner vortex with increase in *De*. Elastic instability seen at large *De*.
Olsen & Fuller	2000	C / E	Abrupt	4:1 / 1:4	Newtonian and non-Newtonian	Newtonian - no vortices in contraction and large inertial vortices in expansion. Non-Newtonian - large vortices in contraction (little or no growth with increase in flow rate), vortices diminished in expansion due to elasticity effects.
Rothstein & McKinley	2001	C / E	Abrupt axisymmetric	Various		Large enhanced pressure drop (larger than that seen in Newtonian flow) that is independent of CR and re-entrant corner curvature. Flow instabilities at large *De*. Rounding corner leads to shift in onset of flow transitions at large *De*.
* C – contraction, E – expansion, C-E – contraction-expansion						

Author	Year	C/E*	Type	Ratio	Fluid	Comments
Nigen & Walters	2002	C	Abrupt planar and axisymmetric	2:1-31:1	Newtonian and Boger	In axisymmetric contraction vortex enhancement observed in Boger fluid. In planar contraction no vortex enhancement is observed and there is an obvious difference between Boger fluid and Newtonian fluid pressure drop and flow-rate data.
Alves *et al.*	2005	C	Abrupt square/square	4:1	2 Boger fluids and 2 Newtonian fluids	In Newtonian flow the vortex length does not change with an increase in flow-rate, whereas in the Boger fluid flow vortex length increases monotonically with flow-rate.
Poole *et al.*	2005	C / E	Planar gradual / planar abrupt	8:1 1:4	0.05% polyacrylamide	Large velocity overshoots observed close to the sidewalls in the contraction – termed ‘cat’s ears’ due to their appearance.
* C – contraction, E – expansion, C-E – contraction-expansion						

Table 1.3: Summary of numerical works on contraction and expansion flow.

Author	Year	C/E*	Type	Ratio	Fluid	Comments
Gatski & Lumley	1978	C	Gradual convex planar		Oldroyd	Smaller recirculation region in non-Newtonian fluids – separation point moved further downstream.
White & Baird	1988	C	Abrupt planar	4:1, 8:1	PS and LDPE, Phan-Thien Tanner (PTT)	Numerical method predicts onset of vortex growth in LDPE and detachment length in both. With all other rheological properties constant extensional viscosity affects vortex size.
Binding	1991	C	Abrupt axisymetric			Decreasing the rapidly increasing Couette correction with increasing *Wi* (due to extentional viscosity rather than elasticity). Higher values of *Wi* leads to 'funnel' flow and lower pressure loss. Extensional viscosity effects cause vortex enhancement.
Samsal	1994	C	Abrupt axisymmetric	4:1	Upper convected Maxwell (UCM) fluid	Simulated *De* upto 6.25. Observed larger corner vortices at higher *De* for the first time.
Purnode & Crochet	1996	C	Planar abrupt, rounded	4:1, 16:1, 80:1	Aqueous PAA, FENE-P (Finitely extensible nonlinear elastic – Peterlin)	Reproduced experimental results of Evans and Walters (1986, 1989), reproduced qualitative trends. Cannot select generic constitutive equation – interaction between rheometry and simulation is required, material parameters are of paramount importance. Massive differences between 1% and 0.25% PAA through 4:1 contraction.
Azaiez *et al.*	1997	C	Abrupt planar	4:1	Rigid fibre suspension in Newtonian matrix (Carreau model) and polymer matrices (PTT and FENE-CR (Chilcott-Rallison)).	Fibres orientated with streamlines for all matrices, corner vortex largest for FENE-CR and smallest in Newtonian matrix (the larger the vortex, less fibre alignment).

* C – contraction, E – expansion, C-E – contraction-expansion

Author	Year	C / E*	Type	Ratio	Fluid	Comments
Hsu & Chu	1997	E	Abrupt planar	1:2	Viscoelastic	At constant *Re* recirculation zone larger and reattachment length longer for small *El*. 'Overshoot' seen in non-Newtonian case.
Mompean & Deville	1997	C	Abrupt planar	4:1	Oldroyd-B	Good agreement with experimental results observed. Corner vortex decreases with increasing flow rate. No evidence of lip vortex.
Xue *et al.*	1998 (a)	C	Abrupt planar	4:1	Shear-thinning, UCM, Boger and PTT	Experimental results are quantitatively reproduced f the fluid is well characterised. Shear-thinning reduces the intensity of the singularity near the re-entrant corner.
Xue *et al.*	1998 (b)	C	Abrupt planar, abrupt square/square	4:1	Viscoelastic, PTT and UCM	Square/square contraction shows correlation between vortex activities and extentional properties. Planar expansion does not show the same correlation.
Alves *et al.*	2000	C	Abrupt planar	4:1	UCM fluid	As *De* increases the lip vortex also increases and the corner vortex decreases. At *De* = 5 the vortices merge and the lip vortex is dominant.
Phillips & Williams	2002	C	Abrupt planar, abrupt axisymmetric	4:1	Oldroyd-B fluid	Vortex behaviour more pronounced in size and strength in axisymmetric contractions, fluid flows through central 'funnel' that elongates as vortex grows.
Alves *et al.*	2003	C	Abrupt planar	4:1	Oldroyd-B, PTT	No upper limit to *De* found for exponential PTT fluid. Approximate limit of *De*~200 for linear PTT. Previous results had achieved *De*~9 for linear PTT and *De*~35 for exponential PTT.

* C – contraction, E – expansion, C-E – contraction-expansion

Author	Year	C / E*	Type	Ratio	Fluid	Comments
Doerpingh aus & Baird	2003	C	Abrupt planar	4:1	PE melts, LDPE and linear low density polyethylene (LLDPE) (PTT and generalised Newtonian fluid (GNF))	Numerical results lower than experimental for both (LDPE 10-15% less, LLDPE 1.5-7% less). Difference between PTT and GNF small.
Oliveira	2003	E	Abrupt axisymmetric	1:3	Viscoelastic fluids	$Re_{CRITICAL}$ approximately 54 for Newtonian fluids and higher for viscoelastic fluids – viscoelasticity slows the onset of bifurcation in expansion flows.
Pinho *et al.*	2003	E	Abrupt axisymmetric	1:2.6	Shear-thinning power law fluids	Recirculation length decreases with shear-thinning. At low *Re* viscous forces dominate the flow.
Kwon *et al.*	2005	C	Abrupt planar	4:1	Viscoelastic - PTT	Numerical results show 3-dimensional secondary flows.
Afonso & Pinho	2006	C	Smooth planar	2.86:1	Viscoelastic, PTT	Reproduced qualitatively overshoots seen by Poole *et al.*, (2005). At high *Re* weak overshoots are seen that disappear with increase in *Re*. Broader velocity peaks seen near to the sidewalls of the contraction at higher *El*. At low *Re* and high *El* no overshoots are observed, the velocity profile becomes 'slim' and triangular in shape.
Ternik *et al.*	2006	E	Abrupt planar	1:3	Non-Newtonian, shear-thickening (quadratic/power law models)	Shear-thickening lowers $Re_{CRITICAL}$ for bifurcation and increases reattachment length. In symmetric regime both vortices increase with *Re*.

* C – contraction, E – expansion, C-E – contraction-expansion

1.8. Figures

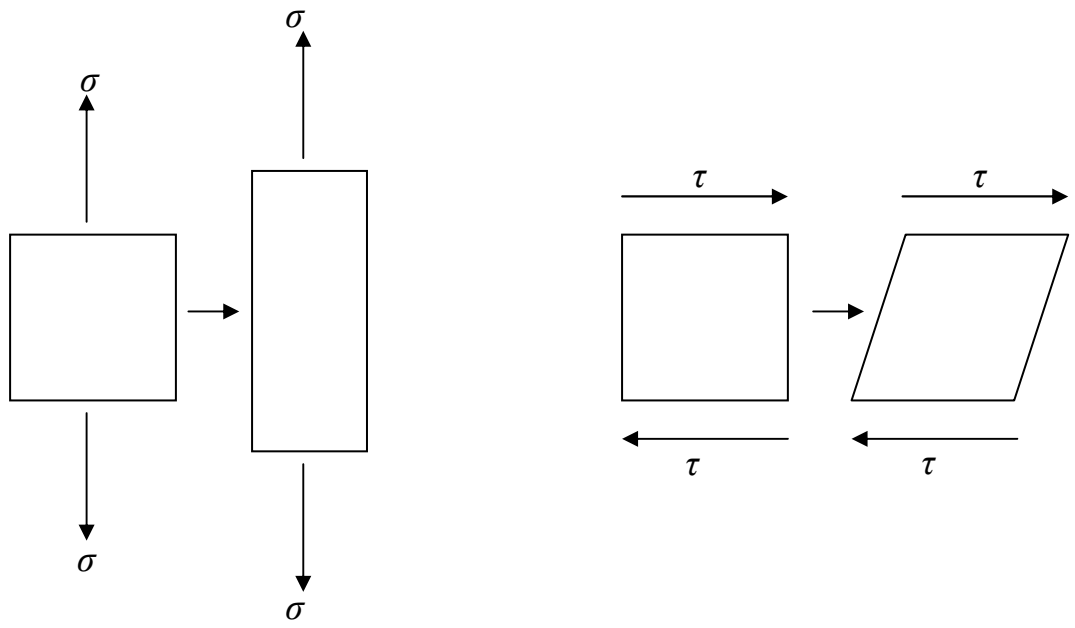

Figure 1.1: Examples of (a) extensional deformation and (b) shear deformation.

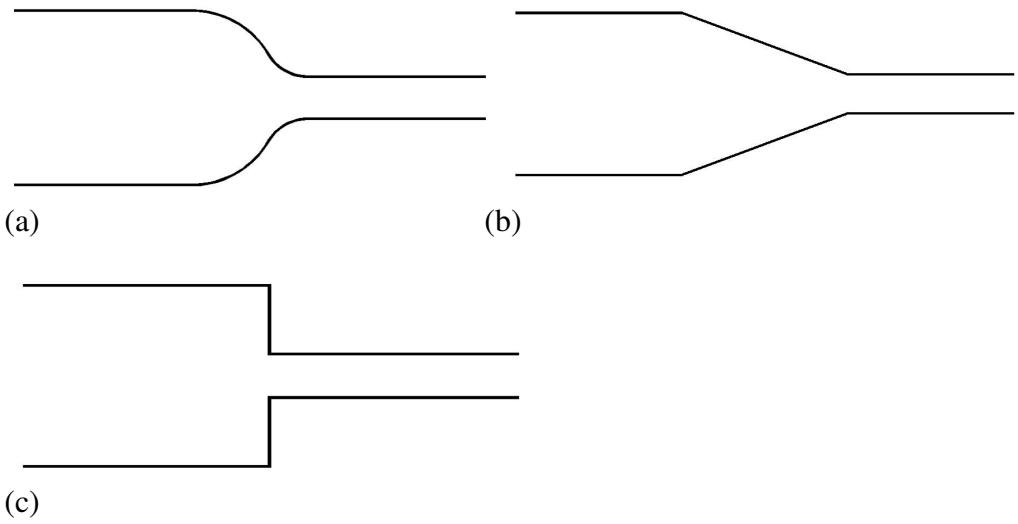

Figure 1.2: Examples of different types of contraction (a) curved gradual contraction, (b) tapered gradual contraction and (c) abrupt contraction.

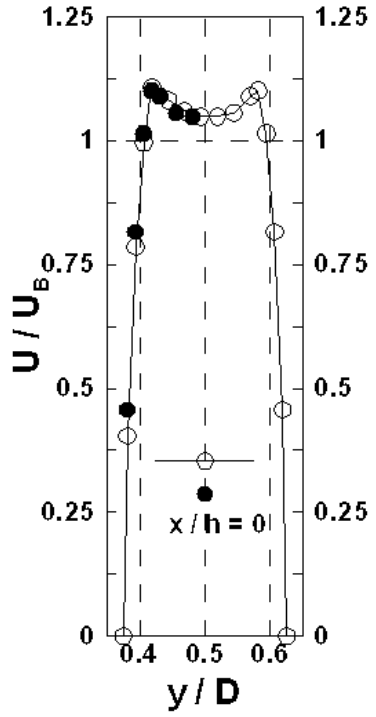

Figure 1.3: Transverse profile measured at the start of the sudden expansion section of an 8:1:4 gradual contraction sudden expansion geometry, which prompted further investigation into the gradual contraction. (Taken from Poole *et al.* (2005))

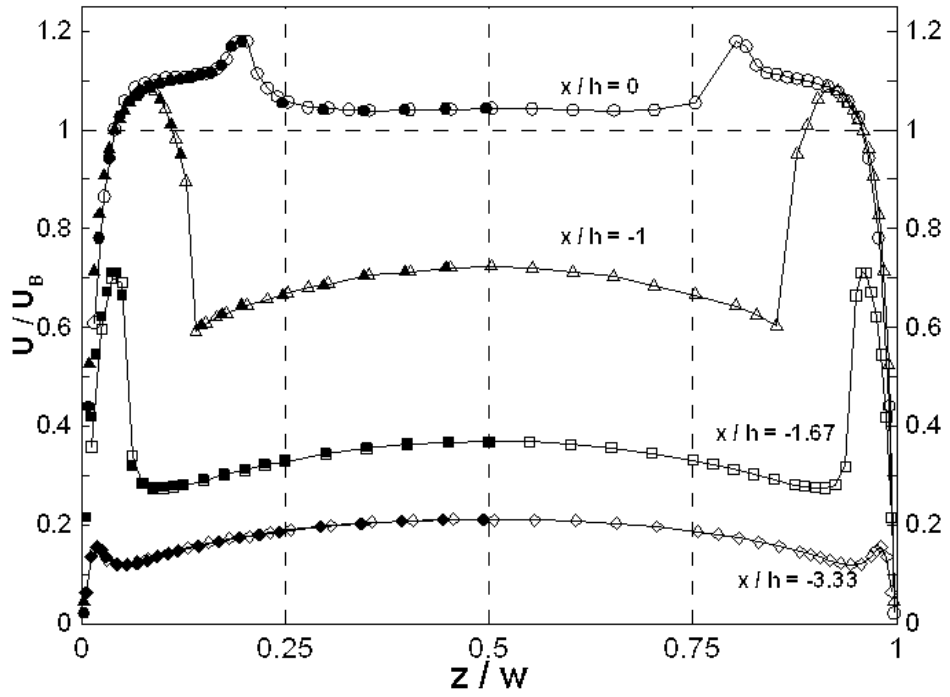

Figure 1.4: Spanwise profiles measured inside the gradual contraction section of an 8:1:4 gradual contraction sudden expansion geometry. (Taken from Poole *et al.* (2005))

2. Fluid Characterisation

2.1. Shear rheology

The TA Instruments Rheolyst AR-1000N is a rotational controlled-stress rheometer used in conjunction with the manufacturer's software (Rheology Advantage Instrumental Control V5.5.0), which can be adapted for use with several different geometries, e.g. the double-concentric cylinder, cone and plate and parallel plates.

The double-concentric cylinder geometry (see Figure 2.1 for schematic) comprises two stationary concentric cylinders and a rotating cylinder; the rotating cylinder fits between the two stationary cylinders. The working fluid is placed between the two stationary cylinders and the rotating cylinder is lowered into position. A metal 'jacket' surrounds the geometry and water is pumped through the jacket to control the temperature. Double-concentric cylinders are used to test samples that have relatively low shear viscosities because they have a much larger contact area than other geometries, this means that for the same viscosity the torque, and consequently the force, is much greater. As a result they can also be used to test at lower shear stresses and their corresponding shear rates and may be used to determine the zero shear rate viscosity for some fluids.

The cone and plate geometry (see Figure 2.2 for schematic) comprises a stationary plate and a rotating cone; the cone is positioned directly above the plate. The working fluid is placed on the plate and the cone is lowered to trap the fluid sample between the plate and the cone. The plate is a Peltier plate, which uses the Peltier effect to control the temperature of the working fluid. The tip of the cone is slightly truncated so that the tip cannot become worn or damage the plate and there is a small gap between the plate and the cone to adjust for this truncation. The main advantage of the cone and plate geometry is that the shear rate is uniform throughout the sample (in the parallel plate geometry it is not).

The parallel plate (see Figure 2.3 for schematic) works in the same way as the cone and plate except the cone is replaced with a flat plate, which is parallel to the

stationary plate and the user can define the gap between the two plates. The shear rate is not uniform across the sample when parallel plates are used, however the software can compensate for this effect (by calculating a 'relevant' shear rate, $\dot{\gamma}_r = R\frac{d\omega}{dR}$, where R is the radius (m) and ω is the angular velocity (rad.s^{-1})) and the resulting shear viscosity measurements are still accurate. Parallel plates can be used to reach higher shear stresses and shear rates than the double concentric cylinder or the cone and plate geometries because parallel plates are available with smaller surface areas than the cone and plate and double concentric cylinder geometries. Parallel plates can often be useful in determining the infinite shear rate viscosity, μ_∞ (Pa.s), of a fluid because the gap can be defined by the user, hence controlling the resultant Reynolds number of the flow within the fluid sample. In steady state shear at high rotational speeds the shear viscosity appears to increase implying that the fluid becomes shear thickening at high shear rates, however this is not necessarily the case if the flow is no longer viscometric[1] (Barnes *et al.* (1989)). High rotational speeds may induce so-called secondary flows, secondary flows absorb energy hence increasing the torque and making the 'shear viscosity' appear to increase. Secondary flows occur within the fluid sample when the Reynolds number is high (approximately 1000 (White (1999))) but if parallel plates are used with a small gap then the Reynolds number will be lower (in this case $\mathrm{Re} = \rho R\omega h / \mu$, where ρ is the density of the sample (kg.m^3), R is the radius (m), ω is the angular velocity (rad.s^{-1}) and h is the gap between the two plates (m)) than if the cone and plate geometry ($Re = \rho\omega R^2 / \mu$) were used for example (Pipe and McKinley (2009)).

2.1.1. Steady-state shear

Steady-state shear measurements are taken over a range of shear stresses determined by the user. The software calculates a torque to correspond to each shear stress. The rheometer applies the calculated torque, and hence shear stress, to the working fluid sample by rotating the non-stationary component from each geometry (see Figures 2.1, 2.2 and 2.3). The resulting shear rate can be found by measuring the angular velocity of the geometry and the shear viscosity can be calculated using

[1] In viscometric flow each fluid element undergoes a steady shearing motion only (Tanner (1985)) and no secondary flows are present.

$$\mu = \frac{\sigma}{\dot{\gamma}} \tag{2.1}$$

where σ is a function of the torque and $\dot{\gamma}$ is a function of the angular velocity, both functions are dependent on the geometry in use. The rheometer changes the torque nominally instantaneously. However even for a Newtonian fluid the corresponding shear rate does not change instantaneously, as it takes some time to come to equilibrium due to inertia effects (due to the instrument, geometry and fluid for example). To determine that a steady-state has been reached the shear rate is calculated (from measurements of the angular velocity) every 15 seconds until three consecutive values are within 3% (3% is an arbitrary value, 1% would have been ideal but time constraints led to 3% being selected) of each other, once these conditions are achieved the corresponding shear viscosity can be calculated. The shear stress is varied as required and the shear viscosities for each shear rate are calculated to enable the variation of shear viscosity with respect to shear rate to be determined.

Several empirical inelastic models can be fitted to steady-state shear data, such as the power law (Barnes *et al.* (1989)) and Cross (Cross (1965)) models for shear-thinning fluids and the Bingham model (Barnes *et al.* (1989)) for fluids exhibiting a yield stress amongst many others. Here we use the Carreau-Yasuda model, which is used to model the complete range for shear-thinning fluids,

$$\mu_{\mathrm{CY}} = \mu_{\infty} + \frac{(\mu_0 - \mu_{\infty})}{\left[1 + (\lambda_{\mathrm{CY}}\dot{\gamma})^a\right]^{n/a}} \tag{2.2}$$

where λ_{CY} is a constant representing the onset of shear thinning (s), a is a parameter introduced by Yasuda *et al.* (1981) and n is a power law index.

The zero and infinite shear rate viscosities can be used to estimate Reynolds numbers at zero shear and infinite shear. The shear viscosity for other characteristic shear rates can be estimated using the Carreau-Yasuda model once all parameters have been determined. The parameters are determined using the least-squares-fitting method as described by Escudier *et al.* (2001), this method minimises the standard deviation

$$\sum\left(1-\mu_{EXP}/\mu_{CY}\right)^2 \qquad (2.3)$$

where μ_{EXP} is the shear viscosity measured by the rheometer and μ_{CY} is the viscosity determined using equation 2.2. This standard deviation is preferable because the fluids investigated during this study cover a wide range of values for the shear viscosity and it will not be heavily weighted toward higher viscosities as other deviations may be (e.g. $(\mu_{EXP}-\mu_{CY})^2$).

2.1.2. Critical overlap concentration, *c**

The critical overlap concentration, *c**, for a polymer in solution is defined as the concentration at which the polymer coils start to overlap with each other (Lapasin and Pricl (1995), Tirtaatmadja *et al.* (2006)). Fluids with concentrations below *c** are said to be in the dilute range, the polymer molecules in a dilute solution are spaced so that they will not interact with each other; fluids with concentrations above *c** are said to be in the semi-dilute range as the polymer molecules are close enough together to begin to interact with each other. One way of estimating the critical overlap concentration of an aqueous polymer is to determine the zero shear-rate viscosity, μ_0 (Pa.s), using the Carreau-Yasuda model fit for example (as described earlier) for several concentrations of the specified polymer (see for example Rodd *et al*. (2000), for a series of xanthan gums). When μ_0 is plotted against concentration two power-law ranges become apparent (See Figure 2.4 for an example). These two ranges are representative of the dilute range and the semi-dilute/concentrated range and the point of intersection between these two ranges is called the critical overlap concentration. In the dilute range the shear viscosity has been found to be proportional to the concentration with a slope approximately equal to one ($\mu \propto c^1$) and in the semi-dilute range the shear viscosity has been found to be proportional to the concentration with a slope of around three to four ($\mu \propto c^{3-4}$) depending on how rigid the polymer is (Lapasin *et al.* (1990), Rodd *et al.* (2000)). If the slope is close to 3 then the polymer is flexible and if it is closer to 4 it is rigid (Lapasin *et al.* (1990)).

2.1.3. Normal-stress difference

In a polymer solution at rest one polymer-chain molecule occupies a spherical volume and the entropic forces within the polymer solution determine this shape (Barnes *et al.* (1989)). When a polymer solution is under shear deformation the same molecule becomes ellipsoidal in shape with its major axis tilted in the direction of shearing and internal restoring forces attempt to return the molecule to its original spherical shape. These restoring forces are larger along the molecule's major axis and the total restoring forces are greater in the direction normal to the shear deformation and this gives rise to the first and second normal-stress differences N_1 and N_2 (Pa).

Several effects are attributed to the development of significant normal forces within a flow, including the Weissenberg or rod climbing effect in which polymer solutions climb a rotating shaft and extrudate swell (also known as die swell) where polymer melts or solutions commonly swell to two or three times the die exit diameter (Barnes *et al*. (1989))

The normal force is generally measured under steady-state shear at the same time as the shear viscosity. During this investigation the geometry used to measure the normal force was a cone and plate; the cone had a diameter of 6cm and an angle of 1°. From the total normal force we can find the first normal-stress difference using (Walters (1975)),

$$F = \frac{\pi R^2}{2} N_1 \Rightarrow N_1 = \frac{2F}{\pi R^2}, \tag{2.4}$$

where F is the total normal force (N) and R is the radius (m). The experimental values for F may be slightly lower than the true values due to the effects of inertia, this effect is known as the 'negative normal stress effect' (Barnes *et al.* (1989)) and can be corrected using (Walters (1975)),

$$\Delta F = \frac{3\pi\rho\omega^2 R^4}{40} \tag{2.5}$$

where ΔF is the reduction in F due to inertia (N), ρ is the density of the sample and ω is the angular velocity (rad.s^{-1}).

2.1.4. Small amplitude oscillatory shear

The rheometer can also be used to apply an 'oscillatory' shear stress to the working fluid by rotating the non-stationary component alternately clockwise and then anti-clockwise. A 'stress sweep', in which the oscillatory shear stress is varied while the frequency of oscillations is kept constant, is performed as a check to determine the linear viscoelastic region for the fluid (i.e. the region where the results are independent of the applied oscillatory stress). A 'frequency sweep' is subsequently performed at an oscillatory shear stress within the linear viscoelastic region, the oscillatory shear stress is kept constant and the oscillation frequency (ω, rad.s^{-1}) is varied in this case. Two frequency sweeps are performed at different values of constant oscillatory shear stress from within the linear viscoelastic region in order to confirm that the observed viscoelastic properties (the storage modulus (G', Pa) and the loss modulus (G'', Pa)) are independent of the oscillatory shear stress. The storage modulus and the loss modulus can be used to calculate the dynamic rigidity (Pa.s^2) and the dynamic viscosity (η', Pa.s) respectively, using (Barnes *et al.*)

$$\text{Dynamic Rigidity} = \frac{2G'}{\omega^2}, \tag{2.6}$$

$$\text{Dynamic Viscosity} = \eta' = \frac{G''}{\omega}. \tag{2.7}$$

The dynamic viscosity should tend towards the same value as the zero shear rate viscosity as the frequency decreases as it is a requirement of continuum mechanics that at low shear rates and frequencies the shear viscosity and the dynamic viscosity are equal (Barnes *et al.* (1989), Al-Hadithi *et al.* (1992)) ,

$$\eta'(\omega)_{\omega\to 0} = \mu(\dot{\gamma})_{\dot{\gamma}\to 0}. \tag{2.8}$$

G' is zero for an inelastic fluid, hence the dynamic rigidity is also zero for an inelastic fluid; if G' is non-zero it shows that the fluid is viscoelastic to some degree. When small amplitude oscillatory shear measurements are performed on water, or another Newtonian fluid, the rheometer may indicate a non-zero value for

the storage modulus. This error is again due to the effects of inertia and this value provides information on the rheometer's resolution: such 'limit' data is highlighted in the results. Any small amplitude oscillatory shear measurements for polymer solutions that are close to these limits (within 10%) have been discounted, as they are unlikely to be reliable.

A maximum relaxation time may be estimated using the storage and loss modulus data by performing a Maxwell model fit using (Bird *et al.* (1977))

$$G' = \sum_i^n \frac{\eta_i \lambda_i \omega^2}{1 + (\lambda_i \omega)^2} \tag{2.9}$$

$$G'' = \sum_i^n \frac{\lambda_i \omega}{1 + (\lambda_i \omega)^2}. \tag{2.10}$$

The maximum relaxation time is then determined from

$$\lambda = \frac{\sum_i^n \lambda_i \eta_i}{\sum_i^n \eta_i}. \tag{2.11}$$

It is also possible to estimate the shear viscosity variation for polymeric solutions from the G' and G'' data using a relationship known as the Cox-Merz rule (Cox and Merz (1958)),

$$\left|\mu^*\right| = \left[\left(G''/\omega\right)^2 + \left(G'/\omega\right)^2\right]^{1/2} \tag{2.12}$$

where $\left|\mu^*\right|$ is the complex viscosity. The rule suggests that the complex viscosity, when plotted against the angular frequency, should coincide with the shear viscosity variation against shear rate data. This essentially empirical rule has been shown to be applicable for many polymer solutions including polyisobutylene in decalin and a polypropylene copolymer melt (Al-Hadithi *et al.* (1992)). Similarly it is possible to estimate the first normal stress difference N_1 from oscillatory data. Al-Hadithi *et al.* suggest that when the elastic equivalent of the complex viscosity, G_C, is plotted against the angular frequency this curve coincides with $N_1/2$ plotted against $\dot{\gamma}$. They give G_C to be

$$G_C = G'\left[\frac{(\mu_0 + G''/\omega)G'}{2\omega(G''/\omega)^2} + 1\right]^{1/2}. \qquad (2.13)$$

This rule was found to hold for the same polymer solutions for which the Cox-Merz rule is valid and would be expected to also hold for the polyacrylamide and xanthan gum solutions that are under investigation here.

2.2. Extensional rheology

For a Newtonian fluid the uniaxial extensional viscosity is always three times that of the shear viscosity (Barnes *et al.* (1989)). This is not true, however, for non-Newtonian fluids. It is not possible to estimate the extensional viscosity from the shear viscosity or vice versa for a non-Newtonian fluid because of the huge variation in properties. Throughout this investigation extensional rheology is used to determine a relaxation time, from which both Deborah and Weissenberg numbers may be estimated and hence Elasticity numbers may also be obtained. It is now well known that the extensional properties of fluids have a strong influence on flow through contractions (see, for example, Debbaut and Crochet (1988), Purnode and Crochet (1998)).

The Thermo Haake **Ca**pillary **B**reak-up **E**xtensional **R**heometer (CaBER) exerts a uniaxial step strain, e.g. by creating a fluid filament, on a sample of the working fluid and measures the reduction in filament diameter due to surface tension over time (Rodd *et al.* (2005)). In the configuration used here a small column of fluid (less than 0.2ml) is placed between two cylindrical platens with diameters of 4mm, the upper platen is moved away from the lower platen almost instantaneously (approximately 50-100ms) (see Figure 2.5 for schematic). An extensional strain is exerted on the fluid sample and an unstable cylindrical fluid filament is formed. Once the stretching has stopped the fluid is subject to an extensional strain rate, which is determined by the extensional properties of the fluid (i.e. not controlled by the instrument). The midpoint of the filament diameter decreases over time due to surface tension and the extensional stresses within the fluid element resist this thinning. A laser micrometer, resolution 10μm, measures the reduction in the midpoint diameter in order to provide information on the extensional properties of

the fluid. Analysis of the filament diameter decay over time gives an estimated relaxation time, which can be used to estimate a Deborah number, the relaxation time can be found using (from Oliveira *et al.* (2006))

$$D_{mid}(t) = \left(D_1 + \frac{k_1}{t + t_1} \right) \exp\left[\frac{-t}{3\lambda}\right] - V_2 (t - t_2) \qquad (2.14)$$

where t is time, λ is the relaxation time for the fluid (perhaps, more correctly, 'characteristic time scale for viscoelastic stress growth in a uniaxial elongational flow' due to the fact that the stress does not relax as such, it grows as the filament diameter decays (Rodd *et al.* (2005)). D_1, t_1, k_1, V_2 and t_2 are fitting parameters (determined using the least-squares-fitting method described in 2.1.1.). Equation 2.14 describes the three regimes usually observed during capillary break-up of flexible polymer solutions, the initial necking, the exponential thinning and the final drainage regimes.

The CaBER experiment and the results are affected by several factors, such as the initial and final aspect ratios and the strike time (Rodd *et al.* (2005)). The initial aspect ratio (Λ_i) is the ratio of the initial sample height to the sample (or platen) diameter. If the initial aspect ratio of the column of fluid is too large sagging will occur because of gravitational effects, i.e. the column will not be cylindrical as there will be more fluid towards the base of the sample than the top. Numerical simulations suggest that the optimal range for the initial aspect ratio is $0.5 \le \Lambda_i \le 1$ (Yao & McKinley (1998) and Rodd *et al.* (2005)). The final aspect ratio (Λ_f) is the ratio of the final sample height to the platen diameter. If the final aspect ratio is too small the filament that is formed will not be cylindrical causing the flow at the mid point not to be purely extensional, but if it is too large the sample will break during the platen separation and the required cylindrical filament will not form. The strike time is the time taken for the top platen to move from its initial position to its final position. It can be varied according to requirements; normally the strike time is of the order 50-100ms. When the strike time is low, e.g. 50ms, and a very elastic fluid is being tested, e.g. 0.05% polyacrylamide, oscillations can be seen within the sample once the filament has formed, this means that the rheometer will not always be measuring the correct part of the fluid filament. If the strike time is increased slightly the oscillations become smaller and the results more reliable.

The Thermo Haake CaBER should be used in conjunction with a high-speed camera in order that the required final aspect ratio and strike time can be correctly selected and amended as necessary. It is useful to be able to view a magnified image of the sample before performing the test to assess whether the correct amount of fluid has been used, and to confirm that the sample is cylindrical and neither slightly concave nor convex. The camera also shows any small air bubbles that may not be visible to the naked eye and the sample can be reloaded before performing the test. Use of a high-speed camera can also provide another method of estimating the filament break up time (by estimating the equivalent length of each pixel) and this result can be compared with results from the laser micrometer. Unfortunately, however, the resolution of the camera used during these investigations was not good enough to precisely determine the variation in the filament diameter over time.

2.3. Fluid selection

2.3.1. Polyacrylamide (PAA)

Polyacrylamide is a water-soluble polymer and was selected because 0.05% PAA in water had previously been used by Poole *et al.* (2005) during the first observations of the 'cat's ears' effect. PAA is transparent making it ideal for obtaining laser Doppler anemometry measurements (see Chapter 3 for details). It is a viscoelastic shear-thinning fluid and generally thought of as having a 'very flexible' molecular structure (Walters *et al.* (1990)). This flexibility means that the fluid has more pronounced elastic properties than other water-soluble polymers such as xanthan gum or carboxymethylcellulose. The polyacrylamide used during the investigation was Separan AP 273 E with a molecular weight of approximately 2×10^6 g/mol.

Figure 2.6 shows the variation of shear viscosity with shear rate for 16 concentrations of PAA in water varying between 25ppm (i.e. 0.0025% w/w) and 0.35%. It can clearly be seen that even at low concentrations PAA is a weakly shear-thinning fluid. The Carreau-Yasuda model (Equation 2.12) has been fitted to each set of results and the corresponding curve is also shown in Figure 2.6. The filled symbols indicate those results deemed to be below the effective resolution of the

rheometer or adversely affected by secondary flows and hence not included in the fit. Table 2.1 presents the corresponding fitting parameters for the fits shown in Figure 2.6. From the Carreau-Yasuda fit a zero shear rate viscosity can be estimated for each concentration of PAA, these values allow the determination of the critical overlap concentration.

Figure 2.7 shows the oscillatory shear data for concentrations above 0.05% PAA, the results for concentrations below 0.05% were deemed to be too close to the limits of the rheometer and hence are not presented. Figure 2.7 (a) shows the variation in the storage modulus with angular frequency and Figure 2.7 (b) shows the variation in the loss modulus; from this data it is possible to calculate the dynamic viscosity and the dynamic rigidity as described earlier in the chapter and these values can be seen in Figures 2.7 (c) and 2.7 (d). Figure 2.7 (c) shows the dynamic rigidity for the various concentrations, calculated from G', which should be zero for an inelastic fluid. As can be seen from Figures 2.7 (a) and (c) neither G' nor the dynamic rigidity are zero hence the fluids are elastic. G' and G'' both increase as the concentration of polyacrylamide increases, hence the dynamic viscosity and dynamic rigidity are also seen to increase with an increase in concentration.

Figure 2.8 shows the variation in zero shear rate viscosity with concentration. Two clear power-law ranges can be seen indicating the dilute range and the semi-dilute range. The point at which the curves intersect allows the determination of the critical overlap concentration, c^*, here found to be approximately 0.03% PAA. As mentioned earlier in the chapter the slope of the dilute curve should be around 1 and Figure 2.8 shows that for this polymer it is, in fact, 0.78. The slope of the semi-dilute power law curve is 3.3 confirming that polyacrylamide is a flexible polymer. The filled symbols show the concentrations selected for the detailed fluid dynamic investigation. The concentrations of PAA chosen for these investigations were 0.05% (c/c^*=1.67) to correspond to the measurements performed by Poole *et al.* (2005), 0.03% because this concentration was determined to be approximately equal to c^*, 0.01% (c/c^*=0.33), which is well within the dilute range and 0.3% (c/c^*=10) was selected with the intention of decreasing the Reynolds number in an attempt to minimise the effects of inertia. Extensional rheology measurements were performed

on these fluids in order to determine a relaxation time for the fluid, which could be used to estimate a Deborah number, De_C.

Because 0.01% PAA is in the dilute range neither N_1, oscillatory nor extensional measurements were obtainable. The shear viscosity variation with shear rate for this fluid can be seen in Figure 2.6 (b). Figure 2.9 shows the material properties for 0.03% PAA. It is seen to be shear thinning and, although the oscillatory data for 0.03% PAA was deemed to be too close to the limits to be reliable, the dynamic viscosity has been included in this figure. At this concentration the G'' data makes up approximately 99% (Barnes *et al.*) of the measurement while the G' data is the remaining 1% meaning the G'' data is still effectively reliable. The dynamic viscosity, which corresponds to the G'' data, agrees well with the zero shear rate viscosity as the shear rate tends towards zero. Figure 2.10 shows the material properties for 0.05% PAA and Figure 2.11 the material properties for 0.3% PAA. Both fluids are seen to be shear thinning and elastic with the dynamic viscosity tending towards the same value as the zero shear rate viscosity as the shear rate tends towards zero as expected (Equation 2.8).

Figure 2.12 presents the normal force data for the 0.03%, 0.05% and 0.3% PAA, along with the corresponding relaxation times (estimated using $N_1 = 2\lambda\tau\dot{\gamma}$ as discussed in Chapter 1). For each concentration the first normal-stress difference is observed to increase with an increase in the shear rate and the relaxation time is seen to decrease with an increase in the shear rate. As might be expected at a given shear rate, the higher the concentration, the larger N_1 and the relaxation time. The power law index of the first-normal stress difference (on a log-log plot at shear rate ranges between approximately 700 and 6000) is approximately the same for each of the three concentrations of polyacrylamide with a value of 0.8 as shown by the full black lines. This result implies that the polymer itself determines this slope, rather than the concentration.

Figure 2.13 shows the extensional rheology data for two samples of 0.03% PAA. The filament diameter is seen to decay over time as expected and is fully broken up after approximately 0.1s. The formula given in equation 2.14 was fitted to the data

(shown as a full line in Figure 2.13) and a relaxation time of λ=0.025s was estimated from this fit. The fitting parameters are given in Table 2.2. Figure 2.14 is a selection of photographs taken with a high-speed camera during the tests. It is clear from these images that the initial sample is correctly loaded and the filament diameter decay over time can be seen. Figure 2.15 gives the extensional rheology measurements for two samples of 0.05% PAA, again the filament diameter is seen to decay over time but for the 0.05% PAA solution the break-up time is longer than for the 0.03% solution, indicating that 0.05% PAA has a longer relaxation time than 0.03% PAA. As for the 0.03% PAA, the data was fitted to Equation 2.14 and a relaxation time of λ=0.056s was estimated. Figure 2.16 shows some of the high-speed camera images taken during the 0.05% PAA measurements. Clearly the sample has been correctly loaded and a suitable cylindrical filament has formed during the test. Figure 2.17 shows the experimental data for two samples of 0.3% PAA. As might have been expected the 0.3% PAA solution takes much longer to break up than either the 0.03% or 0.05% solutions. In this case the relaxation time was estimated to be λ=3.44s, which is an order of magnitude larger than that for the lower concentrations. Figure 2.18 is a sample of the high-speed images obtained during a test on 0.3% PAA. The images show that the fluid sample was loaded correctly and that the filament is cylindrical throughout its decay. On closer inspection of the high-speed camera images (Figures 2.14, 2.16 and 2.18) the filament in each case was found to be perfectly cylindrical with no discernible 'bowing', which means that the flow at the filament mid-point is purely extensional and provides a level of confidence in any relaxation times obtained from the fitted data.

2.3.2. Xanthan gum (XG)

Xanthan gum is classed as 'semi-flexible' (Rodd *et al*. (2000)) i.e. less flexible than polyacrylamide and was chosen for comparison with PAA in an attempt to isolate any effects that may be due to shear thinning. Similar to PAA, xanthan gum is also soluble in water and transparent making it ideal for obtaining LDA measurements. The xanthan gum used during this investigation was Keltrol TF from Kelco with a molecular weight of approximately 10^6g/mol.

Figure 2.19 shows the variation in shear viscosity with shear rate for 13 concentrations of XG varying from 0.01% to 1%. As for polyacrylamide, the Carreau-Yasuda model was fitted to this data (fitting parameters are given in Table 2.3) to estimate the zero shear rate viscosities and determine the critical overlap concentration. Figure 2.20 shows where the dilute and concentrated ranges intersect, giving an estimate for c^* of 0.064%. The slope of the dilute curve is 1.4 and the slope of the semi-dilute curve is 4.6, which means that xanthan gum is more of a rigid polymer than a flexible polymer similar to the polyacrylamide described earlier (Lapasin and Pricl (1995)).

The filled symbols in Figure 2.20 represent the two concentrations chosen for the detailed fluid dynamic measurements. 0.07% xanthan gum was selected because its viscosity at the relevant characteristic shear rates approximately matches that of 0.05% polyacrylamide. Figure 2.21 shows the variations in shear viscosity with shear rate for 0.07% XG and 0.05% PAA for comparison. Figure 2.22 includes a complete set of material properties for 0.07% xanthan gum showing that it is a weakly elastic shear thinning fluid.

Extensional rheology measurements could not be obtained for 0.07% xanthan gum using the CaBER technique previously described, presumably as it is more rigid than polyacrylamide and therefore less tension thickening (Barnes *et al.* (1989)). Measurements of the first normal-stress difference for this fluid were also below the sensitivity of the rheometer and confirm the less elastic nature of xanthan gum in comparison to PAA. This lack of data prevents estimating a Deborah number for 0.07% xanthan gum.

0.5% xanthan gum was selected because a relaxation time can be estimated from CaBER extensional rheology measurements. The relaxation time is similar to that for 0.03% PAA so 0.5% XG was chosen in the hope that velocity overshoots might be observed for the flow of this fluid through the gradual contraction. Figure 2.23 provides a full set of material properties for 0.5% xanthan gum showing that the fluid is shear thinning and much more elastic than the lower concentration. Figure 2.24 shows the extensional rheology results for two samples of 0.5% XG. From these results a relaxation time of 0.034s was estimated for 0.5% xanthan gum and the

fitting parameters are given in Table 2.4. Figure 2.25 shows a selection of images taken by the high-speed camera. They clearly show that the sample was correctly loaded and how the filament diameter decays over time.

2.4. Tables

Table 2.1: Table of fitting parameters for the Carreau-Yasuda fits performed on polyacrylamide solutions.

Conc (%)	μ_0 (Pa.s)	μ_∞ (Pa.s)	λ_{CY} (s)	a	n
0.0025	0.0017	0.0014	0.017	1.23	1.96
0.00375	0.0024	0.0015	0.037	0.94	1.10
0.005	0.0027	0.0016	0.041	0.87	0.95
0.01	0.0058	0.0018	0.095	0.82	0.77
0.02	0.0086	0.0026	0.043	0.70	1.37
0.03	0.012	0.0025	0.086	0.48	1.50
0.04	0.029	0.0023	0.27	0.72	0.56
0.05	0.073	0.0025	0.45	0.52	0.61
0.075	0.28	0.0033	8.89	1.04	0.57
0.1	0.63	0.0031	13.86	1.25	0.56
0.125	1.75	0.0034	13.01	0.72	0.63
0.15	2.90	0.0044	62.12	0.91	0.61
0.2	5.17	0.0076	50.93	0.78	0.68
0.3	22.68	0.0096	104.5	0.77	0.72
0.35	39.91	0.0097	100.9	0.74	0.75

Table 2.2: Table of fitting parameters for the fits performed on the extensional rheology measurements for the polyacrylamide solutions.

Conc (%)	D_1 (mm)	t_1 (s)	k_1 (mm.s)	V_2 (mm.s^{-1})	t_2 (s)
0.03	-0.25	0.23	0.085	0.70	0.10
0.05	-0.16	2.16	0.82	0.26	0.51
0.3	2.32	0.55	0.20	-0.099	20.91

Table 2.3: Table of fitting parameters for the Carreau-Yasuda fits performed on xanthan gum solutions.

Conc (%)	μ_0 (Pa.s)	μ_∞ (Pa.s)	λ_{CY} (s)	a	n
0.01	0.0040	0.0013	0.44	0.37	0.56
0.025	0.015	0.0013	0.30	0.38	0.51
0.04	0.026	0.0013	0.49	0.42	0.53
0.05	0.041	0.014	0.78	0.51	0.51
0.07	0.17	0.0017	1.12	0.34	0.64
0.1	0.18	0.0021	0.73	0.55	0.67
0.15	2.37	0.0028	1.77	0.28	0.85
0.2	11.08	0.0033	7.40	0.27	0.87
0.25	16.01	0.0031	41.50	0.52	0.75
0.38	350	0.0051	563	1.15	0.81
0.5	870	0.0069	500	0.67	0.88
0.75	1200	0.0094	650	1.37	0.85
1	9000	0.018	650	0.74	1.01

Table 2.4: Table of fitting parameters for the fits performed on the extensional rheology measurements for the xanthan gum solutions.

Conc (%)	D_1 (mm)	t_1 (s)	k_1 (mm.s)	V_2 (mm.s^{-1})	t_2 (s)
0.5	5.32	2.52	5.94	4.37	-1.46

2.5. Figures

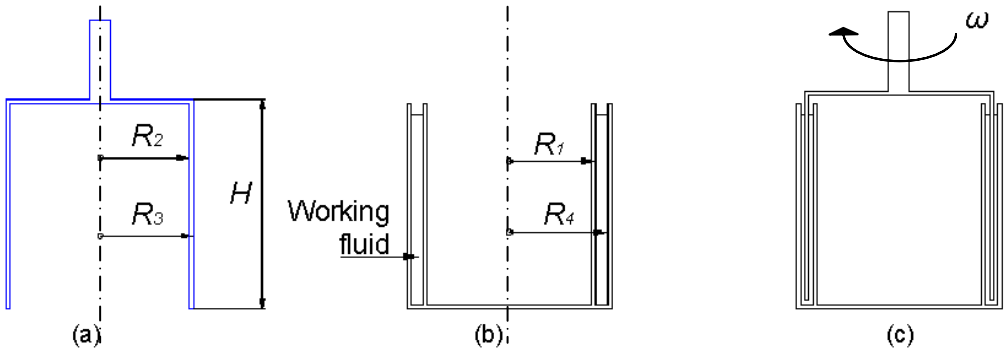

Figure 2.1. Schematic diagram of the double concentric cylinder geometry: (a) Rotating cylinder, (b) Stationary cylinders, (c) Cross section of geometry while in use (R_1=20mm, R_2=20.38mm, R_3=21.96mm and R_4=22.34mm).

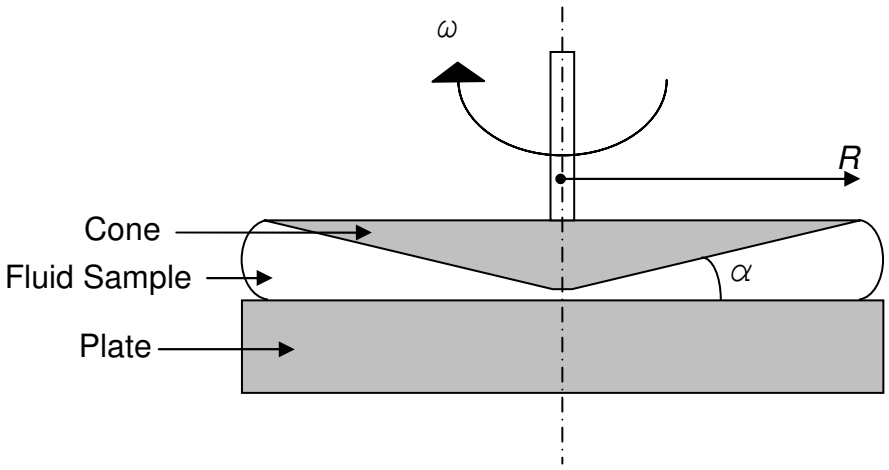

Figure 2.2. Schematic diagram of the cone and plate geometry while in use.

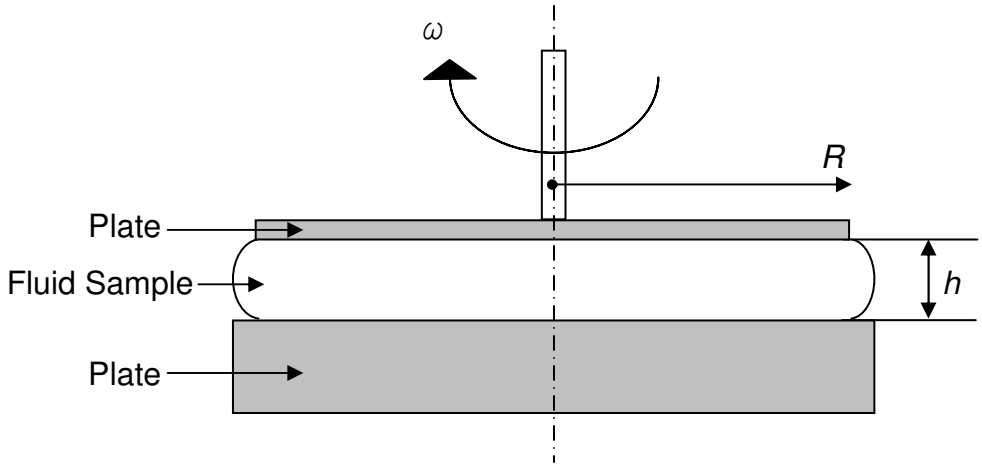

Figure 2.3 Schematic diagram of the parallel plate geometry while in use.

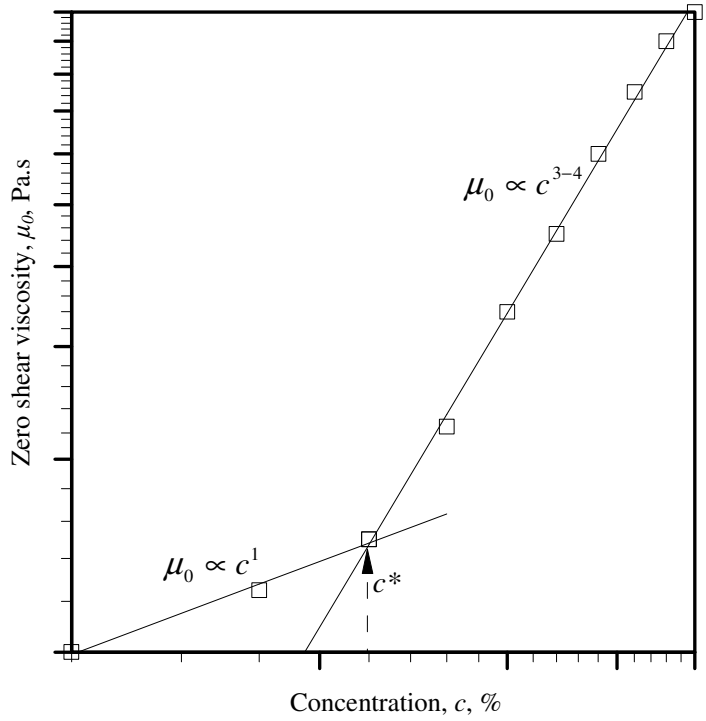

Figure 2.4: Example of the two power law ranges apparent when plotting zero shear rate viscosity against polymer concentration.

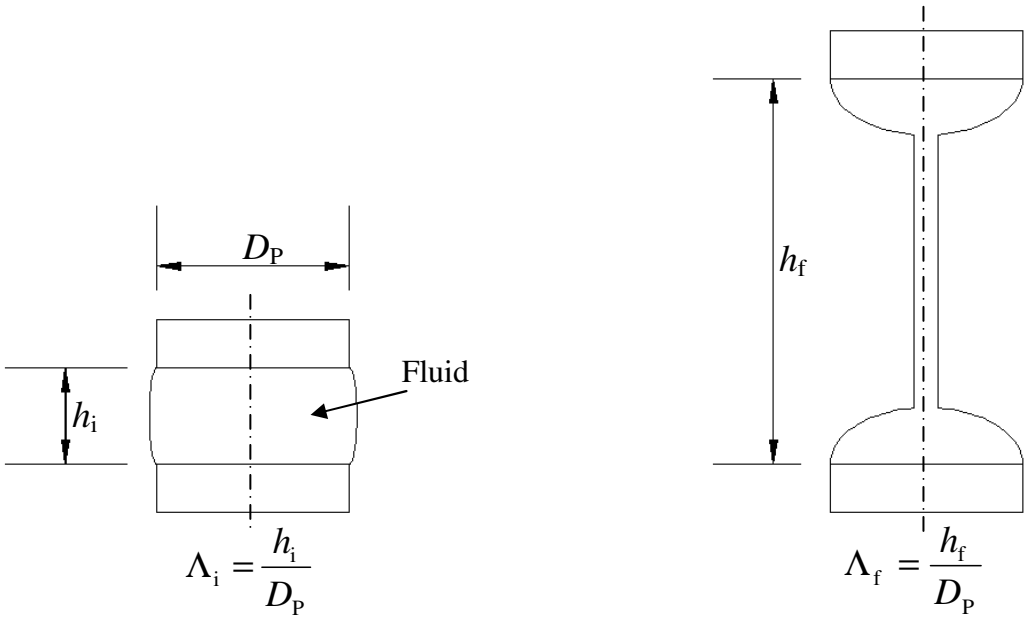

Figure 2.5: Schematic showing the dimensions and aspect ratios for initial and final CaBER plate positions.

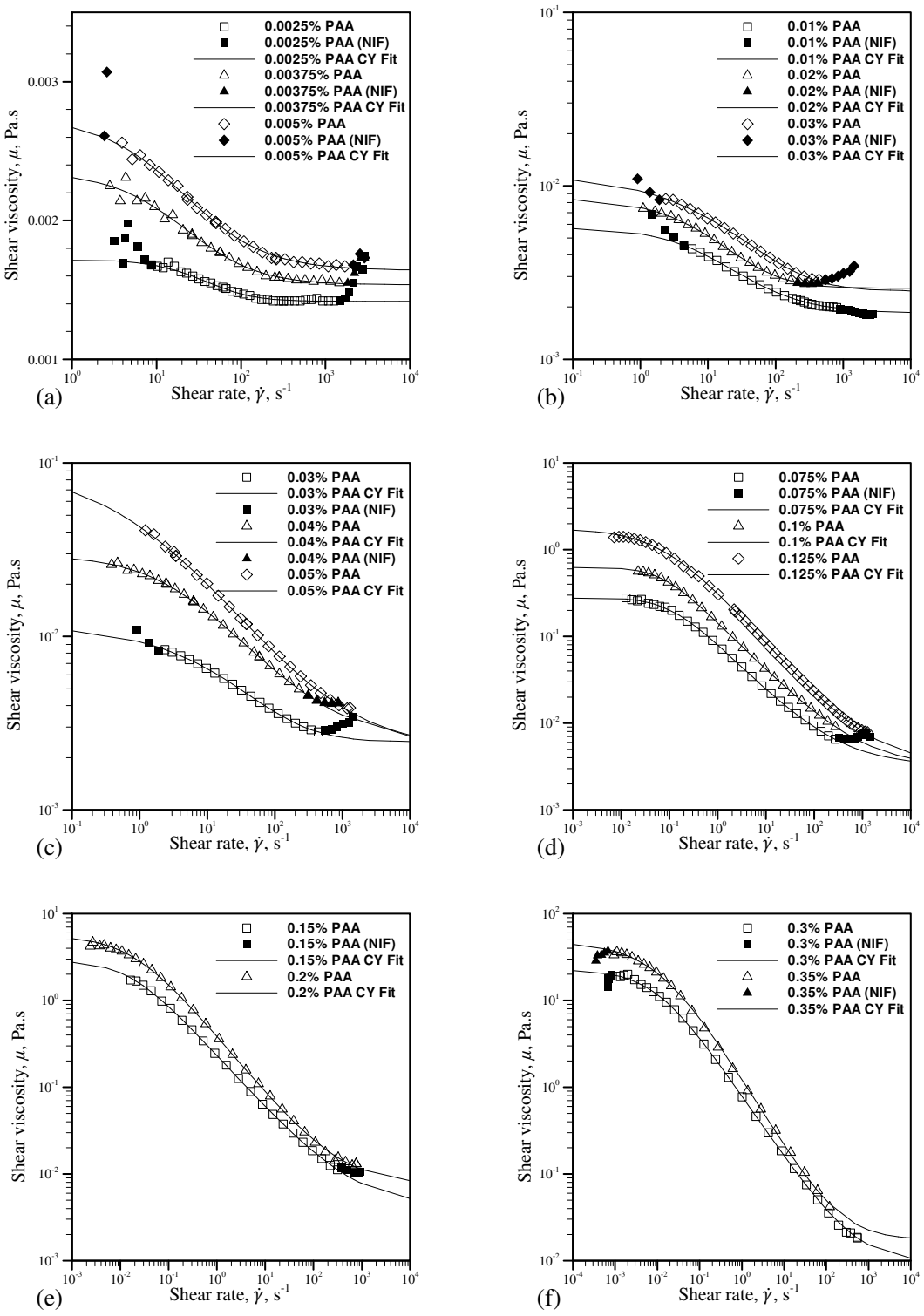

Figure 2.6: Variation of shear viscosity with shear rate and Carreau-Yasuda model fits for various concentrations of polyacrylamide (NIF indicates points not included in the fit).

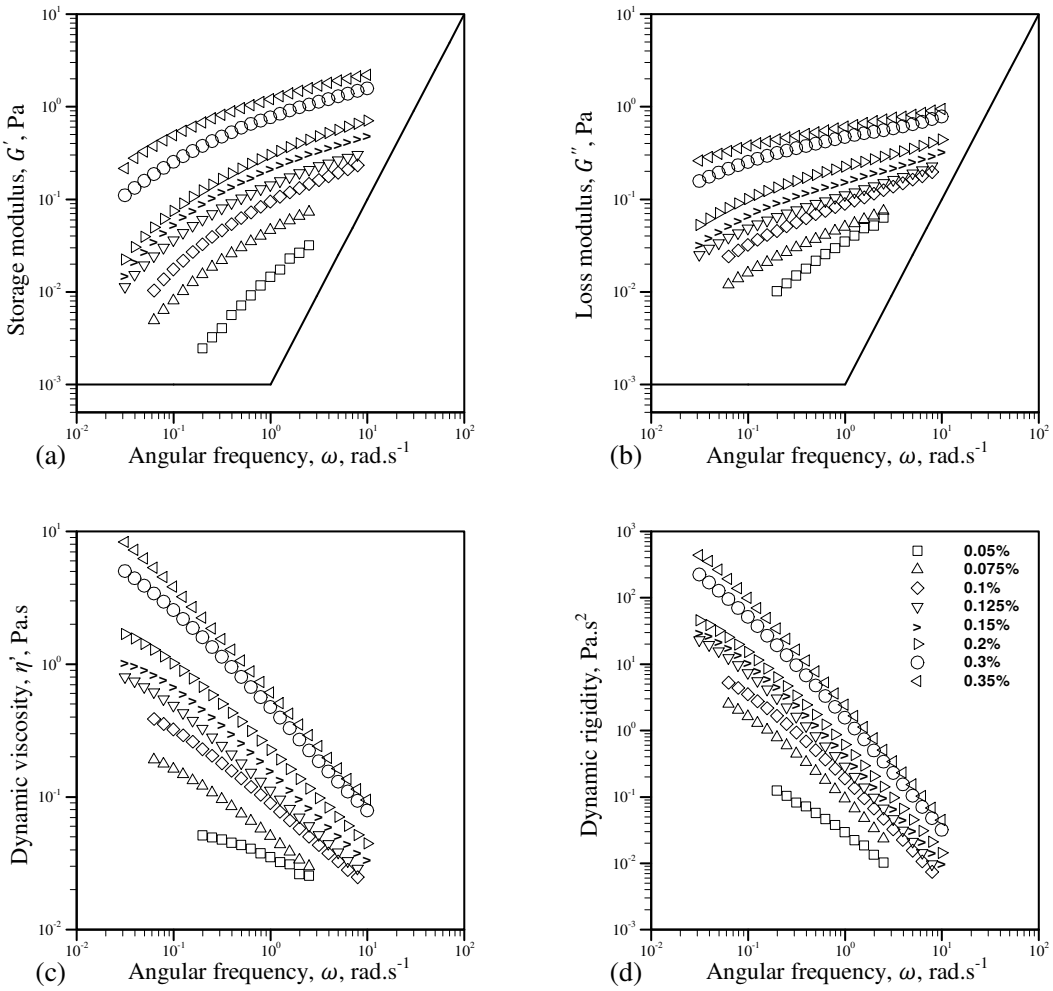

Figure 2.7: Oscillatory shear data for PAA, (a) storage modulus (G') data, (b) loss modulus (G'') data, (c) dynamic viscosity data ($=G''/\omega$) and (d) dynamic rigidity data ($=2G'/\omega^2$), the black line shown in (a) and (b) indicates the limits of the rheometer and the key given in (d) is valid for all figures.

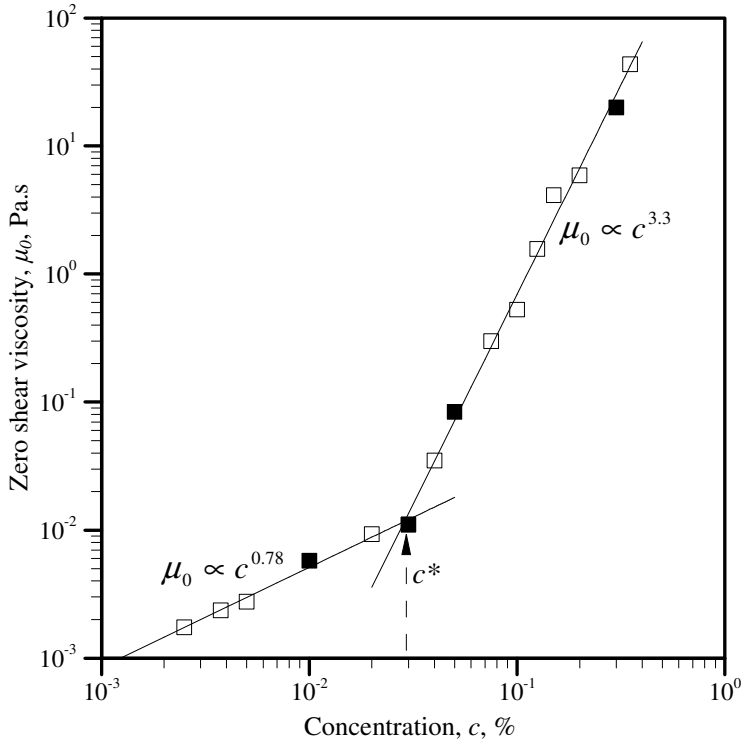

Figure 2.8: Variation in zero shear rate viscosity, determined using the Carreau-Yasuda model fit, with increase in concentration of polyacrylamide showing the critical overlap concentration (≈0.03% PAA), the filled symbols identify the concentrations used during the detailed fluid dynamical measurements.

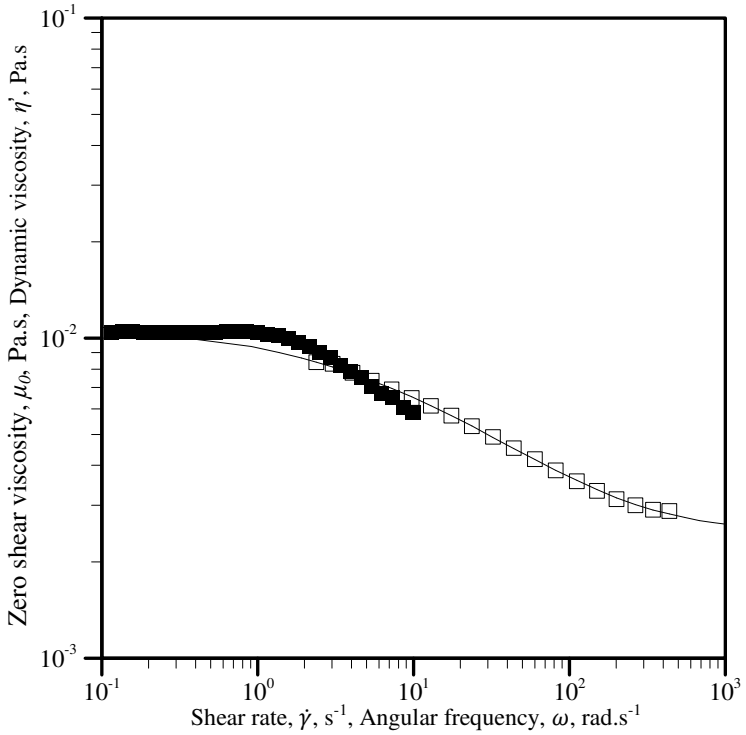

Figure 2.9: Material properties for 0.03% polyacrylamide (□ represents the shear viscosity and ■ the dynamic viscosity).

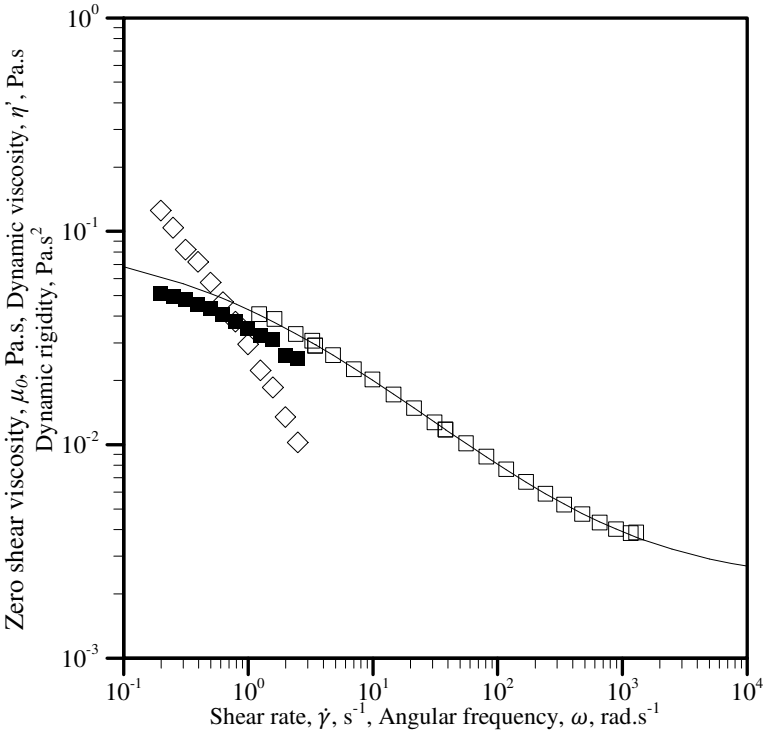

Figure 2.10: Material properties for 0.05% polyacrylamide (□ represents the shear viscosity, ■ the dynamic viscosity and ◇ the dynamic rigidity).

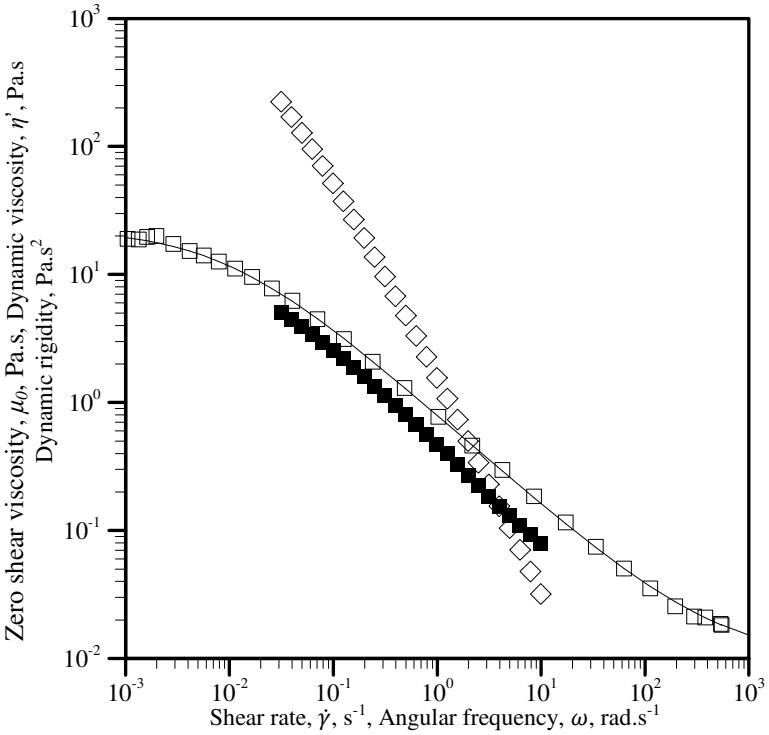

Figure 2.11: Material properties for 0.3% polyacrylamide (□ represents the shear viscosity, ■ the dynamic viscosity and ◇ the dynamic rigidity).

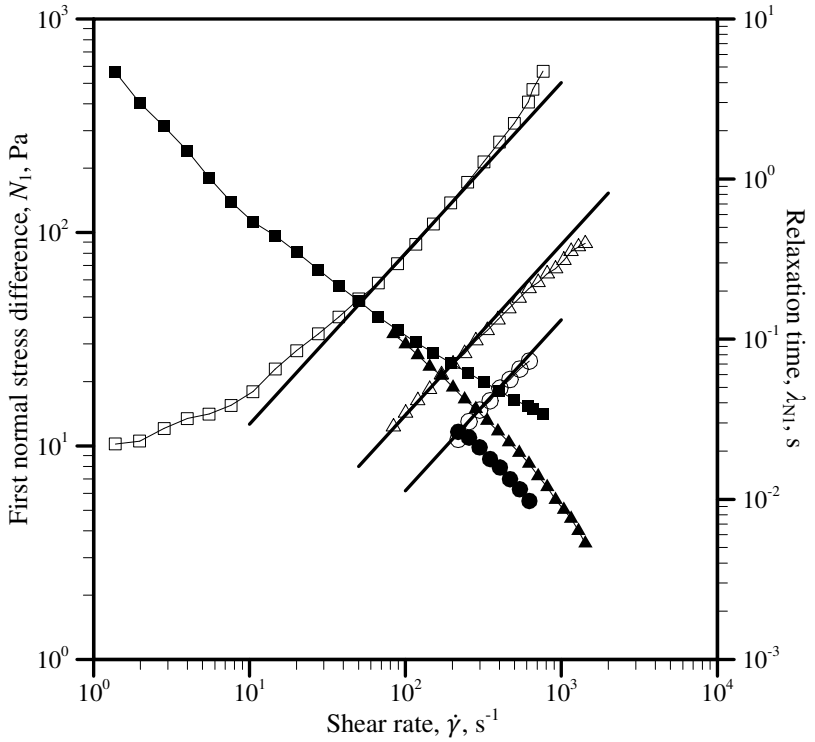

Figure 2.12: First normal-stress difference (open symbols) and relaxation time (filled symbols) data for 0.3% polyacrylamide (■), 0.05% polyacrylamide (▲) and 0.03% polyacrylamide (●).

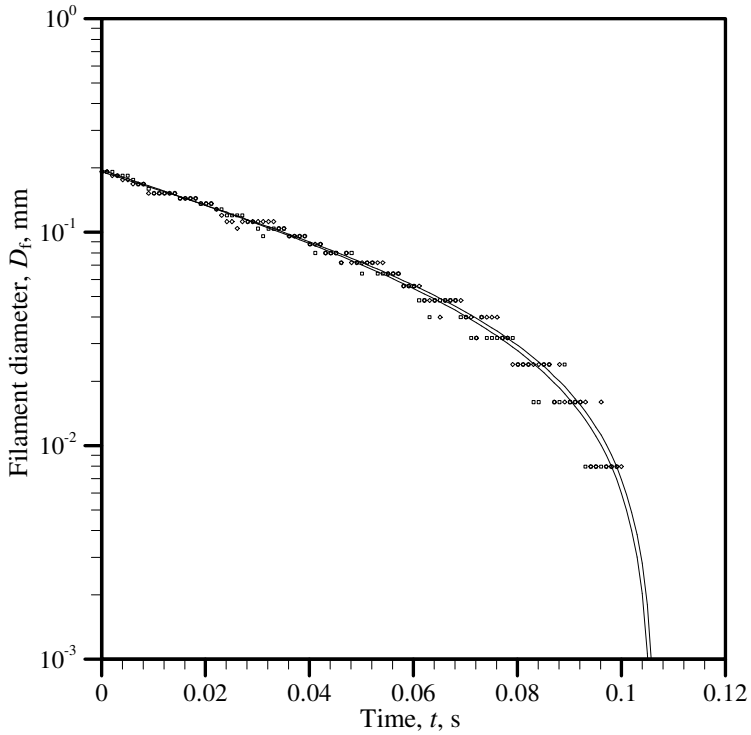

Figure 2.13: Extensional rheology data for 0.03% polyacrylamide, the lines correspond to the fit given in Equation 2.14.

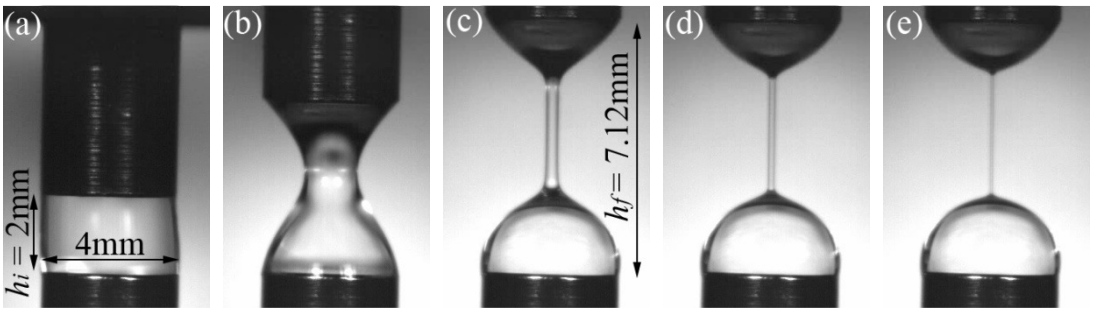

Figure 2.14: High-speed camera images of extensional rheology tests for 0.03% polyacrylamide at (a) -0.1s, (b) -0.05s, (c) 0.0s, (d) 0.05s and (e) 0.1s Λ_i=0.5, Λ_f =1.78 and the strike time is 100ms.

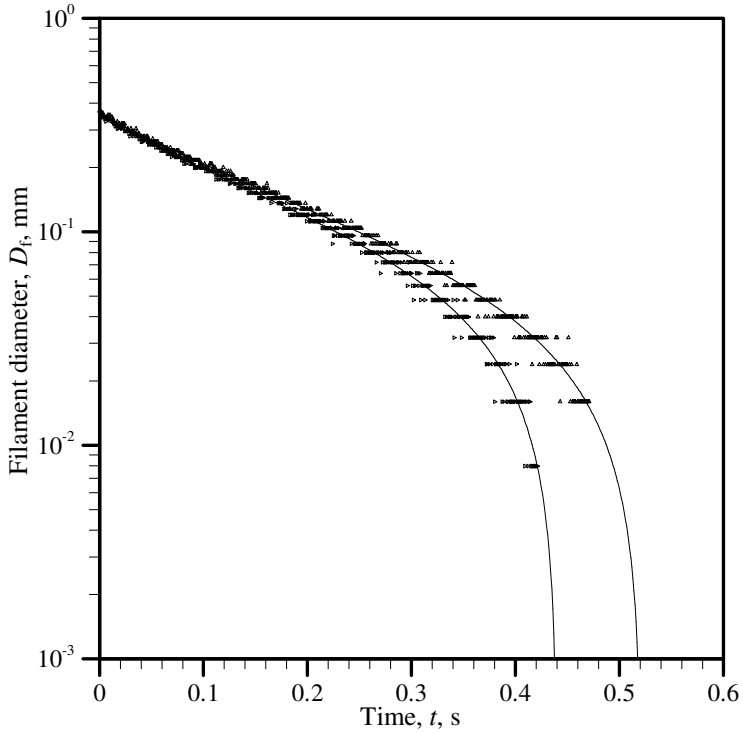

Figure 2.15: Extensional rheology data for 0.05% polyacrylamide, the lines correspond to the fit given in Equation 2.14.

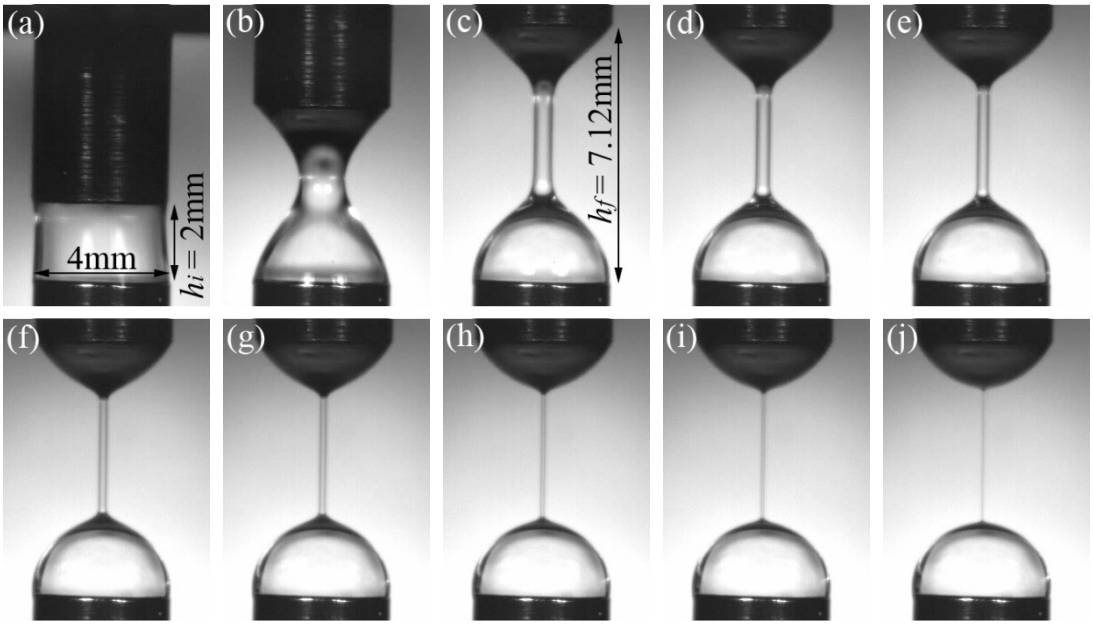

Figure 2.16: High-speed camera images of extensional rheology tests for 0.05% polyacrylamide at (a) -0.1 s, (b) -0.05s, (c) 0.0s, (d) 0.05s, (e) 0.10s, (f) 0.20s, (g) 0.25s, (h) 0.35s, (i) 0.40s, and (j) 0.50s Λ_i=0.5, Λ_f=1.78 and the strike time is 100ms.

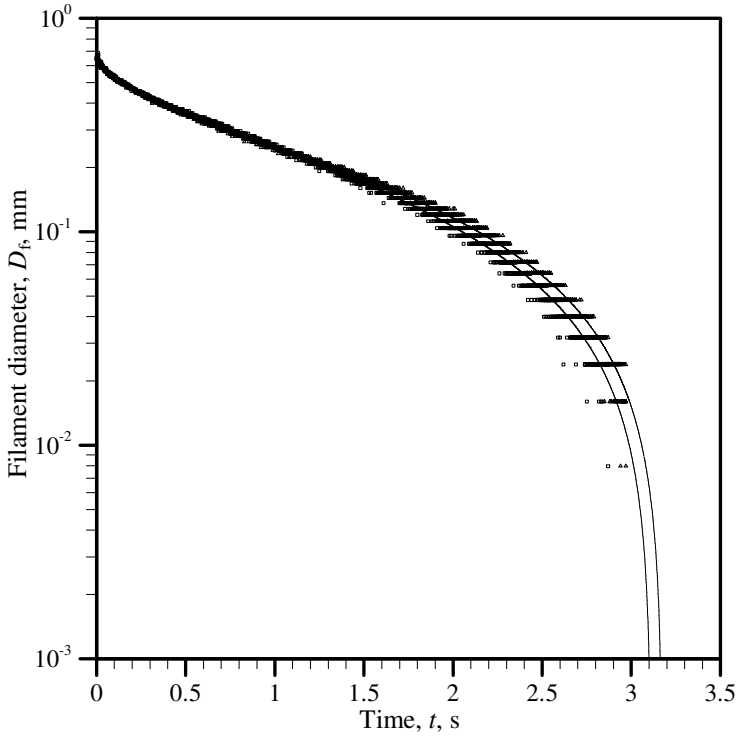

Figure 2.17: Extensional rheology data for 0.3% polyacrylamide, the lines correspond to the fit given in Equation 2.14.

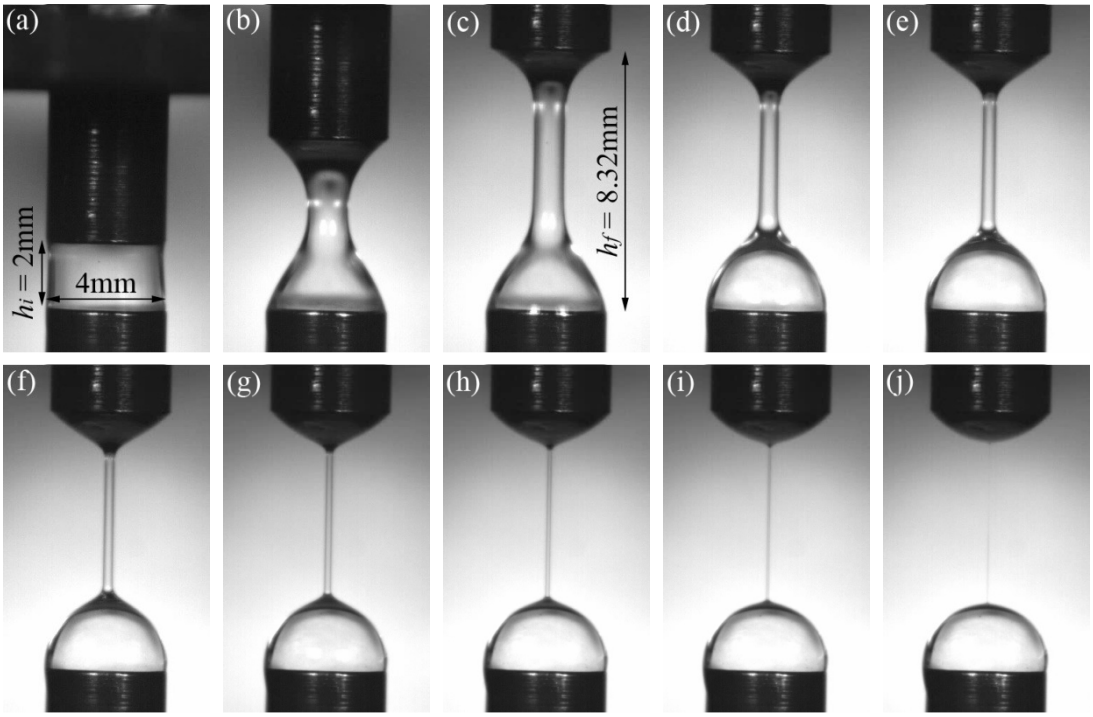

Figure 2.18: High-speed camera images of extensional rheology tests for 0.3% polyacrylamide at (a) -0.1s, (b) -0.05s, (c) 0s, (d) 0.5s, (e) 1s, (f) 1.5s, (g) 2s, (h) 2.5s, (i) 3s and (j) 3.5s in 0.5s intervals Λ_i=0.5, Λ_f=2.08 and the strike time is 100ms.

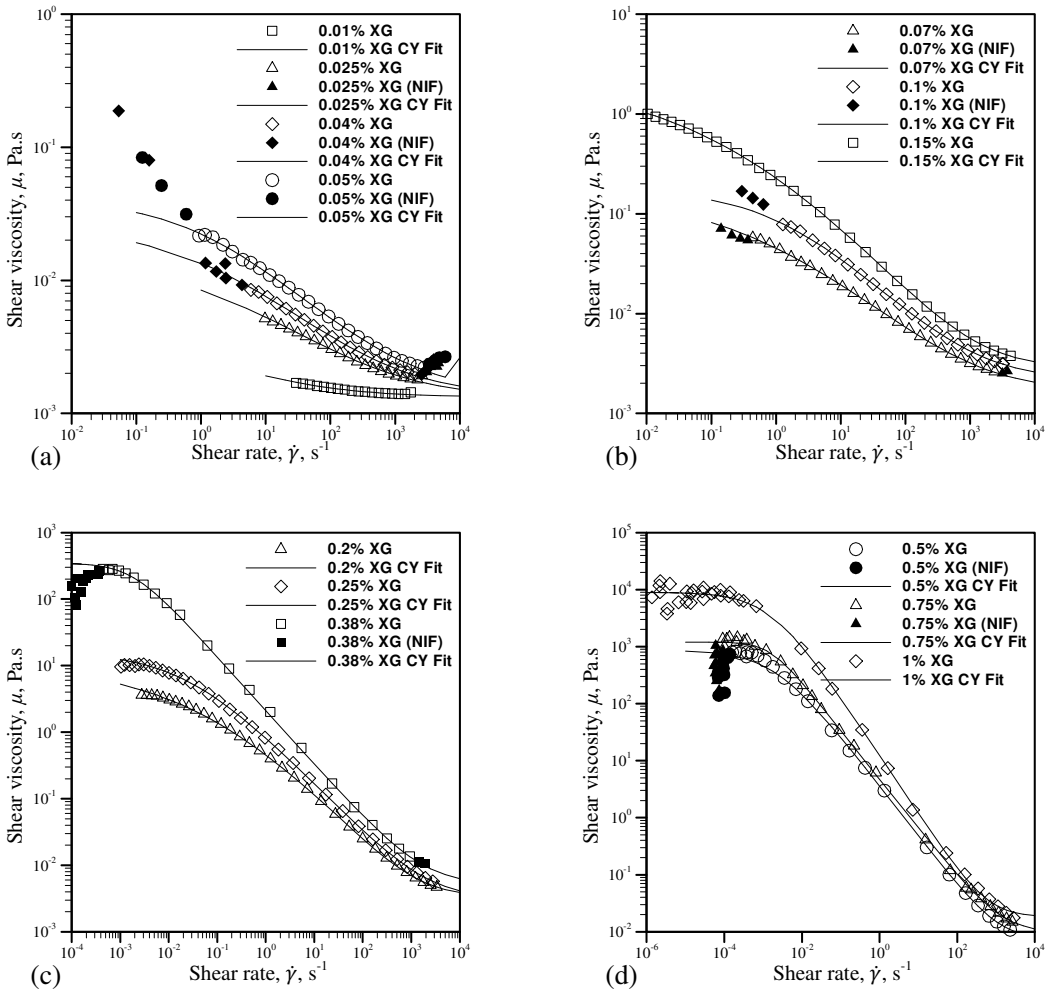

Figure 2.19: Variation of shear viscosity with shear rate and Careau-Yassuda model fits for various concentrations of xanthan gum (NIF indicates not included in fit). (Japper-Jaafar, 2009)

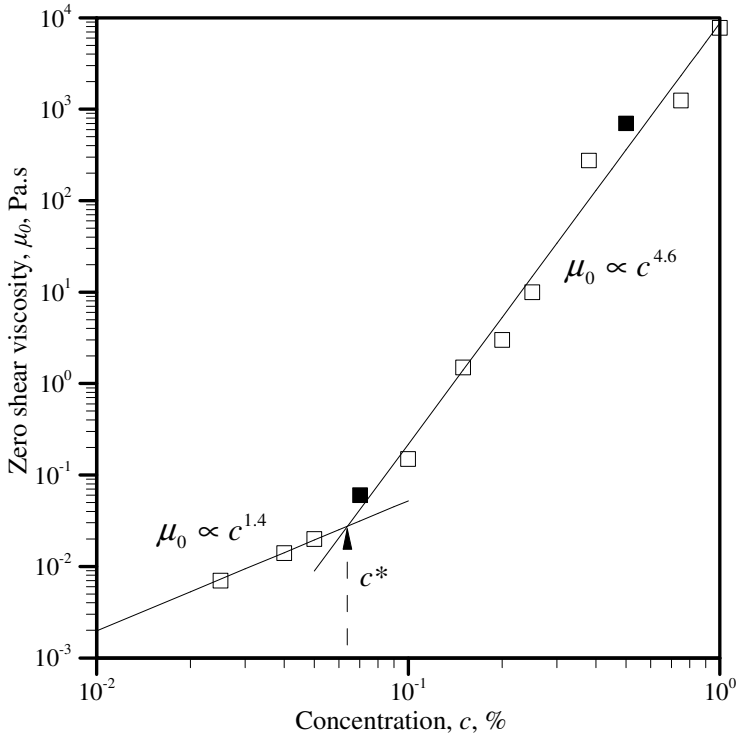

Figure 2.20: Variation in zero shear rate with increase in concentration of xanthan gum showing the critical overlap concentration (≈0.064% XG), the filled symbols identify the concentrations used during the detailed fluid dynamical measurements.

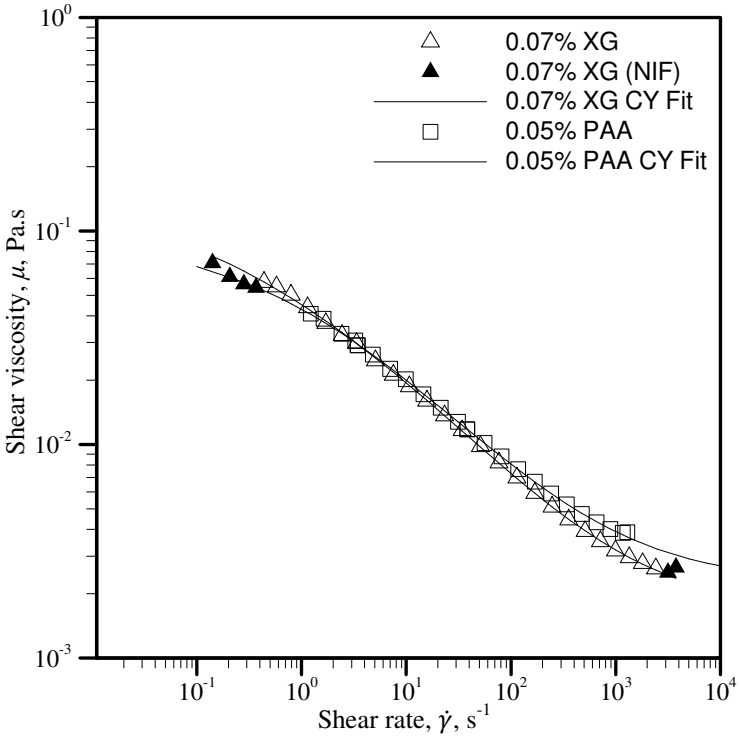

Figure 2.21: Variation in shear viscosity with shear rate and Careau-Yassuda fits for 0.07% xanthan gum and 0.05% polyacrylamide for comparison (NIF indicates points not include in the fit).

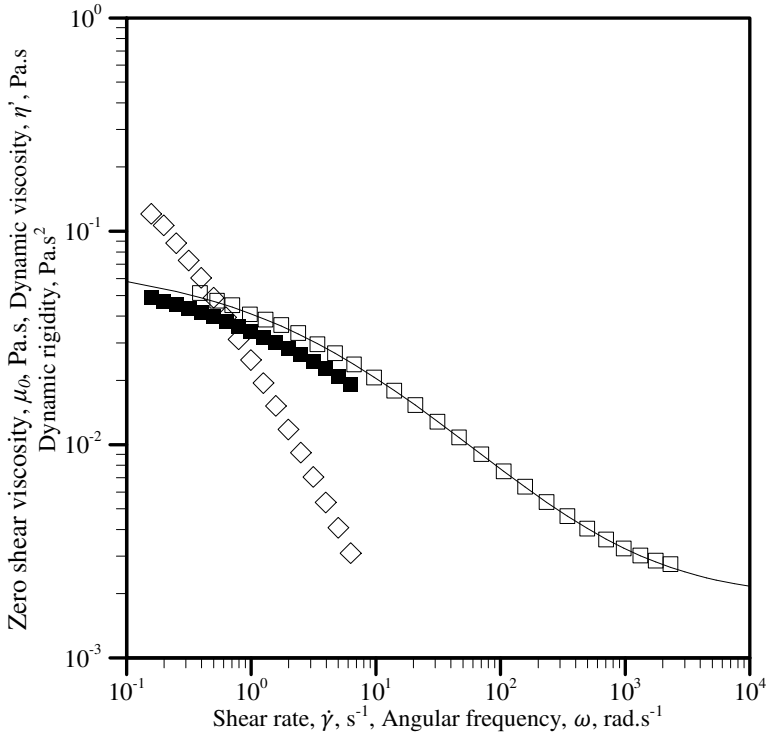

Figure 2.22: Material properties for 0.07% xanthan gum (□ represents the shear viscosity, ■ the dynamic viscosity and ◇ the dynamic rigidity).

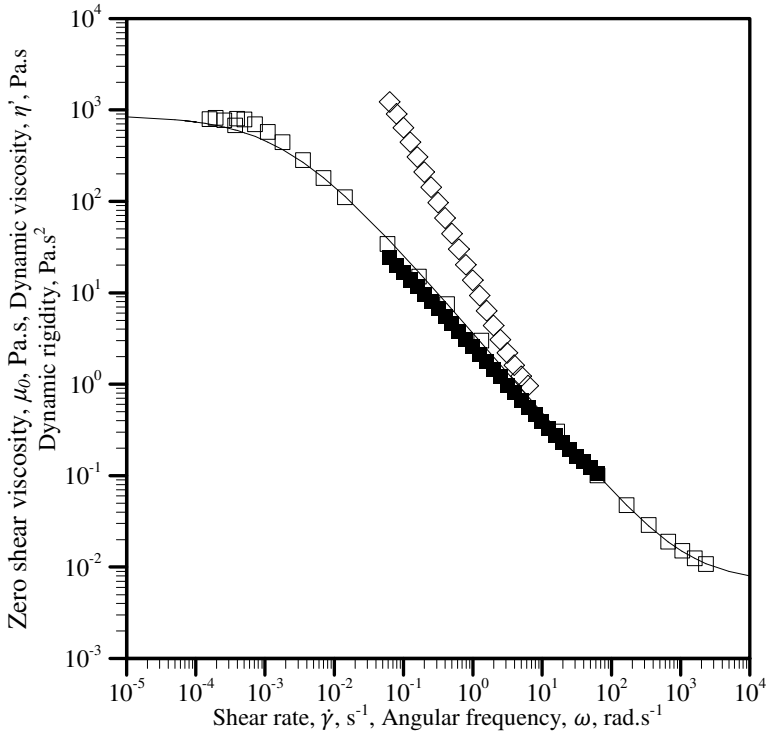

Figure 2.23: Material properties for 0.5% xanthan gum (□ represents the shear viscosity, ■ the dynamic viscosity and ◇ the dynamic rigidity).

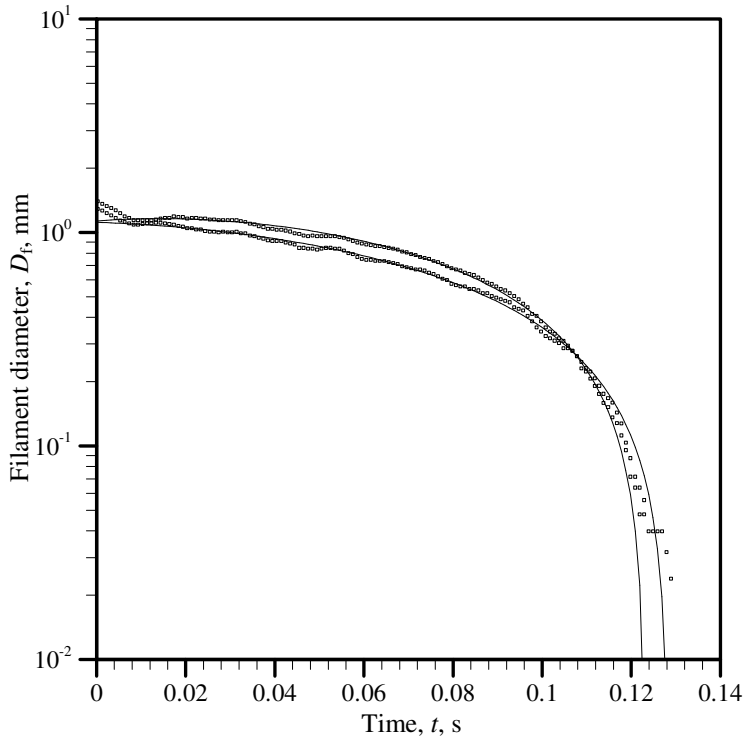

Figure 2.24: Extensional rheology data for 0.5% xanthan gum (Japper-Jaafar, 2009) the lines correspond to the fit given in Equation 2.14.

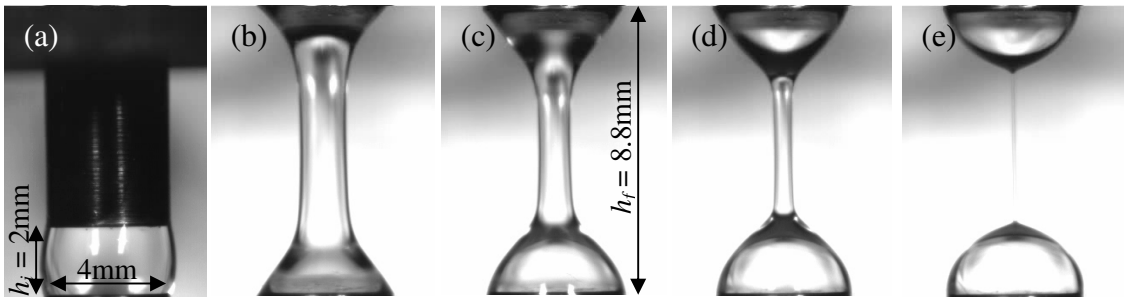

Figure 2.25: High speed camera images of extensional rheology tests for 0.5% xanthan gum at (a) -0.1s, (b) 0s, (c) 0.04s, (d) 0.08s and (e) 0.12s, Λ_i=0.5, Λ_f=2.2 and the strike time is 50ms (Japper-Jaafar, 2008).

3. Experimental Test Rig and Instrumentation

3.1. Test rig and mixing protocol

A schematic diagram of the flow loop is shown in Figure 3.1. A stainless steel tank with a capacity of approximately 80 litres feeds a progressive cavity pump (manufactured by Mono Pumps, type Monobloc B021) capable of pumping up to $3m^3$/hr at maximum power. The flow enters a square duct comprising 1.2m long sections, which have internal dimensions of 80mm by 80mm, i.e. hydraulic diameter D_H = 80mm (where $D_H = (4A)/P$, A being the cross-sectional area (mm^2) and P the wetted perimeter of the duct (mm)). The sections of square duct were manufactured from stainless steel and precision ground to the correct size, two of these sections precede the contraction test section (described below), giving a distance of at least 32 hydraulic diameters before the contraction to ensure that the flow is fully developed (Durst *et al.* (2005)) when it reaches the contraction. The contraction test section is then followed by another 1.2m section of square duct. The flow returns to the tank through a 1¼" plastic pipe via a Coriolis flowmeter (manufactured by Endress and Hauser, type Promass 63), which measures the mass flow rate, $\dot{m}$ ($kg.s^{-1}$), from which the bulk velocity, U_B ($m.s^{-1}$), can be estimated. The uncertainty in the flow rate was estimated to be approximately 1.5%. A Coriolis flowmeter was used since they have been found to be more accurate for non-Newtonian fluids than other flowmeters such as electromagnetic and especially ultrasonic flowmeters (Fyrippi *et al.* 2004). The fluid temperature is monitored using a platinum resistance temperature probe, with resolution of ±0.01°C, mounted within the tank. The variation in fluid temperature was within 1°C for each velocity profile, which typically took 1 hour to measure.

Although a mixing loop is incorporated into the test rig, for the majority of the results in this investigation it was not used to mix the fluids. Initially the polymer solutions were mixed within the mixing loop and the test rig, but early measurements indicated that the polymer solution was degrading before the solution had reached homogeneity. Shear viscosity measurements of the solution were taken during mixing and compared to benchtop results in order to determine whether the fluid was

correctly mixed. In the 'mixing loop' case the shear viscosity never reached the expected level, even after several days of mixing. To overcome this problem an alternative mixing protocol was developed. The polymer solutions were mixed outside of the rig in 10 litre batches using an overhead stirrer then transported into the tank where the solution was mixed for around 30 minutes using the mixing loop before being drained into the rest of the test rig. This mixing method proved to be both more efficient and more reproducible than the previous method. In addition, mixing the polymer solutions external to the rig meant that it was possible to perform velocity measurements on one batch and mix further batches at the same time. This method also meant that the exact amount of polymer was added to the exact amount of water required. When mixing in the rig, ensuring the correct amount of water was more problematic as often there were air bubbles trapped in sections of the rig that were not immediately apparent.

Degradation of the polymer solution before the fluid was fully mixed highlighted that the fluids would have a limited lifetime during which they would produce reliable and repeatable results. To this end a set of degradation tests was performed to determine the length of time that 0.05% polyacrylamide (at two different flow rates) could be used within the test rig in conjunction with the 8:1 contraction section. Velocity profiles were measured and the time at which the maximum velocity was observed for each profile recorded. A fluid sample was taken from the rig (via a tapping immediately upstream of the contraction section) between each velocity profile measurement, then both shear and extensional rheology measurements were performed and the total time that the fluid was pumped for was also recorded. The velocity profiles in the contraction were seen to change dramatically, as shown in Figure 3.2, with the maximum near wall velocity decreasing significantly over time; however there was a period of approximately 5-6 hours where the results, particularly the maximum overshoot velocity, exhibited little variation, as shown in Figure 3.3. The shear viscosity of the fluid and the relaxation time were also seen to decrease with time (see Figures 3.4 and 3.5). The shear viscosities and relaxation times for the first sample and the sample taken after 6 hours give the 'window' in which the shear viscosity or relaxation time is still within acceptable limits (see Figures 3.6 and 3.7). Interestingly, the extensional rheology appeared to be affected to a greater extent than the shear rheology by the degradation

of the polymer. As a consequence, for the remainder of the tests reported here the extensional rheology was used as the primary check to monitor fluid degradation.

3.1.1. Gradual Contraction Test Section

The gradual contraction section is made up of three components, the first being a square cross section with internal dimensions 80mm by 80mm (i.e. the same dimensions as the upstream square duct), the second being the smooth gradual planar contraction of either 8:1 or 4:1 contraction ratio, and the final part being a rectangular cross section with internal dimensions of either 80mm by 10mm or 80mm by 20mm to accommodate the contraction ratio. In order to aid visualisation of the flow at various positions, the walls of the contraction section are all made from Perspex and the section can be rotated about the x-axis. The dimensions for both contractions are given in Table 3.1 and an isometric diagram of both test sections is shown in Figure 3.8. Figure 3.9 is a photograph of the 8:1 contraction test section.

Figure 3.10 shows a schematic of the 8:1 contraction, which is a smooth gradual planar contraction. The contraction has a length, L, of 54.54mm and constant width, w, of 80mm. The contraction comprises two radii, the first being a 40mm concave radius followed by a 20mm convex radius and the height of the contraction varies gradually between the upstream duct height, D=80mm and the downstream duct height d=10mm. A rectangular channel, with internal dimensions 80mm by 10mm, follows the contraction. The end of the contraction is defined as x=0, which means x/L =-1 represents the beginning of the contraction section.

For every fluid investigated in the 8:1 contraction, measurements were made from wall to wall across the XZ-centreplane at six positions, x/L=-1, x/L=-0.72, x/L=-0.45, x/L=-0.27, x/L=-0.17 and x/L=0.10. These positions correspond to the start of the contraction then 15mm, 30mm, 40mm, 45mm and 60mm from the start of the contraction. Once symmetry had been confirmed it was decided to measure only half profiles in the spanwise direction because of the time limit on each batch of fluid imposed by the rate of fluid degradation. For some of the fluids, measurements were made at the same six positions across the XY-centreplane. For 0.3% PAA extra

profiles were measured at x/L=-1.18 and x/L=-0.22 (i.e. 10mm before the start of the contraction and 42.5mm into the contraction). In addition, for all fluids profiles were measured at x/L=-3.2, approximately 120mm upstream of the contraction, across both the XY- and XZ-centreplanes in order to confirm that the flow is fully developed and a 'centreline' profile (i.e. $-3.2<x/L<0$ along $z/w = 0$) was measured to determine the strain rate profile and also to provide a consistency check with the profiles in the XZ-centreplane.

Figure 3.11 shows a schematic of the 4:1 contraction section. It is similar in shape to the 8:1 contraction but there are obvious differences to accommodate the change in contraction ratio. The contraction still comprises two radii, a 40mm concave followed by a 20mm convex, however as the contraction ratio has been changed the downstream duct height, d, is now 20mm and the length, L, is 51.98mm. Again x=0 has been defined at the end of the contraction, making x/L=-1 the start of the contraction.

In the 4:1 contraction measurements were made across both the XY- and XZ-centreplanes at six positions, x/L=-1, x/L=-0.71, x/L=-0.42, x/L=-0.23, x/L=-0.13 and x/L=0.15. These positions, similar to in the 8:1 contraction, correspond to the start of the contraction, 15mm, 30mm, 40mm, 45mm and 60mm from the start of the contraction. For 0.3% PAA two extra profiles were measured 10mm prior to the start of the contraction and 42.5mm after the start of the contraction (i.e. x/L=-1.19 and x/L=-0.18). As for the 8:1 contraction profiles were measured at x/L=-3.2 across both centreplanes to confirm that the flow is fully developed before it reaches the contraction and a 'centreline' profile was also measured.

The following 'definitions' will be used throughout the results and discussion in reference to both contractions. Transverse and top to bottom profiles are measured on XY planes and the 'top' and 'bottom' of the contraction are the curved walls. Spanwise and side to side profiles are those measured on XZ planes and the 'side' walls are the plane walls.

Figure 3.12 is a schematic of both contractions, provided for comparison. Both contractions are identical to start with, changing towards the end of the contraction

resulting in a different end height, *d*, length, *L*, and contraction ratio. The differences between the two contractions are highlighted when the Hencky strain (Collier *et al.* 2002)) is determined for each contraction. The Hencky strain may be calculated using

$$\varepsilon_H = \int_0^t \dot{\varepsilon} \mathrm{d}t \Rightarrow \int_{u_1}^{u_2} \frac{\mathrm{d}u}{u} = ln\frac{u_2}{u_1} \Rightarrow ln\,CR \tag{3.1}$$

where *CR* is the contraction ratio and u_1 and u_2 are the velocities upstream and downstream of the contraction respectively. This gives Hencky strains of $\varepsilon_H = 2.08$ for the 8:1 contraction and $\varepsilon_H = 1.39$ for the 4:1 contraction. It is clear that the Hencky strain exerted on the fluids is much larger (approximately 50%) through the 8:1 contraction than through the 4:1 contraction.

3.2. Estimation of Reynolds, Deborah and Elasticity numbers

As stated in Chapter 1, the Reynolds number is defined as $Re = \rho U_B l / \mu(\dot{\gamma})$ (Equation 1.3). In this investigation the velocity scale has been defined as the bulk velocity at the end of both contractions (i.e. U_d), which can be determined using the contraction width and end heights along with the measured mass flow rate, the length scale is defined as the end height of each contraction (i.e. *d*). For non-Newtonian shear thinning fluids it is impossible to unambiguously define a single value of the viscosity. The method adopted here was to determine a characteristic shear rate, $\dot{\gamma}_{CH}$, using the same velocity and length scales as used to calculate the Reynolds number, giving $\dot{\gamma}_{\mathrm{CH}} = U_\mathrm{d}/d$, and then to use the Carreau-Yasuda model fit (Equation 2.2) to determine a characteristic shear viscosity, μ_{CH}, corresponding to this shear rate. This gives us a redefined Reynolds number of

$$Re = \frac{\rho U_\mathrm{d} d}{\mu_{\mathrm{CH}}}. \tag{3.2}$$

The quantities used to calculate the Reynolds numbers and other parameters for both contractions are given in Table 3.2. The Reynolds number could of course be calculated using different values for the shear viscosity, such as the infinite shear-rate viscosity (μ_∞) or the zero shear-rate viscosity (μ_0). These viscosities are

measured at shear rates much larger or much smaller than those observed throughout these investigations and as such would lead to either very high or very low Reynolds numbers, which would not provide a very good estimate of the importance of inertia forces in the flow. Another alternative is to use the wall shear rate instead of defining a characteristic shear rate, however this method is best suited to fully-developed flow as for contraction flows the wall shear rate is continually changing with location.

The Deborah number was also defined in Chapter 1 as $De = \lambda / T$ (Equation 1.4). T is taken to be the inverse of the characteristic shear rate, i.e. d/U_{d}. It is possible to determine the relaxation time in a number of deformation modes, as discussed in detail in Chapter 2. In this investigation relaxation times have been found using both CaBER extensional viscosity measurements and, where possible, from steady-state shear measurement of the first normal-stress difference. The flow is a combination of shear flow close to the sidewalls of the contraction and extensional flow along the centre of the contraction, which is why relaxation times have been estimated using these two different methods. To this end two relaxation times, λ_{C} and λ_{N1} are defined for each contraction ratio. These relaxation times lead us to define the Deborah numbers as

$$De_{\mathrm{C}} = \frac{\lambda_{\mathrm{C}} U_{\mathrm{d}}}{d}, \tag{3.3}$$

$$De_{\mathrm{N1}} = \frac{\lambda_{\mathrm{N1}} U_{\mathrm{d}}}{d}. \tag{3.4}$$

The Weissenberg number was defined in Chapter 1 as $Wi = \lambda\dot{\gamma}$ or $Wi = \lambda\dot{\varepsilon}$ (Equation 1.6). Because the strain rate, $\dot{\varepsilon}$, is not uniform throughout the contraction it has been estimated along the centreline of the contraction (i.e. where the XY- and XZ-centreplanes intersect) from streamwise velocity measurements taken along the centreline. The strain rate is then simply the change in velocity divided by the change in distance (i.e. dU_C/dx). As discussed above the relaxation time, λ, has been estimated in two different ways, hence two Weissenberg numbers are defined as

$$Wi_{\mathrm{C}} = \lambda_{\mathrm{C}}\dot{\varepsilon}, \tag{3.5}$$

$$Wi_{\mathrm{N1}} = \lambda_{\mathrm{N1}}\dot{\varepsilon}. \tag{3.6}$$

Two Elasticity numbers have been defined in Chapter 1 as $El_1=De/Re$ and $El_2=Wi/Re$ (Equations 1.7 and 1.8). Since there are two Deborah and Weissenberg numbers for each contraction there will be four Elasticity numbers, which are also defined in Table 3.2. As there are so many alternative values for *El*, *De* and *Wi* it was decided to focus primarily on De_C as we had *a priori* knowledge of the CaBER relaxation times and could easily estimate the characteristic shear rates from the flow rates. As a consequence of this, De_C was used to 'match' the Deborah number for some of the fluids in an attempt to isolate various effects.

3.3. Laser Doppler Anemometry (LDA)

Laser Doppler anemometry is a method for measuring the flow velocity of a fluid at discrete locations within a flow. LDA does not disturb the flow so can be used in place of intrusive mechanical probes, such as hot-wire anemometers or pitot tubes, which may become contaminated over time by polymer deposits (Rudd (1972)).

In 1964 Yeh and Cummins measured the velocity profiles in fully-developed laminar pipe flow of water in the first application of LDA to fluid mechanics. Since then many advancements to the technique have been made, including progress in optical arrangements, signal-processing systems and light scattering or seeding particles (Durst *et al.* (1976)). These developments and a thorough description of LDA are given by Durst *et al.* and more recent developments are noted by Tropea (1995). As the technique is so well developed only a brief overview is given here.

3.3.1. Theory

A laser produces a single beam, which is split into two beams by a beam splitter within the probe. The two beams are then focussed on an intersection volume within the flow. Interference fringes form within this intersection volume (see Figure 3.13) and the spacing between these interference fringes (δ, m) can be calculated using

$$\delta = \frac{\lambda_w}{2\sin(\theta/2)} \tag{3.7}$$

where λ_w (m) is the wavelength of the laser light and θ (°) is the angle between the two laser beams.

When a particle crosses one of the interference fringes a burst of reflected and scattered light, known as a Doppler burst, is produced. The frequency of this light (f_D , Hz) is dependent on the fringe spacing (Equation 3.7) and the particle velocity normal to the laser beams. The Doppler burst is detected by a receiving optic and this information is sent to a burst spectrum analyser (BSA) for analysis. The BSA calculates the particle velocity (U , m.s^{-1}) using

$$U = \frac{f_D \lambda_w}{2 \sin(\theta/2)}. \tag{3.8}$$

The probe is set up so that the interference fringes form normally to the direction of the flow and a component of the flow velocity can be measured.

The LDA system may be arranged in either forward scatter or backward scatter. This refers to the position of the receiving optics in relation to the intersection volume and also the direction of the reflected light. If we say that the laser light is travelling forwards from the probe then receiving optics on the same side of the intersection volume as the probe are set up for backward scatter and will see the reflected light from the Doppler burst. Receiving optics on the opposite side of the intersection are set up for forward scatter and will see the scattered light from the burst. Some laser systems have receiving optics incorporated into the laser probe and this may be used for backward scatter rather than separate optics being required. It is, however, preferable to use forward scatter as this will provide a much better data rate (van Maanen (1999)) since more light from the Doppler burst is scattered forwards than is reflected backwards.

3.3.2. Equipment

The LDA system used here (see Figure 3.14 for a schematic) is composed of an integrated laser-optics system comprising a laser connected to a probe by a fibre optic cable (see below for details), receiving optic set up to receive in forward scatter with a focal length of 300mm connected to a photomultiplier (PM) tube and a burst spectrum analyser (BSA), Dantec model number 57N21, in conjunction with a PC to run the accompanying data-processing software. Throughout this investigation two

integrated laser-optics systems were used, the Dantec Flowlite and the Dantec Fibreflow, Table 3.3 presents the specifications for both systems. The Flowlite was used due to the initial unavailability of a Fibreflow system. The Fibreflow has a much smaller measuring volume, which means that the transit time of each particle is shorter, as such there will be less noise in the data and broadening effects are reduced. The average number of bursts collected at each point while using the Flowlite was between 9500 and 10000, while when using the Fibreflow it was increased to between 19000 and 20000 bursts per point. The maximum statistical uncertainty for the data was estimated to be approximately 0.6% using

$$Error_{\text{mean}} = Z_{\text{C}} \frac{\frac{\sigma_D}{\mu_S}}{\sqrt{N_S}} \tag{3.9}$$

where N_S is the sample size, μ_S is the sample average, σ is the standard deviation and Z_{C} is a constant, with value 2, defined by Yanta and Smith (1973).

In order to increase the available data rate seeding particles are used within the flow. These particles have no effect on the fluid characteristics and increase the number of bursts that will be picked up by the BSA (Ikeda *et al.* (1994)). The seeding particles used throughout this investigation were Timiron Supersilk MP-1005, manufactured by S. Black Ltd. These particles have an average particle size of 5μm and approximately 0.05g were added to each solution (total mass approximately 70kg).

Movement of the LDA probe is achieved through use of an in-house three-dimensional traverse with step size resolution of ±5μm. The traverse can be automated or controlled manually and can move in the *x*, *y* and *z* planes, allowing optical access to any region in the flow.

3.3.3. Refraction Correction

When light travels through different materials, such as glass, plastic and water, it travels at different speeds (Overheim and Wagner (1982)). The same is true of a laser beam. The refractive index of a material (n) is the factor by which the speed of the laser light is slowed by the material. As well as being slowed the beam bends at

the interface between the materials, a process called refraction. Snell's Law, which describes this phenomenon, is commonly written as

$$n_1 \sin\theta_1 = n_2 \sin\theta_2 \tag{3.10}$$

and is used to calculate the degree of refraction when light travels from one material to another. This process is shown schematically in Figure 3.15.

Bicen (1982) introduced a refraction correction calculation for use when investigating flow through cylindrical pipes. The laser beam is perpendicular to the refracting surface and the intersection volume is moved along this perpendicular plane, hence the calculation can also be used for flat boundaries, as the laser beam will always be perpendicular to the refracting surface in this case. Bicen's original equation is rearranged to give

$$r_a = \frac{r_f - \left(1 - \frac{n_f}{n_w}\right)t + \left(n_f - 1\right)\left(\frac{w+2t}{2}\right)}{n_f} \tag{3.11}$$

where r_f is the position within the flow (m), r_a is the position of the probe (m), n_f and n_w are the refractive indices of the fluid and the wall respectively, t is the thickness of the wall (m) and w is the internal width of the duct (m). Equation 3.5 is used to calculate the required position of the probe in terms of the position of the intersection volume within the flow. From this equation it was found that the actual distance required to traverse the section (80mm) when the test rig was filled with water or polymer solutions was only 60 mm making a probe movement of 0.75mm outside the flow equivalent to a movement of 1mm inside the flow.

3.3.4. LDA system error

In circular pipe flow it is possible to validate continuity and determine whether mass is conserved within the flow by integrating the velocity profiles. This validation is only possible if the flow is axisymmetric. An alternative for square duct flow is to fit the perform an RMS (root mean square) fit of the experimental data to the fully developed theoretical data using

$$\text{Error} = \sqrt{\frac{\sum_{i=1}^{N}\left(x_{th} - x_{exp}\right)^2}{N}}\,. \tag{3.12}$$

The error within the LDA system was found to be approximately 4.5% using the experimental data from the fully developed velocity profiles in the Newtonian case (presented in detail in Chapter 4).

3.4. Tables

Table 3.1: Dimensions for each contraction.

Contraction ratio	**8:1**	**4:1**
Length, L (mm)	54.54	51.98
Width, w (mm)	80	80
Start height, D (mm)	80	80
End height, d (mm)	10	20
First radius, R_D (mm)	40	40
Second radius, R_d (mm)	20	20

Table 3.2: Values used to calculate Reynolds, Deborah, Weissenberg and Elasticity numbers.

Quantity	**Definition**
U_B (m.s^{-1})	U_d
l (m)	d
μ_{CH} (Pa.s)	μ_{CH} is determined at $\dot{\gamma}_{CH}$
$\dot{\gamma}_{CH}$ (s^{-1})	$\dot{\gamma}_{CH}=U_d/d$
Re	$Re=\frac{\rho U_d d}{\mu_{CH}}$
T (s)	$T=d/U_d$
λ_C (s)	λ_C
λ_{N1} (s)	λ_{N1} is determined at $\dot{\gamma}_{CH}$
De_C	$De_C=\frac{\lambda_C U_d}{d}$
De_{N1}	$De_{N1}=\frac{\lambda_{N1} U_d}{d}$
$El_{1,C}$	$El_{1,C}= De_C/Re$
$El_{1,N1}$	$El_{1,N1}= De_{N1}/Re$
Wi_C	$Wi_C=\lambda_C\dot{\varepsilon}$
Wi_{N1}	$Wi_{N1}=\lambda_{N1}\dot{\varepsilon}$
$El_{2,C}$	$El_{2,C}= Wi_C/Re$
$El_{2,N1}$	$El_{2,N1}= Wi_{N1}/ Re$

Table 3.3: Specifications for the Dantec Flowlite and Fibreflow.

	Flowlite	**Fibreflow**
Type	10mW Helium Neon	500mW Argon Ion
Colour	Red	Green
Focal length, F_L (mm)	160	160
Beam Diameter (mm)	0.998	0.998
Wavelength, λ_w (nm)	633	514.5
Beam separation, (mm)	38.4	51.5
Beam angle, θ (°)	14	18
Fringe spacing, δ (μm)	2.656	1.619
Measuring volume diameter (μm)	75	20
Measuring volume length (mm)	0.63	0.21

3.5. Figures

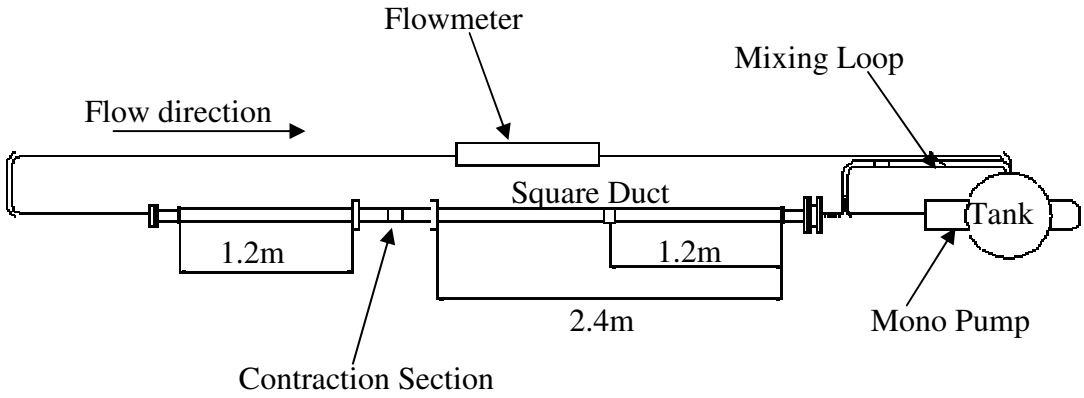

Figure 3.1: Schematic diagram of the test rig (the flow is clockwise).

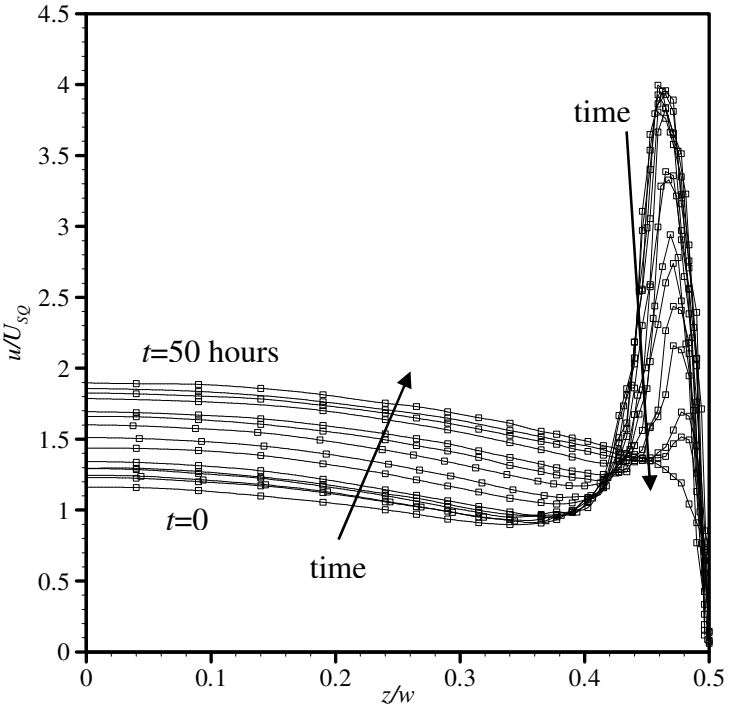

Figure 3.2: Variation in velocity profiles measured at identical positions over a period of approximately 50 hours pumping.

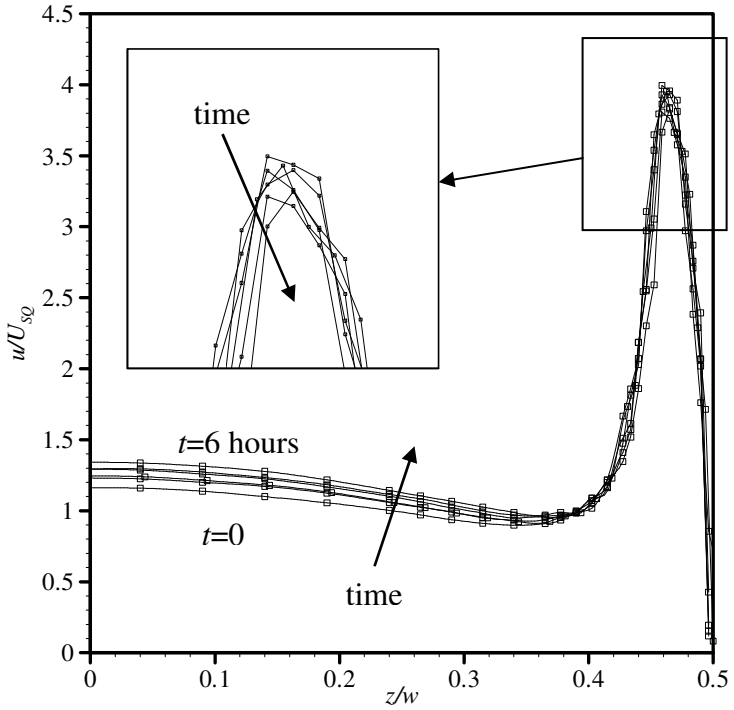

Figure 3.3: Variation in velocity profiles over a period of six hours pumping, inset highlights effect on overshoots.

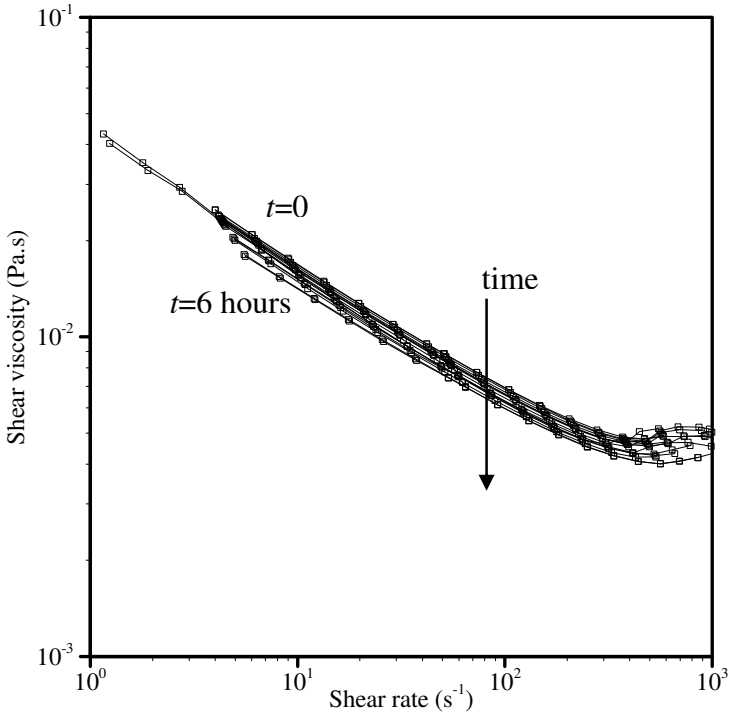

Figure 3.4: Variation in shear viscosity for each sample taken from the test rig over a period of approximately 50 hours pumping.

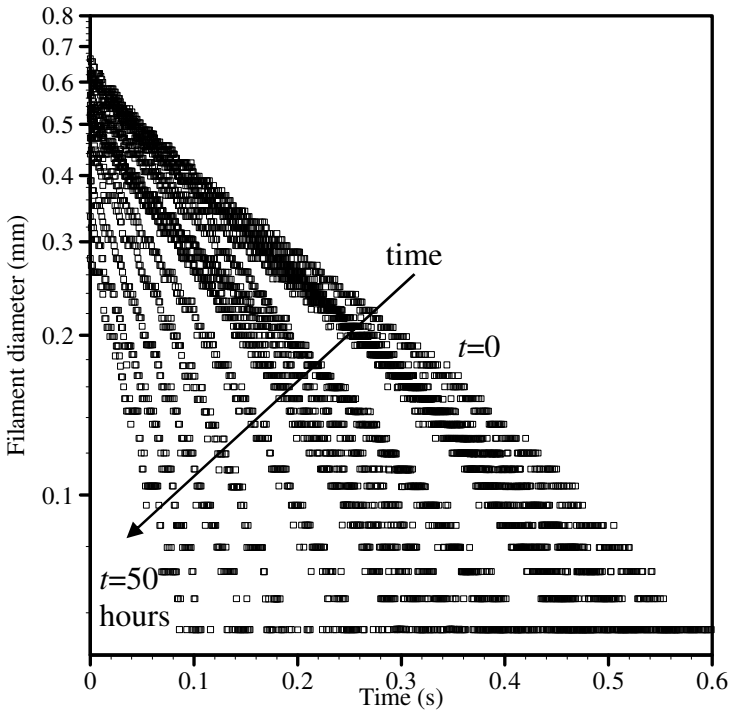

Figure 3.5: Variation in filament diameter decay for each fluid sample taken from the test rig over a period of approximately 50 hours pumping.

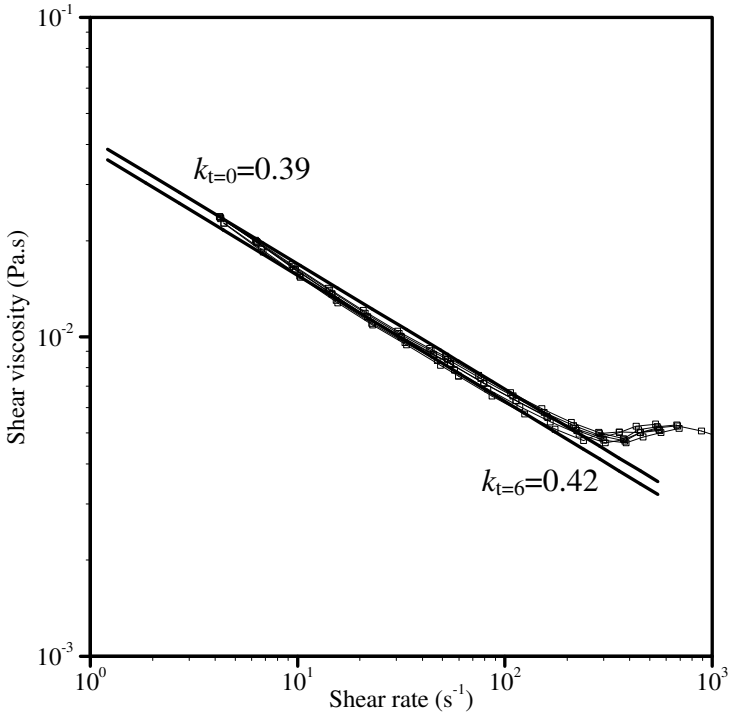

Figure 3.6: Variation in the shear viscosity over the first six hours of pumping (power law fit shown as thick black line).

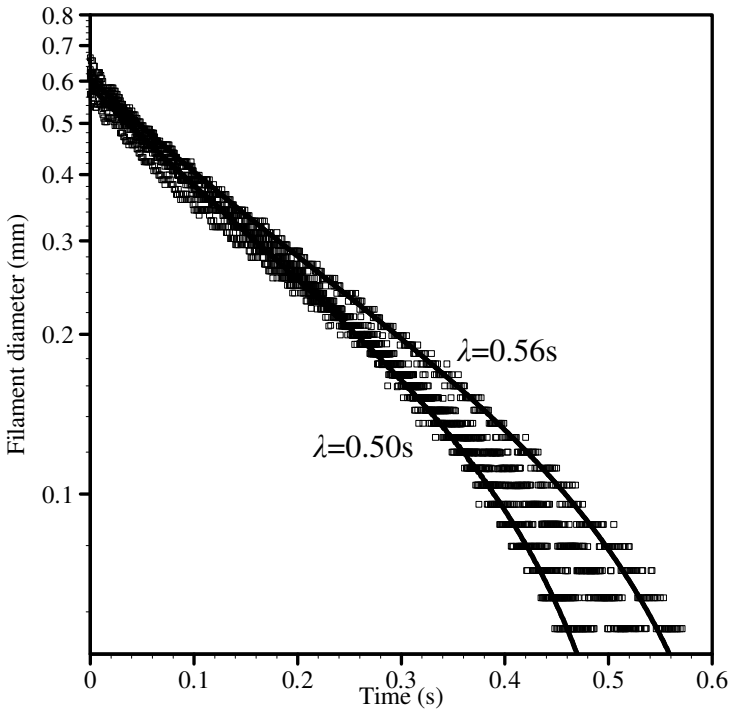

Fig 3.7: Variation in the filament diameter decay over the first six hours of pumping, the full black lines shows the data fitted to equation 2.14 for the limiting cases.

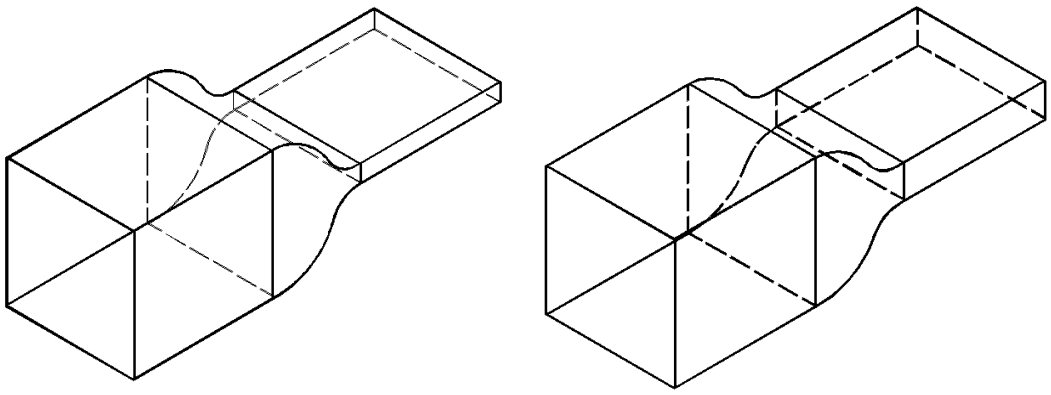

(a) (b)

Figure 3.8: Isometric diagrams of (a) the 8:1 contraction test section and (b) the 4:1 contraction test section.

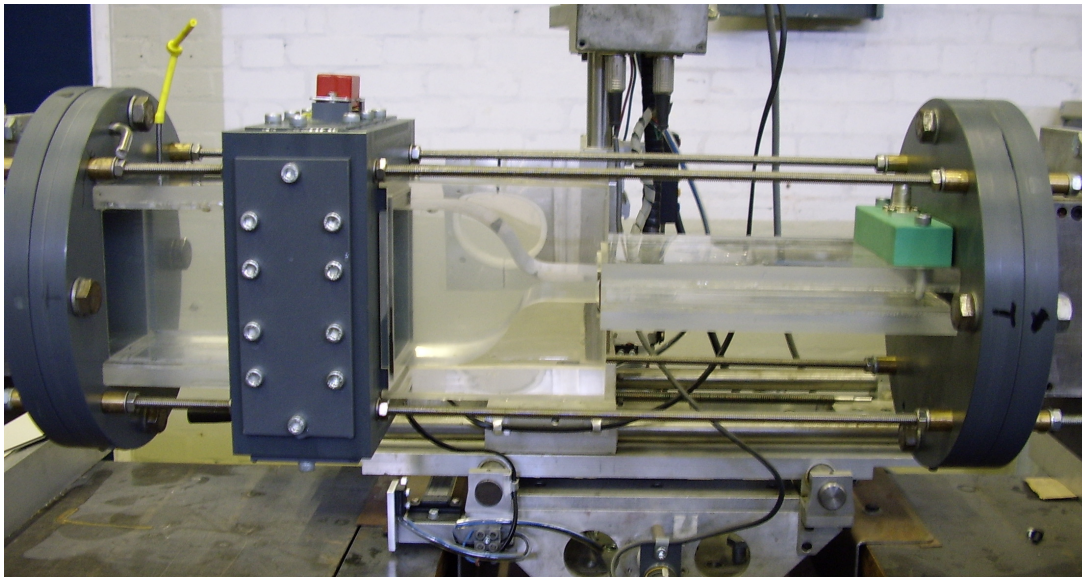

Figure 3.9: Photograph of the contraction section (8:1 contraction shown).

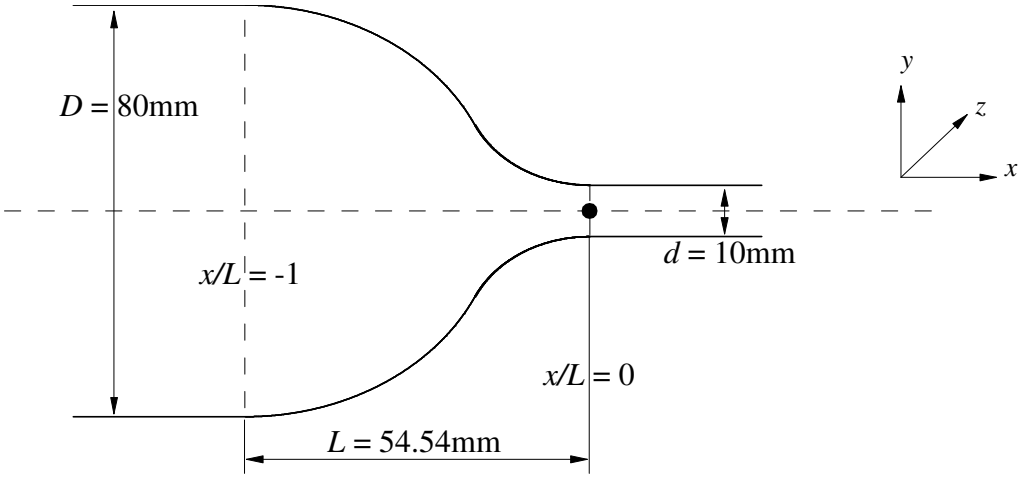

Figure 3.10: Dimensions of the 8:1 contraction.

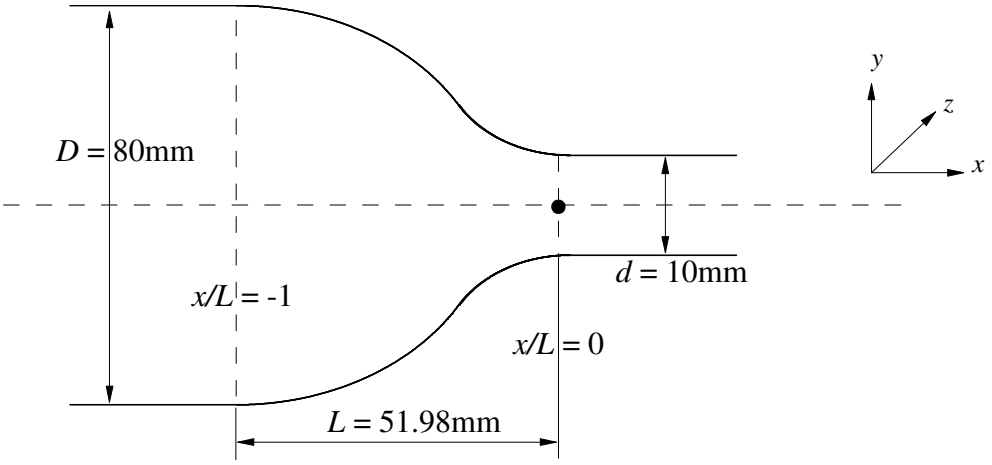

Figure 3.11: Dimensions of the 4:1 contraction.

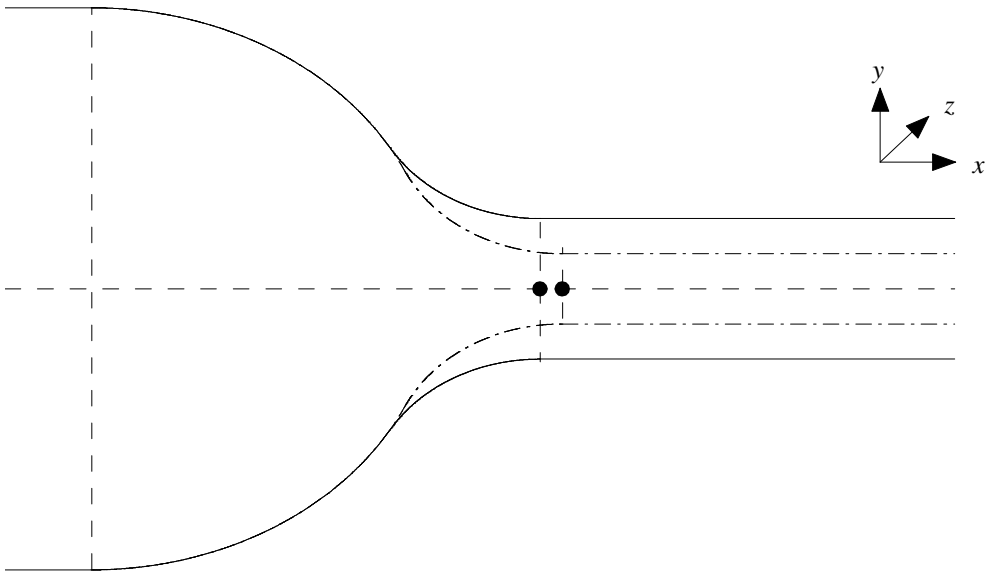

Figure 3.12: Both contractions for comparison, the 8:1 contraction shown as dash/dot line and 4:1 as full line.

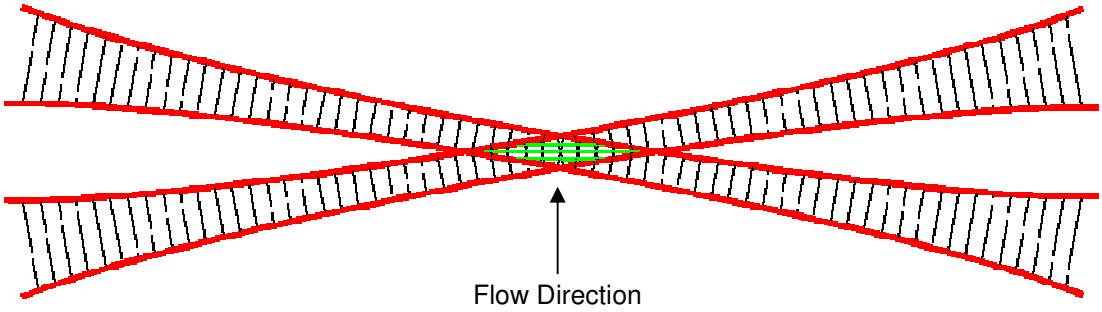

Figure 3.13. Interference fringes, shown in green, formed within the intersection volume.

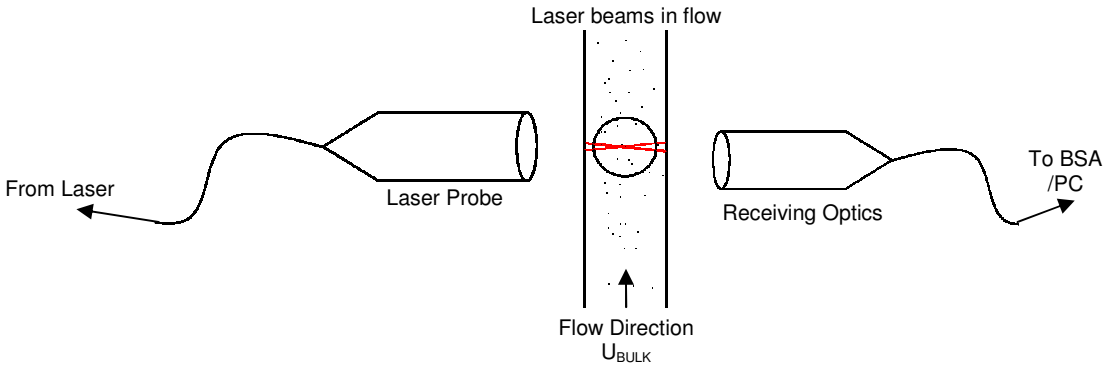

Figure 3.14: Schematic diagram detailing the set up of an LDA system set up in forward scatter.

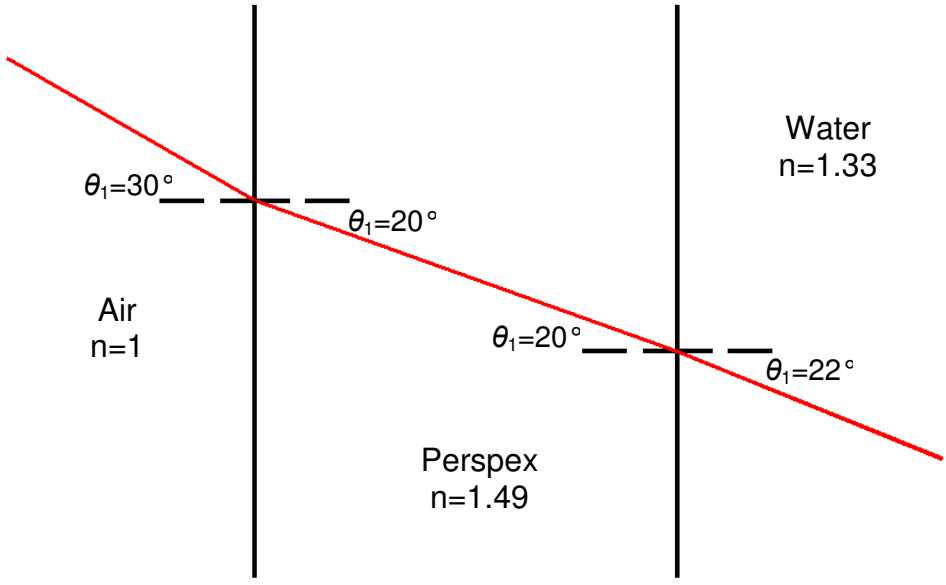

Figure 3.15. Figure showing the refraction angles between air and Perspex and Perspex and water.

4. Presentation of Results

This chapter presents the results of LDA measurements taken in the 8:1 contraction followed by those taken in the 4:1 contraction. Measurements were taken at various positions along the XZ-centreplane and any of the fluids that exhibited 'interesting' results across this plane prompted further investigation into the flow along the XY-centreplane. A schematic diagram indicating the positions of each flow profile accompanies each set of results. All of the flow profiles are non-dimensionalised with respect to the bulk velocity at the end of the contraction, U_d. In each case half profiles were measured on the XZ-centreplane due to the time constraints on the fluids from the degradation effects. Full profiles were measured on the XY-centreplane since these could be measured more quickly due to the reduction in height through the contraction. The velocity profiles presented in this chapter have been offset with respect to the axial distance between each profile unless stated otherwise.

4.1. 8:1 contraction

The fluids selected for measurement in the 8:1 contraction were a Newtonian fluid, four concentrations of polyacrylamide and two concentrations of xanthan gum. These results are presented below. Table 4.1 gives the non-dimensional numbers estimated for each fluid and flow condition in the 8:1 contraction.

4.1.1. Newtonian fluid

As discussed in detail in Chapter 1, it is expected that the velocity profile for Newtonian fluid flow at 'high' ($\geq$10) Reynolds numbers flattens into a 'top hat' shape as the flow progresses through a gradual planar contraction. The Newtonian fluid here investigated was a mixture of glycerine and water (approximately 10% glycerine to 90% water) and it was tested at a Reynolds number of approximately 115, which has been defined at the contraction exit.

Velocity measurements were obtained upstream of the contraction in the square duct in order to ensure that the flow is well developed prior to the contraction. Figure 4.1 shows the spanwise and transverse centreline velocity profiles measured within the square duct section approximately 120mm prior to the start of the contraction (i.e. $x/L \approx -3$). In this case the profiles are non-dimensionalised with respect to the bulk velocity in the square duct U_{SQ}. Also included is the theoretical velocity profile for fully-developed Newtonian fluid flow through a square duct (White (2006)). The measured values have been reflected about $y/w=0$ and $z/w=0$ respectively and these reflected values are shown as filled symbols in Figure 4.1. A good degree of symmetry is observed, which provides confidence in the quality of the flow loop. The measured velocities also agree with the theoretical velocity profile for fully-developed Newtonian fluid flow through a square duct showing that the flow is indeed fully developed before it reaches the contraction.

Figure 4.2 shows six velocity profiles measured at x/L=-1, -0.72, -0.45, -0.27, -0.17 and 0.10 on the XZ-centreplane as indicated; the profiles have been offset with respect to the axial distance between each profile. The velocity profiles are clearly seen to flatten as expected as the flow progresses through the contraction. Velocity overshoots are not anticipated for Newtonian fluid flow through a gradual contraction. The final velocity profile at x/L=0.10, which is measured just after the end of the contraction does indeed look like a 'top hat'.

Figure 4.3 shows the velocity measured along the 'centreline' of the contraction (i.e. z/w and y/w are both zero) for the Newtonian fluid. The flow velocity is seen to increase smoothly as the flow progresses through the contraction as expected of a Newtonian fluid flow.

4.1.2. Polyacrylamide

The flow of four concentrations of a polyacrylamide was investigated. The polymer solutions were characterised in Chapter 2 and each concentration was tested at two flowrates through the 8:1 contraction. 0.05% PAA is discussed first, for reasons that will become apparent to the reader as the discussion progresses.

4.1.2.1. 0.05% PAA

As previously discussed 0.05% PAA was chosen to compare to the results of Poole *et al.* (2005). Some of the results from that investigation are given in Figure 4.4, which clearly shows velocity overshoots close to the sidewalls of the contraction. These profiles were measured along the XZ-centreplane at a Reynolds number of approximately 110 (and a Deborah number (from CaBER) of 0.96) at x/L=0, -0.28, -0.46 and -0.92. It should be borne in mind that a sudden expansion directly followed the contraction in this case and that the results were obtained in a completely different test facility to the one used in this work. Figure 4.5 shows velocity profiles measured along the same plane at the same Reynolds and Deborah numbers at x/L=0.10, -0.17, -0.27, -0.45. -0.72 and -1 in the current 8:1 contraction (i.e. not followed by a sudden expansion). Qualitative agreement is observed between the two flows and clear similarities are observed when comparing Figures 4.4 and 4.5. Comparing the profile x/L=-0.46 (Figure 4.4) to x/L=-0.45 (Figure 4.5) shows that the width of the overshoot in both cases is very similar (x/L~0.06). The profiles at x/L=-0.28 (Figure 4.4) and x/L=-0.27 (Figure 4.5) both show large overshoots with a maximum overshoot velocity of $u/U_d \approx 1$. Any slight differences between the two sets of results may be explained by the fact that the profiles were measured at slightly different locations within the contraction and that the two sets of results were obtained using two different test facilities. Degradation effects may also play a role in the differences between the two sets of data (see detailed discussion in Chapter 3). These results show that the sudden expansion appears to play no significant role in the 'cat's ears' phenomenon.

Figure 4.6 shows the flow profiles seen in Figure 4.5 on the XZ-centreplane along with the profiles measured on the XY-centreplane. The open symbols are the measured velocities and the filled symbols are values reflected about the XY-centreplane to highlight the symmetry of the flow. The profiles on the XZ-centreplane clearly show velocity overshoots close to the sidewalls of the contraction. The overshoots appear to grow in size as the flow progresses through the contraction. The profiles on the XY-centreplane show little of interest except the profile at x/L=0.10, which shows very small overshoots (approximately 1.5% above the centreline velocity) much as was observed in Poole *et al.* (2005).

Once the flow profiles at $Re \approx 110$, $De_C \approx 0.96$ had confirmed that the overshoots could be reproduced in a contraction alone (i.e. not followed by a sudden expansion) it was decided to investigate the flow of 0.05% PAA at a lower flowrate ($Re \approx 50$, $De_C \approx 0.52$). The corresponding flow profiles are presented in Figure 4.7. The XZ profiles show that the velocity overshoots do occur in 0.05% PAA at the lower flowrate. They appear to be narrower, confined more closely to the sidewalls (for example at x/L=-0.27 the overshoots are within 0.1 z/w at the higher flowrate and within 0.06 z/w at the lower flowrate) and less pronounced than at the higher flowrate. The XY profiles show nothing of note and the overshoots apparent at x/L=0 at Re=110, $De_C \approx 0.96$ are not present in this case.

Figure 4.8 shows the velocity measured along the centreline for both flows of 0.05% PAA. At the lower flowrate, $Re \approx 50$, $De_C \approx 0.52$, we see a slight increase in the velocity then a small 'dip' before the flow smoothly increases to a maximum velocity of u/U_d = 1.14 at the end of the contraction. At the higher flowrate, $Re \approx 110$, $De_C \approx 0.96$, we see a slight increase in the velocity around x/L=-0.7 and an apparent plateau between x/L=-0.5 and x/L=-0.3 followed by an increase to a maximum velocity of u/U_d = 1.07, which is lower than that seen at the lower flowrate.

4.1.2.2. 0.01% PAA

Having determined that the velocity overshoots could be reproduced in 0.05% PAA at two flowrates a much lower concentration of PAA was selected next to see if the same effect would be observed in a more dilute solution. 0.01% PAA was chosen because it is well within the 'dilute' range of concentrations for polyacrylamide as described in Chapter 2. As this solution is much less viscous than 0.05% PAA the Reynolds numbers for this solution are much higher at the same flowrate. As such it is difficult to 'separate out' effects that may be due to changes in the Reynolds number. In addition, as was shown in Chapter 2, CaBER data could not be obtained for this solution, which would indicate λ<1ms (Rodd *et al*. (2005)) and therefore observing elastic effects with this experimental setup for this concentration would require much higher flowrates.

Figure 4.9 shows velocity profiles for 0.01% PAA across the XZ-centreplane at Reynolds numbers of approximately 420 (Figure 4.9 (a)) and 830 (Figure 4.9 (b)). It is quite clear that velocity overshoots are not seen at either flowrate. If we compare this figure to Figure 4.2, the 0.01% PAA solution appears to behave as a Newtonian fluid. The velocity profile clearly flattens as it progresses through the contraction section appearing similar in shape to a 'top hat' at x/L=0.10 for both cases, however the flow flattens to a greater extent at the higher flowrate as seen in Figure 4.9 (b).

4.1.2.3. 0.03% PAA

After testing polyacrylamide at concentrations in the dilute range and in the semi-dilute range, the next concentration chosen for examination was at the critical overlap concentration, $c^* \approx 0.03\%$. This concentration was tested at two Reynolds numbers, $Re \approx 140$, $De_C \approx 0.24$ was chosen to approximately match $Re \approx 110$ for 0.05% PAA and $Re \approx 390$, $De_C \approx 0.53$ was chosen because at this Reynolds number the Deborah number estimated from λ_C approximately matches $De_C \approx 0.52$ for 0.05% PAA at $Re \approx 50$. These Reynolds numbers were chosen to compare the fluids in terms of non-dimensional groups and again attempt to 'separate out' effects. However observing the differences due solely to concentration is only possible when both the Reynolds and Deborah numbers match, not just one of the two.

Figure 4.10 shows the flow profiles for 0.03% PAA at $Re \approx 140$, $De_C \approx 0.24$ along the XZ- and XY-centreplanes. The profiles show overshoots very close to the sidewalls in the XZ-centreplane. The overshoots are smaller in magnitude and narrower in width (within 0.05 z/w) than those seen for 0.05% PAA and they also develop further into the contraction at x/L=-0.45 whereas for 0.05% PAA they are seen to develop at x/L=-0.72. The profiles in the XY-centreplane again exhibit little of note. Figure 4.11 shows the flow profiles at $Re \approx 390$, $De_C \approx 0.53$. Again the overshoots are clearly visible along the XZ-centreplane but they are much smaller and narrower (maximum width 0.06 z/w) than those seen for 0.05% PAA. The overshoots are very similar to the results at the lower flowrate (Figure 4.10) apart from the two profiles measured at x/L=0.10, which clearly differ from one another. At the lower Reynolds number the overshoots are 'smooth' whereas at the higher Reynolds number they are more 'pointed'. These results indicate that more dilute concentrations of polyacrylamide

can exhibit the 'cat's ears' effect **provided** the correct *Re-De* parameter space can be achieved.

Figure 4.12 presents the centreline velocity for 0.03% PAA at both flowrates. In both cases the centreline velocity increases smoothly as the flow passes through the gradual contraction but there are some subtle differences between the two flows. The flow at $Re \approx 140$, $De_C \approx 0.24$ appears to take slightly longer before the velocity increase begins and at the end of the contraction its final velocity (u/U_d = 1.18) is larger than at the higher flowrate (u/U_d = 1.01), similar to the final velocities seen in the 0.05% solution.

4.1.2.4. 0.3% PAA

0.3% PAA was chosen because it is approximately ten times the critical overlap concentration for PAA. Increasing the concentration increases the viscosity, which in turn will decrease the Reynolds number at the same flowrate thereby reducing the effects of inertia within the flow. This concentration should therefore reveal whether significant inertial effects are required for overshoots to occur.

0.3% PAA was initially tested at a Reynolds number of approximately 5 and a Deborah number (from CaBER) of 34 and the resulting velocity profiles are shown in Figure 4.13. Overshoots are visible in the XZ-centreplane, although they are very different to those previously seen at the lower concentrations. At the start of the contraction (x/L=-1) the flow is almost stagnant close to the sidewalls and the overshoot peaks are located further away from the sidewall, seemingly growing into a single large overshoot in the centre at the end of the contraction (the velocity at the centre is approximately equal to $2U_d$). A profile measured prior to the contraction at x/L=-1.18 also shows overshoots, indicating that the combined effects of the contraction and the fluid properties occur upstream of the contraction. It is possible that this effect is caused by diffusion, which is more likely to be observed when inertia effects are low. For the first time, significant overshoots are also present in the XY-centreplane. Figure 4.13 shows that the flow is almost stagnant through a large part of the contraction near to the top and bottom curved walls but the flow velocities nearer to the centre of the contraction are much higher than might be

expected (assuming 1d flow for example) to compensate for this. The lack of data in the areas close to the curved top and bottom walls caused by a loss of the LDA signal, presumably due to the very low velocity, does not allow us to see if the flow may be recirculating, as would be expected in flow through a sudden contraction (see background discussion in Chapter 1).

In an attempt to aid the reader's visualisation of the flow, particularly as the contraction height becomes smaller, the data has been replotted in Figure 4.14. In this case the velocity profiles are identical to those shown in Figure 4.13 but they have all been offset by an equal distance rather than by the distance between the actual measurement positions.

Figure 4.15 shows profiles at the same locations as Figure 4.13 but the Reynolds number has been increased to about 15 ($De_C \approx 60$). Again overshoots are visible in both planes and are very similar in appearance to those observed at $Re \approx 5$, $De_C \approx 34$. The overshoots at $Re \approx 15$, $De_C \approx 60$ are more pronounced than those seen at the lower flowrate with a larger difference between the centreline velocity and the overshoot peak. However at $Re \approx 5$, $De_C \approx 34$ the maximum velocity for each profile is higher than at $Re \approx 15$, $De_C \approx 60$. Figure 4.16 has been plotted in the same manner as Figure 4.14, again to aid the reader's visualisation of the 0.3% PAA flow through the contraction at $Re \approx 15$, $De_C \approx 60$. It becomes particularly difficult to distinguish between the profiles towards the end of the contraction and into the rectangular duct.

Figure 4.17 shows the centreline velocities for both flowrates of 0.3% PAA. Throughout the contraction the flow at the lower flowrate has a higher velocity along the centreline in agreement with the earlier discussion. In both cases the flow along the centreline is almost constant over a long section of the contraction before a rapid increase to a maximum velocity at the end of the contraction, which is more or less identical for both flows.

4.1.3. Xanthan gum

Xanthan gum was tested at two concentrations: their rheological characterisation is discussed in Chapter 2. Each concentration was tested at two different flowrates.

4.1.3.1. 0.07% XG

0.07% XG was chosen to match the shear viscosity of 0.05% PAA at the relevant characteristic shear rates in order to be able to match the Reynolds numbers and the degree of shear thinning that 0.05% PAA was tested at. To that end 0.07% XG was tested at $Re \approx 50$ and $Re \approx 120$ and the results are presented in Figure 4.18. In both cases the flow flattens as the fluid travels through the contraction in a similar manner to that seen in the Newtonian fluid (Figure 4.2) and in the 0.01% PAA fluid flow (Figure 4.9). The xanthan gum appears to show a slightly more curved profile than the flat ' top hat' shape observed for glycerine. This may be due to the effects of the shear-thinning exhibited by 0.07% xanthan gum that is not seen at all in the glycerine nor to such a degree in the 0.01% PAA. It is well known that in pipe flow shear-thinning causes flattening of velocity profiles (Fortin *et al.* (2004)). The velocity overshoots observed in 0.05% PAA are not seen in the 0.07% XG.

Figure 4.19 shows the centreline velocities for both flows of 0.07% XG. The flow along the centreline appears to be almost identical up until x/L=-0.2 where it diverges and the higher flowrate tends towards a lower final velocity than the lower flowrate. The lower flowrate also exhibits a very small overshoot (approximately 2% of the final velocity) at the end of the contraction.

4.1.3.2. 0.5% XG

0.5% xanthan gum was tested at $Re \approx 0.86$, $De_C \approx 0.21$ and $Re \approx 2$, $De_C \approx 0.34$. Figure 4.20 shows the flow profiles across the XZ-centreplane for both flowrates. In each case the flow appears to flatten as it progresses through the contraction however in both flows small 'bumps' are visible (around z/w=0.2 at the lower Re and z/w=0.3 at the higher Re). As these 'bumps' are at most 3% of the centreline velocity this is close to the level of experimental uncertainty in the velocity measurements (see Chapter 3). But it is possible that the 'bumps' could be 'embryonic' velocity overshoots and if it were possible to measure higher concentrations of XG, overshoots might be observed similar to those we have seen in polyacrylamide.

Figure 4.21 shows the centreline velocities for 0.5% XG at $Re \approx 0.86$, $De_C \approx 0.21$ and $Re \approx 2$, $De_C \approx 0.34$. At these low Reynolds numbers there is little difference between the flows and the data essentially collapse.

4.2. 4:1 contraction

Three concentrations of PAA were investigated through the 4:1 contraction. The non-dimensional numbers corresponding to each flow are given in Table 4.2.

4.2.1. 0.03% PAA

0.03% polyacrylamide was tested at two flow conditions, $Re \approx 115$, $De_C \approx 0.06$ and $Re \approx 290$, $De_C \approx 0.13$. The flow profiles for $Re \approx 115$, $De_C \approx 0.06$ are presented in Figure 4.22. It is clear that along the XZ-centreplane velocity overshoots are not present and the profiles start to flatten into the 'top hat' shape typical of Newtonian fluid flow. The profiles at x/L=-1 and x/L=-0.71 along the XY-centreplane are of interest due to their shape. The fluid in the top section ($0.5>y/w>0.35$) and bottom section ($-0.35<y/w<-0.5$) of the contraction (i.e. close to the curved walls) is flowing much more slowly than the fluid towards the centre, i.e. the fluid is jetting through the central section. This shape is known as an inflection and is usually observed when there is an adverse pressure gradient present (i.e. a positive pressure) (White (2006)). The profile at x/L=0.15 appears to show the beginnings of overshoots that are approximately 0.4% greater than the centreline velocity. This value is within the experimental uncertainty but it is repeatable so it is believed to be a true effect.

Figure 4.23 shows the velocity profiles for 0.03% PAA at $Re \approx 290$, $De_C \approx 0.13$. Small overshoots are visible close to the flat sidewall along the XZ-centreplane. The overshoots appear much later (x/L=-0.23) and start to disappear much sooner than those seen in the 8:1 contraction and are not as pronounced with the peak overshoot velocity still lower than the centreline velocity. The profile at x/L=-1 along the XY-centreplane shows an inflection, similar to that seen at the same position at $Re \approx 115$, $De_C \approx 0.06$, however the slower moving part of the flow is confined closer to the curved walls ($0.5>y/w>0.4$ and $-0.4<y/w<-0.5$). In the final profile at x/L=0.15 small overshoots are visible and they are slightly larger at approximately 1% above the

centreline velocity compared to 0.4% at the lower flowrate. This value is also within the experimental uncertainty but is again repeatable.

Figure 4.24 shows the centreline velocities for 0.03% PAA at $Re \approx 115$, $De_C \approx 0.06$ and $Re \approx 290$, $De_C \approx 0.13$. The figure shows that as the flow travels through the contraction the centreline velocity increases steadily in both cases in agreement with the profiles shown in Figure 4.22 and Figure 4.23. The centreline velocities are the same for both flows at the start of the contraction but as the flow progresses the flow at the lower flowrate exhibits a higher centreline velocity than at the higher flowrate. This pattern is similar to that observed in the flows of 0.03% and 0.05% PAA discussed earlier in the chapter.

4.2.2. 0.05% Polyacrylamide

0.05% PAA was tested at $Re \approx 30$, $De_C \approx 0.13$ and $Re \approx 65$, $De_C \approx 0.24$. The velocity profiles measured at $Re \approx 30$, $De_C \approx 0.13$ are presented in Figure 4.25. The profiles along the XZ-centreplane show velocity overshoots that develop midway through the contraction. These overshoots are larger than those observed in 0.03% PAA but the peak overshoot velocity is still lower than the centreline velocity, except for the final profile at x/L=0.15. As previously observed for 0.03% PAA at $Re \approx 290$, $De_C \approx 0.13$, along the XY-centreplane we see small overshoots at x/L=0.15 (approximately 1.4% greater than the centreline velocity) and slower moving flow towards the top and bottom curved walls of the contraction at x/L=-1.

Figure 4.26 shows the velocity profiles at $Re \approx 65$, $De_C \approx 0.24$. Velocity overshoots are clearly visible along the XZ-centreplane. The overshoots are more pronounced (the maximum overshoot velocities in this case are larger than the centreline velocities at x/L=-0.27, x/L=-0.17 and x/L=0.10) and develop closer to the start of the contraction than at the lower flowrate. Again in the XY-centreplane profiles we see the inflections at the start of the contraction where the fluid is moving much more slowly towards the top and bottom curved walls of the contraction. In this case the effect is still present at x/L=-0.71 whereas at the lower flowrate it had disappeared by this location. The overshoots after the end of the contraction at x/L=0.15 are observed again; in this case they are more pronounced than at the lower flowrate

(approximately 3.6% larger than the centreline velocity compared to 1.4% at the lower flowrate and 0.4% and 1% in the 0.03% PAA solution).

Figure 4.27 shows the centreline velocities for 0.05% PAA at $Re \approx 30$, $De_C \approx 0.13$ and $Re \approx 65$, $De_C \approx 0.24$. The non-dimensionalised centreline velocity at the higher flowrate is lower than that for the lower flowrate throughout the contraction in agreement with the data at the lower concentration.

4.2.3. 0.3% Polyacrylamide

0.3% PAA was tested at a single flow condition $Re \approx 2$, $De_C \approx 8.4$. The XY- and XZ-centreplane flow profiles are shown in Figure 4.28. The profiles along the XZ-centreline show clear velocity overshoots that are similar in appearance to those previously seen in the 0.3% PAA flow through the 8:1 contraction (see Figures 4.13 and 4.15). The overshoots are not as pronounced as previously and the region of essentially stagnant fluid, seen in the 0.3% PAA flow through the 8:1 contraction, is not present in the 4:1 contraction although the near wall shear rates are quite low. Velocity overshoots are also visible along the XY-centreplane but again are not as pronounced as previously seen in the 8:1 contraction. The profiles at x/L=-0.71 and x/L=-0.42 show almost stagnant zones ($u \approx 0$) close to the curved top and bottom walls of the contraction.

The centreline velocity for 0.3% PAA at $Re \approx 2$, $De_C \approx 8.4$ is shown in Figure 4.29. The velocity increases slowly at the start of the contraction followed by a rapid increase in velocity towards the end resulting in a significant velocity overshoot. Downstream of the contraction the velocity slowly decreases through the rectangular section of duct. The maximum velocity in this case is approximately $2U_d$ whereas for both of the lower concentrations the maximum velocity is between U_d and $1.4U_d$.

4.3. 0.05% PAA in the 8:1 contraction

Since the velocity overshoots readily occurred in the 0.05% PAA solution (and this solution was substantially quicker (1 day compared with 5) and easier to mix than the 0.3% PAA solution) it was decided to measure some velocity profiles away from

the centrelines in this fluid to investigate off-centreline behaviour and provide some indication of the three dimensionality of the flow. Velocity measurements were performed in the 8:1 contraction at both *z/w* and *y/w* = 0, 0.125, 0.25 and 0.375 provided the contraction shape allowed. The flow condition chosen for investigation was $Re \approx 110$, $De_C \approx 0.96$.

Figures 4.30 and 4.31 are 3D visualisations of a quarter of the flow (the top right quadrant as you look downstream into the duct) shown for slightly different angles. These figures shows the development of the velocity overshoots in the spanwise direction as one might expect from the results presented earlier in this chapter. Figures 4.32 and 4.33 are presented in an attempt to aid the reader's visualisation of the flow. The figures show the side view and the top view of the velocity profiles respectively.

A high level of internal consistency has been achieved within the flow. This consistency is seen most significantly in Figures 4.31 and 4.32 where the cross sectional area of the contraction is at its largest. More spanwise off-centreline velocity profiles could be measured at these locations than further into the contraction.

Interestingly Figures 4.30 and 4.31 show the development of velocity overshoots in the transverse plane at *x/L*=-0.17 and *x/L*=0.10 (show circled in Figure 4.30). The overshoots observed at *x/L*=0.10 might have been expected since it was these overshoots that first prompted Poole *et al.* (2005) to investigate the flow through their gradual contraction and they have also been observed throughout this investigation at *y/w*=0. The overshoots seen in the transverse plane at *x/L*=-0.17 are more unexpected as we have not previously observed transverse velocity overshoots at this location during the centreplane measurements. The overshoots develop somewhere between *x/L*=-0.27 and -0.17, this distance in dimensional terms is only 5mm so these overshoots develop fairly rapidly within the latter half of the contraction (i.e. after the change in radius of the contraction at *x/L*≈0.3) before shrinking towards the end of the contraction.

4.4. Tables

Table 4.1: Reynolds, Deborah, Weissenberg and Elasticity numbers estimated for flows through the 8:1 Contraction.

Fluid	$Re = \frac{\rho U_d d}{\mu_{CH}}$	$De_C = \frac{\lambda_C U_d}{d}$	$El_{1,C} = De_C/Re$	$De_{N1} = \frac{\lambda_{N1} U_d}{d}$	$El_{1,N1} = De_{N1}/Re$
0.01% PAA	420	<<1	<<1	<<1	<<1
0.01% PAA	830	<<1	<<1	<<1	<<1
0.03% PAA	140	0.24	0.0016	5.2	0.036
0.03% PAA	390	0.53	0.0013	6.2	0.016
0.05% PAA	50	0.52	0.012	9.2	0.20
0.05% PAA	110	0.96	0.0091	9.4	0.088
0.3% PAA	5	34	5.6	5.3	0.87
0.3% PAA	15	60	3.9	6.2	0.41
0.07% XG	50	<<1	<<1	<<1	<<1
0.07% XG	120	<<1	<<1	<<1	<<1
0.5% XG	0.86	0.21	4.1	<<1	<<1
0.5% XG	2	0.34	6.1	<<1	<<1

Table 4.1 (continued)

Fluid	$Re = \frac{\rho U_d d}{\mu_{CH}}$	$Wi_C = \lambda_C \dot{\varepsilon}$	$El_{2,C} = Wi_C/Re$	$Wi_{N1} = \lambda_{N1} \dot{\varepsilon}$	$El_{2,N1} = Wi_{N1}/Re$
0.01% PAA	420	<<1	<<1	<<1	<<1
0.01% PAA	830	<<1	<<1	<<1	<<1
0.03% PAA	140	0.13	0.00091	2.9	0.020
0.03% PAA	390	0.21	0.00054	2.5	0.006
0.05% PAA	50	0.23	0.0051	4.1	0.089
0.05% PAA	110	0.58	0.0054	5.6	0.053
0.3% PAA	5	42	7.0	6.6	1.09
0.3% PAA	15	62	4.0	6.4	0.42
0.07% XG	50	<<1	<<1	<<1	<<1
0.07% XG	120	<<1	<<1	<<1	<<1
0.5% XG	0.86	0.24	0.28	<<1	<<1
0.5% XG	2	0.24	0.12	<<1	<<1

Table 4.2: Reynolds, Deborah, Weissenberg and Elasticity numbers estimated for flows through the 4:1 Contraction.

Fluid	$Re = \frac{\rho U_d d}{\mu_{CH}}$	$De_C = \frac{\lambda_C U_d}{d}$	$El_{1,C} = De_C/Re$	$De_{N1} = \frac{\lambda_{N1} U_d}{d}$	$El_{1,N1} = De_{N1}/Re$
0.03% PAA	115	0.06	5.3×10^{-4}	5.1	0.045
0.03% PAA	290	0.13	4.6×10^{-4}	5.3	0.018
0.05% PAA	30	0.13	4.7×10^{-3}	8.9	0.31
0.05% PAA	65	0.24	3.8×10^{-3}	9.0	0.14
0.3% PAA	2	8.4	3.7	3.5	1.5
Fluid	$Re = \frac{\rho U_d d}{\mu_{CH}}$	$Wi_C = \lambda_C \dot{\varepsilon}$	$El_{2,C} = Wi_C/Re$	$Wi_{N1} = \lambda_{N1} \dot{\varepsilon}$	$El_{2,N1} = Wi_{N1}/Re$
0.03% PAA	115	0.02	2.1×10^{-4}	2.0	0.018
0.03% PAA	290	0.07	2.4×10^{-4}	2.8	0.010
0.05% PAA	30	0.08	2.8×10^{-3}	5.3	0.18
0.05% PAA	65	0.14	2.2×10^{-3}	5.3	0.082
0.3% PAA	2	18.9	8.3	7.9	3.5

4.5. Figures

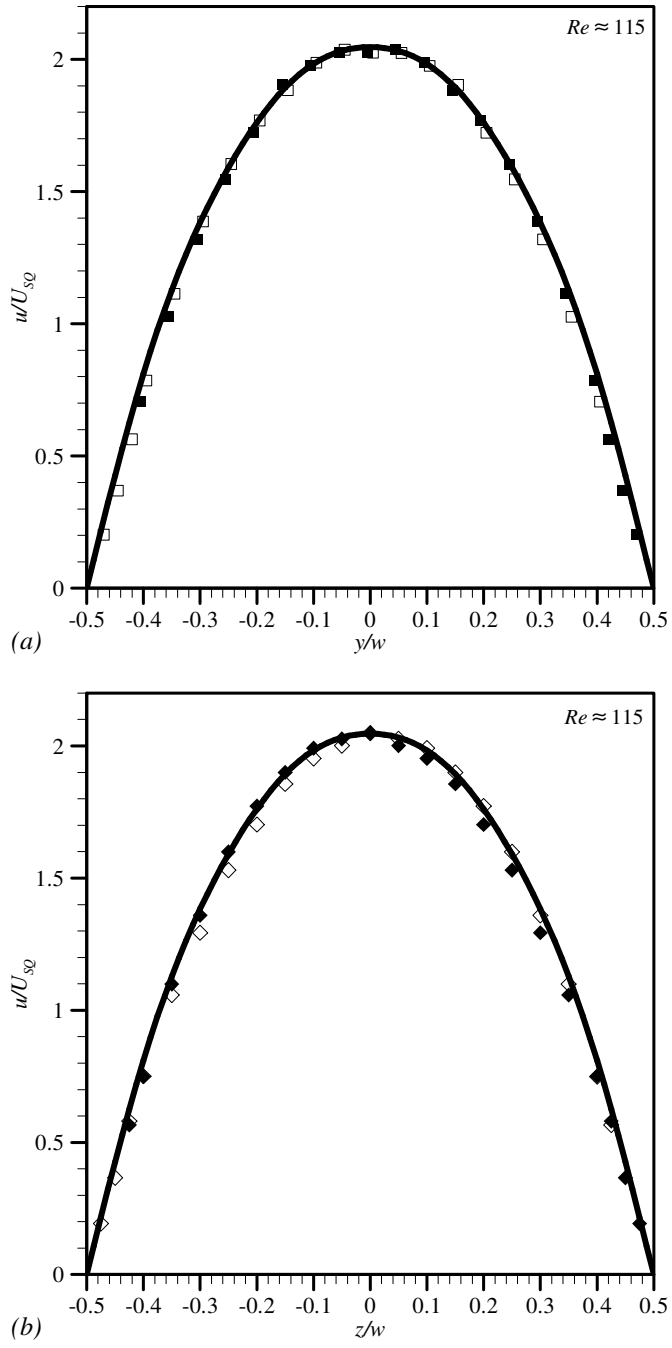

Figure 4.1: Normalised velocity profiles for 10% glycerine measured in the square duct section, prior to the contraction at *x/L*=-3, along (a) the XY-centreplane (□) and (b) the XZ-centreplane (◇) at *Re* ≈ 115. The filled symbols represent reflected values and the full black line represents the theoretical solution (Equation 3-48 in White (2006) p.113).

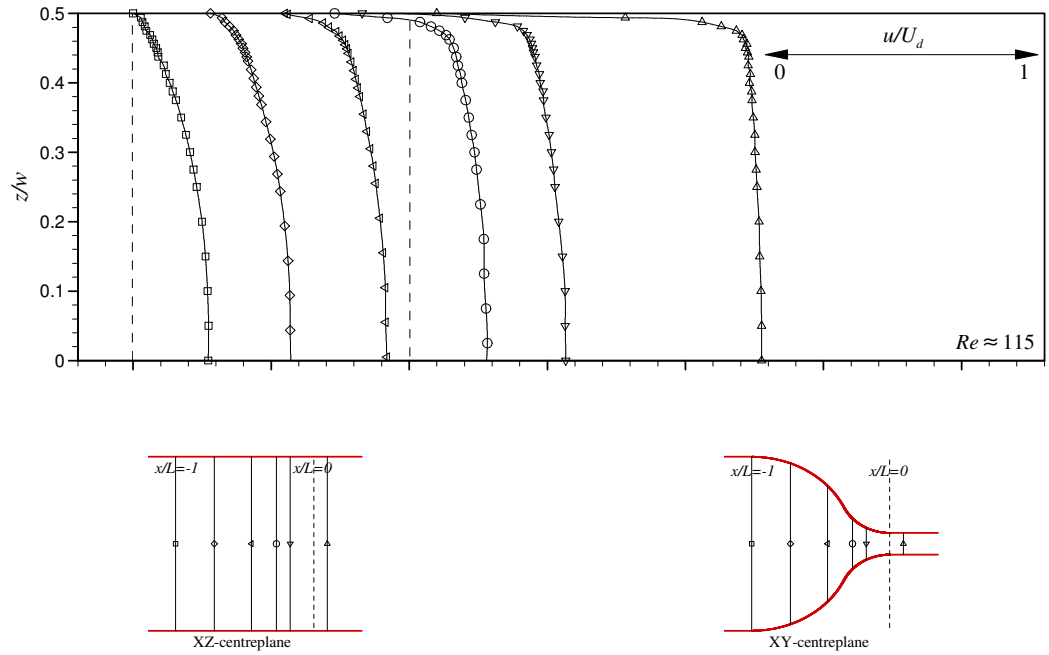

Figure 4.2: Normalised velocity profiles along the XZ-centreplane for 10% glycerine at $Re \approx 115$ measured at x/L=-1 (□), -0.72 (◊), -0.45 (◁), -0.27 (○), -0.17 (▽) and 0.10 (△).

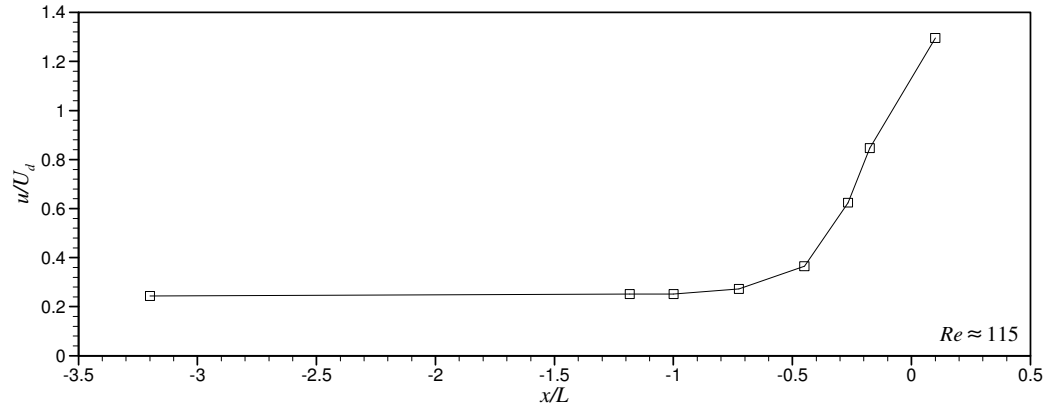

Figure 4.3: Normalised centreline velocity for 10% glycerine at $Re \approx 115$.

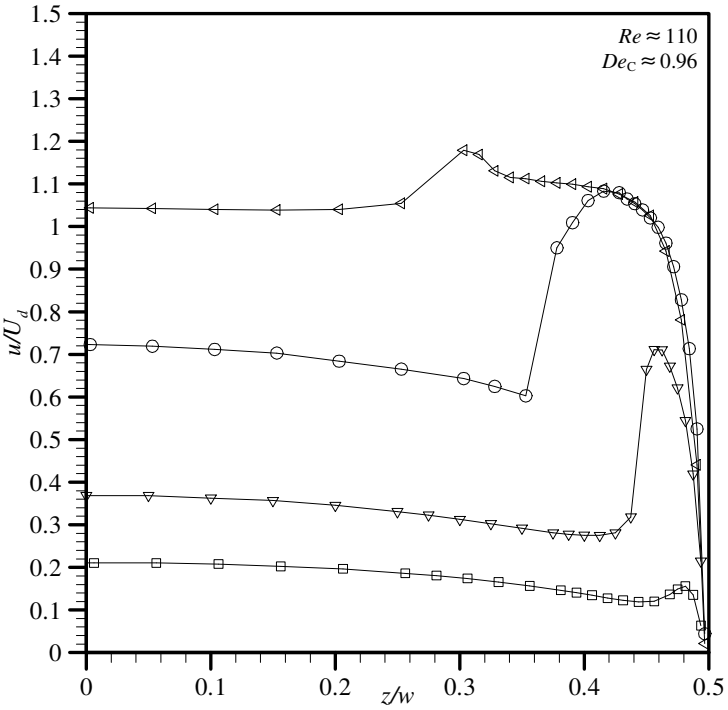

Figure 4.4: Normalised velocity profiles along the XZ-centreplane for 0.05% polyacrylamide at $Re \approx 110$, $De_C \approx 0.96$ measured at x/L=-0.92 (□), -0.46 (▽), -0.28 (○) and 0 (◁), taken from Poole *et al.* (2005).

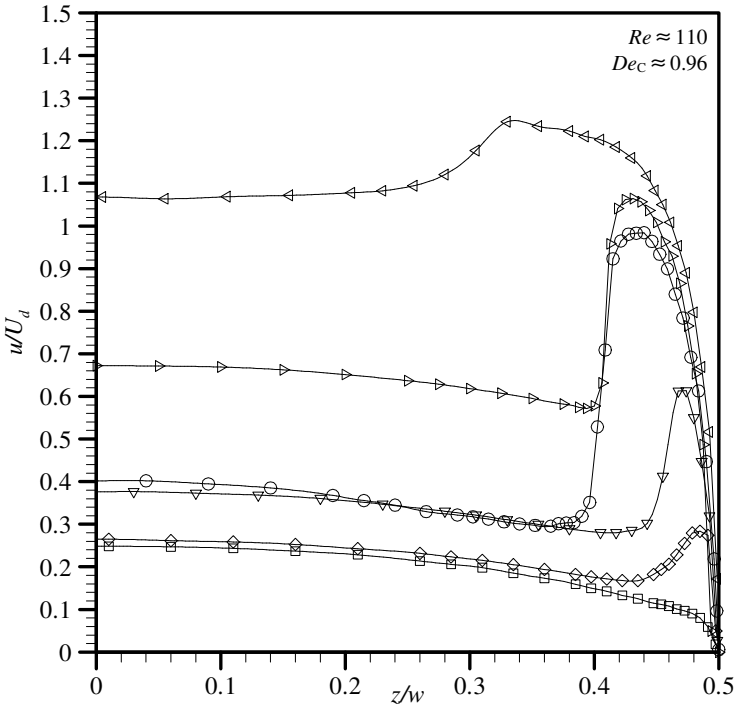

Figure 4.5: Normalised velocity profiles along the XZ-centreplane for 0.05% polyacrylamide at $Re \approx 110$, $De_C \approx 0.96$ measured at x/L=-1 (□), -0.72 (◊), -0.45 (▽), -0.27 (○), -0.17 (▷) and 0.10 (◁).

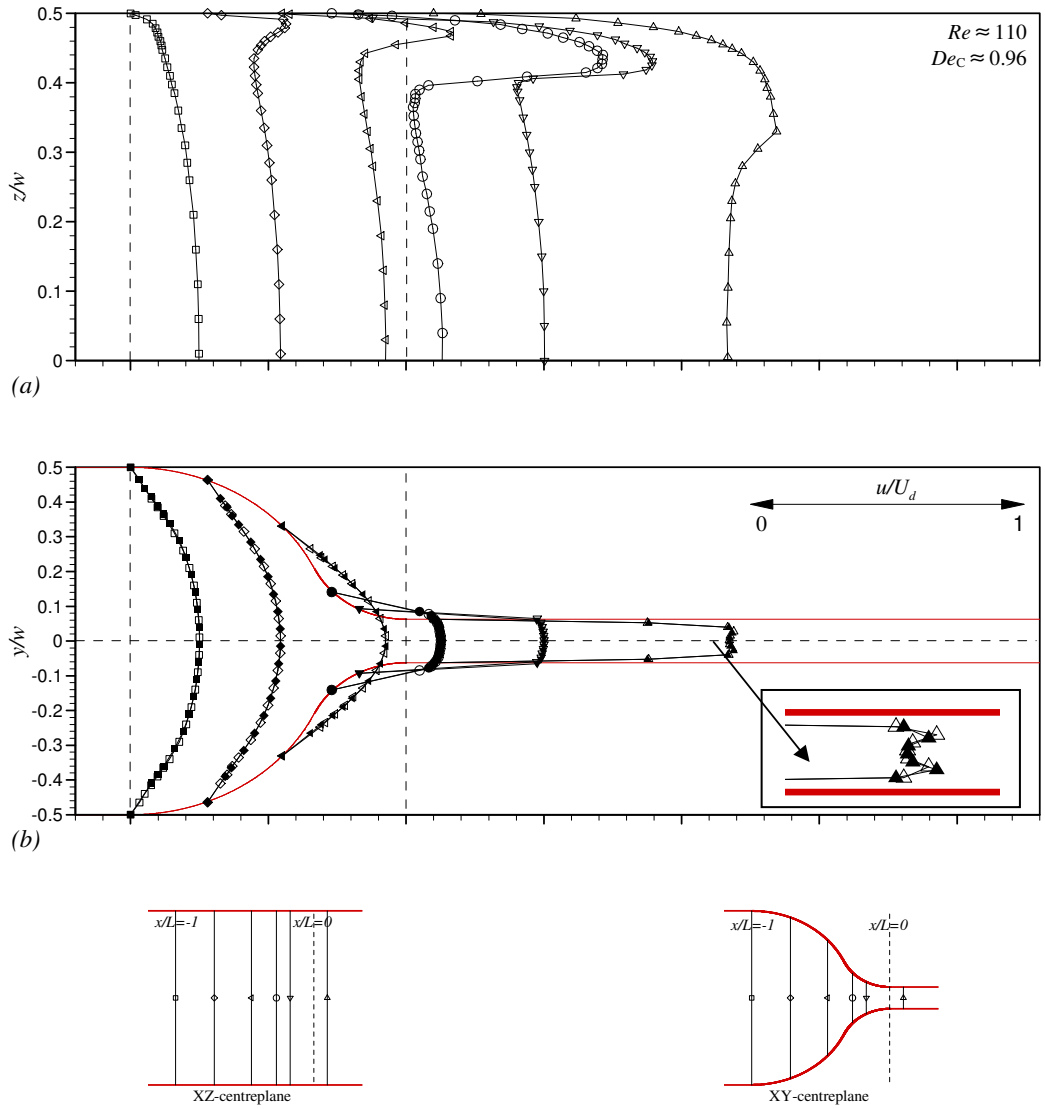

Figure 4.6: Normalised velocity profiles along (a) the XZ-centreplane and (b) the XY-centreplane for 0.05% polyacrylamide at $Re \approx 110$, $De_C \approx 0.96$ measured at x/L= -1 (□), -0.72 (◊), -0.45 (◁), -0.27 (○), -0.17 (▽) and 0.10 (△), filled symbols represent reflected values.

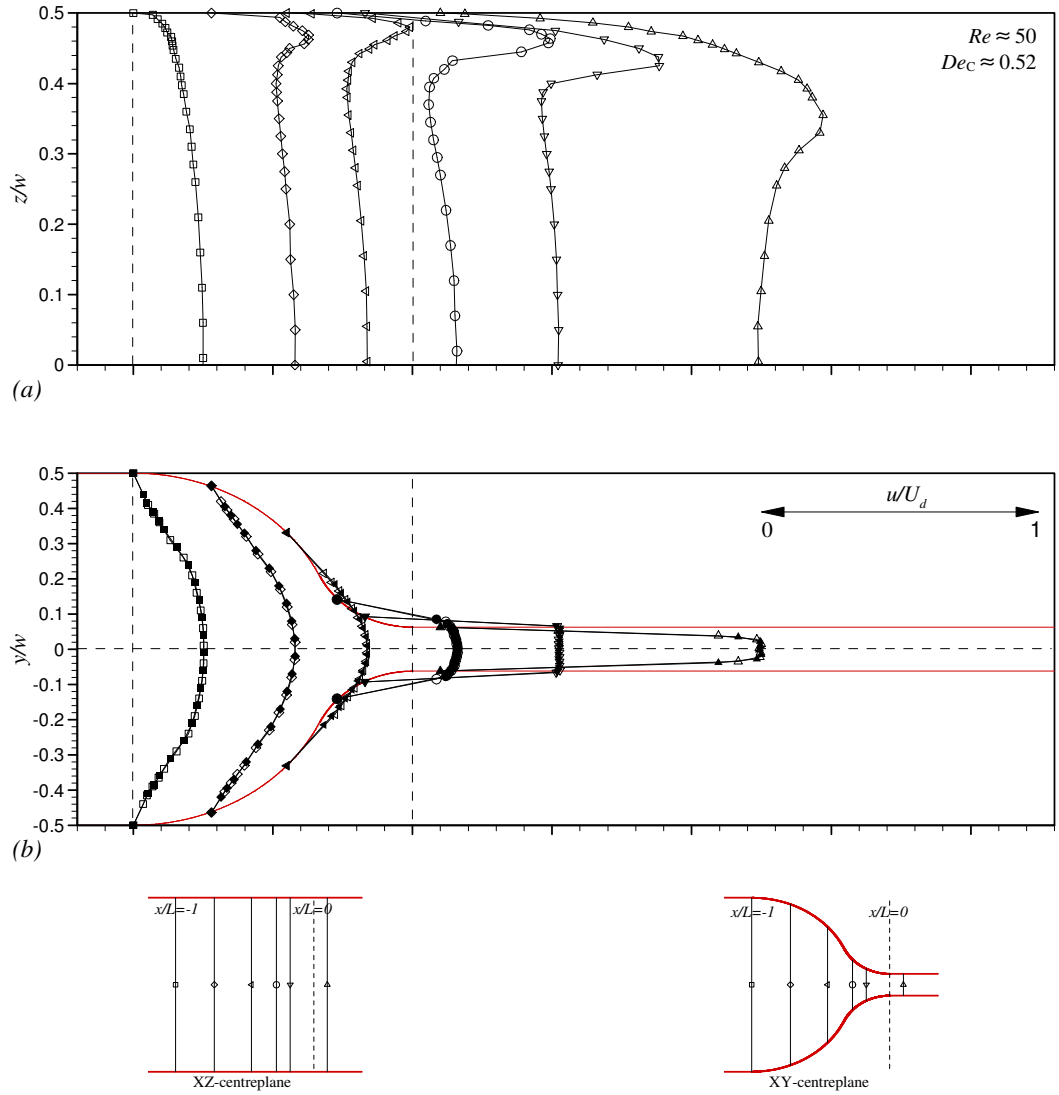

Figure 4.7: Normalised velocity profiles along (a) the XZ-centreplane and (b) the XY-centreplane for 0.05% polyacrylamide at $Re \approx 50$, $De_C \approx 0.52$ measured at x/L=-1 (□), -0.72 (◊), -0.45 (◁), -0.27 (○), -0.17 (▽) and 0.10 (△), filled symbols represent reflected values.

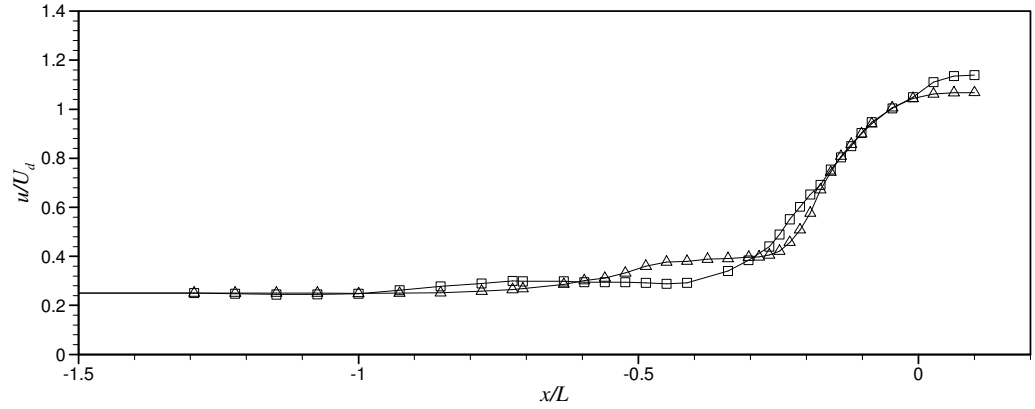

Figure 4.8: Normalised centreline velocities for 0.05% polyacrylamide at $Re \approx 50$, $De_C \approx 0.52$ (□) and $Re \approx 110$, $De_C \approx 0.96$ (△).

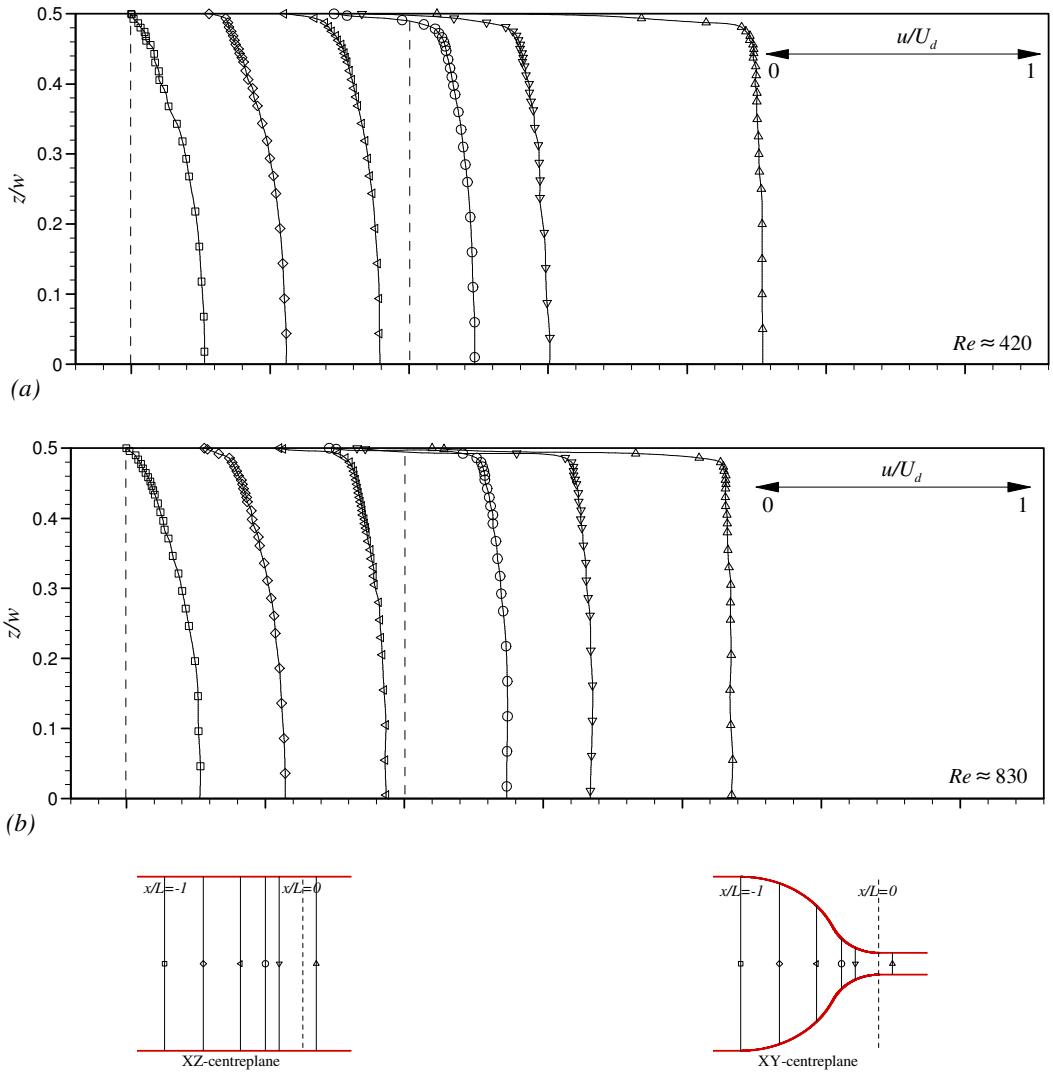

Figure 4.9 Normalised velocity profiles along the XZ-centreplane for 0.01% polyacrylamide at (a) $Re \approx 420$ and (b) $Re \approx 830$ measured at x/L=-1 (□), -0.72 (◊), -0.45 (◁), -0.27 (○), -0.17 (▽) and 0.10 (△).

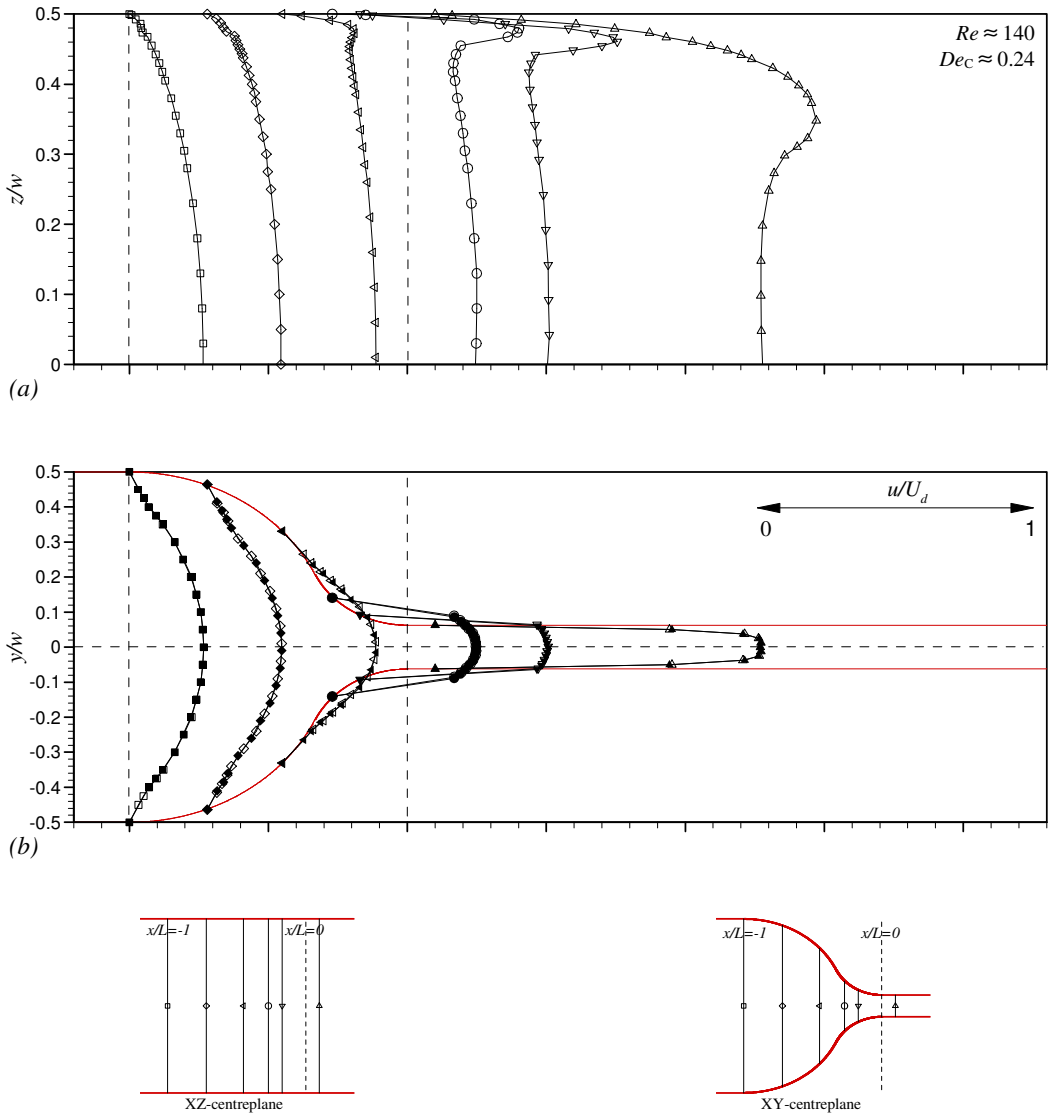

Figure 4.10: Normalised velocity profiles along (a) the XZ-centreplane and (b) the XY-centreplane for 0.03% polyacrylamide at $Re \approx 140$, $De_C \approx 0.24$ measured at x/L= -1 (□), -0.72 (◊), -0.45 (◁), -0.27 (○), -0.17 (▽) and 0.10 (△), filled symbols represent reflected values.

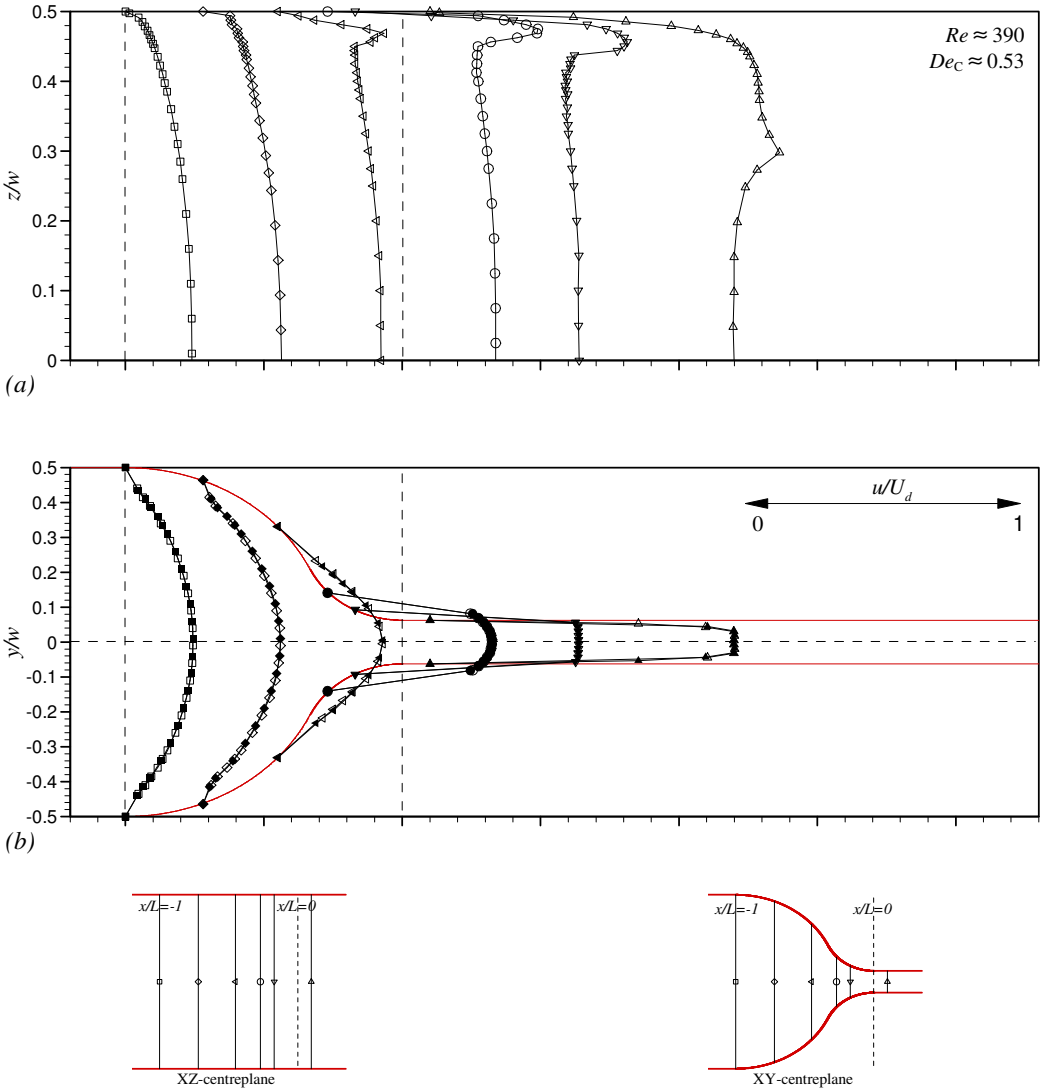

Figure 4.11: Normalised velocity profiles along (a) the XZ-centreplane and (b) the XY-centreplane for 0.03% polyacrylamide at $Re \approx 390$, $De_C \approx 0.53$ measured at x/L= -1 (□), -0.72 (◊), -0.45 (◁), -0.27 (○), -0.17 (▽) and 0.10 (△), filled symbols represent reflected values.

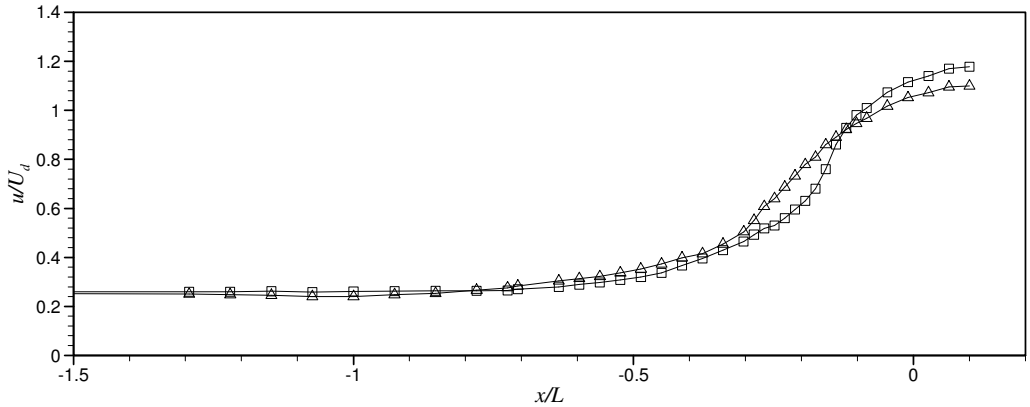

Figure 4.12: Normalised centreline velocities for 0.03% polyacrylamide at $Re \approx 140$, $De_C \approx 0.24$ (□) and $Re \approx 390$, $De_C \approx 0.53$ (△).

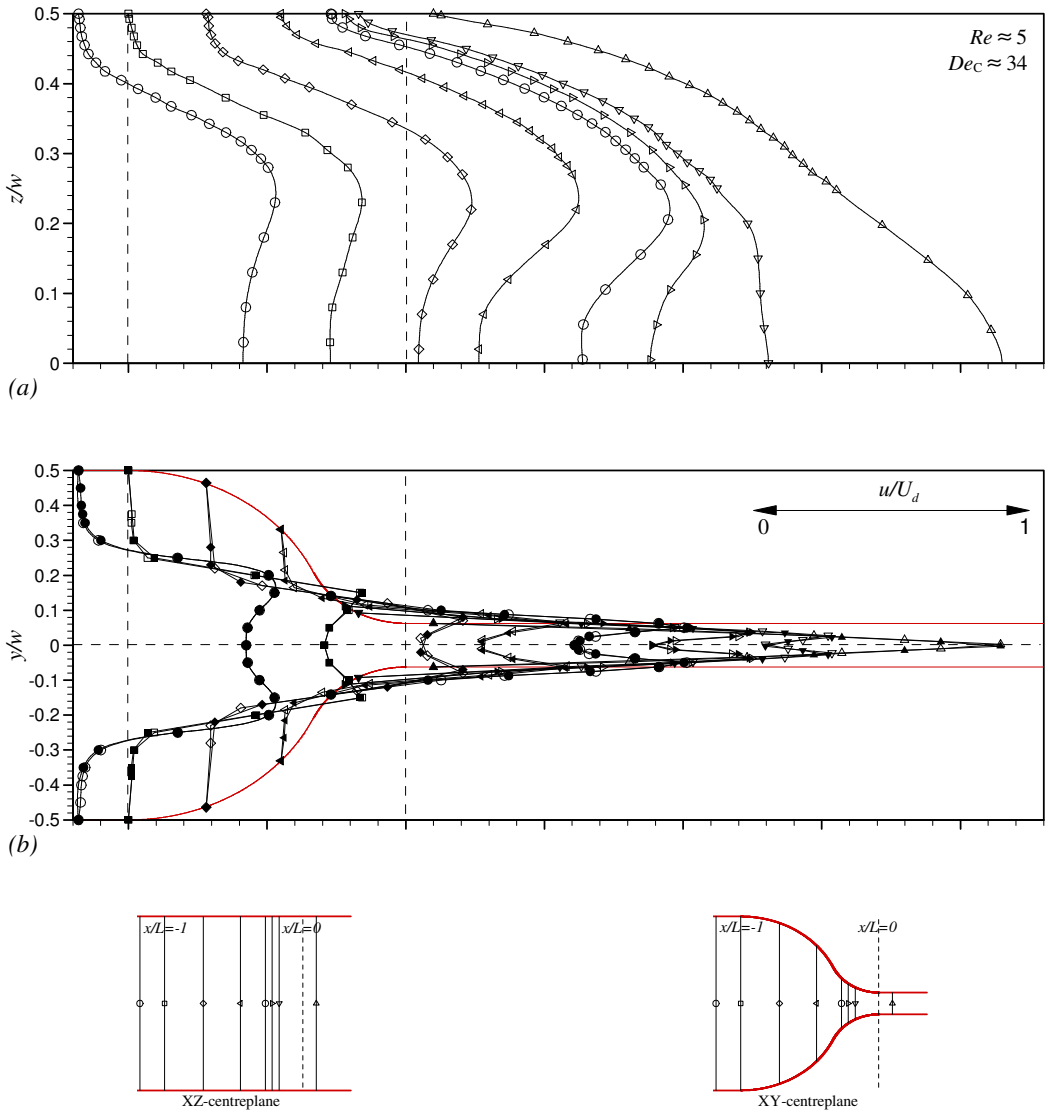

Figure 4.13: Normalised velocity profiles along (a) the XZ-centreplane and (b) the XY-centreplane for 0.3% polyacrylamide at $Re \approx 5$, $De_C \approx 34$ measured at x/L=-1.18 (○), -1 (□), -0.72 (◊), -0.45 (◁), -0.27 (○),-0.22 (▷), -0.17 (▽) and 0.10 (△), filled symbols represent reflected values.

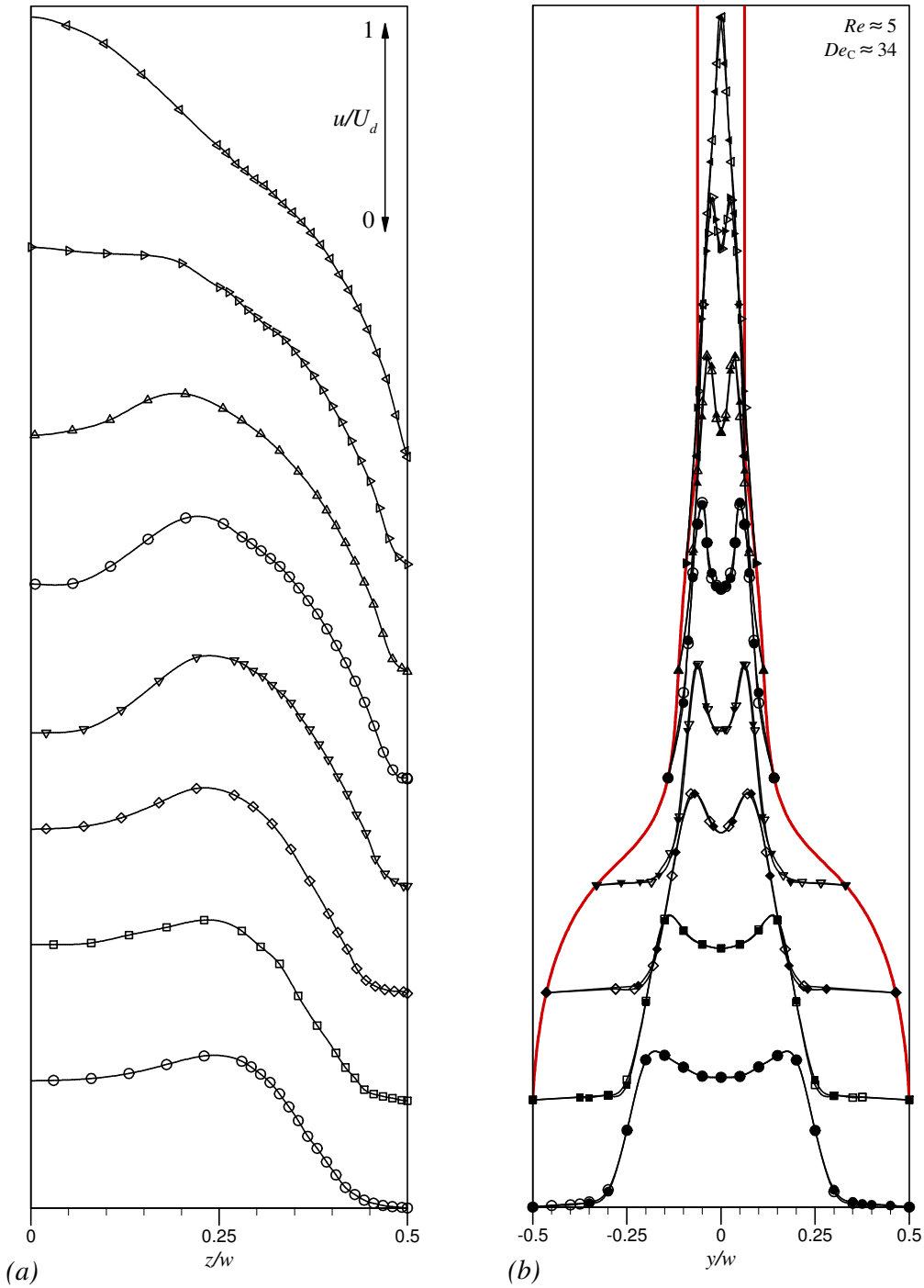

Figure 4.14: Normalised velocity profiles along (a) the XZ-centreplane and (b) the XY-centreplane for 0.3% polyacrylamide at $Re \approx 5$, $De_C \approx 34$ measured at x/L=-1.18 (○), -1 (□), -0.72 (◊), -0.45 (▽), -0.27 (○),-0.22 (△), -0.17 (▷) and 0.10 (◁), filled symbols represent reflected values.

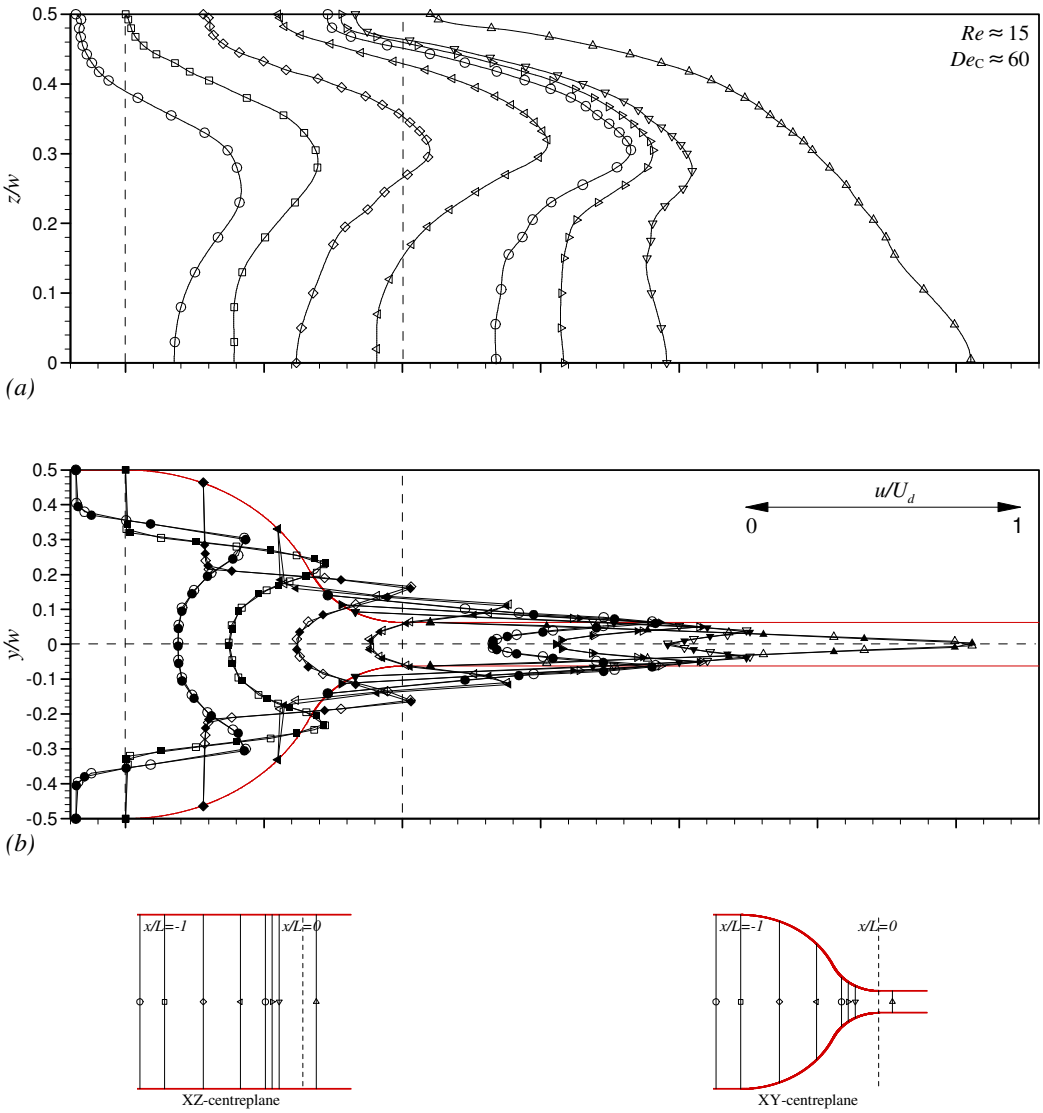

Figure 4.15: Normalised velocity profiles along (a) the XZ-centreplane and (b) the XY-centreplane for 0.3% polyacrylamide at $Re \approx 15$, $De_C \approx 60$ measured at x/L=-1.18 (○), -1 (□), -0.72 (◊), -0.45 (◁), -0.27 (○),-0.22 (▷), -0.17 (▽) and 0.10 (△), filled symbols represent reflected values.

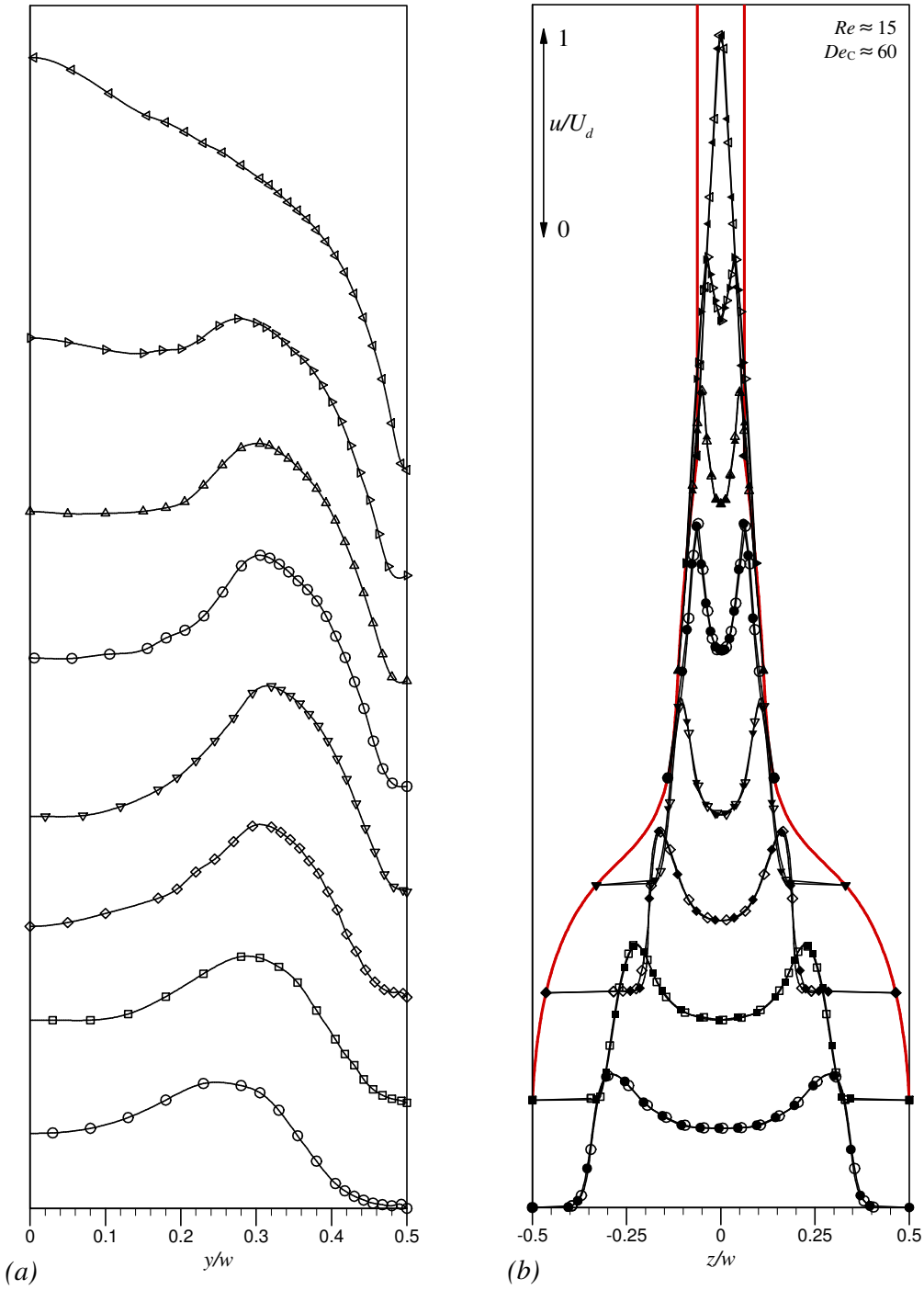

Figure 4.16: Normalised velocity profiles along (a) the XZ-centreplane and (b) the XY-centreplane for 0.3% polyacrylamide at $Re \approx 15$, $De_C \approx 60$ measured at x/L=-1.18 (○), -1 (□), -0.72 (◊), -0.45 (▽), -0.27 (○),-0.22 (△), -0.17 (▷) and 0.10 (◁), filled symbols represent reflected values.

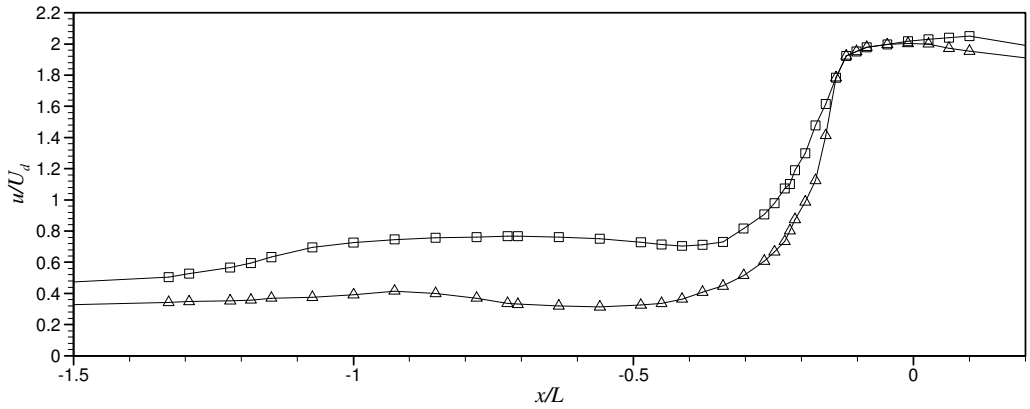

Figure 4.17: Normalised centreline velocities for 0.3% polyacrylamide at $Re \approx 5$, $De_C \approx 34$ (□) and $Re \approx 15$, $De_C \approx 60$ (△).

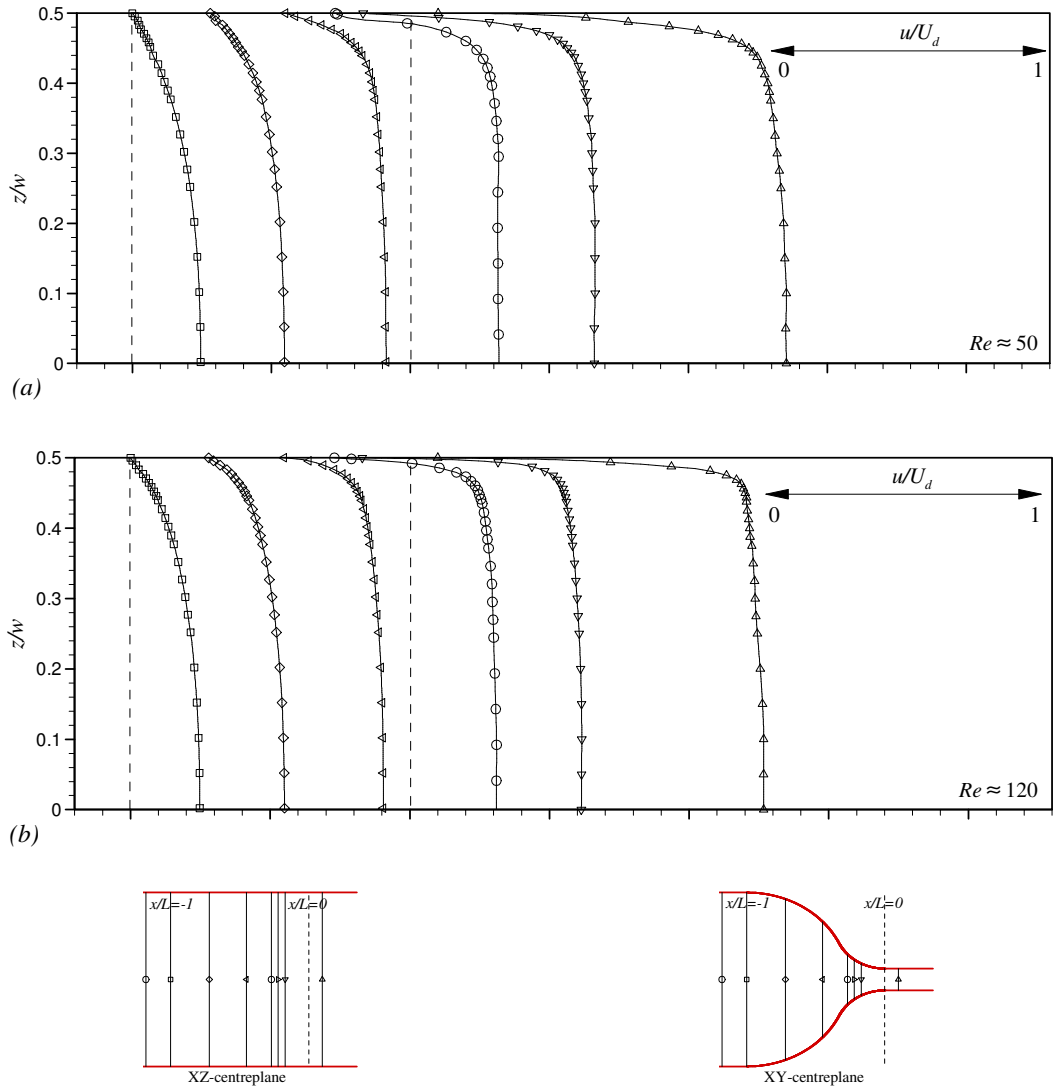

Figure 4.18: Normalised velocity profiles along the XZ-centreplane for 0.07% xanthan gum at (a) $Re \approx 50$ and (b) $Re \approx 120$ measured at x/L=-1 (□), -0.72 (◊), -0.45 (◁), -0.27 (○), -0.17 (▽) and 0.10 (△).

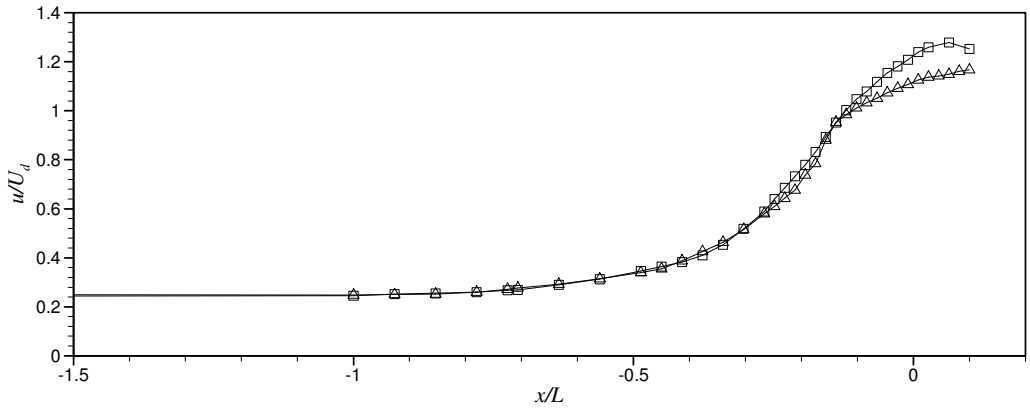

Figure 4.19: Normalised centreline velocity for 0.07% xanthan gum at $Re \approx 50$ (□) and $Re \approx 120$ (△).

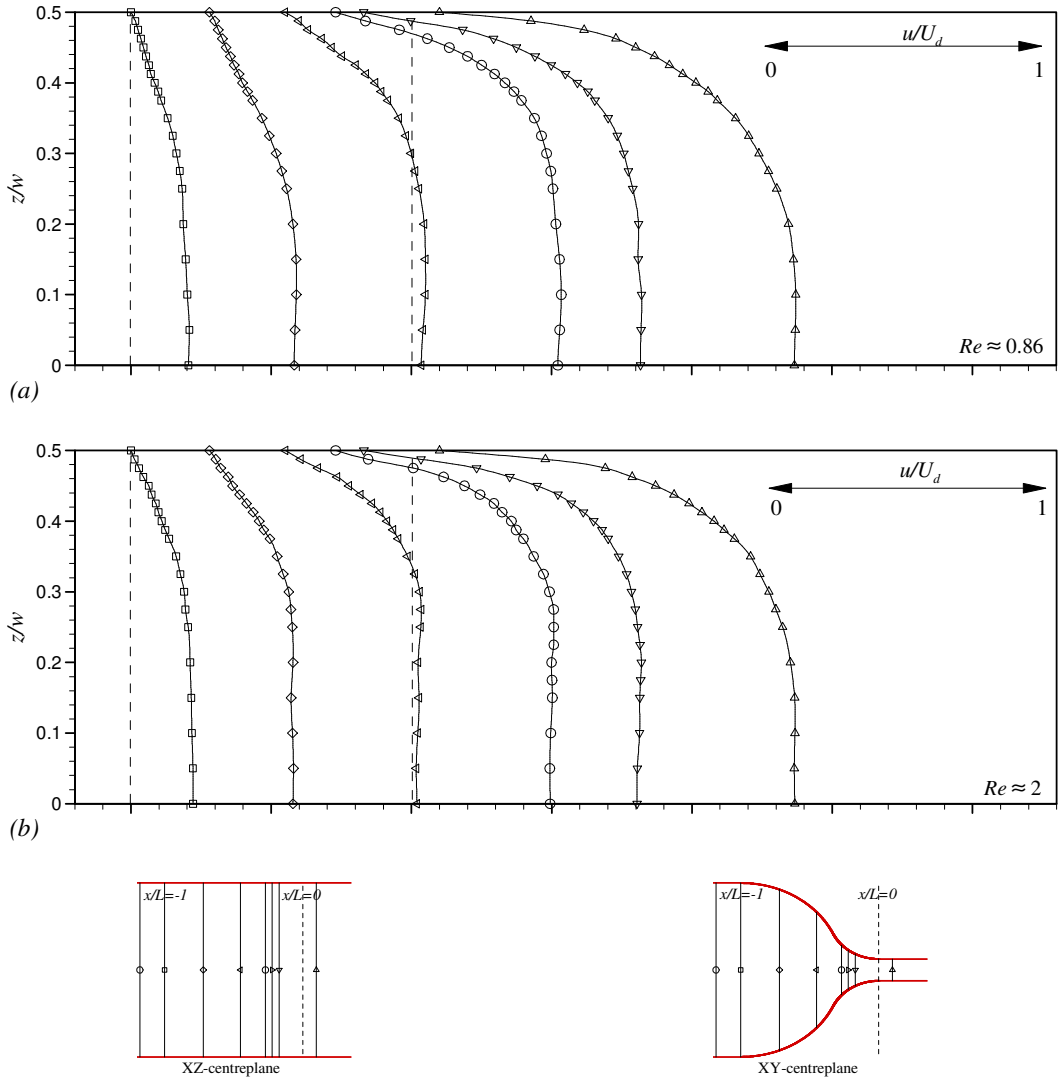

Figure 4.20: Normalised velocity profiles along the XZ-centreplane for 0.5% xanthan gum at (a) $Re \approx 0.86$, $De_C \approx 0.21$ and (b) $Re \approx 2$, $De_C \approx 0.34$ measured at x/L= -1 (□), -0.72 (◊), -0.45 (◁), -0.27 (○), -0.17 (▽) and 0.10 (△).

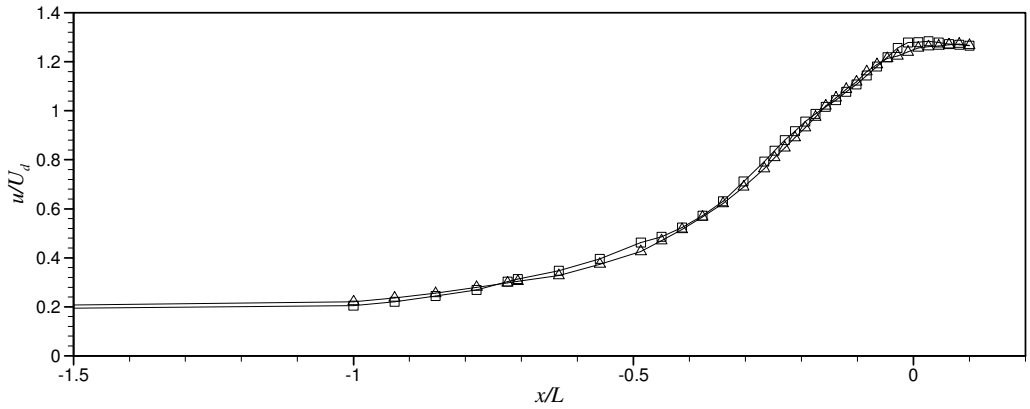

Figure 4.21: Normalised centreline velocities for 0.5% xanthan gum at $Re \approx 0.86$, $De_C \approx 0.21$ (□) and $Re \approx 2$, $De_C \approx 0.34$ (△).

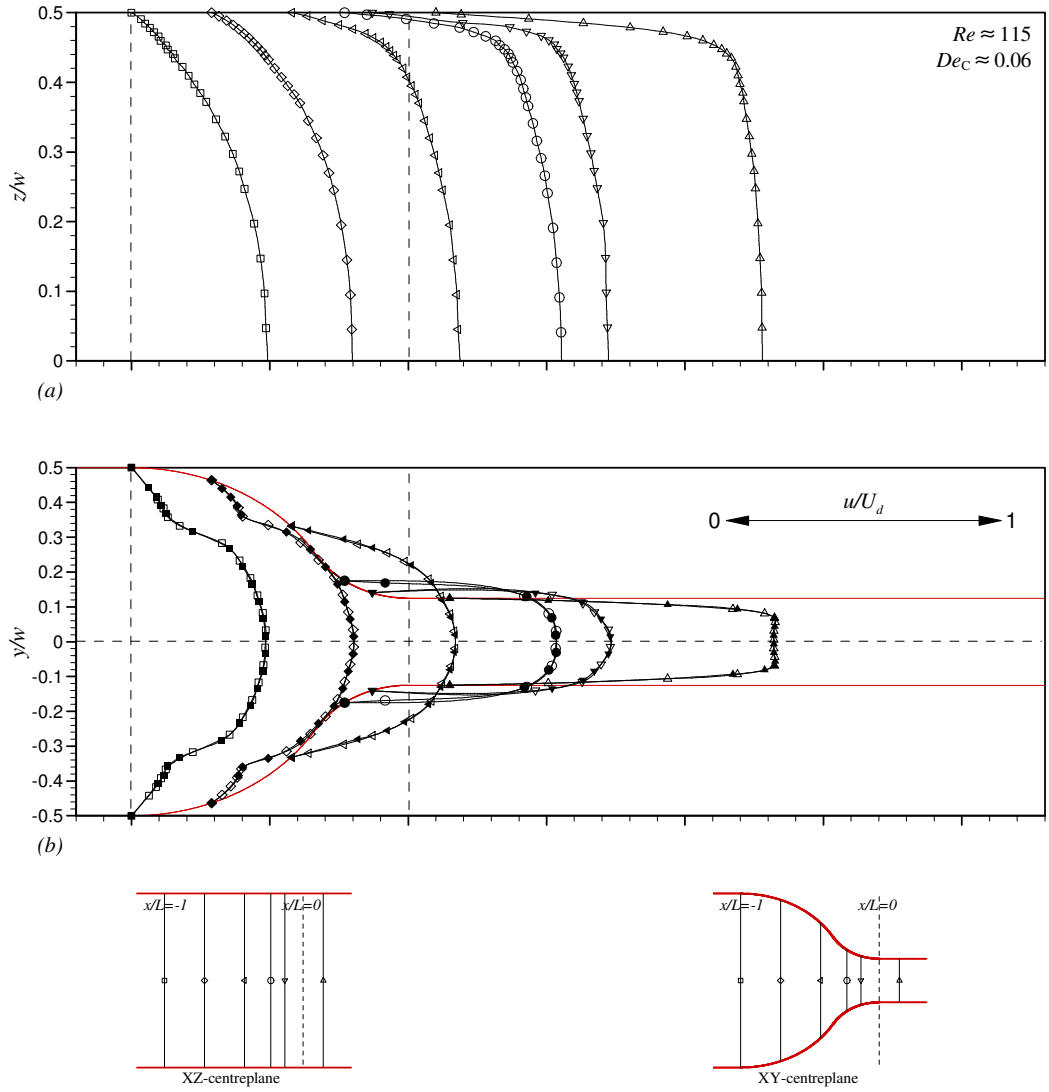

Figure 4.22: Normalised velocity profiles along (a) the XZ-centreplane and (b) the XY-centreplane for 0.03% polyacrylamide at $Re \approx 115$, $De_C \approx 0.06$ measured at x/L=-1 (□), -0.71 (◊), -0.42 (◁), -0.23 (○), -0.13 (▽) and 0.15 (△).

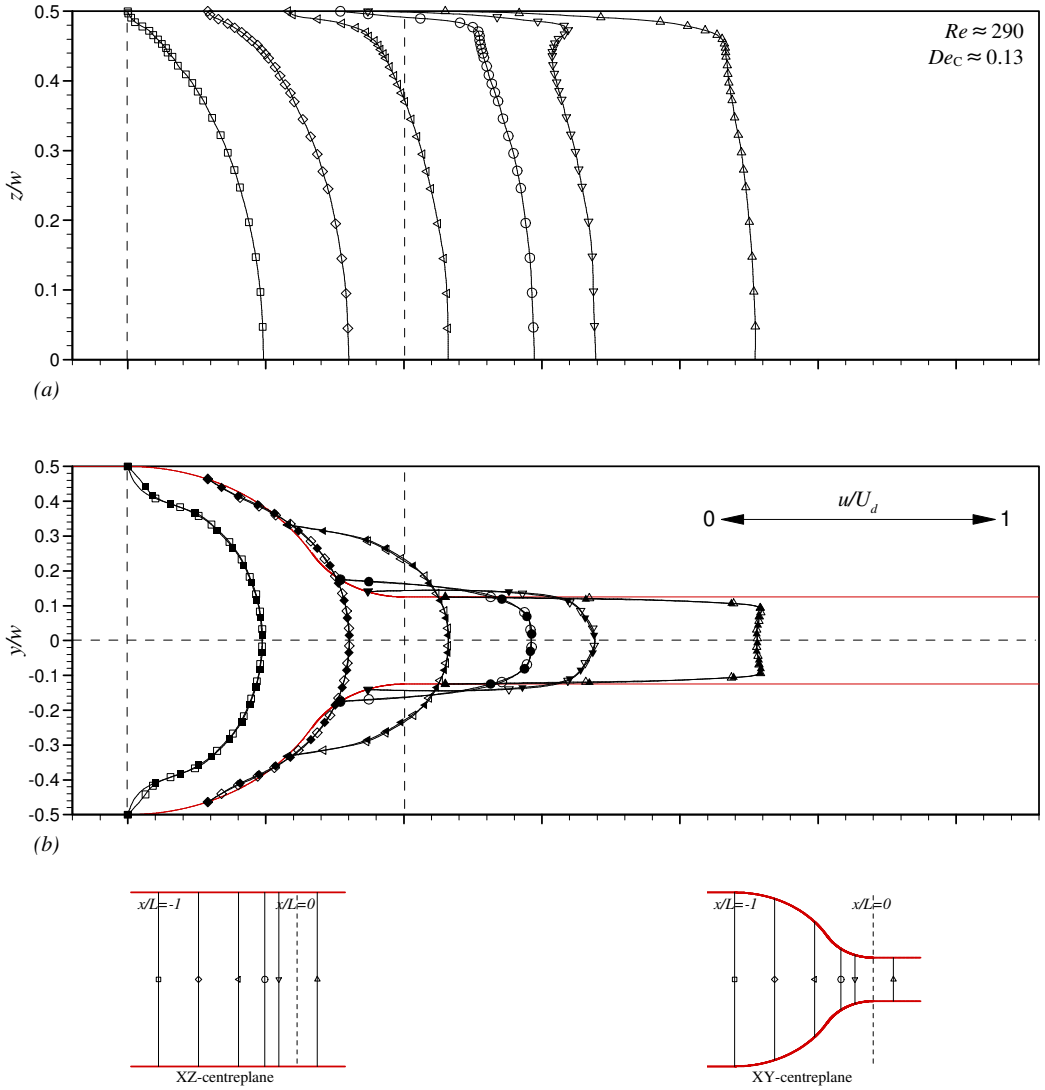

Figure 4.23: Normalised velocity profiles along (a) the XZ-centreplane and (b) the XY-centreplane for 0.03% polyacrylamide at $Re \approx 290$, $De_C \approx 0.13$ measured at x/L=-1 (□), -0.71 (◊), -0.42 (◁), -0.23 (○), -0.13 (▽) and 0.15 (△).

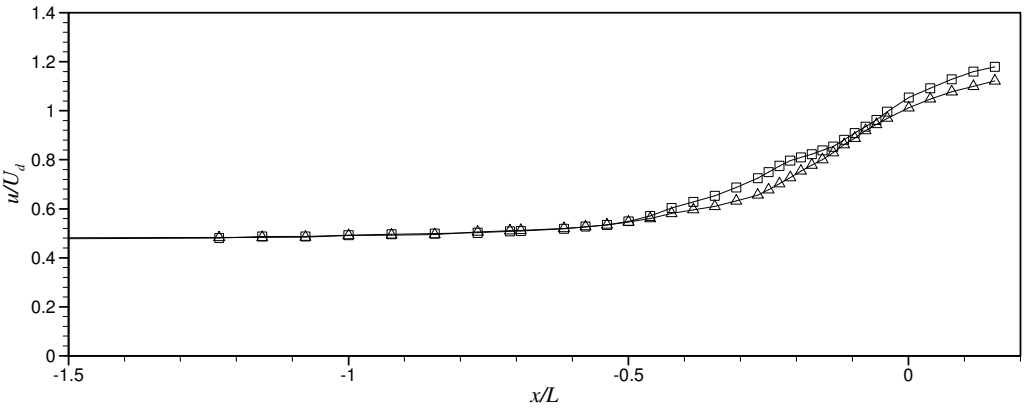

Figure 4.24: Normalised centreline velocities for 0.03% PAA at $Re \approx 115$, $De_C \approx 0.06$ (□) and $Re \approx 290$, $De_C \approx 0.13$ (△).

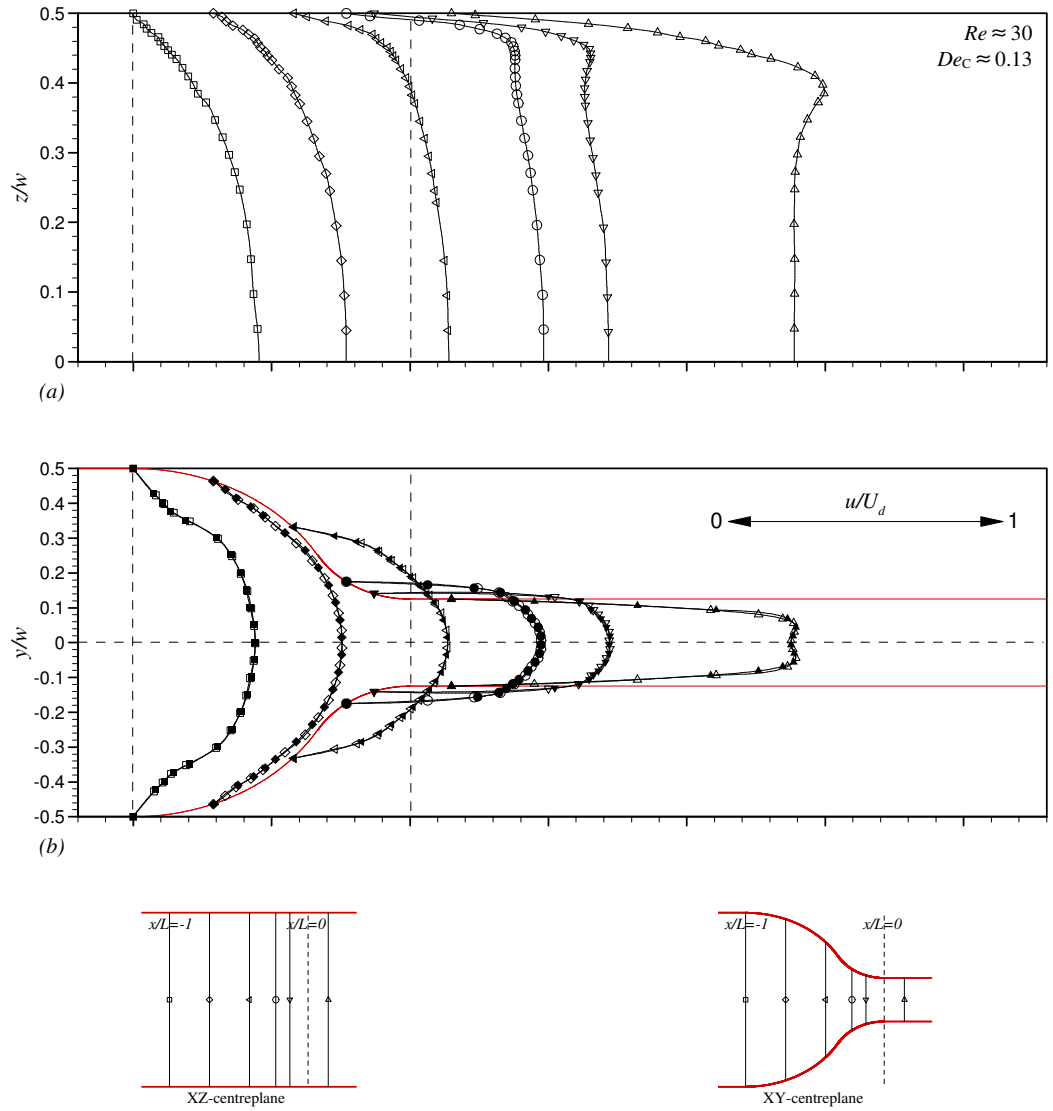

Figure 4.25: Normalised velocity profiles along (a) the XZ-centreplane and (b) the XY-centreplane for 0.05% polyacrylamide at $Re \approx 30$, $De_C \approx 0.13$ measured at x/L=-1 (□), -0.71 (◊), -0.42 (◁), -0.23 (○), -0.13 (▽) and 0.15 (△).

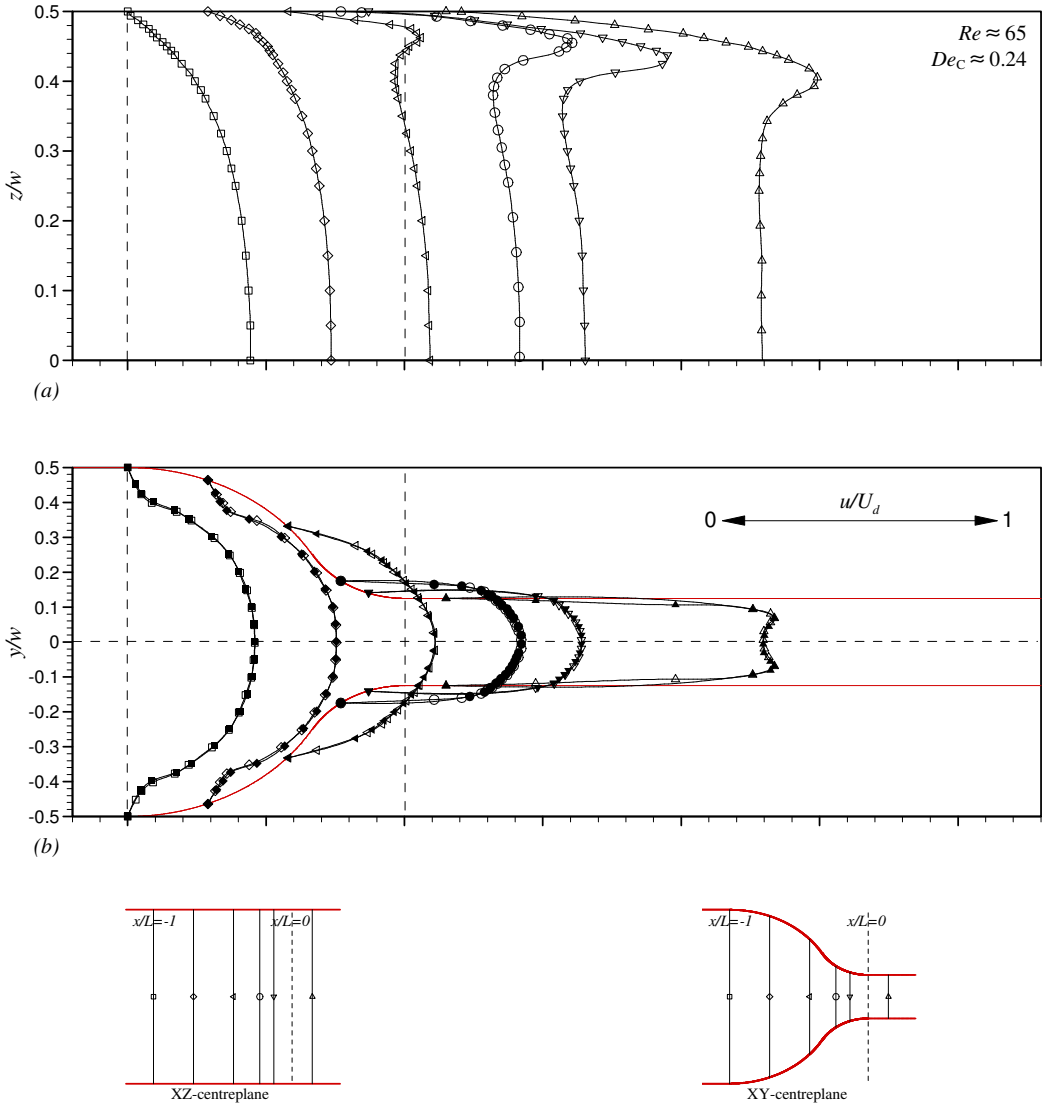

Figure 4.26: Normalised velocity profiles along (a) the XZ-centreplane and (b) the XY-centreplane for 0.05% polyacrylamide at $Re \approx 65$, $De_C \approx 0.24$ measured at x/L=-1 (□), -0.71 (◊), -0.42 (◁), -0.23 (○), -0.13 (▽) and 0.15 (△).

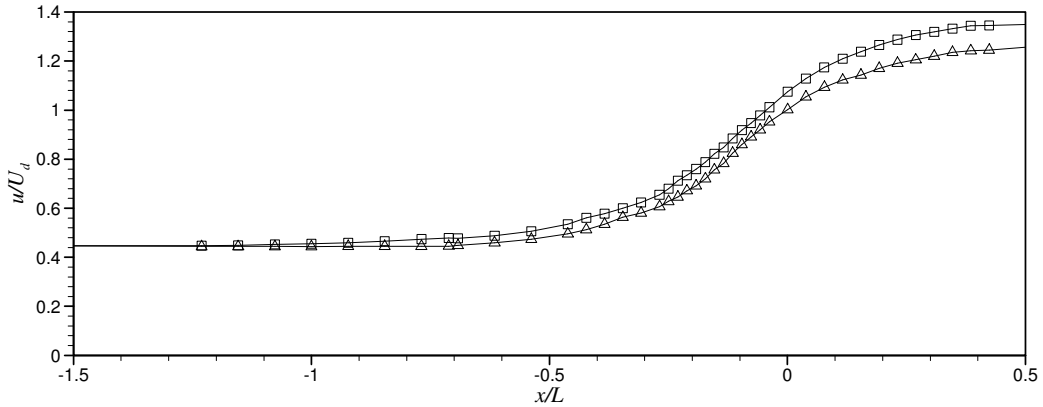

Figure 4.27:Normalised centreline velocities for 0.05% PAA at $Re \approx 30$, $De_C \approx 0.13$ (□) and $Re \approx 65$, $De_C \approx 0.24$ (△).

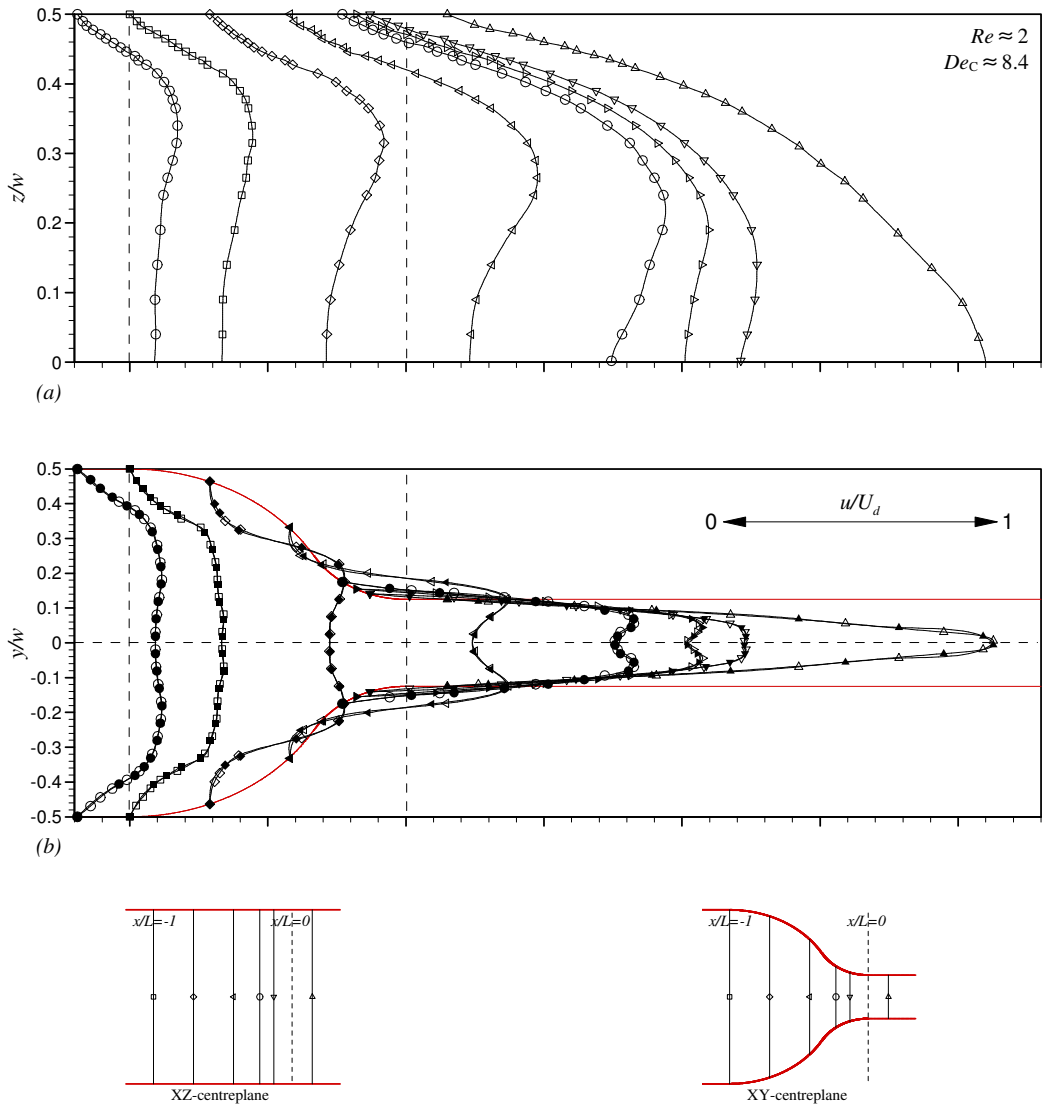

Figure 4.28: Normalised velocity profiles along (a) the XZ-centreplane and (b) the XY-centreplane for 0.3% polyacrylamide at $Re \approx 2$, $De_C \approx 8.4$ measured at x/L=-1.19 (○), -1 (□), -0.71 (◊), -0.42 (◁), -0.23 (○), -0.18 (▷), -0.13(▽) and 0.15 (△).

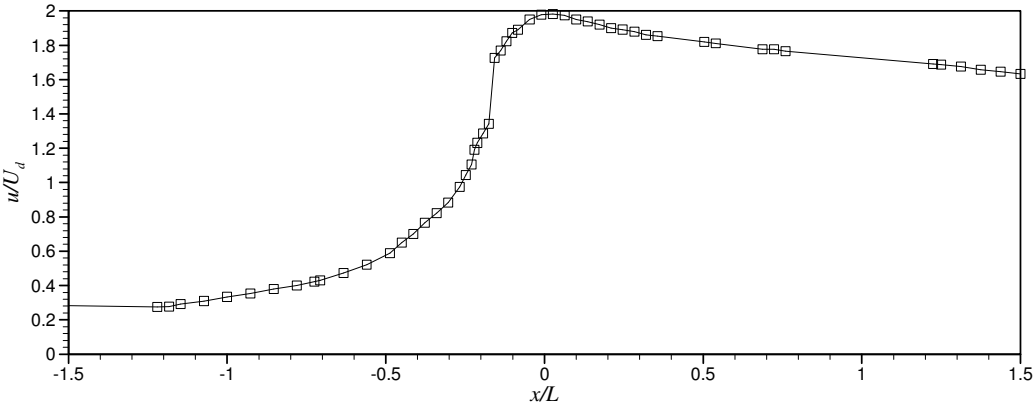

Figure 4.29: Normalised centreline velocity for 0.3% PAA at $Re \approx 2$, $De_C \approx 8.4$.

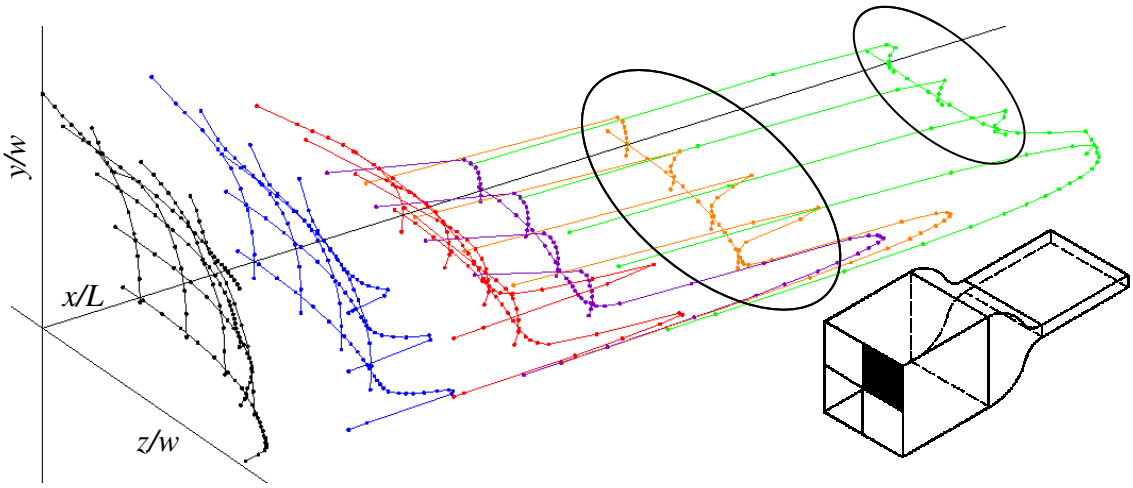

Figure 4.30: 3D visualisation of the flow of 0.05% PAA solution through the 8:1 contraction at $Re \approx 110$, $De_C \approx 0.96$ measured at x/L=-1, -0.72, -0.45, -0.27, -0.17 and 0.10 (flow is from left to right).

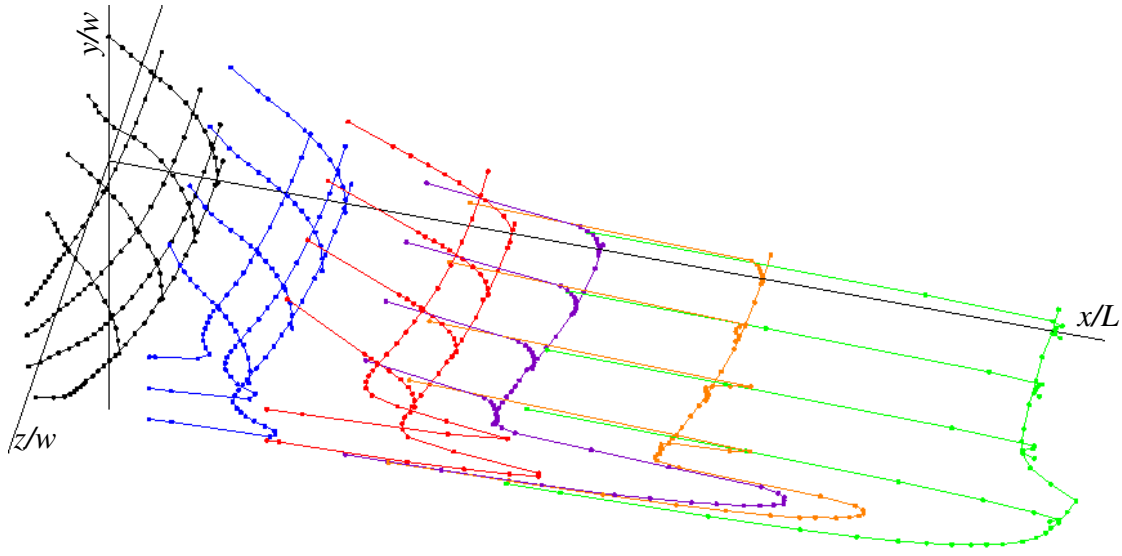

Figure 4.31: 3D visualisation of the flow of 0.05% PAA solution through the 8:1 contraction at $Re \approx 110$, $De_C \approx 0.96$ measured at x/L=-1, -0.72, -0.45, -0.27, -0.17 and 0.10 (flow is from left to right).

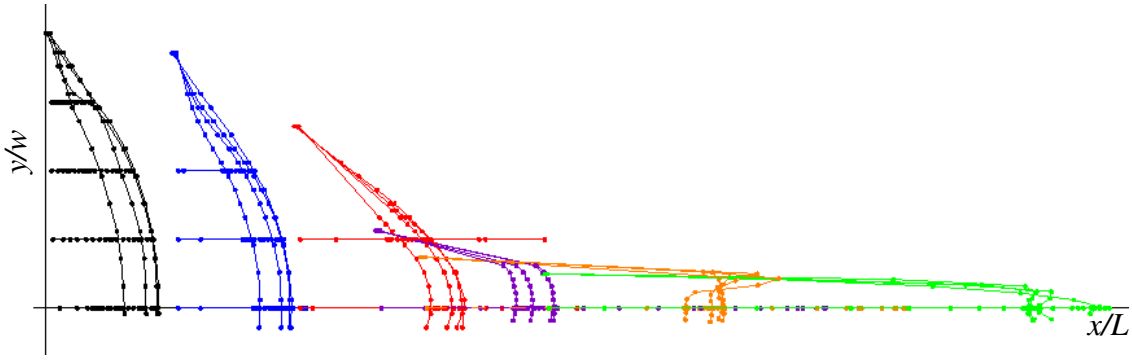

Figure 4.32: Visualisation of the flow of 0.05% PAA solution through the 8:1 contraction at $Re \approx 110$, $De_C \approx 0.96$ measured at x/L=-1, -0.72, -0.45, -0.27, -0.17 and 0.10 (flow is from left to right viewed from the side).

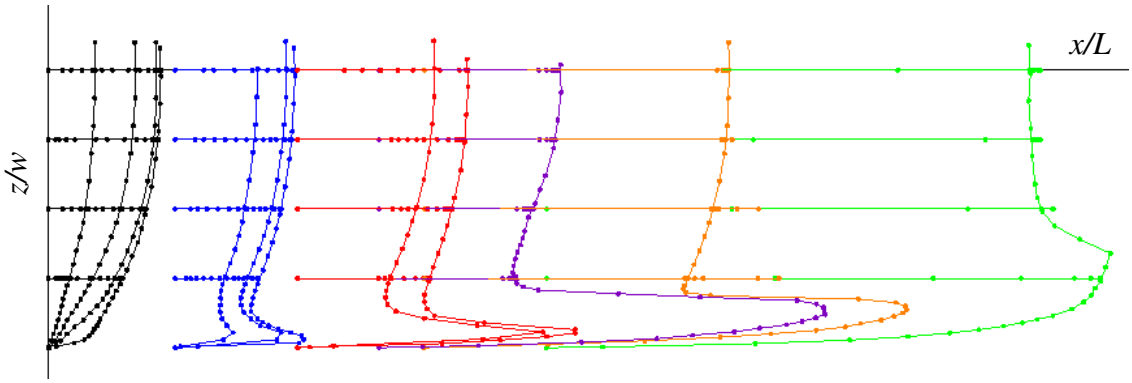

Figure 4.33: Visualisation of the flow of 0.05% PAA solution through the 8:1 contraction at $Re \approx 110$, $De_C \approx 0.96$ measured at x/L=-1, -0.72, -0.45, -0.27, -0.17 and 0.10 (flow is from left to right viewed from the top).

5. Discussion of Results

5.1. Quantification of velocity overshoots

A factor, K, can be determined using

$$K = \frac{U_O/U_d - U_L/U_d}{U_C/U_d} \tag{5.1}$$

where U_O/U_d is the maximum overshoot velocity, U_C/U_d is the centreline velocity and U_L/U_d is the velocity at the change in the gradient of the velocity profile observed at the bottom of the overshoot as defined in Figure 5.1.

Table 5.1 presents the estimated values for K along with the corresponding velocities used to calculate the factors for all fluids in which velocity overshoots were seen along the XZ-centreplane in the 8:1 contraction. The values of K are used to determine the approximate location at which the overshoots develop and the positions of the maximum overshoot for each fluid/flowrate. Figures 5.2 to 5.4 are graphic representations of the K values presented in Table 5.1.

Table 5.1 shows that for both cases of 0.03% PAA the overshoots are seen to develop between x/L=-0.72 and x/L=-0.45 whereas in the 0.05% solution the overshoots are seen to develop earlier, between x/L=-1 and x/L=-0.72. This earlier development agrees with the results seen in Figure 5.2. In all cases the magnitude of the velocity overshoots increases up to a maximum then decreases.

Figure 5.2 shows that the velocity overshoots observed in 0.03% PAA are slightly larger at the lower flowrate than at the higher flowrate, which would not be immediately apparent from looking solely at Figures 4.10 and 4.11. In 0.03% PAA at $Re \approx 140$, $De_C \approx 0.24$ the location of the maximum overshoot size is at x/L=-0.17, whereas for 0.03% PAA at $Re \approx 390$, $De_C \approx 0.53$ and both sets of 0.05% PAA the location of the maximum overshoot is located at x/L=-0.27. This location is approximately at the crossover point between the concave radius and the convex radius that make up the 8:1 contraction.

Table 4.1 shows that as the concentration of PAA increases so does the Elasticity number. The velocity overshoots are seen to develop between *x/L*=-0.72 and -0.45 in 0.03% PAA, between *x/L*=-1 and –0.72 in 0.05% PAA and before *x/L*=-1.18 in 0.3% PAA. This result suggests that the Elasticity number has an effect on where the velocity overshoots develop within the test section, i.e. the larger *El* the earlier the overshoots develop.

Table 5.2 presents the overshoot and centreline velocities and the *K* values for the four flows in which velocity overshoots are observed along the XZ-centreplane of the 4:1 contraction. This table shows that the 0.03% PAA flow at $Re \approx 115$, $De_C \approx 0.13$ the overshoots develop between *x/L*=-0.23 and *x/L*=-0.13 and disappear between *x/L*=-0.13 and *x/L*=0.15. In 0.05% PAA at $Re \approx 30$, $De_C \approx 0.13$ the overshoots develop between *x/L*=-0.42 and *x/L*=-0.23 with the maximum overshoot occurring at *x/L*=0.15 whereas at $Re \approx 65$, $De_C \approx 0.13$ the overshoots develop earlier, between *x/L*=-0.71 and *x/L*=-0.42, with the maximum overshoot also earlier at *x/L*=-0.13. The overshoots develop before the start of the contraction in the 0.3% PAA flow and the maximum overshoot is seen at *x/L*=-0.71.

Table 5.3 gives the overshoot velocities, the centreline velocities and the *K* values for the flow of 0.05% PAA measured at locations away from the centreplanes. There are two locations where side to side overshoots were observed (*x/L*=-0.72 and *x/L*=-0.45) away from the centreplane. Table 5.3 shows that the *K* values decrease (hence the overshoots decrease in size) as the distance from the centreplane increases at *x/L*=-0.72, but at *x/L*=-0.45 the opposite is true and the *K* values increase as the distance from the centreplane increases. Overshoots were observed away from the centreplane in the transverse direction in two locations (*x/L*=-0.17 and *x/L*=0.10). In these cases the overshoots are seen to increase in size the further away from the centreplane they are measured, i.e. the closer the flow is to the plane side walls.

5.2. Comparison between concentrations in the 8:1 contraction

The velocity profile sets presented in this chapter are the same sets that were shown in Chapter 4 but they have not been offset in order to draw comparisons between the data sets. Table 4.1 presents estimated values for Reynolds, Deborah, Weissenberg

and Elasticity numbers for the flows of all the fluids discussed in Chapter 4 through the 8:1 contraction; the values are estimated as described in Chapter 3. This table shows that 0.03% PAA and 0.05% PAA were measured at comparable Reynolds numbers of $Re \approx 140$ and $Re \approx 110$ but different Deborah numbers (both CaBER and N_1) and also at comparable Deborah and Weissenberg numbers ($De_C \approx 0.53$ and $De_C \approx 0.52$ and $Wi_C \approx 0.21$ and $Wi_C \approx 0.23$) but different Reynolds numbers. Comparisons may also be drawn between the Deborah numbers for 0.03% PAA ($De_{N1} \approx 5.2$ and $De_{N1} \approx 6.2$) and 0.3% PAA ($De_{N1} \approx 5.3$ and $De_{N1} \approx 6.2$) and between the Weissenberg numbers for 0.03% PAA ($Wi_C \approx 0.21$), 0.05% PAA ($Wi_C \approx 0.23$) and 0.5% XG at two Reynolds numbers ($Wi_C \approx 0.24$ and $Wi_C \approx 0.24$). The table also shows that 0.05% PAA and 0.07% XG were both measured at $Re \approx 50$ and at comparable Reynolds numbers of $Re \approx 110$ and $Re \approx 120$ and that 0.3% PAA and 0.5% XG may be compared in terms of Elasticity number ($El_C \approx 3.9$ and $El_C \approx 4.1$ respectively). These comparisons will be discussed in what follows.

Figure 5.5 (a) and (b) show the velocity profiles for 0.03% PAA at $Re \approx 140$, $De_C \approx 0.24$ and 0.05% PAA at $Re \approx 110$, $De_C \approx 0.96$; these profiles were measured at comparable Reynolds numbers but it is clear that the profiles are very different. The overshoots in the 0.03% PAA develop between x/L=-0.72 and x/L=-0.45 whereas in 0.05% PAA they are seen to develop earlier between x/L=-1 and x/L=-0.72. In both cases the overshoots increase with respect to U_d through the contraction. The profiles in the 0.05% PAA solution are much broader and rounder than those seen in 0.03% PAA, particularly at x/L=-0.17 and x/L=-0.27; there is a much greater difference between the maximum velocities and the centreline velocities in 0.05% PAA (Table 5.1 shows that the K values are much larger for 0.05% PAA than for 0.03% PAA). The difference in the structure of the overshoots suggests that although the Reynolds numbers are comparable the effects of a larger Deborah number (approximately four times for De_C and nearly seven times for De_{N1}) are of key importance.

Figure 5.5 (c) and (d) present the velocity profiles for 0.03% polyacrylamide at $Re \approx 390$, $De_C \approx 0.53$ and 0.05% PAA at $Re \approx 50$, $De_C \approx 0.52$; the estimated De_C numbers for these flows are obviously similar as are the Wi_C numbers but it is clear that the flows themselves are quite different as seen in the figure. In the 0.03% PAA the overshoots develop between x/L=-0.72 and x/L=-0.45 and in the 0.05% they

develop earlier, between x/L=-1 and x/L=-0.72. The overshoots seen in the 0.05% solution appear to be more 'pointed' than those seen in the 0.03% solution.

On inspection of the results in order of increasing Reynolds number (Figure 5.5 (d), (b), (a), (c)) it seems that no obvious trend can be deduced solely based on this information. However if we look at the results in order of increasing Deborah number (Figure 5.5 (a), (d), (c), (b)) the velocity profiles appear to broaden and become more 'rounded', in particular those at x/L=-0.17 and x/L=-0.27. These subtle changes confirm that the Deborah number, and in particular the extensional properties of the fluid, based on the CaBER relaxation time play a key role in the appearance and strength of the velocity overshoots. It must be borne in mind that there is a notable difference between the Elasticity numbers (both El_C and El_{N1}) for the 0.03% PAA flow and the 0.05% PAA flow; this difference may be the reason for the velocity overshoots developing earlier in the 0.05% PAA flow than in the 0.03% flow.

Figures 5.6 and 5.7 include data for both 0.03% PAA and 0.3% PAA at different Reynolds numbers but comparable Deborah numbers based on N_1 data ($De_{N1} \approx 5.2$ and $De_{N1} \approx 6.2$ respectively). Velocity overshoots are clearly observed in all cases but, although the Deborah numbers are comparable, there is a major difference between the sets of profiles depending on the fluid concentration. This effect is possibly due to the difference in the shear viscosities of the two fluids, as indicated by the difference in the Reynolds and Elasticity numbers. Given that the flow in the contraction is an extensional one, it may also be that De_C is a more appropriate measure of elastic effects than De_{N1}.

Figure 5.8 shows 0.03% and 0.05% polyacrylamide along with 0.5% xanthan gum (at two flowrates) at comparable Weissenberg numbers (Wi_C) of around 0.2. The results in this figure suggest that although the Weissenberg numbers are similar this number cannot be used alone in the determination of the occurance of the velocity overshoots. The Reynolds numbers are much lower for the xanthan gum flows implying that inertia might also play a role in the 'cat's ears' effect. However the results for 0.3% PAA at comparable Re are very different to the 0.5% XG results. It should also be noted that xanthan gum is a more rigid polymer than polyacrylamide,

which may affect the appearance of the velocity overshoots. This rigid behaviour is emphasised by the lack of CaBER data for the XG polymer solution at the lower concentration. The relaxation time for the xanthan gum solution is much lower than for both concentrations of PAA.

Figure 5.9 shows velocity profiles for 0.07% xanthan gum and 0.05% polyacrylamide at similar Reynolds numbers: velocity overshoots are seen in the polyacrylamide solution but not in the xanthan gum solution in agreement with the discussion above. A Deborah number could not be calculated for 0.07% XG as the relaxation time was below the sensitivity of our CaBER so the Deborah number is estimated to be essentially negligible (if λ<1ms, then De_C<0.0013 and 0.0024). The occurrence of the overshoots in the PAA solution and not in the XG solution agrees with the previous suggestion that the Deborah number is vitally important in the appearance of the velocity overshoots.

Figure 5.10 presents the velocity profiles for 0.3% PAA and 0.5% XG at comparable elasticity numbers of 3.9 and 4.1 respectively. The figure clearly shows overshoots in the PAA and not in the XG confirming that the elasticity number alone cannot be used to determine whether the velocity overshoots will occur.

5.3. Comparison across the concentrations in the 4:1 contraction

Table 4.2 presents estimated Reynolds, Deborah, Weissenberg and Elasticity numbers (determined as described in Chapter 3) for the various fluid flows through the 4:1 contraction. The table shows that 0.03% PAA and 0.05% PAA were measured at comparable values of De_C.

Figure 5.11 shows the velocity profiles for both flows of 0.03% polyacrylamide and both flows of 0.05% polyacrylamide. Figure 5.11 (a) and (b) are the profiles for 0.03% PAA at $Re \approx 290$, $De_C \approx 0.13$ and 0.05% PAA at $Re \approx 30$, $De_C \approx 0.13$. The first four velocity profiles (x/L=-1 to x/L=-0.23) are very similar for both sets of results. In the lower concentration (a) the overshoot at x/L=-0.13 is larger than in the higher concentration (b) but by x/L=0.15 the overshoot has disappeared in the 0.03% PAA solution, whereas in 0.05% PAA solution the overshoot continues to grow.

Looking at the velocity profile sets in Figure 5.11 in order of increasing Reynolds numbers (Figure 5.11 (b), (d), (c), (a)) the overshoots occur more easily at the lower Reynolds numbers, although it must be noted that these fluids are at the higher concentration and are therefore more elastic. On inspection of the profile sets in order of increasing Deborah numbers (both De_C and De_{N1}) (Figure 5.11 (c), (a), (b), (d)) the overshoots grow in size as the Deborah number increases. This agrees with the earlier suggestion that the Deborah number and the elastic properties of the flow play an important role in the development of the velocity overshoots.

5.4. Comparison across the contractions

Figure 5.12 shows 0.03% polyacrylamide and 0.05% polyacrylamide in the 8:1 contraction along with 0.03% polyacrylamide in the 4:1 contraction all at comparable Reynolds numbers (110 to 140). Clearly the profile sets differ greatly and *Re* alone is not a good indicator as to whether the velocity overshoots will occur. Both De_C and De_{N1} increase in order (c), (a), (b) and it is obvious that as the Deborah numbers increase the velocity overshoots become much more pronounced.

Figure 5.13 presents 0.05% PAA in both contractions at comparable Reynolds numbers of $Re \approx 50$, $De_C \approx 0.52$ in the 8:1 contraction and $Re \approx 65$, $De_C \approx 0.24$ in the 4:1 contraction. Both De_C and De_{N1} are larger in the 8:1 contraction flow than in the 4:1 contraction flow in this case and although the overshoots look to be very similar in shape, being quite 'pointed', they seem to be slightly larger in the 8:1 contraction. Tables 5.1 and 5.2 confirm that the overshoots are more pronounced in the 8:1 contraction as the *K* values are larger in this case.

In an attempt to 'eliminate' the effects of the contraction ratio the data presented in Figure 5.13 has been normalised with respect to the centreline velocity at each axial location and this replotted data is presented in Figure 5.14. The flow through the 8:1 contraction is represented by open symbols and that through the 4:1 contraction filled symbols. This figure highlights some similarities and differences between the two flows that are not immediately apparent in the original normalisation (Figure 5.13). The flows have comparable Reynolds numbers but the Deborah number (from CaBER data) is higher for the 8:1 flow than the 4:1 flow. The velocity overshoots

observed in the 8:1 flow clearly develop earlier than in the 4:1 flow, they are also larger at each location in the 8:1 flow. Interestingly, the width of the velocity overshoots observed in (c), (d) and (e) is very similar at each location with the change in velocity gradient occurring at more or less the same position for each location. Over the majority of the flow, towards the centre of the contraction, the velocity profiles in all cases, except (f), appear the same at each location for both flows, i.e. the 'cat's ears' effect is confined to within z/w=0.2 of the sidewalls.

Figure 5.15 presents the velocity profiles for 0.03% PAA at $Re \approx 140$, $De_C \approx 0.24$ in the 8:1 contraction and 0.05% PAA at $Re \approx 65$, $De_C \approx 0.24$ in the 4:1 contraction. $De_C \approx 0.24$ for both flows, while the Wi_C values are compared at 0.14 and 0.13 respectively. The overshoots observed in the 4:1 contraction are larger than those in the 8:1 contraction. However the K values for both sets of profiles are very similar. In the 8:1 contraction the overshoots develop between x/L=-0.72 and x/L=-0.45 and in the 4:1 contraction they develop between x/L=-0.71 and x/L=-0.42. The K values for x/L=-0.27, -0.17 and 0.10 in the 8:1 contraction are nearly identical to those for x/L=-0.23, -0.13 and 0.15 in the 4:1 contraction showing that the difference between the maximum overshoot velocities and the centreline velocities are the same for the profiles measured after the radius change in both contractions (i.e.$x/L \approx 0.3$).

The data from Figure 5.15 has been replotted in Figure 5.16 in the same manner as the data shown in Figure 5.14. In this case the flows have the same Deborah number ($De_C \approx 0.24$) but the 8:1 contraction flow (represented by open symbols) has a higher Reynolds number than the 4:1 contraction flow (represented by closed symbols). The two flows are obviously very similar. A larger overshoot is observed at the lower Reynolds number in (c) but this is in fact a higher concentration of polyacrylamide. The overshoots in (d) and (e) have the same magnitude but in the 8:1 contraction they are confined closer to the sidewalls (within 0.06 z/w) than in the 4:1 contraction (within 0.1 z/w). The opposite is true, however, of the profiles at (f), in this case the magnitude of the overshoots is the same but the overshoot observed at the higher flowrate is wider than at the lower flowrate.

Figure 5.17 shows four profile sets for 0.05% PAA at two Reynolds numbers in both contractions at comparable De_{N1} values of between 8.9 and 9.2. Velocity overshoots

are observed to a different extent in each case. On the whole the overshoots are more pronounced in the 8:1 contraction ((a) and (c)), however the Reynolds numbers are higher for these two flows so no direct conclusions can be drawn from the comparison of these velocity profile sets, except that *Re* is a minor influence. Figure 5.18 shows the velocity profiles along the XZ-centreplane for 0.03% polyacrylamide at $Re \approx 290$, $De_C \approx 0.13$ and $Re \approx 115$, $De_C \approx 0.06$ in the 4:1 contraction and at $Re \approx 140$, $De_C \approx 0.24$ in the 8:1 contraction along with 0.3% polyacrylamide at $Re \approx 5$, $De_C \approx 34$ in the 8:1 contraction: these profiles were measured at comparable De_{N1} numbers of between 5.1 and 5.3. It is clear from these profiles that De_{N1} alone is not a good indicator of whether the velocity overshoots will occur. The overshoots are obviously more pronounced within the 8:1 contraction when we look at (b) and (c) which are at similar *Re*. As discussed earlier the flow through the gradual contraction is predominantly extensional flow so the Deborah number found using the relaxation time from CaBER is more likely to be a better indicator of the flow behaviour than the Deborah number found using the N_1 data.

Figures 5.19 to 5.23 each present velocity profile sets that have comparable Elasticity numbers. There are clear differences observed between each set of velocity profiles and the more pronounced overshoots are always seen at the higher Deborah numbers (and also in the 8:1 contraction). Figures 5.19 to 5.23 show that the Elasticity numbers alone cannot be used to determine whether 'cat's ears' will be observed or the magnitude of the effect when it does occur.

5.5. Stresses acting within the flow

The shear rate on the flat side wall in the XZ-centreplane ($\dot{\gamma}_w$, s^{-1}) at a given location can be found by estimating the gradient of the velocity profile next to the wall ($\equiv \frac{\partial u}{\partial z}$). Similarly the strain rate along the centreline ($\dot{\varepsilon}_c$, s^{-1}) can be found at a given location by estimating the gradient of the centreline velocity profile at the same location ($\equiv \frac{\partial u}{\partial x}$). The estimated shear rates may then be used to calculate a shear stress (τ_w, Pa) along the plane wall and the strain rates an extensional stress (τ_c, Pa) along the centreline using the following equations.

$$\tau_w = \dot{\gamma}_w \mu_w \qquad (5.2)$$

$$\tau_c = \dot{\varepsilon}_c \lambda_C , \qquad (5.3)$$

where μ_w (Pa) is the shear viscosity estimated at the wall shear rate using the Carreau-Yasuda model fit as described in Chapter 2 (Equation 2.2) and λ_C (s) is the relaxation time determined from CaBER measurements. To non-dimensionalise both the shear stress and the extensional stress we use the dynamic pressure, $\frac{1}{2}\rho U_d^2$.

Figure 5.24 presents the non-dimensionalised shear stresses at the wall and extensional stresses along the centreline for all flows of 0.03%, 0.05% and 0.3% PAA through the 8:1 contraction. In the 0.03% PAA cases (Figure 5.24 (a)) the shear stresses are fairly constant throughout the first half of the contraction before increasing to maxima around *x/L*=-0.3 then decreasing and stabilising. In the 0.05% case (Figure 5.24 (c)) the shear stresses start to increase immediately up to a maximum value around *x/L*=-0.45 followed by a decrease to minima around *x/L*=-0.3 for the lower flowrate and *x/L*=-0.2 for the higher flowrate. The shear stress at the lower flowrate then increases slightly towards a constant value whereas at the higher flowrate the shear stress suddenly increases again. In the 0.3% PAA flow (Figure 5.24 (e)) at the lower flowrate the shear stress is seen to increase monotonically as the flow progresses through the contraction with a sudden increase observed at around *x/L*=-0.2. The shear stress for the 0.3% PAA flow at the higher flowrate decreases slightly at the start of the contraction until around *x/L*=-0.2 when it begins to increase rapidly. In all cases the extensional stresses (Figure 5.24 (b), (d) and (f)) are low and fairly constant throughout the first half of the contraction, which might be expected due to the very small changes in the cross sectional area. The extensional stresses then increase suddenly around *x/L*=-0.3, which is the approximate location of the crossover between the 40mm concave radius and the 20mm convex radius and where the change in cross sectional area of the flow becomes more significant. The maximum extensional stress is observed around *x/L*=-0.2 (later than the maxima observed in the shear stress) except in the 0.03% PAA flow at the higher flowrate where it occurs slightly earlier at around *x/L*=-0.3. After the contraction ends the extensional stresses return to zero as should be expected once the cross sectional area of the flow stops changing. The shear stress data for the 0.03% and 0.05% PAA (Figure 5.24 (a) and (c)) collapses onto approximately the same curve in both cases whereas the 0.3% PAA data (Figure 5.24 (e)) does not to

the same degree. This data shows that for the 0.03% and 0.05% PAA flows the shear stresses along the walls behave in a similar manner regardless of the flow rate. The extensional stress data for the 0.03% PAA solution (Figure 5.24 (b)) collapses onto the same curve for the first half of the contraction then diverges in the second half of the contraction. For the 0.05% and 0.3% PAA (Figure 5.24 (d) and (f)) the data collapses onto approximately the same curve in each case.

Figure 5.25 shows the non-dimensionalised shear and extensional stresses for the flows of 0.03%, 0.05% and 0.3% PAA through the 4:1 contraction. In all cases, except the 0.05% PAA flow at the higher flowrate, the shear stress at the wall increases monotonically through the contraction. The shear stress for the 0.05% PAA flow at the higher flowrate exhibits a similar pattern to that observed in the 8:1 contraction for both the 0.03% and 0.05% flows and the maximum is around the same location as for the 0.03% PAA flow through the 8:1 contraction. This information shows that for all flows in which velocity overshoots do not occur throughout the whole contraction the shear stresses at the wall increase monotonically and where velocity overshoots are present throughout the whole contraction the shear stresses increase non-monotonically. The extensional stresses through the 4:1 contraction for 0.03% and 0.05% PAA (Figure 5.25 (b) and (d)) slowly increase to a maxima at around x/L=-0.2. The pattern seen in 0.03% PAA at the lower flowrate is similar to that seen in the 8:1 contraction; the extensional stress is around zero for over half of the contraction in this case. For 0.03% PAA at the higher flowrate and the 0.05% PAA the extensional stresses increase from the start of the contraction. In the 0.3% PAA flow the extensional stress along the centreline is around zero until x/L=-0.3 before a large increase followed immediately by a decrease towards the end of the contraction. The data collapses to the same order of magnitude in each case, the collapse is better for the 0.05% PAA than for the 0.03% PAA solution.

In both the 8:1 and 4:1 contractions the centreline extensional stresses are much larger than the sidewall shear stresses. It is also noted that the stresses in the 0.03% and 0.05% PAA solutions are much lower than those in the 0.3% PAA, most likely due to the difference in shear viscosity at the relevant shear rates.

Since this investigation is looking at contraction flow the shear stresses along the curved walls will probably be more useful than those along the plane walls since the curved walls of the contraction must be causing the velocity overshoots to occur. It is not possible however, to estimate the shear stresses along the curved walls as the flow component that has been measured is along a plane that is not perpendicular to the curved wall.

5.6. Tables

Table 5.1: Non-dimensionalised maximum overshoot and centreline velocities used to quantify velocity overshoots for all fluids where the overshoots are seen along the XZ-centreplane of the 8:1 contraction.

Fluid	*Re*	De_C	*x/L*	U_O/U_d	U_C/U_d	U_I/U_d	*K*
0.03% PAA	140	0.24	-1.00				
			-0.72				
			-0.45	0.26	0.34	0.24	0.06
			-0.27	0.67	0.52	0.43	0.46
			-0.17	0.93	0.68	0.61	0.47
			0.10	1.37	1.18	1.17	0.17
0.03% PAA	390	0.53	-1.00				
			-0.72				
			-0.45	0.38	0.37	0.28	0.27
			-0.27	0.76	0.61	0.54	0.36
			-0.17	0.98	0.81	0.78	0.25
			0.10	1.26	1.10	1.10	0.15
0.05% PAA	50	0.52	-1.00				
			-0.72	0.35	0.30	0.30	0.17
			-0.45	0.44	0.29	0.22	0.76
			-0.27	0.76	0.43	0.33	1.00
			-0.17	1.05	0.69	0.64	0.59
			0.10	1.37	1.14	1.14	0.20

Table 5.1 (continued)

Fluid	*Re*	De_C	*x/L*	U_O/U_d	U_C/U_d	U_I/U_d	*K*
0.05% PAA	110	0.96	-1.00				
			-0.72	0.28	0.27	0.17	0.67
			-0.45	0.61	0.38	0.29	0.84
			-0.27	0.98	0.40	0.30	1.70
			-0.17	1.06	0.67	0.58	0.72
			0.10	1.24	1.07	1.08	0.15
0.3% PAA	5	34	-1.18	0.70	0.60	0.59	0.18
			-1.00	0.84	0.73	0.73	0.16
			-0.72	0.96	0.77	0.77	0.25
			-0.45	1.07	0.71	0.71	0.49
			-0.27	1.22	0.91	0.91	0.34
			-0.22	1.29	1.10	1.10	0.18
			-0.17				
			0.10				
0.3% PAA	15	60	-1.18	0.59	0.36	0.36	0.65
			-1.00	0.69	0.39	0.39	0.77
			-0.72	0.81	0.34	0.34	1.41
			-0.45	0.87	0.36	0.36	1.44
			-0.27	1.10	0.61	0.61	0.80
			-0.22	1.12	0.80	0.80	0.40
			-0.17	1.22	1.13	1.13	0.082
			0.10				

Table 5.2: Non-dimensionalised maximum overshoot and centreline velocities used to quantify velocity overshoots for all fluids where the overshoots are seen along the XZ-centreplane of the 4:1 contraction.

Fluid	*Re*	De_C	*x/L*	U_O/U_d	U_C/U_d	U_I/U_d	*K*
0.03% PAA	115	0.13	-0.13	0.72	0.82	0.67	0.06
0.05% PAA	30	0.13	-0.13	0.78	0.85	0.76	0.02
			0.15	1.34	1.23	1.24	0.08
0.05% PAA	65	0.24	-0.42	0.48	0.51	0.39	0.20
			-0.23	0.84	0.65	0.55	0.45
			-0.13	1.08	0.78	0.70	0.49
			0.15	1.34	1.14	1.13	0.18
0.3% PAA	2	8.4	-1.19	0.36	0.28	0.28	0.31
			-1.00	0.44	0.33	0.33	0.33
			-0.71	0.63	0.42	0.42	0.49
			-0.42	0.90	0.65	0.65	0.38
			-0.23	1.16	0.97	0.97	0.19
			-0.18	1.28	1.19	1.19	0.072
			-0.13	1.40	1.34	1.34	0.044

Table 5.3: Non-dimensionalised maximum overshoot and centreline velocities used to quantify velocity overshoots for all off centreplane locations where the overshoots are seen in 0.05% PAA solution flowing through the 8:1 contraction.

x/L	*y/w*	*z/w*	U_O/U_d	U_C/U_d	U_L/U_d	*K*
-0.72	0		0.28	0.27	0.17	0.41
-0.72	0.125		0.23	0.25	0.15	0.32
-0.72	0.25		0.13	0.18	0.10	0.17
-0.45	0		0.61	0.38	0.28	0.87
-0.45	0.125		0.54	0.30	0.20	1.13
-0.27	0		0.98	0.40	0.30	1.70
-0.17	0		1.06	0.67	0.58	0.72
-0.17		0.125	0.68	0.66	0.65	0.05
-0.17		0.25	0.74	0.64	0.64	0.16
-0.17		0.375	0.78	0.58	0.58	0.34
0.10	0		1.24	1.07	1.08	0.15
0.10		0	1.09	1.07	1.07	0.02
0.10		0.125	1.09	1.08	1.08	0.01
0.10		0.25	1.12	1.09	1.09	0.03

5.7. Figures

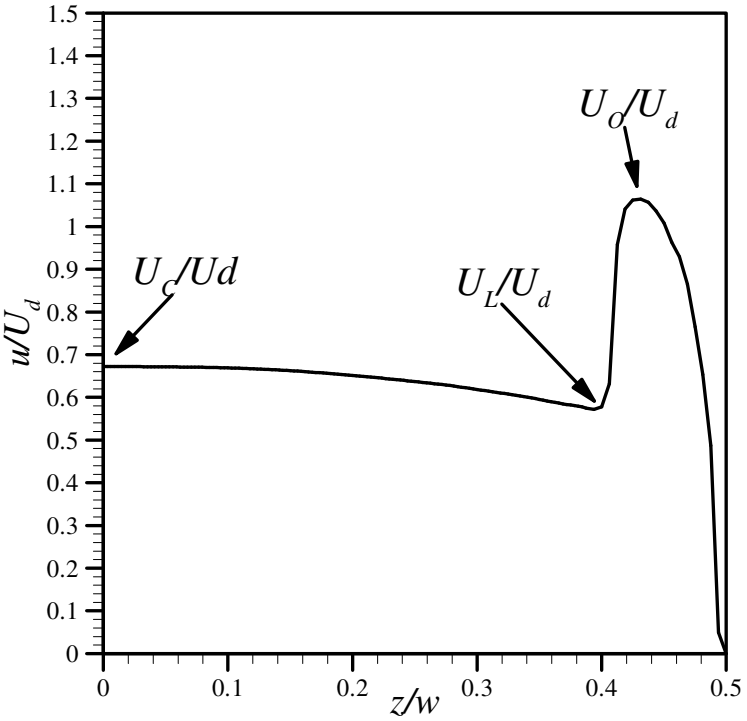

Figure 5.1: Diagrams indicating U_C/U_d, U_L/U_d and U_O/U_d, which are used to quantify the velocity overshoots.

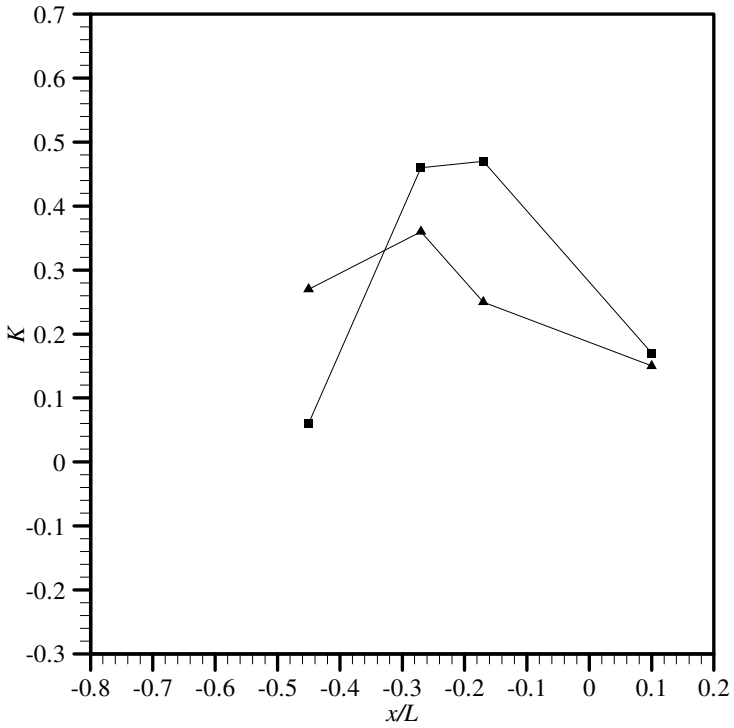

Figure 5.2: K values for flows of 0.03% PAA at $Re \approx 140$, $De_C \approx 0.24$ (■) and $Re \approx 390$, $De_C \approx 0.53$ (▲).

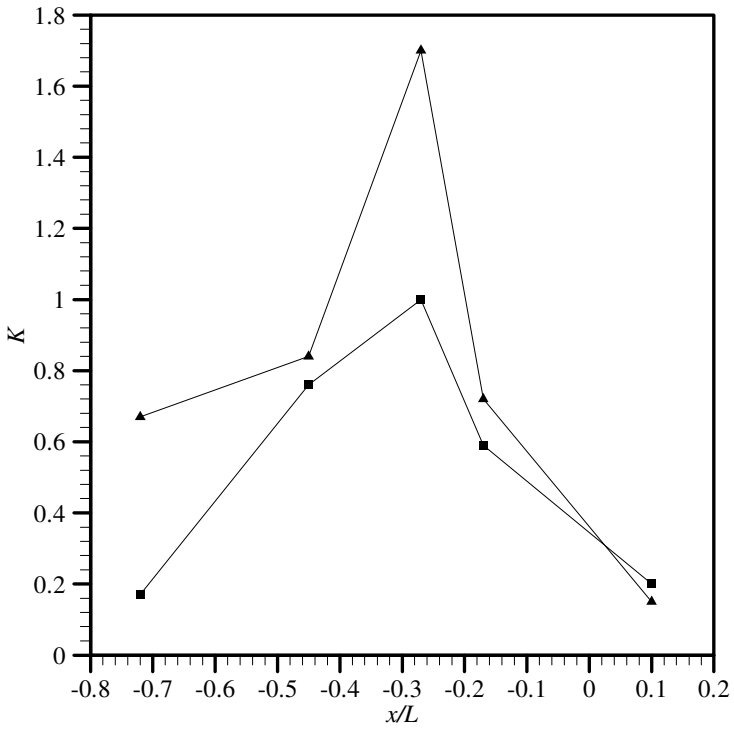

Figure 5.3: K values for flows of 0.05% PAA at $Re \approx 50$, $De_C \approx 0.52$ (■) and $Re \approx 110$, $De_C \approx 0.96$ (▲).

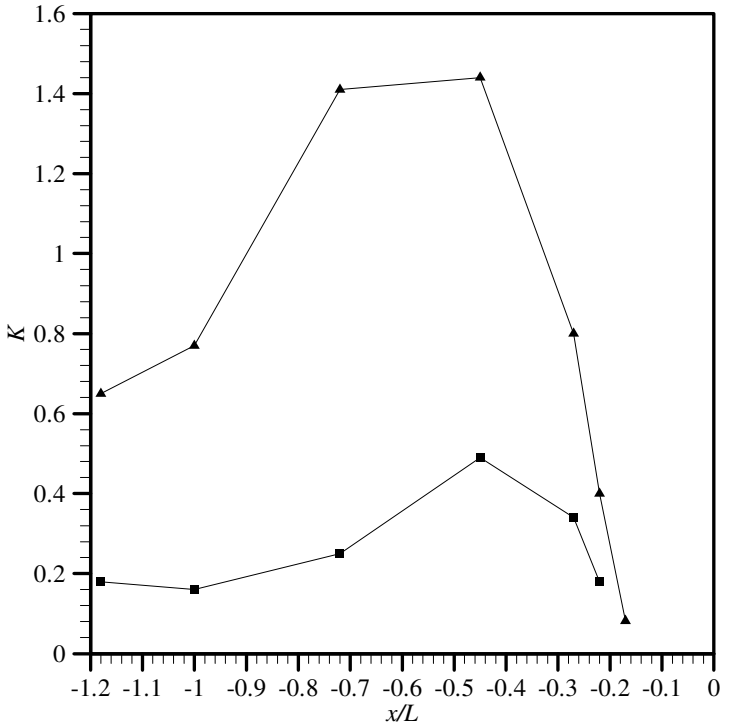

Figure 5.4: K values for flows of 0.3% PAA at $Re \approx 5$, $De_C \approx 34$ (■) and $Re \approx 15$, $De_C \approx 60$ (▲).

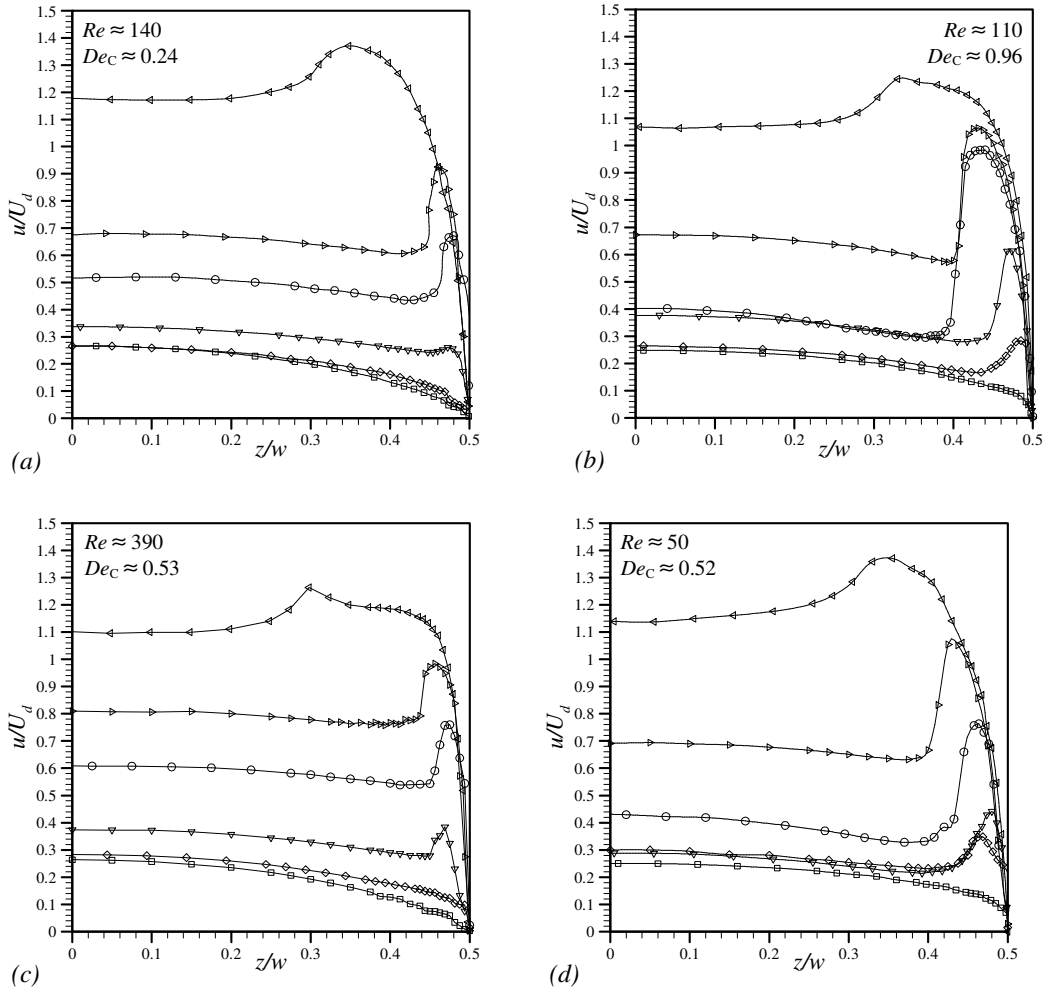

Figure 5.5: Normalised velocity profiles along the XZ-centreplane for (a) 0.03% polyacrylamide at Re ≈ 140, $De_C \approx 0.24$, (b) 0.05% polyacrylamide at Re ≈ 110, $De_C \approx 0.96$, (c) 0.03% polyacrylamide at Re ≈ 390, $De_C \approx 0.53$ and (d) 0.05% polyacrylamide at Re ≈ 50, $De_C \approx 0.52$ (In the 8:1 contraction □ represents x/L=-1, ◊ x/L=-0.72, ▽ x/L=-0.45, ○ x/L=-0.27, ▷ x/L=-0.17 and ◁ x/L=0.10. These symbols are valid for all figures for the 8:1 contraction unless stated).

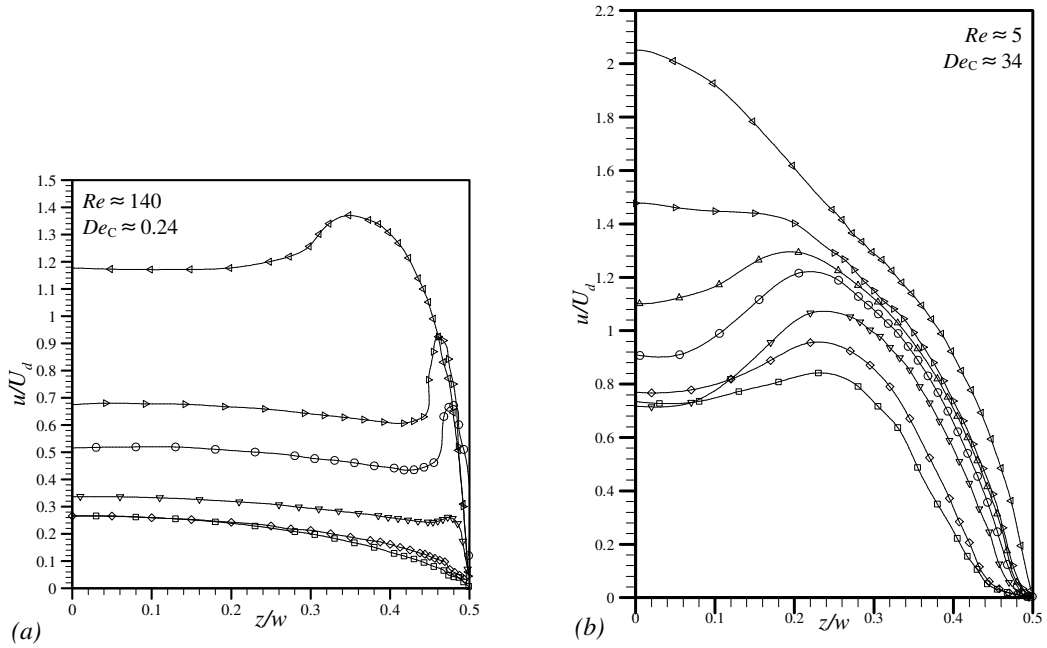

Figure 5.6: Normalised velocity profiles along the XZ-centreplane for (a) 0.03% polyacrylamide at Re ≈ 140, $De_C \approx 0.24$, $De_{N1} \approx 5.2$ and (b) 0.3% polyacrylamide at Re ≈ 5, $De_C \approx 34$, $De_{N1} \approx 5.3$.

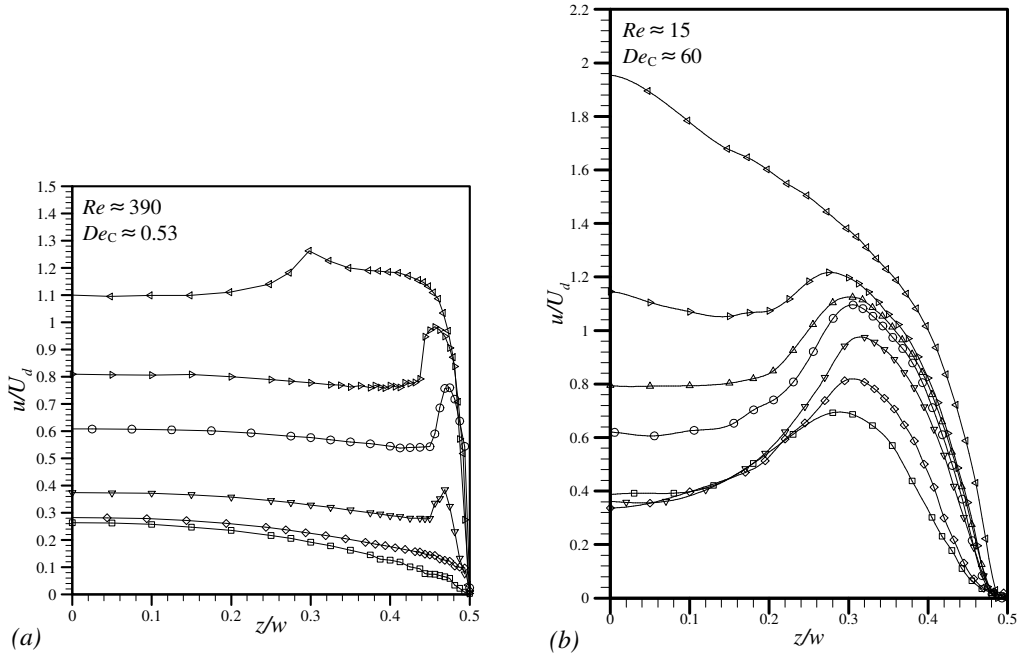

Figure 5.7: Normalised velocity profiles along the XZ-centreplane for (a) 0.03% polyacrylamide at Re ≈ 390, $De_C \approx 0.53$, $De_{N1} \approx 6.2$ and (b) 0.3% polyacrylamide at Re ≈ 15, $De_C \approx 60$, $De_{N1} \approx 6.2$.

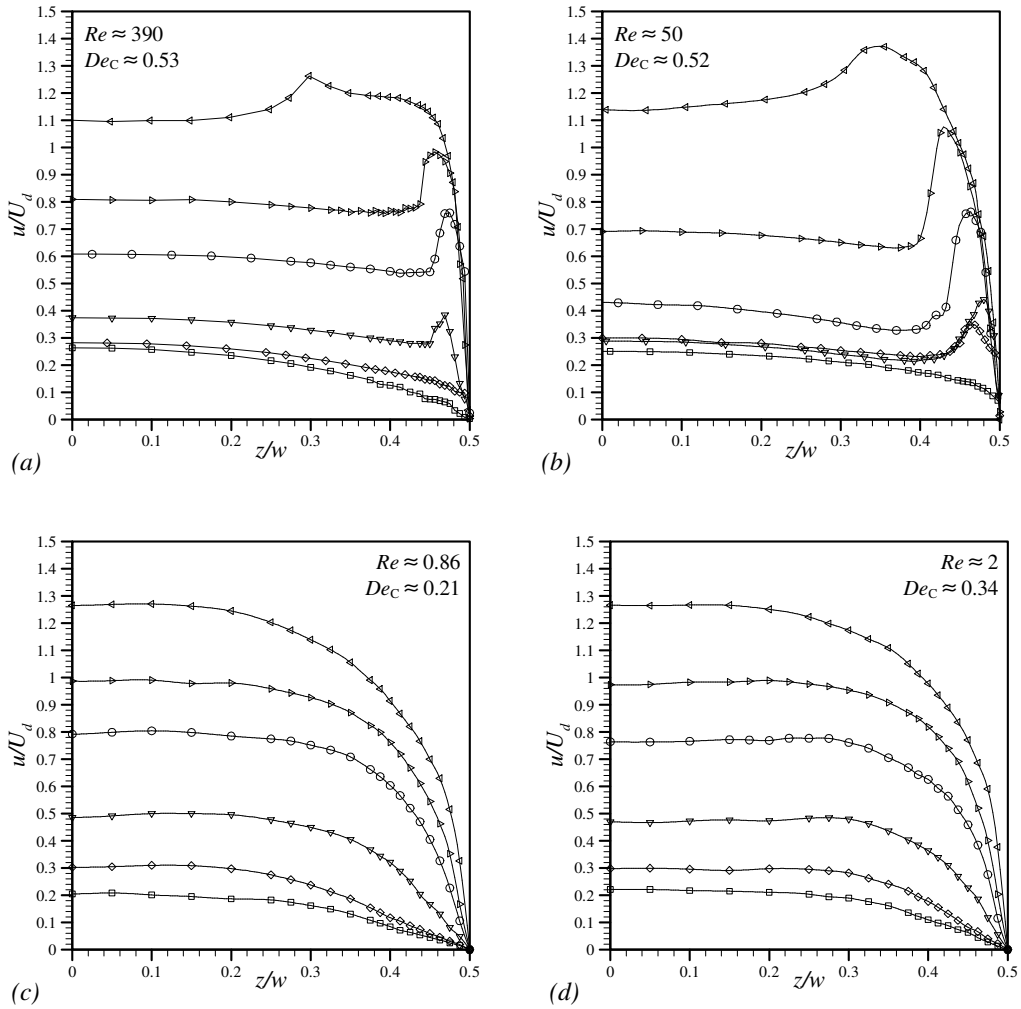

Figure 5.8: Normalised velocity profiles along the XZ-centreplane for (a) 0.03% polyacrylamide at Re ≈ 390, $De_C \approx 0.53$ and (b) 0.05% polyacrylamide at Re ≈ 50, $De_C \approx 0.52$, (c) 0.5% xanthan gum at Re ≈ 0.86, $De_C \approx 0.21$ and (d) 0.5% xanthan gum at Re ≈ 2, $De_C \approx 0.34$.

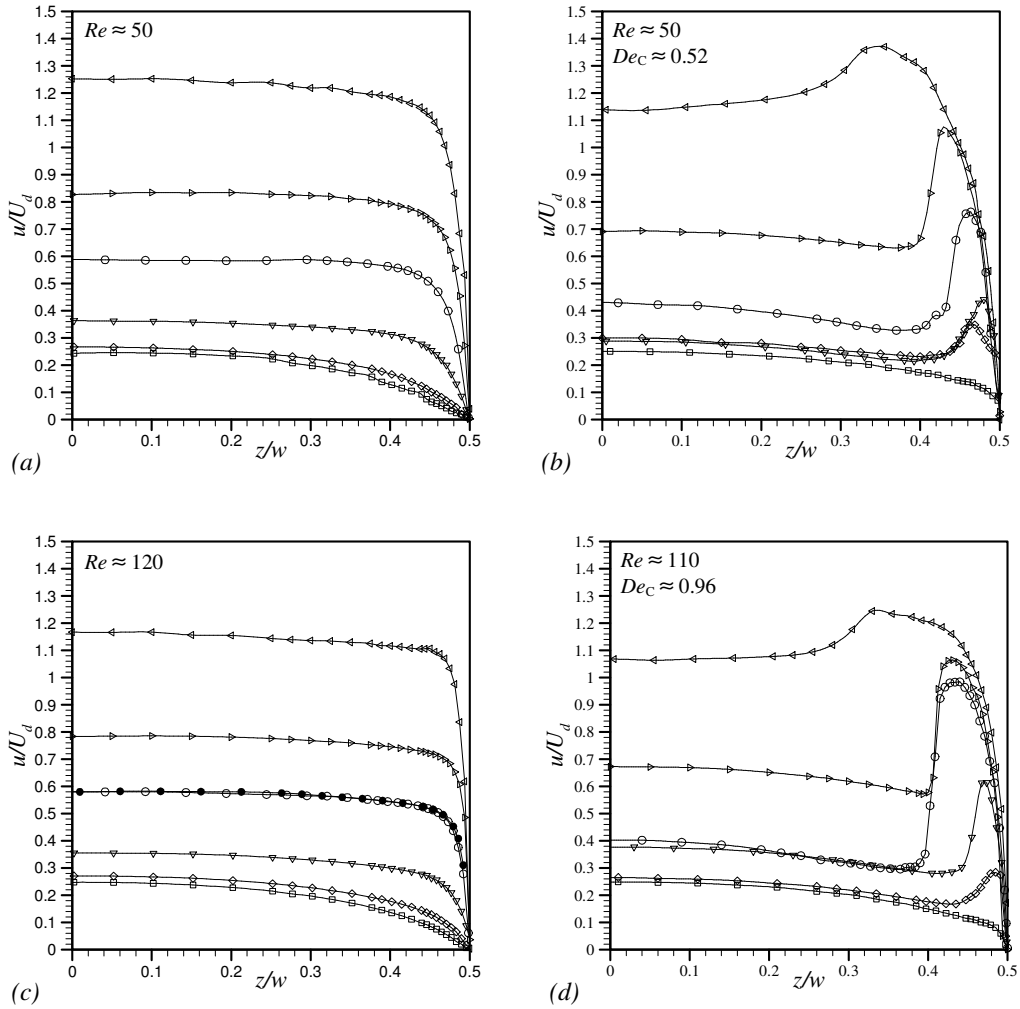

Figure 5.9: Normalised velocity profiles along the XZ-centreplane for (a) 0.07% xanthan gum at Re ≈ 50, (b) 0.05% polyacrylamide at Re ≈ 50, $De_C \approx 0.52$, (c) 0.07% xanthan gum at Re ≈ 120 (filled symbols represent reflected values) and (d) 0.05% polyacrylamide at Re ≈ 110, $De_C \approx 0.96$.

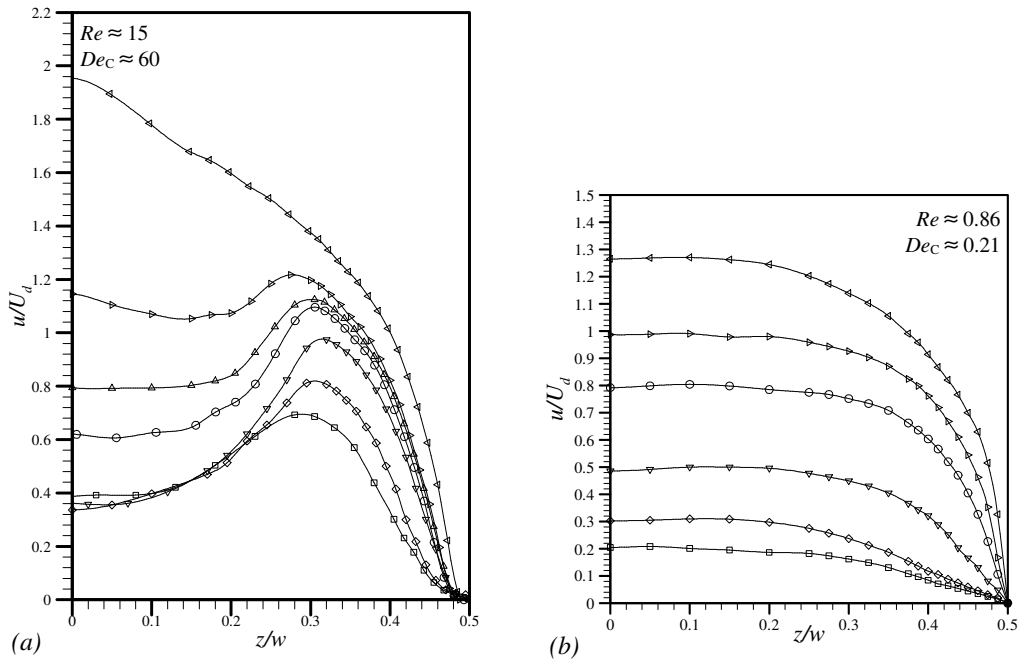

Figure 5.10: Normalised velocity profiles along the XZ-centreplane for (a) 0.3% polyacrylamide at Re ≈ 15, $De_C \approx 60$ and (b) 0.5% xanthan gum at Re ≈ 0.86, $De_C \approx 0.21$.

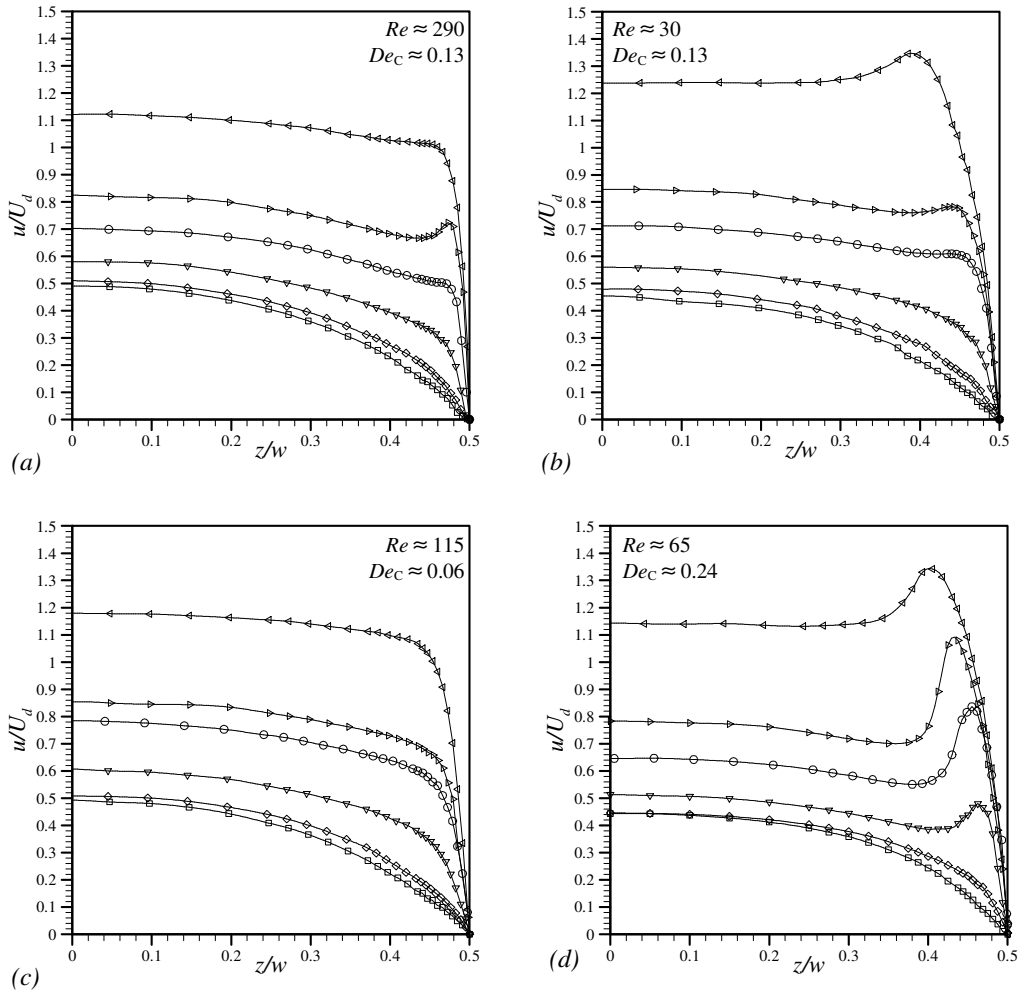

Figure 5.11: Normalised velocity profiles along the XZ-centreplane for (a) 0.03% polyacrylamide at $Re \approx 290$, $De_C \approx 0.13$, (b) 0.05% polyacrylamide at $Re \approx 30$, $De_C \approx 0.13$, (c) 0.03% polyacrylamide at $Re \approx 115$, $De_C \approx 0.06$ and (d) 0.05% polyacrylamide at $Re \approx 65$, $De_C \approx 0.24$ (In the 4:1 contraction □ represents x/L=-1, ◊ x/L=-0.71, ▽ x/L=-0.42, ○ x/L=-0.23, ▷ x/L=-0.13 and ◁ x/L=0.15. These symbols are valid for all figures for the 4:1 contraction unless stated).

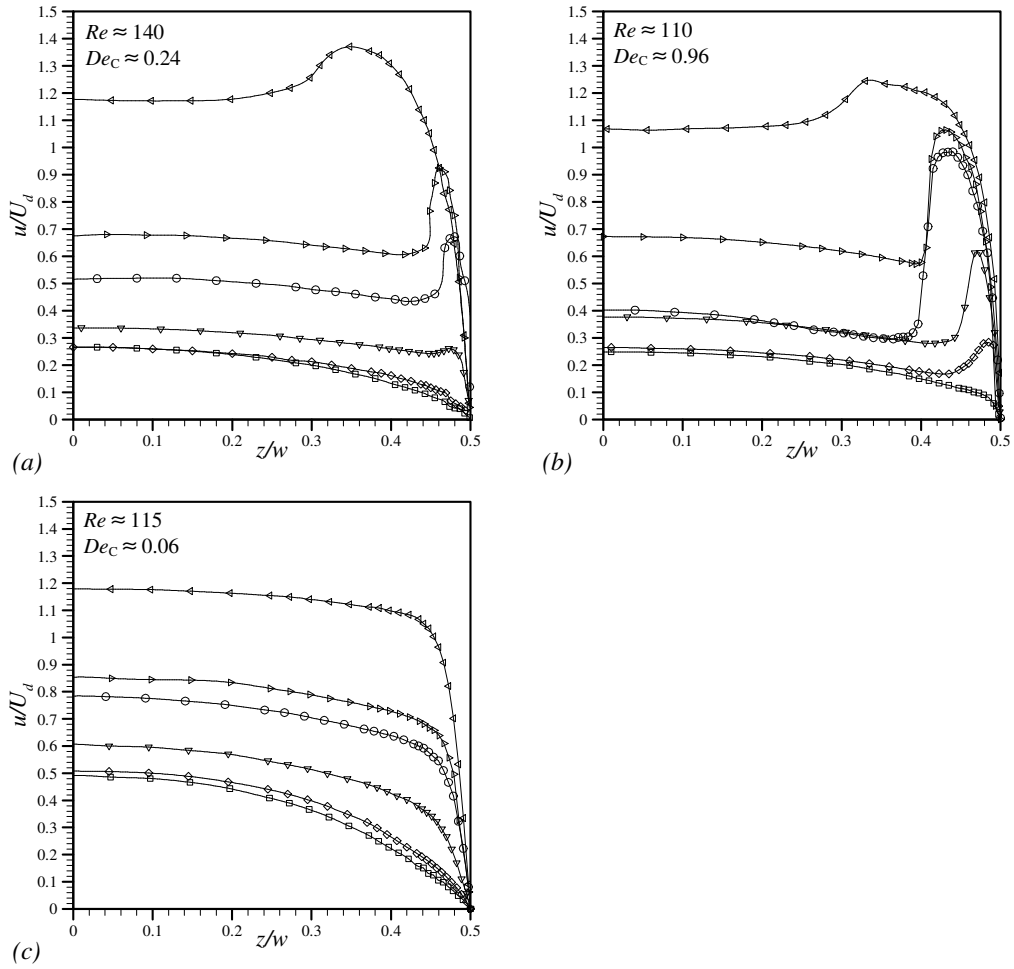

Figure 5.12: Velocity profiles along the XZ-centreplane for (a) 0.03% polyacrylamide at $Re \approx 140$, $De_C \approx 0.24$ in the 8:1 contraction, (b) 0.05% polyacrylamide at $Re \approx 110$, $De_C \approx 0.96$ in the 8:1 contraction and (c) 0.03% polyacrylamide at $Re \approx 115$, $De_C \approx 0.06$ in the 4:1 contraction, the key shown in (b) is valid for (a).

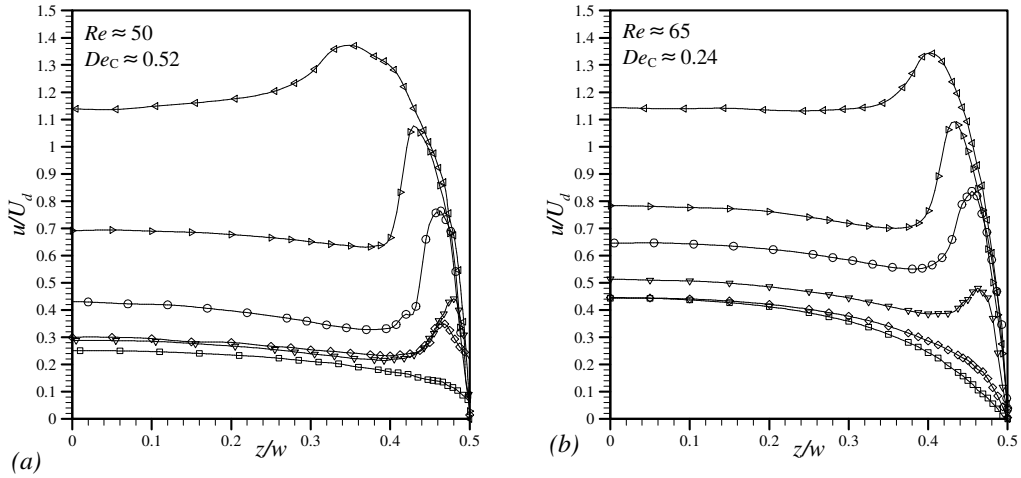

Figure 5.13: Velocity profiles along the XZ-centreplane for (a) 0.05% polyacrylamide at $Re \approx 50$, $De_C \approx 0.52$ in the 8:1 contraction and (b) 0.05% polyacrylamide at $Re \approx 65$, $De_C \approx 0.24$ in the 4:1 contraction, the keys shown in Figure 5.10 are valid for the relevant contraction.

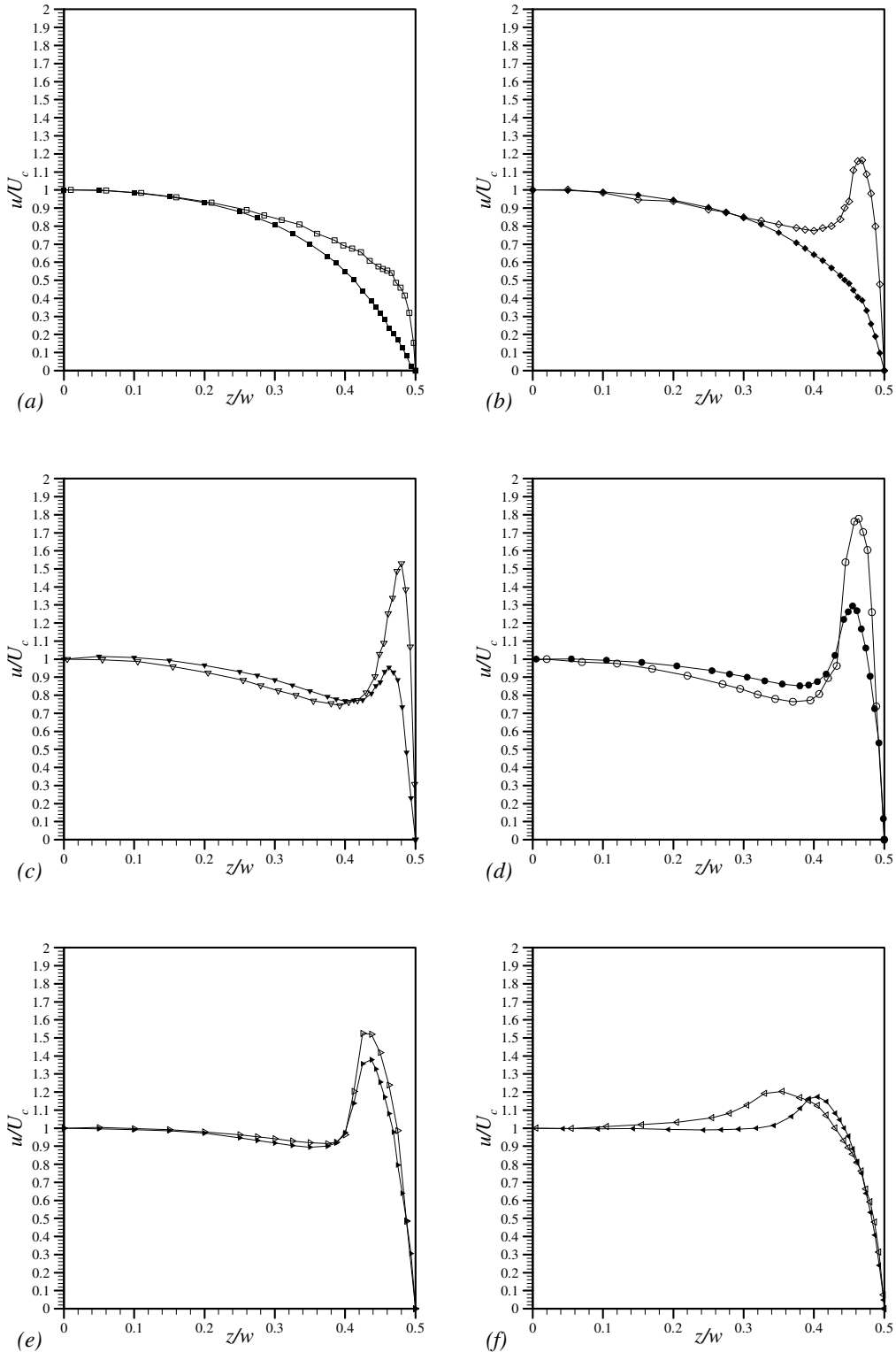

Figure 5.14: Velocity profiles along the XZ-centreplane for 0.05% polyacrylamide at $Re \approx 50$, $De_C \approx 0.52$ in the 8:1 contraction (open symbols) and 0.05% polyacrylamide at $Re \approx 65$, $De_C \approx 0.24$ in the 4:1 contraction (filled symbols) at (a) *x/L*-1, (b) *x/L*= -0.72 and -0.71, (c) *x/L*=-0.45 and -0.42, (d) *x/L*=-0.27 and -0.23, (e) *x/L*=-0.17 and -0.13 and (f) *x/L*=0.10 and 0.15.

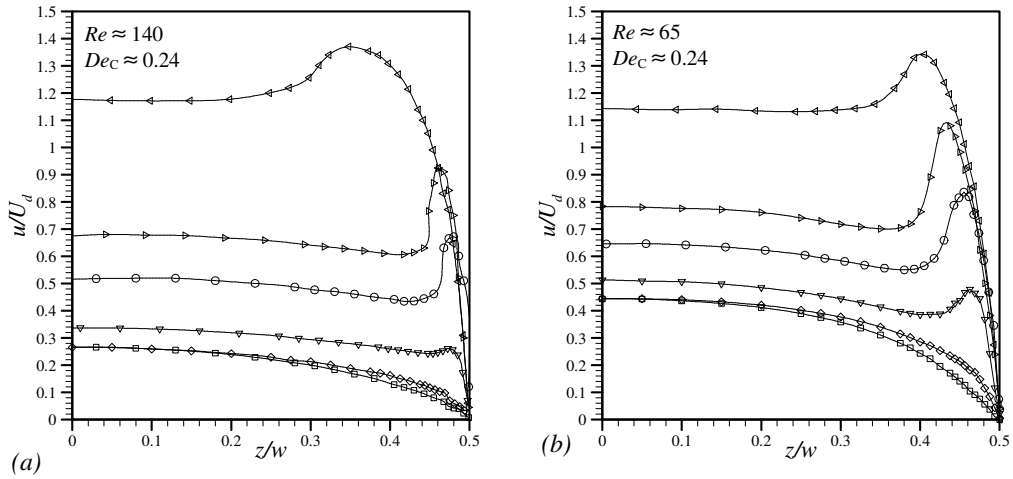

Figure 5.15: Velocity profiles along the XZ-centreplane for (a) 0.03% polyacrylamide at $Re \approx 140$, $De_C \approx 0.24$ in the 8:1 contraction and (b) 0.05% polyacrylamide at $Re \approx 65$, $De_C \approx 0.24$ in the 4:1 contraction, the keys shown in Figure 5.10 are valid for the relevant contraction.

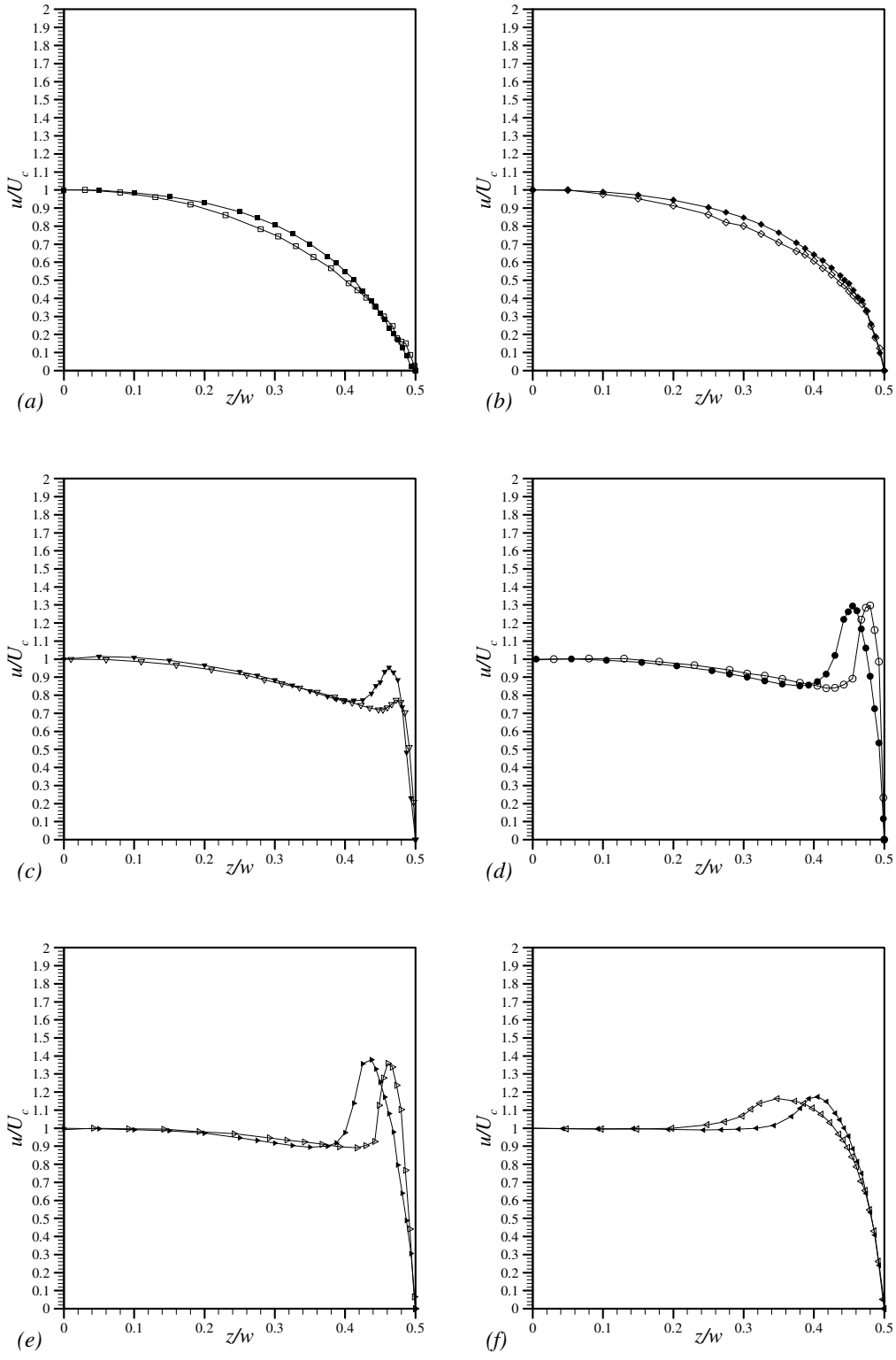

Figure 5.16: Velocity profiles along the XZ-centreplane for 0.03% polyacrylamide at $Re \approx 140$, $De_C \approx 0.24$ in the 8:1 contraction (open symbols) and 0.05% polyacrylamide at $Re \approx 65$, $De_C \approx 0.24$ in the 4:1 contraction (filled symbols) at (a) *x/L*-1, (b) *x/L*= -0.72 and -0.71, (c) *x/L*=-0.45 and -0.42, (d) *x/L*=-0.27 and -0.23, (e) *x/L*=-0.17 and -0.13 and (f) *x/L*=0.10 and 0.15.

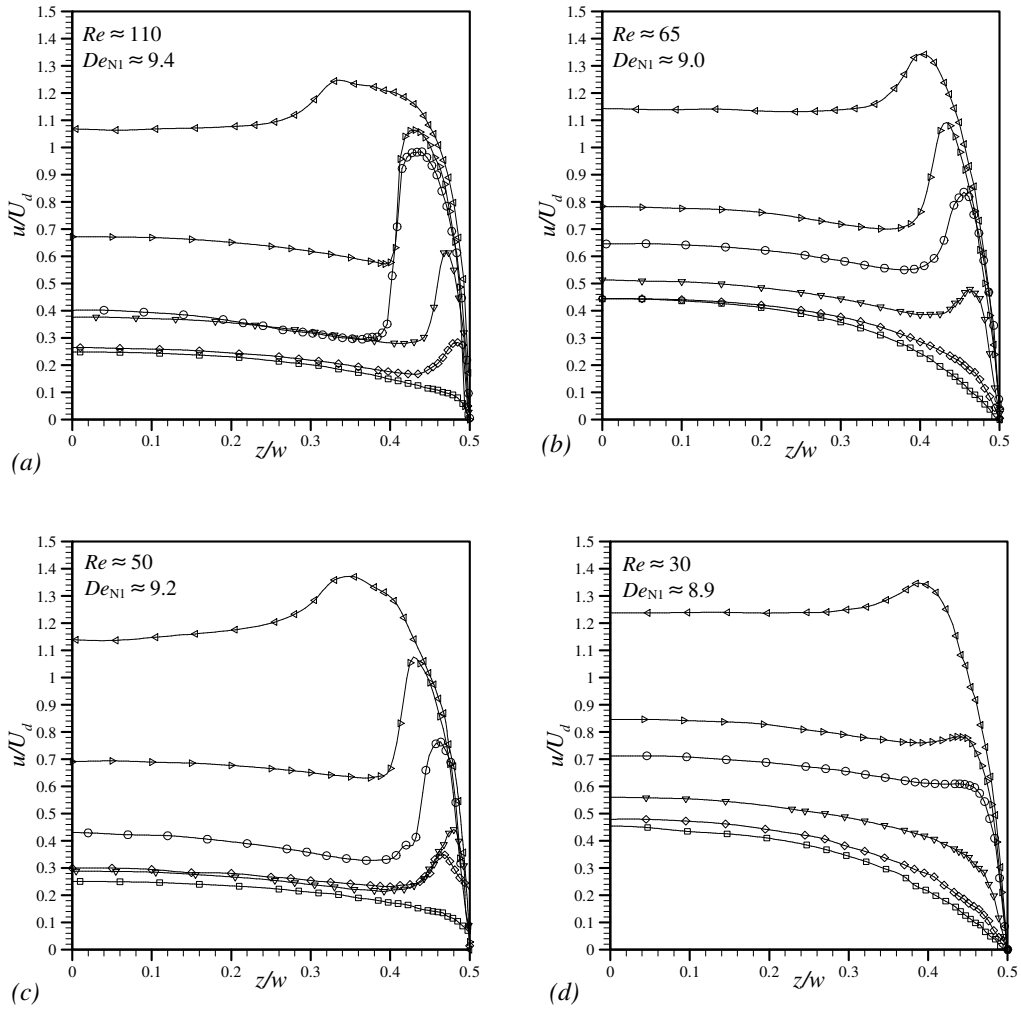

Figure 5.17: Velocity profiles along the XZ-centreplane for (a) 0.05% polyacrylamide at $Re \approx 110$, $De_{N1} \approx 9.4$ in the 8:1 contraction (b) 0.05% polyacrylamide at $Re \approx 65$, $De_{N1} \approx 9.0$ in the 4:1 contraction (c) 0.05% polyacrylamide at $Re \approx 50$, $De_{N1} \approx 9.2$ in the 8:1 contraction and (d) 0.05% polyacrylamide at $Re \approx 30$, $De_{N1} \approx 8.9$ in the 4:1 contraction, the keys shown in Figure 5.10 are valid for the relevant contraction.

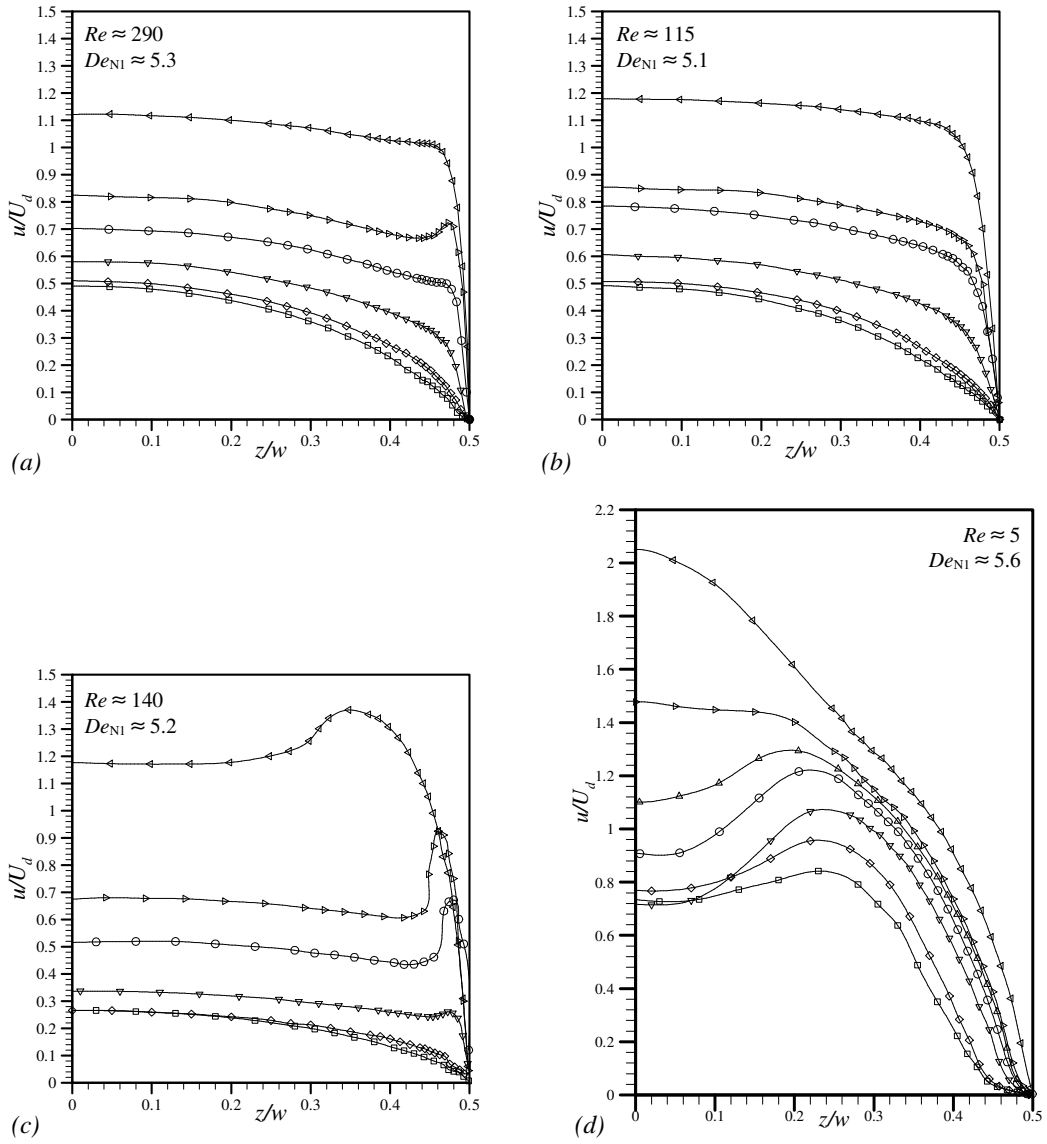

Figure 5.18: Velocity profiles along the XZ-centreplane for (a) 0.03% polyacrylamide at $Re \approx 290$, $De_{N1} \approx 5.3$ in the 4:1 contraction (b) 0.03% polyacrylamide at $Re \approx 115$, $De_{N1} \approx 5.1$ in the 4:1 contraction (c) 0.03% polyacrylamide at $Re \approx 140$, $De_{N1} \approx 5.2$ in the 8:1 contraction and (d) 0.3% polyacrylamide at $Re \approx 5$, $De_{N1} \approx 5.6$ in the 8:1 contraction, the keys shown in Figure 5.10 and 5.14 are valid for the relevant contraction.

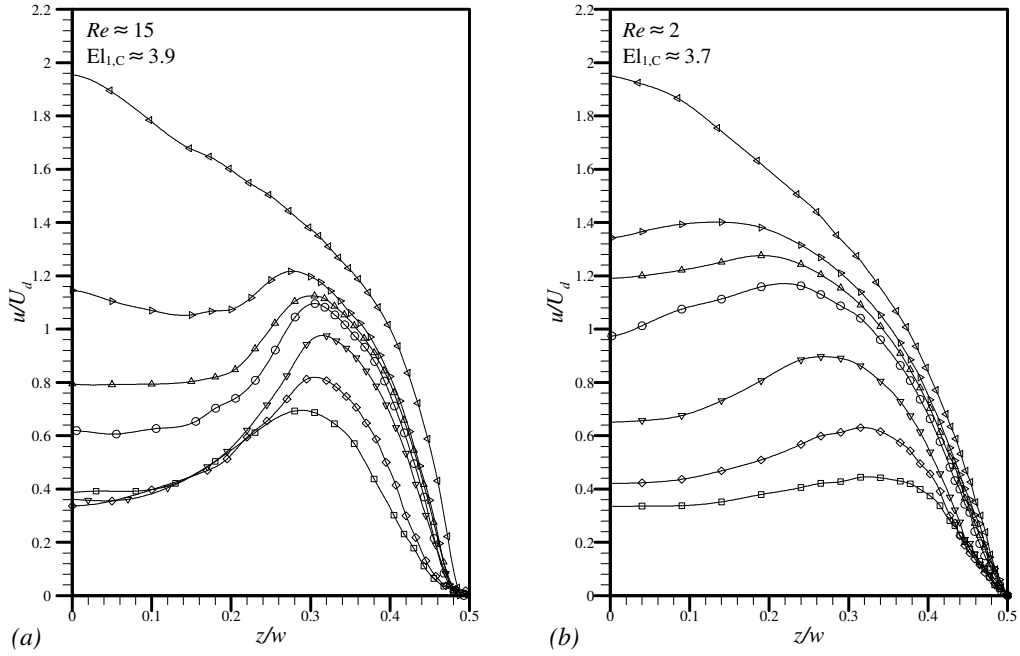

Figure 5.19: Velocity profiles along the XZ-centreplane for (a) 0.3% polyacrylamide at $Re \approx 15$, $El_{1,C} \approx 3.9$ in the 8:1 contraction and (b) 0.3% polyacrylamide at $Re \approx 2$, $El_{1,C} \approx 3.7$ in the 4:1 contraction.

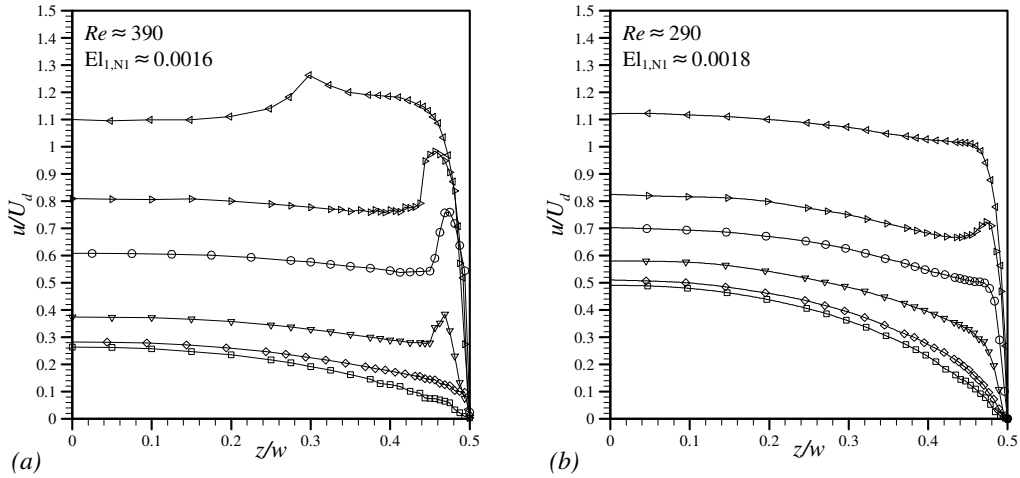

Figure 5.20: Velocity profiles along the XZ-centreplane for (a) 0.03% polyacrylamide at $Re \approx 390$, $El_{1,N1} \approx 0.0016$ in the 8:1 contraction and (b) 0.03% polyacrylamide at $Re \approx 290$, $El_{1,N1} \approx 0.0018$ in the 4:1 contraction, the keys shown in Figure 5.10 are valid for the relevant contraction.

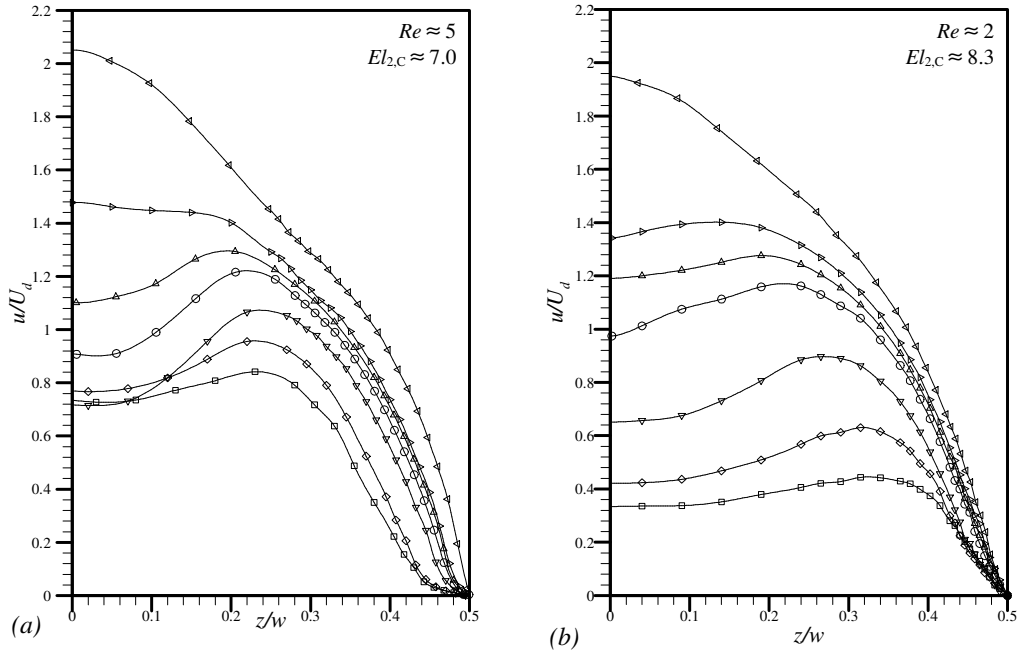

Figure 5.21: Velocity profiles along the XZ-centreplane for (a) 0.3% polyacrylamide at $Re \approx 5$, $El_{2,C} \approx 7.0$ in the 8:1 contraction and (b) 0.3% polyacrylamide at $Re \approx 2$, $El_{2,C} \approx 8.3$ in the 4:1 contraction, the keys shown in Figure 5.14 are valid for the relevant contraction.

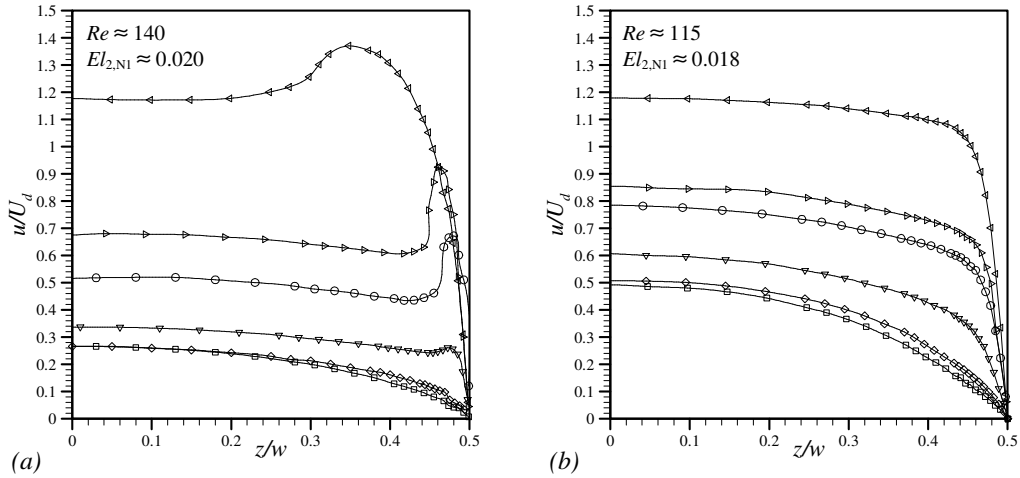

Figure 5.22: Velocity profiles along the XZ-centreplane for (a) 0.03% polyacrylamide at $Re \approx 140$, $El_{2,N1} \approx 0.020$ in the 8:1 contraction and (b) 0.03% polyacrylamide at $Re \approx 115$, $El_{2,N1} \approx 0.018$ in the 4:1 contraction, the keys shown in Figure 5.10 are valid for the relevant contraction.

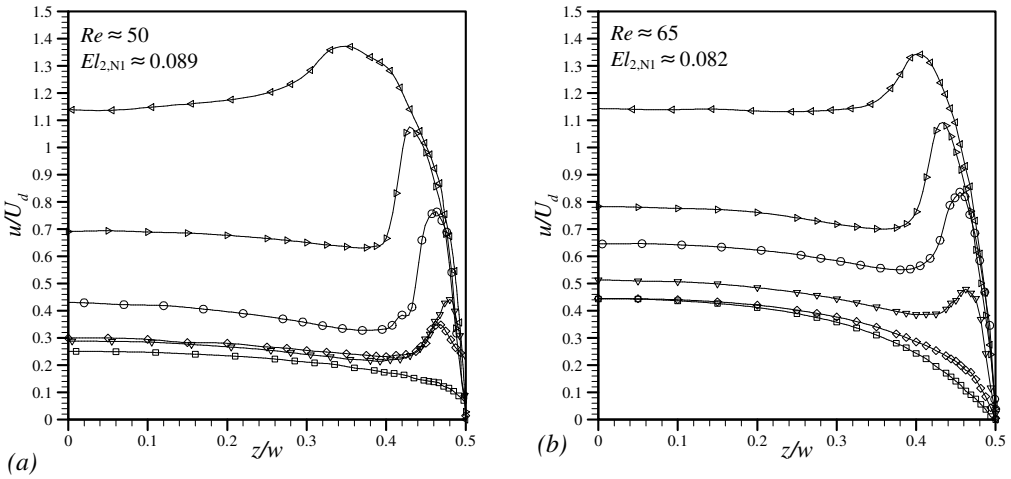

Figure 5.23: Velocity profiles along the XZ-centreplane for (a) 0.05% polyacrylamide at $Re \approx 50$, $El_{2,N1} \approx 0.089$ in the 8:1 contraction and (b) 0.05% polyacrylamide at $Re \approx 65$, $El_{2,N1} \approx 0.082$ in the 4:1 contraction, the keys shown in Figure 5.10 are valid for the relevant contraction.

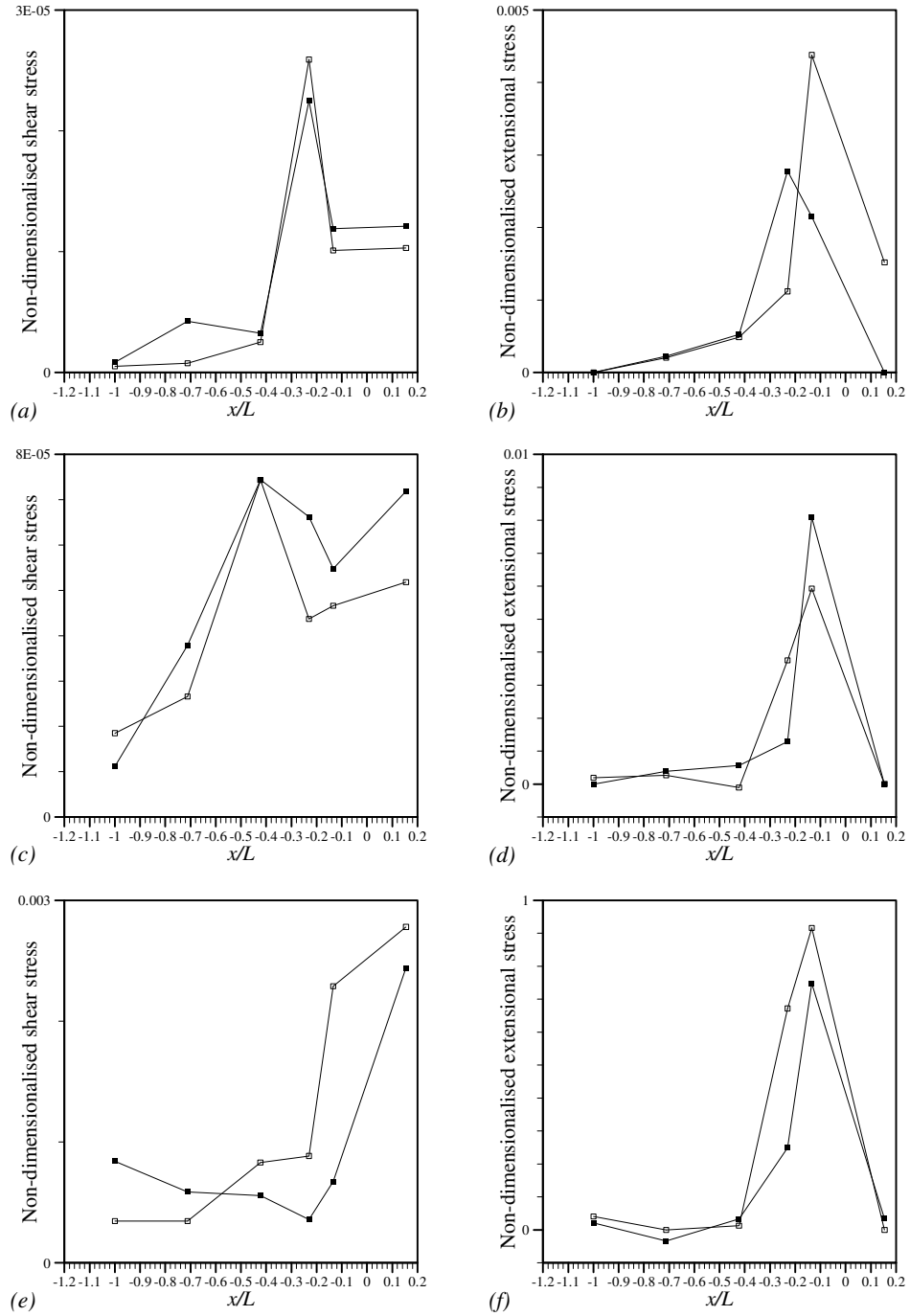

Figure 5.24: Non-dimensionalised (a) shear and (b) extensional stresses for 0.03% PAA in the 8:1 contraction at $Re \approx 140$, $De_C \approx 0.24$ (□) and $Re \approx 390$, $De_C \approx 0.53$ (■); (c) shear and (d) extensional stresses for 0.05% PAA in the 8:1 contraction at $Re \approx 50$, $De_C \approx 0.52$ (□) and $Re \approx 110$, $De_C \approx 0.96$ (■); (e) shear and (f) extensional stresses for 0.3% PAA in the 8:1 contraction at $Re \approx 5$, $De_C \approx 34$ (□) and $Re \approx 15$, $De_C \approx 60$ (■).

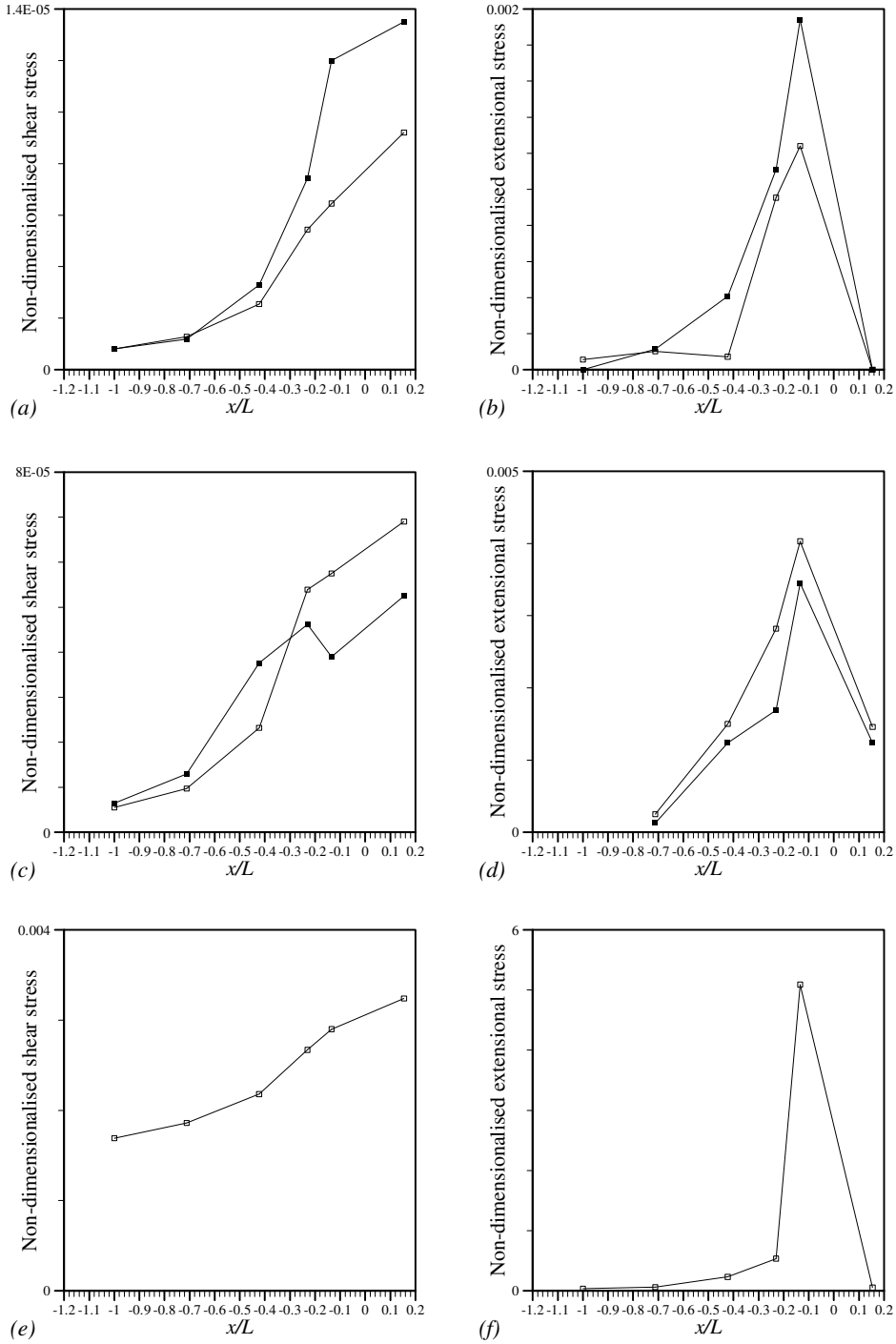

Figure 5.25: Non-dimensionalised (a) shear and (b) extensional stresses for 0.03% PAA in the 4:1 contraction at $Re \approx 115$, $De_C \approx 0.06$ (□) and $Re \approx 290$, $De_C \approx 0.13$ (■); (c) shear and (d) extensional stresses for 0.05% PAA in the 4:1 contraction at $Re \approx 30$, $De_C \approx 0.13$ (□) and $Re \approx 65$, $De_C \approx 0.24$ (■); (e) shear and (f) extensional stresses for 0.3% PAA in the 4:1 contraction at $Re \approx 2$, $De_C \approx 8.4$.

6. Conclusions and Recommendations

One of the main objectives of this research was to determine whether the velocity overshoots first observed by Poole *et al.* (2005) could be reproduced when a sudden expansion did not follow the gradual contraction. The results presented in Chapter 4 clearly show that 'cat's ears' are reproducible in a gradual contraction (both 8:1 and 4:1 contraction ratios) when a sudden expansion is not present. Another objective was to provide a set of 'benchmark' experimental results for researchers interested in numerical modelling of non-Newtonian contraction flow to use to compare their results to and to test the accuracy of the constitutive equations and their codes. A wide variety of high quality velocity data of quantified accuracy has been presented for two contraction ratios, two types of polymer and several concentrations of each polymer. All of the fluids have been carefully characterised in terms of both shear and, more importantly, extensional behaviour. In addition great care was taken to ensure that the results were free from polymer degradation effects.

6.1. Contraction ratio effects

Two contraction ratios were investigated during this work: 8:1 and 4:1. The results show that the velocity overshoots are more likely to occur in the 8:1 contraction and in this contraction the overshoots will be larger than those seen in the 4:1 contraction. This is most likely due to the difference in the strain exerted on the flow through the two contractions. The Hencky strain (discussed in Chapter 3) is larger for the 8:1 contraction than the 4:1 contraction meaning that the flow through the 4:1 contraction undergoes a less severe extension than the flow through the 8:1 contraction. This fact implies that the extensional properties of the contraction, i.e. the shape and the ratio, are important in the development of the velocity overshoots. However when the velocity data is renormalized by the local centreline velocity in an attempt to eliminate the effect of contraction ratio a fairly good collapse of the data is observed, particularly when the flows have comparable Deborah numbers.

6.2. Effect of polymer type and concentration

The polymers under investigation throughout this thesis were polyacrylamide (classed as flexible) and xanthan gum (classed as semi-rigid). Velocity overshoots were observed in polyacrylamide solutions at concentrations above the critical overlap concentration whereas the same was not true of xanthan gum. The reason for the overshoots occurring in the PAA solutions and not the XG solutions is probably due to the way the polymers behave under extension. The PAA will stretch more readily than the XG because it is more flexible. This difference in behaviour is seen most strikingly in the results of the CaBER tests. We know that the extensional properties of the contraction are important to the occurrence of 'cat's ears' but it is also clear that the behaviour of the polymer solution under extension also plays a role.

Polyacrylamide was tested at four concentrations: 0.01%, 0.03%, 0.05% and 0.3%. Velocity overshoots were not observed in the 0.01% PAA solution. These flows were at high Reynolds numbers but extremely low Deborah numbers. Velocity overshoots were seen to differing degrees in 0.03%, 0.05% and 0.3% PAA. Those seen in the 0.3% solution were very different to those on 0.03% and 0.05% PAA solutions. At the lower concentrations the effect is confined close to the sidewalls and the central section of the flow seems to be largely unaffected. At the higher concentration the entire flow is affected and the overshoots are a different shape to those seen in the 0.03% and 0.05% PAA solutions. In this case the overshoots are further away from the sidewalls and grow into one large central overshoot at the end of the contraction. The shape of the overshoots observed in the 0.3% PAA solution may be due to the concentration of the polymer and the greater effects of shear thinning or it could also be the lower Reynolds and higher Deborah numbers than those at the lower concentrations. Further tests with a high-viscosity Boger fluid may help unravel which effects are responsible for the occurrence of the velocity overshoots.

Xanthan gum was tested at two concentrations, 0.07% and 0.5%. The lower concentration was seen to flatten as the flow progressed through the gradual contraction, similar to the Newtonian fluid and the 0.01% PAA solution. In the

higher concentration xanthan gum solution very small 'bumps' were observed, which may have been the start of velocity overshoots. Testing this (or a higher) concentration of xanthan gum solution over a wider range of flow conditions may provide an insight into how the overshoots develop.

6.3. Reynolds, Deborah and Elasticity numbers

It has not been possible to determine whether the Reynolds number alone has an effect on the occurrence of 'cat's ears', although in the absence of elastic effects (i.e. when De=0 and the flow is Newtonian) the overshoots are never observed. In both contractions 0.03% and 0.05% PAA were each measured at two Reynolds numbers – giving a total of eight Reynolds numbers. No conclusions can be drawn solely from looking at the variations in Reynolds numbers for these two concentrations of PAA. At the higher concentration (0.3%) the Reynolds numbers are much lower and a different shape of overshoot is seen. In these cases, however, the Deborah numbers from CaBER are much larger so this effect cannot be attributed only to the effects of inertia.

As the flow is predominantly an extensional flow the Deborah, Weissenberg and Elasticity numbers found using the extensional properties of the fluid, i.e. CaBER data, are more realistic values by which to judge the fluid behaviour. In the lower concentrations of PAA the velocity overshoots increase in size as the Deborah number determined from the CaBER data increases. In both contractions there are two flows that have comparable Deborah numbers but the flows are visibly different to each other. This is because the flows have different Reynolds numbers and the solutions are different concentrations. This makes providing a definitive 'reason' for the 'cat's ears' occurrence incredibly difficult. It seems that the Deborah number and the extensional fluid properties play more of a role but the extent to which the flow rate or the concentration of the polymer affects the overshoot cannot, at this time, be determined. This effect of the extensional properties is highlighted in Figures 5.14 and 5.16 where an attempt has been made to eliminate the effects of the contraction. The flows with comparable De (Figure 5.16) are very similar for different Reynolds numbers whereas the flows with comparable Re (Figure 5.14) are different to each other and the flow with the higher Deborah number produces much larger velocity

overshoots, which might be expected given that when *De*=0 (i.e. Newtonian flow) no overshoots are observed.

In the polyacrylamide solutions the Elasticity number seems to be responsible for the location at which the velocity overshoots develop. The higher the Elasticity number the earlier the overshoots are seen to develop. At the highest *El* (i.e. in the 0.3% PAA solutions) the overshoots develop even before the start of the contraction.

6.4. Off-centre velocity profiles

The velocity profiles measured away from the two centreplanes in the 0.05% PAA solution (Figures 4.30-4.36) show that it is important to measure a broader range of locations than just the XY- and XZ-centreplanes. The transverse velocity profiles measured towards the end of the contraction show velocity overshoots that were not apparent on the XY-centreplane. Ideally detailed 3D flow visualisation (such as Particle Image Velocimetry) would be performed to provide a better insight into the flow.

6.5. Recommendations

In order to understand the 'cat's ears' phenomenon completely more research must be completed in this area.

- Pressure-drop measurements made across the gradual contraction would determine whether an 'enhanced' pressure drop occurs as it does across a sudden contraction and whether the 'cat's ears' effect has any effect on the pressure drop (increasing or decreasing it for example) across the contraction.
- Investigation of variations in contraction ratio, shape and length in an attempt to vary the total strain and the strain rate exerted on the flow would determine how important the contraction properties are in the development of the velocity overshoots.
- Measuring the flow of a Boger fluid, which is elastic but has constant viscosity (Boger (1977)), would eliminate the effects of shear thinning (if any).

- Examining different polymer solutions such as carboxymethylcellulose (CMC, semi-rigid) and polyethylene oxide (PEO, flexible) would confirm whether the conclusion drawn above that the polymer type affects the occurrence of 'cat's ears' is correct.
- Studying a wider range of concentrations of PAA and observing differences in the overshoot shapes would determine whether there is a 'critical' concentration at which the overshoots shape changes between those seen in the 0.03% and 0.05% PAA solutions and those seen in the 0.3% PAA solution. This difference in shape may be due to the lower Reynolds numbers and the higher Deborah numbers. The Reynolds and Deborah numbers investigated here were constrained by the test rig design. Different pumps may be able to reach higher or lower flow rates to adjust *Re* and *De* accordingly.
- Performing particle image velocimetry (PIV) measurements would enable visualisation of the entire flow rather than discrete profiles within the flow. At present profiles have only been measured along the XY- and XZ-centreplanes and we have no idea what is happening in the corners of the contraction or on the other planes in most cases, for example.

References

Afonso, A. and Pinho, F.T., 2006, Numerical investigation of the velocity overshoots in the flow of viscoelastic fluids inside a smooth contraction, Journal of Non-Newtonian Fluid Mechanics, vol. 139, pp. 1-20.

Al-Hadithi, T.S.R., Barnes, H.A. and Walters, K., 1992, The relationship between the linear (oscillatory) and nonlinear (steady-state) flow properties of polymer and colloidal systems, Colloid & Polymer Science, vol.270, pp. 40-46.

Alves, M.A., and Poole, R.J., 2007, Divergent flow in contractions, Journal of Non-Newtonian Fluid Mechanics, vol. 144, pp. 139-147.

Alves, M.A., Oliveira, P.J. and Pinho, F.T., 2003, Benchmark solutions for the flow of Oldroyd-B and PTT fluid in planar contractions, Journal of Non-Newtonian Fluid Mechanics, vol. 110, pp. 45-75.

Alves, M.A., Pinho, F.T. and Oliveira, P.J., 2000, Effect of a high-resolution differencing scheme on finite-volume predictions of viscoelastic flows, Journal of Non-Newtonian Fluid Mechanics, vol. 93, pp. 287-314.

Alves, M.A., Pinho, F.T. and Oliveira, P.J., 2005, Visualizations of Boger fluid flows in a 4:1 square-square contraction, American Institute of Chemical Engineers Journal, vol. 51, pp. 2908-2922.

Astarita, G. and Greco, G., 1968, Excess pressure drop in laminar flow through sudden contraction: Newtonian liquids, Industrial and Engineering Chemistry Fundamentals, vol. 7, pp. 27-31.

Astarita, G. and Marucci, G., 1974, Principles of non-Newtonian Fluid Mechanics, McGraw-Hill, London.

Astarita, G., Greco, G. and Peluso, L., 1968, Excess pressure drop in laminar flow through sudden contraction: non-Newtonian liquids, Industrial and Engineering Chemistry Fundamentals, vol. 7, pp. 595-598.

Azaiez, J., Guénette, R. and Ait-Kadi, A., 1997, Investigation of the abrupt contraction flow of fiber suspensions in polymeric fluids, Journal of Non-Newtonian Fluid Mechanics, vol. 73, pp. 289-316.

Barnes, H.A., Hutton, J.F. and Walters, K., 1989, An Introduction to Rheology, Elsevier BV.

Barnes, H.A., 2000, A Handbook of Elementary Rheology, University of Wales Institute of Non-Newtonian Fluid Mechanics.

Bicen, A.F., 1982, Refraction correction for LDA measurements in flows with curved optical boundaries, TSI Quarterly, vol. 8, pp. 10-12.

Binding, D.M., 1991, Further considerations of axisymmetric contraction flows, Journal of Non-Newtonian Fluid Mechanics, vol. 42, pp. 27-42.

Binding, D.M., Phillips, P.M. and Phillips, T.N., 2006, Contraction/expansion flows; the pressure drop and related issues, Journal of Non-Newtonian Fluid Mechanics, vol. 137, pp. 31-38.

Bird, R., Armstrong, R.C. and Hassager, O., 1977, Dynamics of Polymeric Liquids Volume 1 Fluid Mechanics, John Wiley & Sons, Inc, U.S.A.

Boger, D.V., 1977, A highly elastic constant-viscosity fluid, Journal of Non-Newtonian Fluid Mechanics, vol. 3, pp. 87-91.

Boger, D.V., 1987, Viscoelastic flows through contractions, Annual Review of Fluid Mechanics, vol. 19, pp. 157-182.

Brinson, H.F., and Brinson, L.C., 2008, Polymer Engineering Science and Viscoelasticity: An Introduction, Springer, New York.

Cable, P.J., and Boger, D.V., 1978 (a), A comprehensive experimental investigation of tubular entry flow of viscoelastic fluids: Part I. Vortex characteristics in stable flow, American Institute of Chemical Engineers Journal, vol. 24, pp. 869-879.

Cable, P.J., and Boger, D.V., 1978 (b), A comprehensive experimental investigation of tubular entry flow of viscoelastic fluids: Part II. The velocity field in stable flow, American Institute of Chemical Engineers Journal, vol. 24, pp. 992-999.

Cable, P.J., and Boger, D.V., 1979, A comprehensive experimental investigation of tubular entry flow of viscoelastic fluids: Part III. Unstable flow, American Institute of Chemical Engineers Journal, vol. 25, pp. 152-159.

Collier, R.J., Petrovan, S. and Patil, P., 2002, Hencky strain shifting of convergent flow measured effective elongational viscosity, Journal of Applied Polymer Science, vol. 87, pp. 1397-1404.

Cox, W.P. and Merz, E.H., 1958, Correlation of dynamic and steady flow viscosities, Journal of Polymer Science, vol. 28, pp. 619-622.

Cross, M.M., 1965, Rheology of non-Newtonian fluids: a new flow equation for pseudo-plastic systems, Journal of Colloid Science, vol. 20, pp. 417-437.

Debbaut, B. and Crochet, M.J., 1988, Extensional effects in complex flows, Journal of Non-Newtonian Fluid Mechanics, vol. 30 pp. 169-184.

Doerpinghaus, P.J. and Baird, D.G., 2003, Pressure profiles along an abrupt 4:1 planar contraction, American Institute of Chemical Engineers Journal, vol. 49, pp. 2487-2498.

Drikakis, D., 1997, Bifurcation Phenomena in incompressible sudden expansion flows, Physics of Fluids, vol. 9, pp. 76-87.

Durst, F., Melling, A. and Whitelaw, J.H., 1976, Principles and Practice of Laser-Doppler Anemometry, Academic Press Inc. (London) Ltd.

Durst, F., Ray, S. Ünsal, B. and Bayoumi, O.A., 2005, The Development Lengths of Laminar Pipe and Channel Flows, Journal of Fluids Engineering, vol. 127, pp. 1154-1160.

Escudier, M.P., 1998, The Essence of Engineering Fluid Mechanics, Prentice Hall Europe.

Evans, R.E. and Walters, K., 1986, Flow characteristics associated with abrupt changes in geometry in the case of highly elastic liquids, Journal of Non-Newtonian Fluid Mechanics, vol. 20, pp. 11-29.

Evans, R.E. and Walters, K., 1989, Further remarks on the lip-vortex mechanism of vortex enhancement in planar-contraction flows, Journal of Non-Newtonian Fluid Mechanics, vol. 32, pp. 95-105.

Fortin, A., Bertrand, F., Fortin, M., Chamberland, É., Boulanger-Nadeau, P.E., Maliki, A.El. and Najeh, N., 2004, An adaptive remeshing strategy for shear-

thinning fluid flow simulations, Computers & Chemical Engineering, vol. 28, pp. 2363-2375.

Fyrippi, I., Owen, I. and Escudier, M.P., 2004, Flowmetering of non-Newtonian liquids, Flow Measurement and Instrumentation, vol. 15, pp. 131-138.

Gatski, T.B. and Lumley, J.L., 1978, Steady flow of a non-Newtonian fluid through a contraction, Journal of Computational Physics, vol. 27, pp. 42-70.

Haas, R. and Durst, F., 1982, Viscoelastic flow of dilute polymer solutions in regularly packed beds, Rheologica Acta, vol. 21, pp. 566-571.

Hassager, O., 1988, Working group on numerical techniques, in: Proceedings of the Fifth International Workshop on Numerical Methods in Non-Newtonian Flows, Lake Arrowhead, USA, Journal of Non-Newtonian Fluid Mechanics, vol. 29, pp. 2-5.

Hsu, C.H. and Chou, T.Y., 1996, Unsteady flow of a second-grade fluid past a backward-facing step, International Journal of Non-Linear Mechanics, vol. 32, pp. 947-960.

Ikeda, Y., Nishigaki, M., Ippommatsu, M. and Nakajima, T., 1994, Optimum seeding particles for successful laser Doppler velocimeter measurements, Particle and Particle Systems Characterization, vol.11, pp 127-132.

Japper-Jaafar, A., 2009, Private communication.

Kwon, Y.I., Seo, D. and Youn, J.R., 2005, Three-dimensional numerical simulation of viscoelastic flow through and abrupt contraction geometry, e-Polymers, no. 053.

Lapasin, R. and Pricl, S., 1995, Rheology of Industrial Polysaccharides: Theory and Applications, Blackie Academic and Professional, Glasgow.

Lapasin, R., Pricl, S., Paoletti, S. and Zanetti, F., 1990, Novel Rheological Model for the gelation kinetics of ionic polysaccharides, Journal of Applied Polymer Science, vol. 41, pp. 1395-1410.

Letelier, M.F. and Siginer, D.A., 2003, Secondary flows of viscoelastic liquids in straight tubes, International Journal of Solids and Structures, vol. 40, pp. 5081-5095.

McKinley, G.H., 1991, Nonlinear Dynmics of Viscoelastic Flows in Complex Geometries, PhD Thesis, Massachusetts Institute of Technology.

Mehta, R.D. and Bradshaw, P., 1979, Technical Notes: Design rules for small low speed wind tunnels, The Aeronautical Journal of The Royal Aeronautical Society, vol. 83, pp. 442-449.

Mompean, G., and Deville, M., 1997, Unsteady finite volume simulation of Oldroyd-B fluid through a three-dimensional planar contraction, Journal of Non-Newtonian Fluid Mechanics, vol. 72, pp. 253-279.

Newton, I., a new translation by Cohen, I.B. and Whitman, A. assisted by Budenz, J., 1999, The Principia, Mathematical Principles of Natural Philosophy, University of California Press.

Nigen, S. and Walters, K., 2002, Viscoelastic contraction flows: comparison of axisymmetric and planar configurations, Journal of Non-Newtonian Fluid Mechanics, vol. 102, pp. 343-359.

O'Callaghan, S., Walsh, M. and McGloughlin, T., 2003, Comparison of finite volume, finite element and theoretical predictions of blood flow through an idealised femoral artery, 2003 Summer Bioengineering Conference.

Oliveira, M.S.N., Yeh, R. and McKinley, G.H., 2006, Iterated stretching, extensional rheology and formation of beads-on-a-string structures in polymer solutions, J. Non-Newtonian Fluid Mech., vol. 137 pp. 137-148.

Oliveira, P.J., 2003, Asymmetric flows of viscoelastic fluids in symmetric planar expansion geometries, Journal of Non-Newtonian Fluid Mechanics, vol. 114, pp. 33-63.

Olson, D.J. and Fuller, G.G., 2000, Contraction and expansion flows of Langmuir monolayers, Journal of Non-Newtonian Fluid Mechanics, vol. 89, pp. 187-207.

Overheim, R.D. and Wagner, D.L., 1982, Light and Colour, John Wiley & Sons, Inc USA

Owens, R.G. and Phillips, T.N., 2002, Computational Rheology, Imperial College Press, London.

Pankhurst, R.C. and Holder, D.W., 1965 (reprint), Wind Tunnel Technique: An account of experimental methods in low- and high-speed wind tunnels, Pitman Press, Bath.

Phan-Thien, N., 2002, Understanding Viscoelasticity: Basics of Rheology, Springer-Verlag, Berlin.

Phillips, T.N. and Williams, A.J., 2002, Comparisons of creeping and inertial flow of an Oldroyd B fluid through planar and axisymmetric contractions, Journal of Non-Newtonian Fluid Mechanics, vol. 108, pp. 25-47.

Pinho, F.T., Oliveira, P.J. and Miranda, J.P., 2003, Pressure losses in the laminar flow of shear-thinning power-law fluids across a sudden axisymmetric expansion, International Journal of Heat and Fluid Flow, vol. 24, pp. 747-761.

Pipe, C.J. and McKinley, G.H., 2009, Microfluidic Rheometry, Mechanics Research Communications, vol. 36, pp. 110-120.

Poole, R.J., Escudier, M.P. and Oliveira, P.J., 2005, Laminar flow of a viscoelastic shear-thinning liquid through a plane sudden expansion preceded by a gradual contraction, Proceedings of The Royal Society London A, vol. 461, pp. 3827-3845.

Poole, R.J., Escudier, M.P., Afonso, A. and Pinho, F.T., 2007, Laminar flow of a viscoelastic shear-thinning liquid over a backward facing step preceded by a gradual contraction, Physics of Fluids, vol.19, pp. 093101-1-093101-17.

Purnode, B. and Crochet, M.J., 1996, Flows of polymer solutions through contractions, Part 1: flows of polyacrylamide solutions through planar contractions, Journal of Non-Newtonian Fluid Mechanics, vol. 65, pp. 269-289.

Purnode, B. and Crochet, M.J., 1998, Polymer solution characterization with the FENE-P model, Journal of Non-Newtonian Fluid Mechanics, vol. 77 pp. 1-20.

Quinzani, L.M., Armstrong, R.C. and Brown, R.A., 1994, Birefringence and laser-Doppler velocimetry (LDV) studies of viscoelastic flow through a planar contraction, Journal of Non-Newtonian Fluid Mechanics, vol. 52, pp. 1-36.

Ramachandran, A. and Leighton, D.T., 2008, The influence of secondary flows induced by normal stress differences on the shear-induced migration of

particles in concentrated suspensions, Journal of Fluid Mechanics, vol. 603, pp. 207-243.

Rodd, A.B., Dunstan, D.E. and Boger, D.V., 2000, Characterisation of xanthan gum solutions using dynamic light scattering and rheology, Carbohydrate polymers, vol. 42, pp. 159-174.

Rodd, L.E., Cooper-White, J.J., Boger, D.V. and McKinley, G.H., 2007, Role of elasticity number in the entry flow of dilute polymer solutions in micro-fabricated contraction geometries, Journal of Non-Newtonian Fluid Mechanics, vol. 143, pp. 170-191.

Rodd, L.E., Scott, T.P., Boger, D.V., Cooper-White, J.J. and McKinley, G.H., 2005, The inertio-elastic planar entry flow of low-viscosity elastic fluids in micro-fabricated geometries, Journal of Non-Newtonian Fluid Mechanics, vol. 129, pp. 1-22.

Rodd, L.E., Scott, T.P., Cooper-White, J.J. and McKinley, G.H., 2005, Capillary break-up rheometry of low-viscosity elastic fluids, Appl. Rheol. vol. 15:1 pp.12-27.

Rosen, S.L., 1993, Fundamental Principles of Polymeric Materials, John Wiley & Sons, New York.

Rothstein, J.P. and McKinley, G.H., 1999, Extensional flow of a polystyrene Boger fluid through a 4:1:4 axisymmetric contraction/expansion, Journal of Non-Newtonian Fluid Mechanics, vol. 86, pp. 61-88.

Rothstein, J.P. and McKinley, G.H., 2001, The axisymmetric contraction-expansion: the role of extensional rheology on vortex growth dynamics and the enhanced pressure drop, Journal of Non-Newtonian Fluid Mechanics, vol. 98, pp. 33-63.

Rudd, M.J., 1972, Velocity measurements made with a laser Dopplermeter on the turbulent pipe flow of a dilute polymer solution, Journal of Fluid Mechanics, vol. 51, pp. 673-685

Samsal, G.P., 1995, A finite volume approach for calculation of viscoelastic flow through an abrupt axisymmetric contraction, Journal of Non-Newtonian Fluid Mechanics, vol. 56, pp. 15-47.

Tanner, R.I., 1985, Engineering Rheology, Clarendon Press, Oxford.

Ternik, P., Marn, J. and Žunič, Z., 2006, Non-Newtonian fluid flow through a planar symmetric expansion: Shear-thickening fluids, Journal of Non-Newtonian Fluid Mechanics, vol. 135, pp. 136-148.

Tirtaatmadja, V., McKinley, G.H. and Cooper-White, J.J., 2006, Drop formation and breakup of low viscosity elastic fluids: Effects of molecular weight and concentration, Physics of Fluids, vol. 18, p. 043101.

Townsend, P. and Walters, K., 1994, Expansion flows of Non-Newtonian liquids, Chemical Engineering Science, vol. 49, pp. 749-763.

Tropea, C., 1995, Laser Doppler anemometry: recent developments and future challenges, Measurement Science and Technology, vol. 6, pp. 605-619.

Van Maanen, H.R.E., 1999, Retrieval of turbulence properties from randomly sampled laser-Doppler anemometry data with noise, PhD Thesis, Technical University of Delft.

Wachs, A. and Clermont, J., 2000, Non-isothermal viscoelastic flow computations in an axisymmetric contraction at high Weissenberg numbers by a finite volume method, Journal of Non-Newtonian Fluid Mechanics, vol. 95, pp. 147-184.

Walters, K. 1975, Rheometry, Chapman and Hall.

Walters, K., 1985, Overview of Macroscopic Viscoelastic Flow, Viscoelasticity and Rheology, Academic Press.

Walters, K., Bhatti, A.Q. and Mori, N., 1990, The influence of polymer conformation on the rheological properties of aqueous polymer solutions, Recent developments in structured continua, vol. 2, Pitman, London.

Weber, W., 1835, Ueber die Elasticität der Seidenfäden, Annual Review of Physical Chemistry, vol. 34, pp. 247-257.

White, F.M. 1999, Fluid Mechanics, Fourth Edition, McGraw-Hill International Editions.

White, F.M., 2006, Viscous Fluid Flow, Third Edition, McGraw-Hill International Editions.

White, S.A. and Baird, D.G., 1986, The importance of extensional flow properties on planar entry flow patterns of polymer melts, Journal of Non-Newtonian Fluid Mechanics, vol. 20, pp. 93-101.

White, S.A. and Baird, D.G., 1988, Flow visualization and birefringence studies on planar entry flow behaviour of polymer melts, Journal of Non-Newtonian Fluid Mechanics, vol. 29, pp. 245-267.

White, S.A. and Baird, D.G., 1988, Numerical simulation studies of the planar entry flow of polymer melts, Journal of Non-Newtonian Fluid Mechanics, vol. 30, pp. 47-71.

White, S.A., Gotsis, A.D. and Baird, D.G., 1987, Review of the entry flow problem: experimental and numerical, Journal of Non-Newtonian Fluid Mechanics, vol. 24, pp. 121-160.

Xue, S., Phan-Thien, N. and Tanner, R.I., 1998 (a), Three dimensional numerical simulations of viscoelastic flows through planar contractions, Journal of Non-Newtonian Fluid Mechanics, vol. 74, pp. 195-245.

Xue, S., Phan-Thien, N. and Tanner, R.I., 1998 (b), Numerical investigations of Lagrangian unsteady extensional flows of viscoelastic fluids in 3-D rectangular ducts with sudden contractions, Rheologica Acta, vol. 37, pp. 158-169.

Yanta, W.J. and Smith, R.A., 1973, Measurements on turbulence-transport properties with a laser-Doppler anemometer, AIAA Paper, 71-287.

Yao, M. and McKinley, G.H., 1998, Numerical Simulation of Extensional Deformations of Viscoelastic Liquid Bridges in Filament Stretching Devices, Journal of Non-Newtonian Fluid Mechanics, vol. 74, pp. 47-88.

Yasuda, K., Armstrong, R.C. and Cohen, R.E., 1981, Shear flow properties of concentrated solutions of linear and star branched polystyrenes, Rheologica Acta, vol. 20, p. 163.

Yeh, Y. and Cummins, H.Z., 1964, Localized flow measurements with a He-Ne laser spectrometer, Applied Physics Letters, vol. 4, p. 176.